SOFT TISSUE CHARACTERIZATION
FROM MINIATURIZED IMAGING PROBES

Dissertation (monograph) approved

by the Doctoral Degree Committee of
Hamburg University of Technology

in pursuit of the academic degree of

Doktor-Ingenieurin (Dr.-Ing.)

written by
Sarah Latus

from
Hamburg, Germany

2025

Chair of Examination Board: Prof. Dr.-Ing. Hoc Khiem Trieu
1st Reviewer: Prof. Dr.-Ing. Alexander Schlaefer
2nd Reviewer: Prof. Dr.-Ing. Tobias Knopp
Date of oral examination: 10th December 2025

https://doi.org/10.15480/882.16342
ORCID: https://orcid.org/0000-0002-9796-7001

Dedication

This work is dedicated to my father, who taught me that every problem has a solution.

Acknowledgments

This work was created out during my time as a research associate at the Institute of Medical Technology and Intelligent Systems (MTEC) at Hamburg University of Technology. During this period, I had the opportunity to conduct research together with many different people. For this opportunity and the intensive supervision, I would first like to sincerely thank Professor Alexander Schlaefer. I also thank Professor Tobias Knopp for the joint research and the review of this work.

During my time at the MTEC Institute, I was accompanied by many colleagues to whom I am very grateful for their continuous support, professional discussions, and many special moments. I would especially like to highlight Matthias, Max, Thore, and Marco, who accompanied me not only as colleagues but also as friends throughout the entire time. I would like to thank Finn and Robin for their constructive and appreciative criticism throughout the process, but especially towards the end of my doctoral studies. Furthermore, I was able to build upon important work by my predecessors, without which my research would not have been possible. Special thanks go to Christoph, Nils, Sven, and Omer. I would also like to thank Johanna, Martin, Stefan, Lennart, Sarah, Debayan, Lennart, and Konrad for the collaboration on the different joint projects. In addition to the scientific work, Katrin, Michael, Martin, and Katja supported me in organizational matters, thanks to all.

Big thanks go to my friend and former boss Henning, who opened the door to the doctorate for me. Thanks to you and also to Gerd for the final push to successful completion. Moreover, I would like to thank my colleagues from UKE (Florian Griese, Philipp Breitfeld, and Axel Heinemann), UKSH Kiel (Matthias Lutz), and the University of Lübeck (Tim Eixmann and Gereon Hüttmann) for the cooperation.

Most importantly, I would like to thank my family and friends, especially my husband and my two children, for their constant support, patience, and understanding of my goals.

Table of Contents

Abstract

Characterizing soft tissue properties is crucial for diagnosing and treating diseases with high morbidity and mortality, such as cancer and atherosclerosis. Changes in tissue morphology, structure, or elasticity can serve as important indicators of pathological conditions. Traditionally, physicians relied on manual observations, such as palpation, to assess tissue properties. But these methods are of a qualitative fashion and limited when investigating deep tissue structures or during minimally invasive interventions. In these scenarios, the physician must receive feedback on the haptic and visual impressions of the tissue, as direct viewing and palpation are no longer possible. Externally applied imaging modalities, such as Magnetic Resonance Imaging or Computed Tomography, offer high spatial resolution and functional capabilities that enhance disease detection and treatment planning. However, their real-time application is often limited. Especially when navigating medical instruments towards small tissue lesions, a local and real-time assessment of soft tissue properties and interactions is crucial. Therefore, miniaturized imaging and sensing concepts are of interest for assessing soft tissue properties in real-time and from within the body.

Optical coherence tomography (OCT) offers various advantages for this purpose. First, it provides micrometer-scale resolution and high temporal sampling of one-dimensional depth scans. Second, this modality facilitates the integration of compact, fiber-based imaging optics into medical instruments. However, when applying miniaturized OCT probes in-vivo, relative motion between the probe and tissue results in a varied spatial orientation of the probe's imaging coordinate systems. Reconstructing and interpreting image data with unknown spatio-temporal sampling schemes poses a major challenge for this thesis. Three miniaturized OCT probe designs and their corresponding image analysis methods are studied. In particular, the influence of probe and tissue motion on the transformation of OCT depth scan sequences into pseudo-spatial, two-dimensional, or three-dimensional images is examined. Additionally, advanced image analysis methods are explored to derive information on the tissue morphology, elastography, and instrument-tissue interactions from the complex OCT data. The conducted experimental studies demonstrate the potential in assessing cardiovascular morphology, characterizing sosft tissue elasticity, and aiding needle navigation during epidural punctures. Highlighting the benefits of innovative miniaturized probe designs and advanced imaging processing for real-time soft tissue analysis, while preserving visual and tactile feedback during minimally invasive procedures.

Chapter 1

Introduction

The human body consists of several soft tissue structures. Each type of tissue, e.g., organs, muscles, fat tissue, or skin, has a different composition and structure of water, collagen, and elastin, resulting in specific morphological and mechanical properties [1]. Determining the morphological structure, e.g., shape, size, color, or mechanical features, is relevant for the characterization of soft tissue [2]. In addition to localizing and distinguishing soft tissues and their boundaries, it is crucial to identify changes in tissue features associated with diseases. For example, soft tissue enlargements have been associated with fatty deposits [3], calcifications, or lesions such as tumors or cysts. A change in tissue stiffness has been correlated to tissue abnormalities for various diseases ranging from cancer to atherosclerosis [4].

Assessing these variations is crucial for early diagnosis and treatment. Thus, methods for characterizing soft tissue have been iteratively developed. Initially, physicians relied on their subjective impression, e.g., when palpating soft tissue structures or examining their macroscopic morphology [5]. In subcutaneous tissue structures or open surgery, altered tissue properties are usually directly visible [6, 7] or palpable. However, this manual palpation or direct visual examination is no longer possible for deep tissue structures. Therefore, various medical imaging modalities have been studied to assess variations inside the human body. X-ray imaging and Computed Tomography (CT) scans are typically used to analyze bone structures and surrounding tissues like cartilage, whereas Magnetic Particle Imaging (MPI) and Ultrasound (US) imaging are generally employed to assess soft tissue structures. The enhanced spatial resolution of recent imaging modalities, combined with functional imaging techniques, allows for the early detection of small cancer lesions [8]. Improving the assessment of the lesion's size and position, and therefore allowing for an accurate diagnosis and treatment plan. Additionally, imaging methods for interventional characterization of soft tissue structures have been investigated in recent years. Interventional imaging is primarily utilized to guide the navigation of instruments toward specific lesions. For example, in Percutaneous Coronary Intervention (PCI), miniaturized devices must be carefully steered toward the plaque lesion. Similarly, during a biopsy, precise needle placement relative to the lesion is crucial for obtaining the correct sample. For all scenarios, the physician must receive feedback on the haptic and visual impression of the tissue and the instrument's motion, while direct viewing and palpation are no longer possible. This is especially important when navigating towards small tissue lesions that are prone to relative motion. Thus, imaging modalities are required that enable the localization and characterization of soft tissue with high spatial and temporal resolution.

Interventional imaging modalities that are applied from outside the human body include X-ray imaging, Digital Subtraction Angiography (DSA) [9], CT [10], or Magnetic Resonance Imaging (MRI) [11]. CT and MRI, for example, have been utilized during neurosurgery [12, 13] to assist instrument placement. However, the application of these modalities during interventions is limited due to the long imaging period and susceptibility to relative tissue and instrument motion [14]. Due to the patient's breathing and pulsation, or when interacting with medical instruments, the tissue is deformed and displaced, causing the lesion's position to change during interventions. Another limitation of interventional MRI or CT imaging is the restricted exposure to ionizing radiation and energy. In contrast, US as a non-ionizing imaging modality shows substantial benefits for application during interventions. Although US has a smaller Field of View (FOV) and penetration depth (up to 10 cm) compared to CT or MRI, it provides real-time acquisition of two- or three-dimensional images with axial resolution of up to 100 µm. Making it especially beneficial for needle or instrument navigation tasks US, where the images are captured from subcutaneous tissue structures [15]. Optical Coherence Tomography (OCT) is an additional imaging modality that has been studied for enface tissue characterization, e.g., in ophthalmology [16], or neurosurgery [17]. Infrared light is coupled through small optical fibers towards superficial tissue structures. The acquired one-dimensional depth-resolved scans (A-scans) deliver speckle information also from a few millimeters beyond the tissue surface and offer a high spatial resolution of up to 5 µm in air. Recent OCT system support A-scan rates of up to 6 MHz [18], enabling high spatial and temporal imaging resolution. Combined with rapid scanning setups, these systems allow high-speed acquisition of volumetric data. Local deviations in tissue structure can be resolved in the signals and associated speckle patterns. However, due to light absorption within soft tissue, the penetration depth of OCT is limited to a few millimeters [19]. Hence, OCT has most frequently been applied for the analysis of ex-vivo tissue samples or superficial tissue structures during open surgery.

To address the limitations of traditional externally or superficially applied imaging modalities, recent developments have focused on miniaturized sensing and imaging probes, which are additionally utilized from inside the human body to enhance navigation and tissue characterization [20]. In particular, the integration of small sensors and imaging probes into instrument tips, catheters, or needles has been investigated [21]. White light endoscopy is well established for surgical navigation or intraluminal tissue analysis [22], e.g., during bronchoscopy, gastroscopy, or laryngoscopy. The recorded images enable a macroscopic analysis of the tissue, provided the line of sight is not obscured, e.g., by blood or fluids. A significant disadvantage of these endoscopic probes is that they are limited to analyzing superficial tissue structures. In contrast, miniaturized US imaging probes have been developed with the potential to visualize subsurface tissue structures, e.g., for intraluminal imaging [23]. In addition, OCT imaging probes have been proposed for minimally invasive tissue characterization. With its increased axial image resolution, OCT enables microscopic analysis of tissue morphology and elasticity with an order of magnitude higher resolution compared to US probes. As such, the application of OCT is promising for high-resolution intraoperative analysis of tissue properties and is considered a vital precursor to histological examination [24].

However, applying miniaturized OCT imaging probes inside the human body poses relevant challenges for localization, spatial sampling, and navigation, which are systematically studied in this thesis. First, in contrast to externally applied imaging modalities, the position of the imaging probe's coordinate system is unknown. Therefore, methods to localize the imaging probe using global position information, e.g., from externally applied US imaging, need to be investigated. Second, respiration, pulsation, and contractions induce relative motion between probe and tissue, resulting in an unknown spatial sampling of the OCT data. Therefore, methods to quantify these relative motion patterns are investigated to correctly assign the OCT image data in 3D space. Third, OCT image data acquired during instrument motion contain information on the tissue properties in a complex fashion that is not directly interpretable. Thus, image processing methods are developed for systematically analyzing tissue properties that can be converted into externally applied modalities. To address these three challenges, this thesis develops various methods to facilitate the spatial organization, sampling, and interpretation of OCT data, thereby optimizing navigation and precision in minimally invasive procedures.

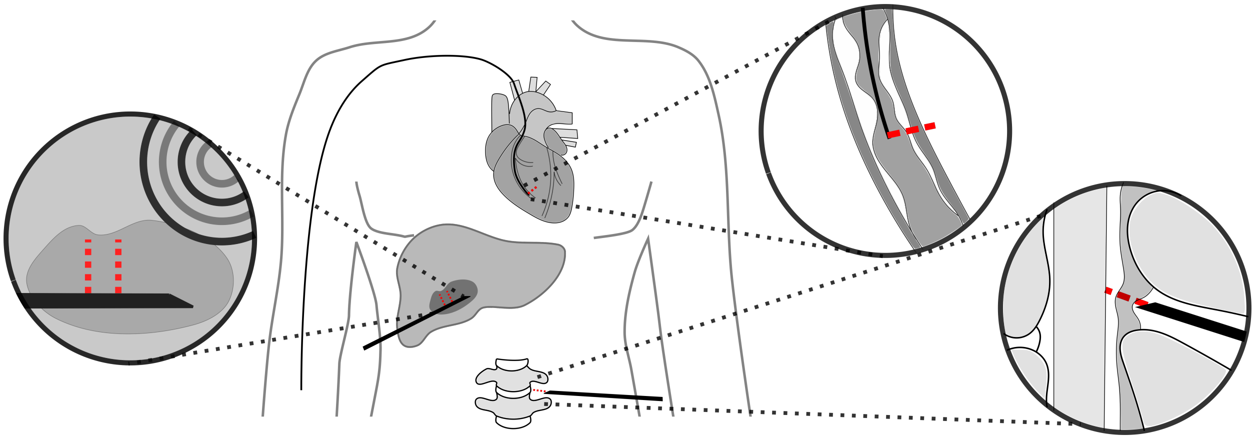

Figure 1.1 Overview of studied application scenarios for miniaturized imaging probes: Analyzing coronary disease by quantification of vascular morphology, analyzing cancer lesions by quantification of elasticity, assistance for epidural punctures by quantification of soft tissue interactions. The investigated miniaturized imaging probes are sketched with their one-dimensional OCT imaging axes highlighted in dashed red.

1.1 Applications for Miniaturized Imaging Probes

In this work, miniaturized OCT imaging probes are investigated to assess tissue properties locally and in real-time, thereby optimizing modern minimally invasive interventions. Three different application scenarios for improved soft tissue characterization are studied and visualized in Figure 1.1.

Quantification of Soft Tissue Morphology

Our first application uses an Intravascular Optical Coherence Tomography (IVOCT) probe to characterize vascular morphology. Coronary diseases lead to critical stenosis in the arteries, which have different morphological and elastic properties. The number of people suffering from coronary heart disease is rising in the aging society [25]. Therefore, early detection and treatment of coronary diseases are crucial. Consequently, assessment of vascular tissue morphology is getting more important to assist treatment planning, e.g., selection of stent type and size [26–28]. Furthermore, accurate detection and characterization of plaque formations are crucial for determining the stenosis dimension and associating the stage of atherosclerosis, ranging from lipid-rich to calcified plaque [29]. To prevent stenting and other invasive interventions, atherosclerosis should be detected in the early lipid stage, where medication helps to prevent later infarction. In DSA, the blood circulation and thereby the position and extension of a stenosis is visible, but the resolution and projection errors affect the quantification. A distinction between stenosis stages is not possible, and early-stage stenoses are hardly visible. Furthermore, the necessary injection of contrast agent is restricted or even prohibited for patients with kidney diseases [30, 31]. Alternatively, intracoronary pressure wires are used to physically measure the impact of a stenosis on blood flow and utilize this information as a surrogate for risk assessment of myocardial infarction. Nevertheless, an extensive characterization of the vascular tissue is not possible. For the characterization and detection of early-stage lesions, the imprecise morphological information from X-ray images or intracoronary pressure measurement is incomplete. Thus, imaging catheters have been applied for intravascular observation of vascular structures. A relevant optimization of diagnostic and therapeutic results of PCI with intravascular image guidance, i.e., using Intravascular Ultrasound (IVUS) and IVOCT, has been observed to be associated with a lower number of deaths from cardiac causes [32]. An imaging probe attached to the proximal end of the catheter is pulled through the stenosis during the image acquisition process. IVUS offers cross-sectional images of the arteries with a penetration depth of up to 10 mm. The arterial wall can be segmented in the IVUS images to extract the stenosis diameter. Furthermore, the speckle pattern of the vascular wall can be used to classify different stenosis stages [33]. IVOCT serves as an alternative imaging modality, offering increased image resolution but reduced imaging depth. However, when imaging vessel structures in the lower cardiovascular branches, the quantification of diameters and the classification of stenosis stages are enhanced. Furthermore, the apposition of stents can be analyzed in follow-ups, which is vital for novel bioresorbable stents and helps prevent restenosis.

With miniaturized probes, we can reach lesions and locally acquire image data with high spatial resolution. Most clinical decisions are made based on two-dimensional cross-sectional images of intravascular structures. The sequence of OCT A scans obtained during retraction and rotation of the imaging probe also contains three-dimensional information. However, due to the relative movements between the probe and tissue, this information is distorted. In contrast to external imaging systems with fixed coordinate systems, reconstructing the three-dimensional morphology of vascular lesions presents a significant challenge. Relying only on the intravascular image data, registration to a global coordinate system is not directly possible. Therefore, in recent studies, external tracking of the imaging probes has been proposed to support not only navigation but also spatial image registration. This also yields in the first research scope of this thesis, assessing the vascular morphology from intravascular OCT data while compensating for artifacts, e.g., resulting from catheter bending or heartbeat motion. In particular, a systematic study of imaging and catheter movement parameters is conducted to investigate the influence on the reconstruction of vascular morphology.

Quantification of Soft Tissue Elasticity

Our second application focuses on characterizing soft tissue elasticity using miniaturized probes. Most diseases affect the elastic properties of tissue. A variation of these properties can be observed through manual palpation of the subcutaneous tissue structures [5] and can be used as an initial indicator in diagnosis. A correlation between increased tissue stiffness and disease has been shown for conditions ranging from cancer to atherosclerosis [4, 34, 35]. Manual palpation is no longer feasible in deeper tissue structures and during Minimal Invasive Surgery (MIS). Furthermore, manual palpation is a strongly subjective estimate. Therefore, methods for the objective quantification of elastic properties from medical image data, known as elastography, have been derived [36]. Initially, the elastic properties were assessed by analyzing soft tissue deformation induced by a known compression, known as compression-based elastography. Alternatively, shear waves have been excited to quantify their propagation through soft tissue structures. As the wavelengths and velocities of mechanical waves vary depending on the stiffness, these wave characteristics are crucial in determining the elasticity of soft tissues. Advantages of shear wave elastography include the ability to reach areas deep inside the tissue and the simpler quantitative interpretation of the measurements. Optical Coherence Elastography (OCE) allows for high resolution analysis of elastic tissue properties [37]. However, due to the limited penetration depth of light, miniature probes are necessary to reach structures within the body, such as vessel walls. Consequently, the second scope of this thesis focuses on the design of a miniaturized elastography probe and the investigation of necessary shear wave sampling and excitation schemes to enable the quantification of tissue elasticities from within the tissue.

Quantification of Soft Tissue Interactions

Our third application focuses on characterizing soft tissue interaction to assist in needle navigation. Needles are either applied for minimally invasive diagnosis or therapy of soft tissue structures. In the case of diagnosis, the most common application of needles is the biopsy. External imaging is used for initial diagnosis, and then the examined tissue is punctured to obtain small tissue samples for further pathological analysis. During therapy, needles are used to inject medicine at a specific region, e.g., for anesthesia, or antibiotic treatment. Furthermore, needles are applied for Brachytherapy. Here, small radiation sources have to be accurately injected into a tumorous region. External image data acquired before the needle insertion is used for treatment planning and navigation during insertion [38]. However, the tissue gets compressed, deformed, and cut with arbitrary courses during needle insertion, and the planned insertion trajectories become inappropriate. The unknown tissue mechanics during insertion impede the needle placement and require high expertise and a fast response to abrupt motion. A simulation of these movements has been proposed in several studies, assuming perfectly matched tissue phantoms, but the translation to in-vivo punctures is limited. Therefore, several sensing modalities have been studied to assess relevant parameters during in-vivo needle placement. For example, external imaging or needle tracking is usually applied using US imaging, MRI, C-arm, electromagnetic tracking [39, 40]. Using these externally applied modalities, the evaluation of needle pose and orientation based on external imaging is limited due to the resolution of the images. Imaging artifacts, e.g., those caused by the needle itself, essentially impede navigation and needle placement assistance. Consequently, sensors and imaging probes are embedded in needles to sense tissue properties at the needle tip. For example, needles have been developed with force sensing at the needle tip [Q]. Moreover, miniaturized imaging probes are integrated into instruments to analyze tissue and instrument interactions, enabling intraoperative navigation that is adapted to tissue deformation and displacements. As the third milestone of this thesis, the question arises whether motion and deformation of tissue during instrument interaction can be sensed with OCT imaging and serve as information for tissue characterization. In particular, relevant features from OCT signals captured at a needle tip should be investigated to quantify the soft tissue motion.

For all of these application scenarios, we rely on the same conditions. We aim to sense tissue characteristics from miniaturized OCT imaging probes. To simplify manufacturing, we do not embed complex optical scanning setups in the probes. We therefore face several challenges when processing the one-dimensional OCT data. Firstly, the soft tissue information is only available as a temporal sequence of single-column depth images lacking uniform spatial sampling. Secondly, the position and orientation of miniaturized imaging probes within the tissue are usually unstable and unknown. Hence, a position of the OCT image data relative to target tissue structures needs to be determined. Thirdly, the complex OCT signals promise soft tissue analysis with high axial resolution. However, extracting relevant signal features from both the OCT intensity and phase signals is crucial. This is particularly relevant for scenarios where relative tissue motion needs to be assessed for the characterization of soft tissue.

1.2 Outline

This thesis is structured as follows. Following this general introduction, an overview of the imaging modalities employed in this thesis is provided. Additionally, the theoretical background of methods for image acquisition and reconstruction is introduced. In the following chapter, the state of the art regarding miniaturized imaging probes for soft tissue characterization is summarized. Based on these findings, the research questions of this thesis are introduced. Subsequently, the methods and materials investigated for characterizing soft tissue in terms of morphology, elastography, and motion are presented. For each subtopic, the developed or customized miniaturized imaging probes and the proposed image processing methods for quantifying soft tissue properties are introduced. In chapter five, the respective experimental studies for the systematic evaluation of our tissue characterization approaches are described. In the following chapters, the experimental results are illustrated, summarized, and discussed. Finally, a conclusion is presented for the developed and investigated miniaturized imaging probes and image processing and interpretation methods.

Chapter 2

Medical Imaging for Miniaturized Probes

Several imaging modalities are applied in clinical practice to assess soft tissue properties. In this thesis, we aim to investigate tissue characterization by estimating the tissue morphology, motion, or elasticity from miniaturized OCT imaging probes. Furthermore, we consider imaging modalities capable of external assessment of tissue properties and instrument motion, such as X-ray imaging, MPI, and US. We use these external imaging modalities as a reference to evaluate the soft tissue characteristics derived from the complex OCT signals. We introduce the respective imaging modalities, their measurement principle, and concepts for multi-dimensional image acquisition in the following sections. Furthermore, relevant concepts for assessing motion information are summarized, with a special focus on phase-sensitive imaging approaches.

2.1 Optical Coherence Tomography

OCT is an imaging modality measuring the interference patterns of infrared light reflected by tissue. In general, the absorption and reflection of electromagnetic light waves in tissue depend on the frequency and wavelength of the emitted light. Using low-coherent infrared light sources, axial imaging resolutions of 5 to 20 µm are possible with the drawback of limited penetration depths of a few millimeters [41]. In the following sections, we introduce the characteristics of electromagnetic waves and the OCT imaging technologies, namely Time-Domain OCT (TD-OCT), Spectral-Domain OCT (SD-OCT), and Swept-Source OCT (SS-OCT). Additionally, we describe common image acquisition techniques, such as optical scanning setups and miniaturized probes, as well as related image reconstruction methods. Please note that this summary is based on findings by Fujimoto et al. [42] and Aumann et al. [41], describing the fundamentals of OCT imaging.

Infrared light can be expressed as a plane electromagnetic wave $\mathbf{E}(z,t)$ with spatial and temporal components, assuming a simplified one-dimensional wave propagation along z

$$\mathbf{E}(z,t) = \mathbf{E}_0 e^{i(k_\mathrm{o} z - w_\mathrm{o} t + \phi)}. \tag{2.1}$$

The wave characteristics are mainly described by the electric field amplitude $\mathbf{E}_0$, the wavelength λ_o, wavenumber $k_\mathrm{o} = 2\pi/\lambda_\mathrm{o}$, and the frequency f_o with $w_\mathrm{o} = 2\pi f_\mathrm{o}$. An optional phase shift is expressed with the angle ϕ.

OCT imaging utilizes the interference properties of two coherent light waves. Constructive or destructive interference patterns result depending on the respective phase shift difference $\Delta\phi$ and path length difference Δz_o of the light waves.

OCT imaging system setups are based on the principle of Michelson-interferometry [43]. A low-coherent infrared light source is used, whose light is split into a sample arm and a reference arm. The reflected light waves are superimposed, and the respective interference patterns are measured on a detector. The most prominent OCT system setups, namely TD-OCT, SD-OCT, and SS-OCT, are shown in Figure 2.1 with variations in the applied light source, detector, or reference arm. In the following, we will describe the relevant physical relationships and influences of these OCT setup components on the acquired signals.

The light source properties are described by the central wavelength $\lambda_{\mathrm{o},0}$, bandwidth $\Delta\lambda_\mathrm{o}$, or spectral bandwidth Δk_o. Most commonly, broadband infrared light sources with a Gaussian spectrum of width $\Delta\lambda_\mathrm{o}$ and central wavelengths $\lambda_{\mathrm{o},0}$ from 900 to 1300 nm are applied. The coherence length l_c of a light source is described as

$$l_\mathrm{c} = \delta z_\mathrm{o} = \frac{2\ln 2}{\pi}\frac{\lambda_{\mathrm{o},0}^2}{\Delta\lambda_\mathrm{o}} = \frac{2\sqrt{\ln 2}}{\Delta k_\mathrm{o}}, \tag{2.2}$$

forming an important property determining the axial resolution of the OCT system.

The interference signal measured at the OCT system's detector depends on the optical path lengths of the reference z_R and sample z_S arm as well as the respective reflectivity functions (r_R, r_S). Assuming a light wave $\mathbf{E}_\mathrm{i}$ emitted by the light source, defined as in Equation 2.1, the light waves refracted from the reference and sample arm can be expressed as

$$\mathbf{E}_\mathrm{R}(z,t) = \frac{E_\mathrm{i}}{\sqrt{2}}\left(r_\mathrm{R}(z_\mathrm{R}) \otimes e^{i2kz_\mathrm{R}}\right) \tag{2.3}$$

and

$$\mathbf{E}_\mathrm{S}(z,t) = \frac{E_\mathrm{i}}{\sqrt{2}}\left(r_\mathrm{S}(z_\mathrm{S}) \otimes e^{i2kz_\mathrm{S}}\right). \tag{2.4}$$

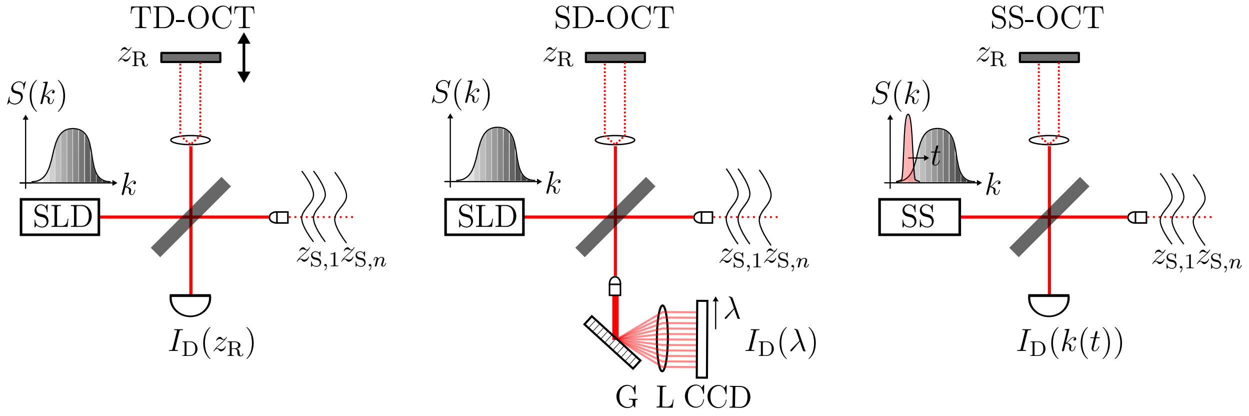

Figure 2.1 Variation of OCT system components, i.e., light source, interferometer, reference arm, measurement arm, and detector, for TD-OCT, SD-OCT, and SS-OCT systems.

In the literature [42], the sample arm reflectivity function $r_S(z_S)$ is simplified by assuming that light backscattered from N soft tissue boundaries at the depths $z_{S,m}$ correspond to a discrete number of delta-function reflections with

$$r_S(z_S) = \sum_{m=1}^{M} r_{S,m}\delta(z_S - z_{S,n}). \tag{2.5}$$

The interfering wave field measured at the detector $\mathbf{E}_D$ will result as

$$\mathbf{E}_D = \frac{\rho_o}{2}(\mathbf{E}_R + \mathbf{E}_S), \tag{2.6}$$

with ρ_o stating the responsivity of the detector as defined by Izatt et al. [43].

Initially, TD-OCT systems were studied that are composed of a broadband light source, a single element detector, and a motorized reference arm (see Figure 2.1). Using this setup, the temporal coherence of interfering light waves is measured. The axial movement of the reference arm and the attached mirror varies the imaging depth $z_{S,m}$ in the sample arm. The interference signals are sequentially measured at the detector for each reference arm position z_R. This iterative reference arm motion results in comparatively long measurement times, which may potentially influence image quality, especially when imaging perfused tissue structures [44].

Alternatively, Fourier-Domain OCT (FD-OCT) systems have been proposed, offering much faster image acquisition. FD-OCT systems are based on spectral interferometry, which assumes measurable spectral interference patterns for each path length difference of two coherent waves [43]. In SD-OCT imaging systems (Figure 2.1), a broadband light source, a fixed reference arm, and a sample arm are applied. The backscattered and interfered light waves are separated at a grating in the system's detector. In particular, using spectral sampling on a spectrometer and a measurement with a line scan camera, such as a Charge-Coupled Device (CCD) camera. SS-OCT systems achieve spectral sampling by applying a swept light source (Figure 2.1). Again, the reference arm is kept at a stable position. Sweeping through the overall light source spectrum Δk_{o} effectively results in a narrow spectral sampling interval δk_{o} with different central wavenumbers k_0. Subsequently, interference patterns $I_{\mathrm{D}}(k)$ are measured as a function of time. The spectral interference patterns are measured with FD-OCT system and have been expressed by Izatt et al. [43] as

$$I_{\mathrm{D}}(k_{\mathrm{o}}) = \frac{\rho_{\mathrm{o}}}{2} \langle |\mathbf{E}_{\mathrm{R}} + \mathbf{E}_{\mathrm{S}}|^2 \rangle. \tag{2.7}$$

Expanding the magnitude squared function, a spectral interference signal $I_{\mathrm{D}}(k_{\mathrm{o}})$ is introduced by Fujimoto et al. [42] results as a function of the wavenumber k and the sample depth $z_{\mathrm{S},m}$

$$\begin{aligned} I_{\mathrm{D}}(k_{\mathrm{o}}) &= \frac{\rho_{\mathrm{o}}}{4} \big(S(k_{\mathrm{o}})(R_{\mathrm{R}} + \sum_{m=1}^{M} R_{\mathrm{S},m})\big) \\ &+ \frac{\rho_{\mathrm{o}}}{2} \Bigg(S(k_{\mathrm{o}}) \sum_{m=1}^{M} \sqrt{R_{\mathrm{R}} R_{\mathrm{S},m}} \Big(\cos\big(2k_{\mathrm{o}}(z_{\mathrm{R}} - z_{\mathrm{S},m})\big)\Big)\Bigg) \\ &+ \frac{\rho_{\mathrm{o}}}{4} \Bigg(S(k_{\mathrm{o}}) \sum_{m=1}^{M} \sqrt{R_{\mathrm{R}} R_{\mathrm{S},m}} \Big(\cos\big(2k_{\mathrm{o}}(z_{\mathrm{S},m} - z_{\mathrm{S},l})\big)\Big)\Bigg). \end{aligned} \tag{2.8}$$

Thus, for an evaluated wavenumber k_{o}, light reflections from the reference arm R_{R} and different tissue depths $R_{\mathrm{S},m}$ lead to cosine oscillations. The frequency of these oscillations is proportional to the optical path length difference Δz_{o}, causing constructive interference. Continuous-time inverse Fourier Transformation is applied on Equation 2.8, resulting in the intensity profile over the imaging depth z is given as

$$\begin{aligned} i_{\mathrm{D}}(z) &= \frac{\rho_{\mathrm{o}}}{8} \big(\gamma(z)(R_{\mathrm{R}} + \sum_{n=1}^{N} R_{\mathrm{S},n})\big) \\ &+ \frac{\rho_{\mathrm{o}}}{4} \Bigg(\sum_{n=1}^{N} \sqrt{R_{\mathrm{R}} R_{\mathrm{S},n}} \Big(\gamma\big(2(z_{\mathrm{R}} - z_{\mathrm{S},n})\big) + \gamma\big(-2(z_{\mathrm{R}} - z_{\mathrm{S},n})\big)\Big)\Bigg) \\ &+ \frac{\rho_{\mathrm{o}}}{8} \Bigg(\sum_{n=1}^{N} \sqrt{R_{\mathrm{S},n} R_{\mathrm{S},m}} \Big(\gamma\big(2(z_{\mathrm{S},n} - z_{\mathrm{S},m})\big) + \gamma\big(-2(z_{\mathrm{S},n} - z_{\mathrm{S},m})\big)\Big)\Bigg). \end{aligned} \tag{2.9}$$

Similarly, the OCT phase signal can be extracted after Fourier transformation of the spectral signal described in Equation 2.8. In the following sections, we will refer to these depth profiles as one-dimensional depth scans or A-scans.

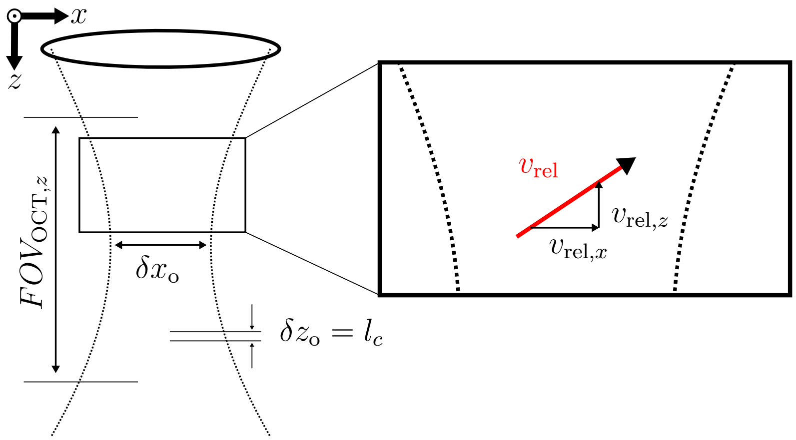

Figure 2.2 OCT sample beam characteristics that rely on the optical parameters of the used lens (NA) and the light source of the imaging system. While the axial resolution δz_o of the beam depends solely on the laser light source, the parameters of the associated lens determine the lateral resolution δx_o and the maximal axial field of view $FOV_{\mathrm{OCT},z}$. Assuming a particle movement between subsequent depth scans, the velocity $v_{\mathrm{rel},z}$ can be estimated from the OCT phase signal.

The previous section outlines the fundamental principles for acquiring spectral OCT signals to assess one-dimensional depth scans. An essential requirement for achieving high lateral and axial resolution in these depth scans is the application of appropriate imaging optics in the sample arm. The axial resolution δz is determined solely by the laser's coherence length (see Equation 2.2). However, optimizing the sample light beam and defining a focal point are achievable with optical lenses, even in a miniaturized fashion, using Gradient-Index (GRIN) fibers [45].

In Figure 2.2, the influence of the optical lens parameters on the sample beam profile is sketched. Based on Aumann et al. [41], adjusting the lens's numerical aperture NA influences the axial FOV and lateral resolution δx_o, being defined as

$$\delta x_\mathrm{o} = \sqrt{2\ln 2}\frac{\lambda_{\mathrm{o},0}}{\pi NA} \tag{2.10}$$

Generally, it is assumed that signal quality is optimized at the focal depth and diminishes with increasing depth beyond this point. In addition, the axial FOV size is defined by [46] as

$$FOV_{\mathrm{OCT},z} = \frac{0.221\lambda_{\mathrm{o},0}}{sin^2(\frac{sin^-1(NA)}{2})}. \tag{2.11}$$

Consequently, a low numerical aperture increases the axial FOV but reduces the lateral resolution. Depending on the application scenario, either a high lateral resolution with increased

NA, e.g., for optical coherence microscopy [47], or a high imaging depth, e.g., for intravascular applications [48], is meaningful. It should be noted that the optical principles described are defined for light propagation in air, which is assumed to be a homogeneous medium. When the infrared light beam encounters soft tissue structures, several optical effects, such as absorption, diffraction, and scattering, occur. As the penetration depth increases, the amount of light backscattered from the tissue structures decreases. Consequently, the OCT depth scans acquired from soft tissue structures usually show a decrease in signal intensity with the imaging depth z. In addition, the design of the focal depth may no longer be suitable.

For multi-dimensional acquisition of OCT image data, optical scanning setups have been proposed. Most commonly, optical mirrors or galvanometer scanners have been integrated into scan heads to deflect the infrared laser beam along one or two spatial axes [49, 50]. These benchtop setups, also called enface setups, have mainly been applied for ex-vivo tissue analysis, i.e., for analyzing the tissue morphology or detecting lesion boundaries [51]. Surgical microscopes with integrated OCT scanning setups enable the in-vivo analysis at the tissue surface, e.g., in ophthalmology [52, 53]. For MIS applications, optical setups have been developed that are small enough to be integrated into medical instruments. Optical mirrors or prisms are used to deflect the light beam, e.g., to enable OCT depth scanning perpendicular to the probe axis [54]. A two- or three-dimensional sampling of tissue features is possible with additional translation or rotation of the whole imaging probe or several optical components. Intravascular imaging probes for IVOCT are one example of these designs that are commonly applied in medical practice [55]. These probes have also been embedded in medical needles for multi-dimensional imaging during insertion. Recent research on miniaturized OCT imaging probes also focuses on multi-core fiber probes to enable the parallel acquisition of optical signals without mechanically varying the optical axis [56–58].

Depending on the optical setup and the system specifications, the OCT image data can be arranged in various spatial and temporal representations. Assuming a stationary recording position and one-dimensional scanning, the following recorded OCT depth scans can be placed side by side, with the columns indicating the time and the rows the imaging depth. This arrangement is also referred to as OCT M-scan, indicating motion-invariant imaging. With optical scanning devices, such as scan heads, the depth scans are arranged according to the specified scanning parameters. Deploying a single galvanometer scanner enables the acquisition of two-dimensional images, referred to as OCT B-scans. Similarly, using a second scanner, three-dimensional image acquisition is possible. These volume scans are also referred to as C-scans.

It should be noted that with OCT scanning setups, such as scan heads, depth scans are typically acquired one after another for each spatial position. In the literature, two spatiotemporal scanning profiles are differentiated [59]. First, the acquisition of two- or three-dimensional images through the fast execution of a complete lateral scanning profile per time point. This scanning mode is also referred to as BM-scan when acquiring two-dimensional images. Second, a triggered and fast sequential acquisition of one-dimensional scans on the same position and subsequent adjustment of the scanning position. For the latter, high temporal resolutions are achieved per A-scan position. Assuming a two-dimensional scan pattern, the following image data sets are referred to as MB-scan. Considering the different application scenarios, it is crucial to find a feasible trade-off between spatial and temporal sampling. Recent SS-OCT systems enable fast temporal sampling of depth scans with frequencies f_{OCT} of up to 6 MHz [18, 60]. Together with fast optical scanning setups, OCT volume rates of up to 800 Hz are possible. However, the fast volume rate is only possible with a reduction in spatial resolution, especially for lateral sampling. For MIS probes, the scanning schemes are not necessarily arranged along Cartesian coordinate systems. For example, the imaging optics of the IVOCT probes are rotated around the probe axis and retracted, allowing the sequence of one-dimensional depth scans to be arranged diversely. With other single-fiber probe designs, the acquired depth scans are mainly arranged over time. However, this representation is not necessarily equivalent to the motion-invariant OCT M-scan mentioned above, as probe or relative movements of the tissue occur.

In addition to the morphological tissue characteristics that can be extracted as a magnitude complex OCT signal, the phase signal has been analyzed to estimate the functional and physiological tissue parameters. For example, to assess the propagation characteristics of shear waves [61] or the deformation of tissue [62, 63]. By determining the phase difference between sequentially acquired depth scans, changes in the optical path length caused by relative sample motion or other dynamic processes can be observed [64]. In particular, the axial motion components of particles traveling through the sample's light beam are analyzed. According to the Doppler effect [65], this measurement is possible because the motion of particles induces a frequency shift in the detected interference signal. This shift manifests as phase differences between sequentially acquired depth scans $\Delta\Phi$. After simplifying the complex interference signal in Equation 2.8 the phase difference $\Delta\Phi$ has been defined by Kennedy et al. [66] as

$$\Delta\Phi(z) = \Phi_{j+1}(z) - \Phi_j(z) = \frac{4\pi n_{\mathrm{o}} v_{\mathrm{rel},z} T_{\mathrm{OCT}}}{\lambda} \tag{2.12}$$

after the multiplication of subsequent complex interference signals

$$I_{j+1}(z) \cdot I_j^*(z) = A_{j+1}(z) A_j(z) e^{(\Phi_{j+1}(z) - \Phi_j(z))}. \tag{2.13}$$

Please note, that the velocity v_z and period T_{OCT} in Equation 2.12 state the particle velocity along the axial imaging axis z as visualized in Figure 2.2 and the average time interval between acquiring two OCT depth scan, respectively. n_{o} has been introduced in [66] as average refractive index along the optical beam. The particle movement relative to the sample light beam is shown in Figure 2.2, whereby an oblique movement relative to the imaging axis is assumed. Since the phase difference $\Delta\Phi$ is evaluated per imaging pixel along z and is inherently modulo 2π, phase unwrapping algorithms are necessary to reconstruct true phase shifts when they exceed this range, e.g., due to decorrelation effects [67], timing jitter problems [68], or speckle noise [69].

These phase analysis approaches are also referred to as phase-sensitive OCT. An essential prerequisite for analyzing relative tissue motion is the stability of the phase signal. Thus, for subsequently acquired depth scans, the path length differences between the reference and sample arms should be constant. Effects influencing the system's optical path length differences and causing phase shifts include temperature variations, mechanical vibrations, or other instabilities of the optical setup, such as the light source. Most commonly, phase shift is described as a continuous but slow drift in phase values that impede the interpretation of motion from the phase data [70]. Consequently, optimal OCT signal conditions are fulfilled if the optical setup remains stationary and the measurement is performed at the same spatial position. Whenever transversal movements of probe or tissue occur, the sample light beam of two subsequent depth scans should overlap at least for the full half-width maximum to remain reliable OCT phase analysis.

Especially for high-speed SS-OCT systems, phase instability is a common issue that needs to be compensated [68]. On the one hand, adaptations of the OCT system components have been proposed, e.g., additional reference arm setups [71]. As the speckle noise and signal decorrelation effects are primarily related to the random modulations of the OCT signals, e.g., due to the spatial and temporal coherence of random light wave reflections, a mathematical formulation for compensation is not straightforward. Therefore, deep learning methods have been applied in recent years to extract the complex signal variations, thereby optimizing the OCT signal quality. For example, generative adversarial network architectures have been studied to reduce speckle noise and increase the image contrast [72, 73]. Similarly, network structures combining generative components and complex neural networks have been presented for phase unwrapping [74].

2.2 Ultrasound Imaging

US is an imaging modality that operates without ionizing radiation, making it a safe and versatile choice. Typically portable, US imaging systems offer flexibility across various applications. US imaging is widely employed to examine subcutaneous soft tissues. It facilitates the investigation of morphological, functional, and elastographic information, offering valuable insights into diverse medical conditions. Its capability for real-time imaging makes ultrasound an essential tool in medical practice, particularly for guiding instruments during procedures such as anesthesia. Given these benefits, ultrasound imaging is increasingly utilized in diagnostic and interventional medical settings. In the following sections, the measurement principle, concepts for imaging transducers, and related image reconstruction approaches are introduced. Please note that this introduction to US imaging summarized is based on findings by Szabo et al. [75], Chan et al. [76], and Jenderka et al. [77].

Investigating the propagation of acoustic waves through tissue structures is the basic idea of US imaging. Acoustic waves are excited, and the intensity and runtime of wave echoes reflected from soft tissue boundaries are measured. The tissue characteristics, e.g., density, influence the wave parameters of induced acoustic waves. In general, the wave velocity c_a of an acoustic wave in fluids can be stated as

$$c_\mathrm{a} = \frac{1}{\sqrt{\rho_\mathrm{a}\kappa_\mathrm{a}}}, \tag{2.14}$$

with ρ_a and κ_a as material parameters of density and compressibility, respectively. The acoustic impedance Z_a combines these parameters as

$$Z_\mathrm{a} = \sqrt{\frac{\rho_\mathrm{a}}{\kappa_\mathrm{a}}}. \tag{2.15}$$

In soft tissue structures, wave velocities c_a ranging between 1400 and $1585\,\mathrm{m\,s^{-1}}$ are estimated [75].

During US image acquisition, frequencies f_a from 2 to $60\,\mathrm{MHz}$ are applied to excite piezoelectric elements, resulting in acoustic wavelengths λ_a in the range of sub-millimeters, based on the general wave equation

$$\lambda_\mathrm{a} = \frac{c_\mathrm{a}}{f_\mathrm{a}}. \tag{2.16}$$

In soft tissue structures, acoustic waves are either transmitted through or reflected from boundaries. The reflected or transmitted acoustic waves' intensities I_a depend on the respective acoustic impedance Z_i of adjacent tissue structures. For a perpendicular wave incidence, the coefficients of reflected and transmitted waves are given as

$$R = \frac{I_{\mathrm{a,R}}}{I_{\mathrm{a,0}}} = \frac{Z_2 - Z_1}{Z_2 + Z_1} \tag{2.17}$$

and

$$T = \frac{I_{\mathrm{a,T}}}{I_{\mathrm{a,0}}} = \frac{4 \cdot Z_1 \cdot Z_2}{(Z_2 + Z_1)^2}, \tag{2.18}$$

respectively, with $R + T = 1$. Whenever the impedance difference of neighboring soft tissue structures is small, large transmission coefficients T follow. Hence, acoustic waves can propagate deeply into the tissue, and their echoes remain measurable. However, absorption and scattering affect the propagation of acoustic waves. Consequently, additional damping coefficients $\alpha(f_{\mathrm{a}})$ are used by Szabo et al. [75] to describe the acoustic intensity I_{a} along the imaging depth z with

$$\frac{I_{\mathrm{a}}(z, f_{\mathrm{a}})}{I_0} = e^{-2\alpha(f_{\mathrm{a}}) \cdot 2z}. \tag{2.19}$$

In addition, it has been shown that damping and frequency are proportional to each other [76]. Thus, the damping of acoustic waves increases with higher frequencies and imaging depth.

In US imaging, a sequence of echoes is received after emitting an acoustic wave, with the timing of each echo corresponding to the spatial distances between the piezoelectric element and the respective tissue surfaces. The following descriptions for complex US signal extraction are based on Dössel et al. [78]. When considering multiple cycles C of ultrasound pulses, the received signal is typically a high-frequency signal composed of several summed cosine waves. Each component wave reflects variations in the acoustic impedance of the tissues caused by differences in tissue density and elasticity. This superposition of waves forms the composite signal that carries essential information about the anatomical structures. By processing these signals, e.g., using the Hilbert transform, complex US signal representations are possible, which aid in better resolving tissue characteristics and improving the resolution of the ultrasound images.

Piezoelectric actuators are most commonly embedded in US imaging transducers to excite and measure acoustic waves. Based on the piezoelectric effect [79], applying a sinusoidal voltage leads to mechanical expansion and relaxation of the piezoelectric material. With a good mechanical coupling to the skin and for high actuation frequencies ($f_{\mathrm{a}} > 2\,\mathrm{MHz}$), this vibration excites an acoustic wave that propagates perpendicular to the piezoelectric surface. When acoustic waves reflected from tissue structures return to the transducer,

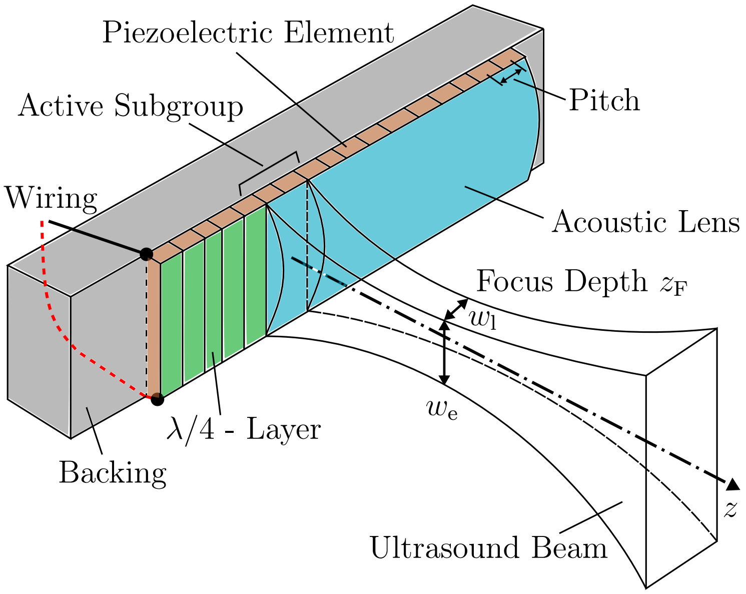

Figure 2.3 Linear array transducer sketch with piezoelectric actuators embedded between damping body (backing), $\lambda/4$-adaption layer, and acoustic lens. A subgroup of elements is used for US beamforming. The number of active elements and set focus depth define the lateral imaging resolution (w_l). The piezoelectric aperture and the acoustic lens define the elevational resolution (w_e).

they stimulate the piezoelectric material, generating a measurable electrical voltage. This conversion from electric into acoustic energy and vice versa is also known as the reciprocal or direct piezoelectric effect. Thus, the same piezoelectric element can be used for both transmitting and receiving acoustic waves.

In US imaging transducers, piezoelectric actuators are usually embedded between a damping body, an adaption layer, and an acoustic lens. An exemplary schematic is shown in Figure 2.3, adapted from [77, 80]. The damping body, also called backing, prevents acoustic waves from propagating backward. Especially for miniaturized US transducers, a huge effort has been devoted to designing these backing layers to improve imaging quality [81, 82]. To minimize impedance differences between the piezoelectric material and the environment, the $\lambda/4$-adaption layer is attached. For generating acoustic wave fields with a thin and almost constant cross-section, acoustic lenses are attached to the $\lambda/4$-layer. This achieves a focusing of the acoustic field in the distance of z_F.

Please note that the focusing of US beams is separated in defining the required elevational resolution (w_e), concerning the previously described geometries of the piezoelectric elements and lens materials. During image acquisition, the number of active elements and the set focus depth z_F define the lateral imaging resolution (w_l). Similar to the OCT imaging principles described before, the axial image resolution in US imaging depends solely on the set wave actuation parameters. In particular, the axial resolution is determined to be equal to half the spatial pulse length (SPL), which is defined as the product of the number of cycles C in an ultrasound pulse and the wavelength λ_a of the acoustic wave [83]. Based on the wave equation in Equation 2.16, the wavelength relies on the set frequency f_a for actuating the piezoelectric elements. Consequently, Ng et al. [83] defined the axial imaging resolution as

$$SPL = C\frac{c_0}{f_\mathrm{a}}. \tag{2.20}$$

A shorter spatial pulse length enhances axial resolution, thereby improving the system's ability to resolve structures that are closely spaced. Thus, imaging transducers with higher actuation frequencies are beneficial for the high-resolution analysis of tissue structures. However, following Equation 2.19, increasing axial resolution comes with the disadvantage of increased damping and, thus, limited imaging depths.

US imaging transducers differ in the number, dimension, and arrangement of integrated piezoelectric actuators. The pitch, defined as the equidistant distance between actuator centers [75], and the overall actuator width, also called aperture size, directly influence the imaging width and resolution. In clinical linear array transducers, up to 192 piezoelectric actuators are arranged in a straight line. To ensure high axial resolutions, it involves piezoelectric actuation frequencies of $f_\mathrm{a} > 5\,\mathrm{MHz}$. These imaging parameters and transducer designs are usually applied to image tissue structures close to the surface. In phased array transducers, fewer piezoelectric actuators are installed to minimize the overall width of the probe. The piezoelectric elements are actuated with phase differences in the triggered waves to steer the acoustic wave field with different angles relative to the probe [84]. This phase of delayed actuation is also referred to as beam steering [85]. Together with the probe design, it minimizes acoustic damping from planar tissue surfaces, enabling the imaging of deep tissue structures, such as those behind or between the ribs. Alternatively, curved array transducers have been developed to image structures deep inside the human body, e.g., for abdominal gynecological sonography [86]. The actuator elements are arranged on a curved line of different radii, enabling versatile imaging patterns [87]. Typically, operation frequencies of 2.5 to 10 MHz are used for increased focus depths. In novel US volume probes, piezoelectric actuators have also been arranged in two-dimensional arrays. Due to the comparatively small aperture width of up to 3 cm [88], beam steering is necessary to increase the lateral imaging width. Miniaturized US transducers with a curved arrangement of piezoelectric elements have, for example, been proposed for endobronchial [89] applications. Alternatively, single piezoelectric elements with widths smaller than 3 mm have been embedded in medical instruments. Here, proximal attached motors translate or rotate the piezoelectric element, enabling multi-dimensional image acquisition [90, 91]. Alternatively, several miniaturized piezoelectric actuators have been combined in a ring formation, using beam steering for spatial tissue scanning [92]. For these miniaturized US transducers [93], small focus depths z_F and high image resolutions are necessary, utilizing actuation frequencies of up to 40 MHz.

There are various approaches for extracting functional soft tissue information from the complex US signals, beyond the morphological features contained in the amplitude of these signals. Analogous to phase-sensitive OCT imaging, approaches to assess relative tissue motion from US signals are investigated. According to the principles of the Doppler effect, changes in the frequency of acoustic waves Δf_a they are reflected from moving objects occur as

$$\Delta f_\mathrm{a} = \frac{2 f_\mathrm{a}}{c_\mathrm{a}} v_\mathrm{rel} cos(\theta), \tag{2.21}$$

with θ stating the angle between the US beam and the moving particle and v_rel the relative particle motion velocity. To determine this frequency shift from the US signals received, the process involves quadrature demodulation of the signal followed by a Fourier transformation. In particular, peaks in the resulting spectral signals are identified to estimate the difference from the initial actuation frequency f_a. Doppler US is widely used in medical diagnostics to detect abnormalities in blood flow, such as blockages, narrowing of vessels, or irregular heartbeats, thereby aiding in the diagnosis and management of various cardiovascular conditions [94]. In addition to these frequency-based Doppler techniques, approaches to assess the tissue elasticity based on the propagation of induced shear waves have been investigated. Depending on the motion amplitude analyzed, different computational methods have been considered [95]. Since shear wave-induced displacements are typically of subpixel size, evaluating phase differences offers advantages. Consequently, the Loupas algorithm, as detailed by Loupas et al. [96] in their study on blood flow estimation, is predominantly utilized as a phase-based motion estimator. Unlike the Doppler method, which estimates the frequency shift Δf_a from the continuous return of acoustic waves and their corresponding frequency shifts, this phase-based approach evaluates the temporal phase variations across successive US scans to determine relative tissue motion.

For the acquisition of US image data, it is important to transmit and receive the acoustic signals with precise timing. Once a transmit pulse is sent, echoes traveling back to the transducer are associated with an US image until the next transmit pulse is started. There are two main concepts to control the transmit and receive cycles, namely B-mode and plane wave imaging.

B-mode imaging, also known as brightness-mode imaging, utilizes multiple piezoelectric elements to direct the acoustic wave field onto a one-dimensional beam. This steering is achieved by delaying the excitation of the selected transducer elements, also known as transmit beam forming. Afterward, the time differences t of echoes received at all transducer elements are used to estimate the echo amplitudes in different depths z along the excited beam. Specifically, the high-frequency echo signal is processed, for example, with a Hilbert transformation or IQ demodulation, to estimate the envelope of the received signal. To compensate for echo attenuation with increasing run times, a Time Gain Compensation (TGC) is applied, which enables a depth-dependent amplification of the received echo signals. The distance z of objects relative to the transducer elements can be estimated, assuming a constant wave velocity c_a

$$z = c_\mathrm{a}\frac{t}{2}. \tag{2.22}$$

This transmit and receive sequence is repeated for several beams to sequentially record scan lines of the US image. An increase in the number of beams acquired per US image results in higher image resolutions with the drawback of longer image acquisition time. The duration T_RX of one transmit and receive sequence is dependent on the set imaging depth and assumed wave velocity. Hence, the maximum Pulse Repetition Frequency (PRF) is inversely proportional to the duration T_RX. For example, a B-mode image acquisition with $N_\mathrm{US} = 64$ scan lines results in an imaging speed of

$$f_\mathrm{US} = 1/(N_\mathrm{US}T_\mathrm{RX}) = 50\,\mathrm{Hz}. \tag{2.23}$$

For general clinical applications, such as needle guidance, this frame rate is sufficiently high.

As an alternative high-speed US imaging concept, plane wave imaging has been developed [97]. All transducer elements are utilized during the transmit sequence for plane-wave image acquisition. All elements are simultaneously excited to generate a plane wave parallel to the transducer. Alternatively, a delayed excitation of the elements is possible to steer the plane wave with a certain angle β_US relative to the transducer. After plane-wave excitation, the echoes are received by all elements. The raw US data received from the elements is processed by considering the time delays of the echos relative to the spatial arrangement of the excited plane wave, also referred to as receive beam forming. As the transmit and receive sequences are controlled in parallel for all elements, the image acquisition speed is significantly increased compared to B-mode imaging approaches. Using modern US systems plane wave imaging frequencies of $f_\mathrm{PRF} = 20\,\mathrm{kHz}$ are possible. The increased imaging speed is beneficial for imaging soft tissue motion, such as tracking the propagation of shear waves.

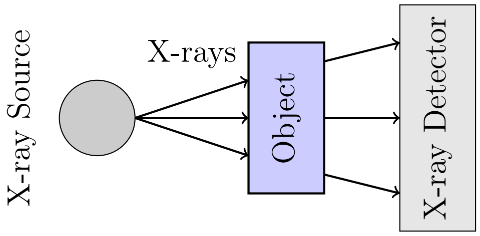

Figure 2.4 X-ray imaging measurement principle: X-ray beams travel radially from the source through the object towards a two-dimensional detector. Depending on the material properties that influence the absorption, scattering, and attenuation of X-rays, different intensity values are measured at the detector.

2.3 X-Ray Imaging

X-ray imaging is one of the earliest medical imaging modalities and remains one of the most commonly applied imaging techniques in medical diagnostics [98]. Application scenarios range from projection radiography, e.g., for fracture [99] or lung examinations [100], to functional X-ray imaging for temporal analysis of body functions [101], e.g., of lung [102] or heart [103]. The following descriptions of the measurement principle and imaging systems are based on Seibert et al. [104] and Bushberg et al. [105].

The measurement principle for projection radiography is depicted in Figure 2.4. An X-ray tube generates radiation that travels through an object, i.e., the human body, towards a two-dimensional detector. Assuming the X-ray tube to be the origin of radial ray generator with an opening angle defined by the focusing elements, the beams proceed through the object and cause a projection signal at a specific two-dimensional detector position. Due to absorption and scattering effects at tissue and bone structures, different radiation patterns are measured at the detector. According to the Lambert-Beer law [105], the attenuation depends on the material properties through which the beam propagates. Hence, the intensity I_{D} measured at the detector has been defined in [105] as

$$I_{\mathrm{X}} = I_{\mathrm{X},0} \cdot e^{-\int_0^d \mu(x)dx}, \tag{2.24}$$

whereas the overall tissue thickness d and attenuation coefficients $\mu(x)$ of the individual tissue structures x needs to be considered. The attenuation coefficient μ is due to various physical effects, including the photoelectric effect, Compton-scattering, and Rayleigh-scattering [106].

X-ray imaging systems were initially constructed for single-shot image acquisitions, where the orientation of the detector and the X-ray source is variable by simple manual mechanical adjustments. The X-ray tube and detector are most commonly installed in a C-arm setup for fluoroscopic or angiographic X-ray imaging to enable versatile orientations and projection views relative to the human body [107]. Due to its flexible alignment, a C-arm system is especially suitable for interventional applications, e.g., to assist instrument navigation during percutaneous coronary interventions [108]. Sequence of X-ray images are acquired with frequencies f_C of up to 40 Hz. Here, DSA enables vascular imaging by subtracting two consecutive images with and without exposure to a contrast agent. Examining the blood circulation and vessel structure allows a fast analysis of cardiovascular diseases [109]. Plaque formation in the vessel wall is one marker of coronary heart disease, which can lead to critical occlusions. These stenosis can be visualized with DSA, and their impact on the heart muscle´s blood supply can be analyzed.Analyzing the blood circulation after stent placement enables an optimization of stent apposition and expansion.

In modern catheter laboratories, bi-plane DSA systems are installed to enable the interventional analysis of tissue structures from two projective views. Bi-plane angiography systems consist of two C-arms that allow synchronous image acquisition. In PCI, the C-arms are usually positioned in Right Anterior Oblique (RAO) and Left Anterior Oblique (LAO) orientation. More specifically, RAO is an orientation with the X-ray tube placed dorsal on the left and the image detector placed ventral on the right of the patient. These orientations are further defined with the set angle γ relative to the patient couch. By triangulating the two projective views, the three-dimensional geometry of the tissue can be estimated [110]. Beyond vascular tissue analysis, minimally-invasive instrument navigation is optimized with fluoroscopic imaging from at least two orthogonal directions, e.g., to prevent injury to the vessel structure. Moreover, the application of the bi-plane DSA system is suitable for interventions with high risk, such as the treatment of brain aneurysms [111].

In addition to radiation exposure, one limitation of X-ray imaging is the limited contrast in images of tissue structures with similar attenuation coefficients. While bone or lung tissues with high or low attenuation, respectively, are visible on X-ray images, soft tissue structures mainly consisting of collagen structures, fat, and water are hardly distinguishable from each other. The injection of contrast agents enhances the visibility of tissue structures, such as vessels or organs. However, iodine components of the contrast medium are deposited in organs and can last over a long period of time [31, 112].

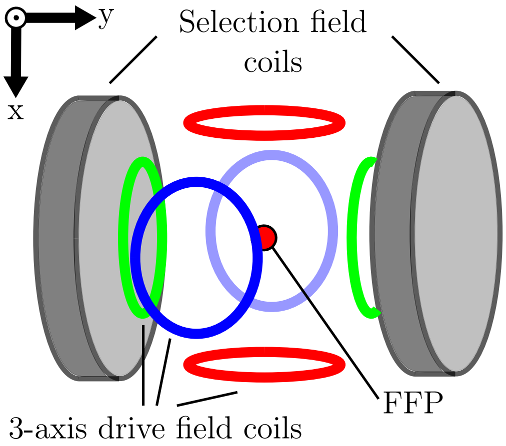

Figure 2.5 MPI system setup with highlighted magnetic coils to generate a selection field and drive field. The drive field coils are colored according to the respective magnetic field directions in x, y, and z. Using these drive fields, the highlighted field free point (FFP) can be shifted. Additional focus field assemblies are not shown.

2.4 Magnetic Particle Imaging

MPI is a novel non-invasive imaging modality that has been recently developed to image the spatial and temporal distribution of injected Superparamagnetic Iron Oxide Nanoparticles (SPIONs) [113, 114]. Still, a clinical application has not been achieved. However, preclinical studies demonstrate its significance as a future medical imaging modality [115]. As a first application, blood circulation and vascular morphology have been analyzed after SPIONs injection. Alternatively, the SPIONs are combined in a solid medium and attached to instruments. These markers can be used to estimate the position or orientation of an instrument, also in submillimeter resolution [116].

Multiple magnetic coils are required to generate specific magnetic field properties in a predefined three-dimensional space over time to measure the spatial and temporal distribution of SPIONs. A general MPI system setup is depicted in Figure 2.5.The SPIONs exhibit nonlinear magnetization behavior that is used for localization and concentration estimation. During image acquisition, an external modulation field is applied to change the magnetization of the particles periodically over time. This periodic field variation should have a high amplitude to bring the particles into saturation. With excitation frequencies f_{MPI} ranging between 25 and 100 kHz, a rectangular magnetization curve will follow. Measuring the induced voltages with a receiving coil yields a spectral signal with harmonic components, multiples of the excitation frequency. These harmonic components are only caused by SPIONs in saturation and are thereby used to detect the particles.

An additional selection field is necessary for the spatial localization of SPIONs. Here, two permanent magnets face each other to generate a Field Free Point (FFP) in the center of these magnets. For all positions outside of this FFP, the remaining strong magnetic field prevents a period magnetization of the particles excited by the modulation field. This means that a signal can only be measured from those SPIONs that are located at the FFP. By moving the target relative to the FFP, a three-dimensional MPI measurement is possible. However, this iterative positioning of the measurement object leads to increasingly longer measurement times, which are not suitable for fast spatial and temporal data acquisition.

A manual displacement of the measurement object is a time-consuming process. Therefore, three additional magnetic coils are embedded in the MPI system setup with orthogonal orientations to each other. These drive field coils induce homogeneous magnetic fields in the x-, y-, and z-directions to shift the FFP in three spatial dimensions. FFP shifting enabled with the drive field coils is limited to a few centimeters. Hence, three additional orthogonal homogeneous fields are used as focus fields with higher magnetic field strengths but low frequencies. This focus field shifts the three-dimensional volume stimulated by the drive field in space. Additionally, this focus enables a general downsizing of the evaluated volume to minimize the image acquisition time and energy.

Summarized, a MPI measurement of three-dimensional targets is composed of several magnetic field stimulations affecting a sequential positioning of the FFP. During this series of L sequential measurements, values U_l are recorded. To estimate the three-dimensional particle concentration, a preliminary calibration of the imaging setup is necessary. Moving a small object of precisely known particle concentration successively through the measurement volume of Q positions and measuring the inducted field amplitude provides a system matrix G_{lq}. Finally, the particle concentration per position $c_{\mathrm{MPI},q}$ can be expressed in a linear system of equations

$$U_l = \sum_q G_{lq} C_q. \tag{2.25}$$

Applying the Thikhonov-regularisation, a stabilized solution of the inverse problem in Equation 2.25 is achieved with

$$\|U_l - \sum_n G_{lq} c_{\mathrm{MPI},q}\|^2 + \lambda^2 \|\sum_q c_{\mathrm{MPI},q}\|^2 = \min. \tag{2.26}$$

Solving this equation results in the particle concentration per position $c_{\mathrm{MPI},q}$. Finally, depending on the drive field frequencies applied for three-dimensional shifting of the FFP, the MPI volume rates vary.

Several research MPI imaging setups have been developed in the past years. The first commercially available MPI scanner setups for pre-clinical image analysis are sold by Bruker Corporation. These scanner systems enable small-animal studies, e.g., investigating blood flow or drug delivery in mouse, rat, guinea pig, or rabbit models, with volume rates of up to 46 Hz. In addition, Magnetic Insight offers preclinical MPI systems with integrated CT imaging. The combination of CT and MPI promises increased sensitivity and MPI image resolution. While these MPI system setups are built for the preclinical analysis, the maximum FOV is limited by the bore diameter of a few centimeters. Therefore, the current research focuses on next-generation human-sized MPI system setups, addressing the challenges of maximized bore diameter while achieving high imaging resolution and volume rates [117]. For functional brain imaging, a MPI head scanner setup has been proposed in recent years [118, 119]. In addition to increasing the imaging FOV, the development of transportable MPI systems has also been considered in recent developments [120] to facilitate interventional applications. Beyond the advancements of system setups, the MPI research community focuses on investigating novel tracers and optimizing the image reconstruction methods, aiming for even higher imaging resolutions [121]. Furthermore, combined SPIONs and virtual FFP have been investigated to apply a motion via focused magnetic stimulation [122–124].

Chapter 3

State of the Art

To assess soft tissue characteristics with high resolution, several concepts for miniaturized probes have been developed in recent years [125, 126]. Imaging probes have been commonly investigated for acquiring RGB, ultrasound, or optical image data from within tissue. In the following sections, we provide an overview of different imaging probes and sensors studied to quantify soft tissue morphology, elastography, and motion during tissue-instrument interactions.

3.1 Quantification of Vascular Morphology

Minimal-invasive PCI involves intraluminal analysis and treatment of cardiovascular lesions by passing instruments and imaging catheters through arteries, e.g., transfemoral or transradial. Guidewires are initially positioned at the region of interest, e.g., under external X-ray angiography guidance. Subsequently, these wires and external imaging assist in navigating the instruments and imaging catheters.

Intravascular imaging has been proposed to improve the diagnosis and therapy of cardiovascular diseases [127–130]. During PCI, intravascular imaging is performed interventional in addition to previous external imaging, e.g., X-ray angiography or MRI. Local examination of tissue structures with higher image resolution promises a more differentiated diagnosis, e.g., in determining the stage and extent of plaques [33, 131–134], assessing coronary stenting [135–137], or monitoring the course of therapy [138, 139]. Several studies demonstrate the increased diagnostic and therapeutic impact of intravascular imaging compared to conventional X-ray angiography [32, 140]. Most commonly, IVUS and IVOCT have been applied for intravascular imaging. While IVUS offers a penetration depth of up to 15 mm [141], the imaging depth of IVOCT is limited to a few millimeters [142]. Thus, IVUS is preferred

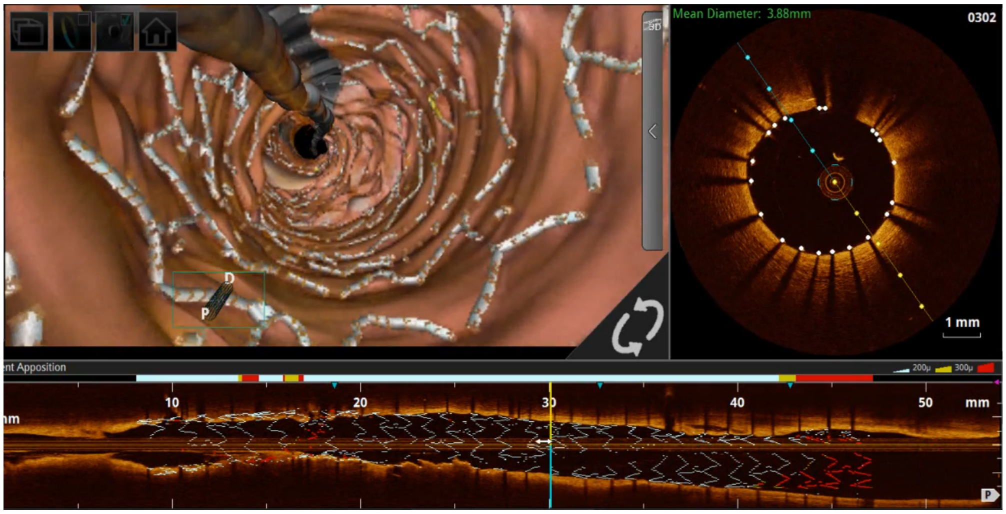

Figure 3.1 Exemplary view on user interface of the clinical IVOCT imaging system, Ilumien Optis. The cross-sectional IVOCT images (right) enable an analysis of vascular layers. The long section (bottom) displays the vascular geometry, assuming a straight probe trajectory. A rendered three-dimensional visualisation of the image data is shown on the left.

for examining lesions in the main trunk of coronary arteries that have a luminal diameter of up to 6 mm. However, IVOCT has been reported as a promising tool for detailed tissue examination due to its increased resolution compared to IVUS [143, 144]. Especially, the differentiation of plaque stage, e.g., lipid and calcified, and estimation of morphological dimension is improved with IVOCT [145].

An exemplary visualization of IVOCT image data is shown in Figure 3.1. While two-dimensional cross-sectional views of intravascular image data have primarily been investigated to assess luminal diameters or distinguish vascular lesions, the three-dimensional representation of intravascular images promises an additional benefit, e.g., by analyzing the longitudinal expansion of a plaque formation. However, the spatial reconstruction is based on simplified probe motion assumptions, hampering the assessment of the actual three-dimensional shape of vascular structures. Imaging catheters are fed through the vessel structures at unknown spatio-temporal trajectories during imaging acquisition. In modern clinical catheter labs, intravascular imaging is therefore often combined with external imaging or catheter tracking systems to enable spatial registration of intravascular imaging data. Even if vessel geometry can be assessed from external imaging, detecting and compensating for the relative motion between the probe and tissue is difficult. These unknown relative motion profiles lead to imaging artifacts caused, for example, by heartbeat motion or catheter bending [146, 147]. Given the need for accurate quantification of plaque diameter and length, as well as the importance of three-dimensional reconstruction and spatial registration of intravascular image data, these have become essential research challenges.

In the following sections, we give an overview of intravascular imaging systems that have been applied for PCI. Furthermore, we will present several miniaturized probe designs that have been developed for intravascular imaging applications. In addition, various concepts for three-dimensional image reconstruction involving external imaging or catheter tracking have been investigated and are described below.

3.1.1 Intravascular Imaging Probes

In recent years, miniaturized probes for intravascular imaging have been introduced that encompass different modalities and mechanical designs. On the one hand, probes differ in the type of motion required to acquire cross-sectional or three-dimensional images. IVOCT imaging probes are usually composed of a single side-viewing imaging optic that needs to be rotated and translated for three-dimensional image acquisition [148–152]. For IVUS image acquisition, single-element or multi-element probe designs have been developed [153–155]. Arranging multiple piezoelectric elements in a circular shape enables beam forming and cross-sectional image acquisition without probe rotation, also referred to as solid-state IVUS probes [156, 157].

For IVUS and IVOCT probes with a single imaging optics or a single piezoelectric element embedded, also referred to as mechanical probes, rotation by either proximally or distally positioned motors has been proposed. Proximal actuation allows for a simplified probe design with the disadvantage that the acquired image data may be distorted due to heartbeat motion [146] or non-uniform torsion of the catheter, also referred to as Non-Uniform Rotational Distorsion (NURD) artifact [158–161]. Miniaturized motors have been embedded at the distal end of imaging catheters to minimize the influence of catheter bending and torsion on the image acquisition [162–165]. Furthermore, probe designs with a distally actuated prism have been proposed, e.g., for analyzing lung tissue [166]. In these probe designs, piezoelectric actuators enable an oscillating motion of the prism positioned in front of the optical fiber. These distally actuated probes have the major drawback of increased dimensions and require a large number of wires that need to be passed through the catheter. Imaging catheters are designed for single-use, which requires a very low-cost and straightforward production process for the probes. Therefore, affordable imaging probes with distally positioned motors have not yet been developed for clinical practice.

In addition to the mechanical probe design, different optical designs have been studied to improve the imaging characteristics for IVOCT. Imaging optics developed for IVOCT catheter usually comprise single-mode fibers spliced to GRIN fiber lenses for optimal focusing. Employing an angle-polished fiber-tip enables lateral deflection of the imaging laser beam [167, 168] with small core diameters of up to 0.02 mm. Alternatively, lens-free optical probes have been proposed with angle-polished multi-mode fiber optics spliced to a single-mode fiber [169]. Further miniaturization of IVOCT imaging optics has been achieved by novel 3D printed optics [170, 171] or fiber ball lens setups [172]. A significant drawback of IVOCT imaging is the need to administer contrast agents to prevent imaging artifacts caused by blood particles. Thus, IVOCT catheters with expandable balloons have been presented to minimize imaging artifacts and astigmatism [145, 173].

3.1.2 Image Reconstruction Methods

Two- or three-dimensional representations of intravascular imaging data are used to analyze cardiovascular disease. While cross-sectional views help to diagnose the type of artery lesions or stent apposition at a particular position, three-dimensional models are necessary to interpret the extent of a lesion [174]. Assuming perfect imaging conditions for single-element or single-optic probes without catheter bending and rotational artifacts, three-dimensional reconstruction of intravascular image data can be performed solely based on the set motion parameters for probe rotation and translation. However, these optimal conditions are no longer valid for in-vivo image acquisition. The imaging probes follow trajectories of unknown curvature through the artery, and heartbeat motion influences the image acquisition. Thus, various methods have been proposed for optimizing the three-dimensional arrangement of intravascular image data.

For example, the co-registration of IVOCT and DSA image data has been studied, e.g., based on rigid registration methods [175–177], to improve the interpretation of IVOCT image data. In these studies, the cross-sectional IVOCT images are registered to spatial positions within the DSA images. As the DSA images are usually acquired from one orientation, only projective views of the three-dimensional vessel structures are available. This leads to potential inaccuracies in registration and spatial interpretation. Therefore, advanced methods for extracting three-dimensional vessels from a single DSA image have been studied in recent research.

As a first approach, the DSA image data acquired successively from two projective views have been triangulated, which allows an optimized reconstruction of three-dimensional vessel structures [178–181]. Subsequently, the cross-sectional intravascular images are arranged on the resulting three-dimensional luminal centerline of the vessel structure [182]. However, this approach neglects the heart motion and related vascular deformation that occur during image acquisition. In particular, an equidistant temporal sampling is assumed even though non-uniform IVOCT probe translation might occur. With the recent developments in SS-OCT systems, high A-scan rates of up to 6 MHz have been achieved, enabling the acquisition of IVOCT image data within one heart cycle [183] and minimizing heart motion artifacts. However, catheter bending might still influence the spatial sampling of the IVOCT images.

In more advanced approaches, bi-plane angiography systems have been applied to estimate the pose of objects in three dimensions and over time [184], e.g., for stereoscopic tracking of instruments [185] or catheters [186]. Using this spatio-temporal information on the imaging probe trajectory, the cross-sectional IVOCT images are arranged.

Even with optimized spatio-temporal probe trajectory estimation, inaccuracies in three-dimensional vascular reconstruction arise due to the unknown occurrence of NURD artifacts. Consequently, assigning too many or too few A-scans to one cross-sectional image leads to a distorted representation of the reconstructed artery volume. Thus, additional methods for NURD correction have been presented [187–189]. One approach considers speckle decorrelation to quantify the distortion [190]. Furthermore, non-rigid registration using fiducial markers at the catheter shell has been proposed [191].

In addition to the spatial arrangement of the intravascular image data, various methods focusing on the segmentation of vascular tissue structures have been studied [192]. Beyond the segmentation and classification of vascular lesions, i.e., different stages of plaque formations [33, 193–195], the segmentation of the vascular lumen wall is of interest for volumetric vessel analysis [196, 197]. In particular, deep learning approaches show significant benefits when processing in-vivo intravascular image data with varying speckle characteristics, e.g., for the segmentation of lumen [198, 199] or stent struts [135].

In this thesis, we study IVOCT to quantify vascular morphology and aim to systematically assess the limitations in three-dimensional reconstruction using different external imaging modalities, i.e., bi-plane DSA and MPI. In contrast to previous studies that were conducted in-vivo, the demonstrated methods are examined in an artificial experimental setting with reasonable ground truth information on the three-dimensional vessel geometry and the imaging probe motion. First, we investigate the performance of different volume reconstruction methods. Specifically, we introduce a concept for A-scan wise volume reconstruction and analyze the quantitative difference to conventional slice-wise approaches. Second, we explore MPI as an alternative non-invasive imaging modality for external catheter tracking and reference quantification of vascular morphology.

3.2 Quantification of Soft Tissue Elasticity

Various diseases, e.g., cancer or fibrosis, lead to morphological changes in the soft tissue. In addition to the morphology, variations in elastic properties are often a decisive clue for the diagnosis. While diagnosis by manual palpation of tissues is prone to subjective impressions and requires a lot of experience, various sensor technologies, e.g., strain gauges or imaging probes for quantitative analysis, have been investigated in recent years [200]. In particular, several methods for quantifying the elastic tissue properties have been introduced [35, 201–203]. Initially, sensors or imaging probes for examining tissue properties from outside the body have been explored. For example, ultrasound imaging has been combined with Acoustic Radiation Force (ARF) to excite shear waves and image their two- or three-dimensional propagation. In addition, miniaturized sensing and imaging probes have been proposed to analyze deep tissue structures during MIS [204]. In the following, we will introduce the main principles of elastography and provide an overview of different miniaturized OCE probe designs for sensing elastic properties.

3.2.1 Principles of Elastography

Compression-based and shear wave elastography are the two primary methods considered when estimating the mechanical response of soft tissue [205, 206]. The tissue is mechanically stimulated or deformed in both methods while image data is acquired. Subsequently, the soft tissue displacements and deformations are estimated from the image data to determine the elastic properties. The compression-based elastography approach involves analyzing elastic properties based on the relationship between the applied stress, σ, and the measured strain, ε [207]. Local deformations Δd in tissue of width d subjected to loading with a particular force F_{ind} and over an area A are imaged with a high axial resolution to estimate the elasticity, also referred to as palpography [208, 209]. The Young's modulus E results as

$$E = \frac{\sigma}{\varepsilon} = \frac{F_{\text{ind}} d}{A \Delta d}. \tag{3.1}$$

Shear wave elastography approaches promise the quantitative analysis of soft tissue elasticities. By stimulating a fast periodic movement of the soft tissue, a transverse wave, also known as a shear wave, propagates in addition to the initiated longitudinal pressure wave. These shear waves oscillate perpendicularly to the direction of movement. In general, the velocity of mechanical waves increases with the stiffness of the medium. Thus, the modulus of elasticity E for homogeneous, isotropic materials can be determined from the measured shear wave velocity v_s with

$$E = 2\rho_\mathrm{s} v_\mathrm{s}^2(1+\nu). \tag{3.2}$$

When solving this equation for soft tissue, a poisson ratio of $\nu = 0.5$ and the tissue density ρ_s is assumed as introduced in [210].

In summary, the shear wave elastography approach requires the excitation of mechanical shear waves and the quantification of their wave propagation characteristics through tissue. For this purpose, two different wave-sampling approaches have been considered, i.e., transient and wavelength elastography. Transient OCE approaches require an accurate calibration of the spatial distance Δs between wave excitation and imaging. The duration Δt_s a single wave travels between excitation and imaging position is extracted from the acquired image data to estimate the shear wave velocity with

$$v_\mathrm{s} = \frac{\Delta s}{\Delta t_\mathrm{s}}. \tag{3.3}$$

On the other hand, wavelength elastography approaches involve deriving the shear wave velocities from the general wave characteristics, namely wavelength λ_s and frequency f_s. The shear wave velocity v_s results as

$$v_\mathrm{s} = \lambda_\mathrm{s} f_\mathrm{s}. \tag{3.4}$$

Here, it is assumed that the shear wave frequency fs remains constant when traveling through tissues of varying densities under isotropic conditions. Consequently, to estimate the shear wave velocities with these OCE approaches, it is essential to assess the variations in shear wavelength λ_s.

Compression-based and shear wave elastography approaches involve applying a mechanical load to the tissue and imaging the related tissue response over space and time. The OCE imaging setups are differentiated by their spatial orientation of excitation and imaging, as shown in Figure 3.2. In compression-based approaches, the imaging and excitation axes are usually oriented confocally to each other [211]. This configuration ensures that the motion is applied and imaged at the same point in the sample. In wave-based elastography, various setup configurations have been proposed to analyze different spatial components of the shear wave propagation [212]. Most commonly, imaging setups have been investigated where the wave motion and the imaging axis are parallel, thereby maximizing the measured motion amplitude. For benchtop OCE setups, most commonly, surface acoustic waves are studied that require the excitation of the shear wave at the tissue surface and with a certain distance to the OCT imaging FOV (see Figure 3.2, right). In most confocal excitation and imaging

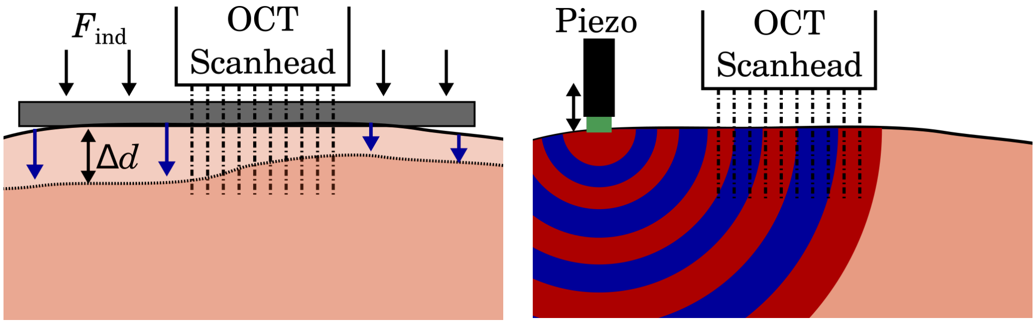

Figure 3.2 Visualizations of exemplary mechanical loading approaches applied at the tissue surface relative to an OCT imaging scan head. For compression-based OCE, by applying an indentation F_{ind} quasi-stationary tissue deformations (blue arrows) are induced, leading to height differences Δd. In wave-based OCE, shear waves with small motion amplitudes (blue and red circles) are excited, e.g., using a piezo.

setups [211, 213], the excitation source is positioned around the imaging optics. In addition, confocal wave-based OCE setups have been proposed where the longitudinally propagating shear waves are measured [214].

The spatial and temporal variation of the mechanical loading for different OCE approaches is visualized in Figure 3.3. The elastography approaches differ in the spatial extent of the applied stress, i.e., whether it is broad or punctual excitation on the tissue surface or local stress applied within the tissue. The temporal characteristics also vary depending on the elastography principle and the type of loading. In Figure 3.3, the different loading schemes are highlighted in color and arranged according to their spatial and temporal excitation type. For compression-based OCE, quasi-static mechanical loadings are applied. Here, slow variations in mechanical compression are used, and deformation and relaxation processes of the tissue are analyzed. In shear wave elastography, faster mechanical excitations are applied, usually forming a point excitation in space. Referring to the temporal characteristics, harmonic or multi-frequency actuation schemes have been presented, e.g., involving small Piezoelectric Transducer (PZT)s or ARF [215]. In addition, single-impulse loadings, e.g., using ARF, air-puff, or laser excitation, are considered for shear wave elastography. These single-wave excitation schemes are often employed in transient elastography approaches, as introduced in Equation 3.3. In Figure 3.3 studies investigating the application of miniaturized imaging probes from within the tissue are highlighted with black circles. Considering this small number of studies, the importance of studying the application of OCE probes not also on the tissue surface but also from within the tissue is highlighted.

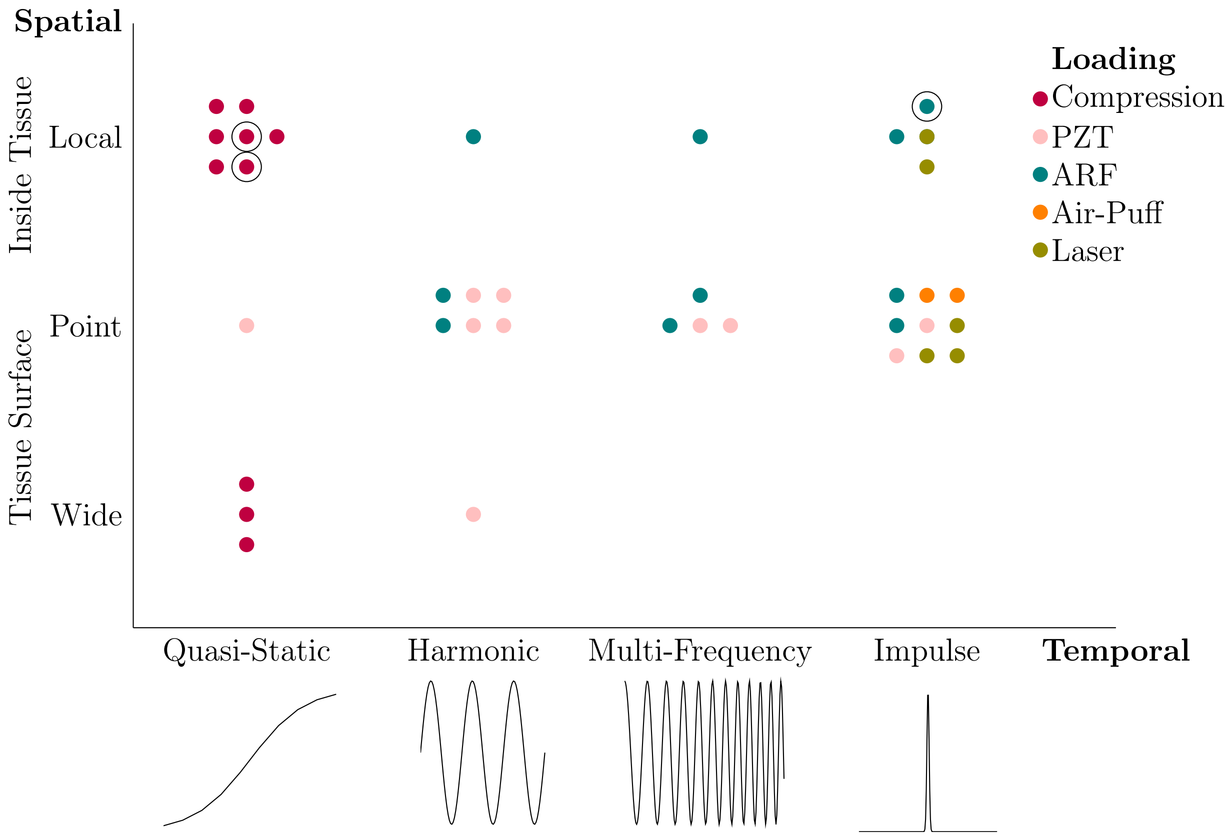

Figure 3.3 Overview of OCE approaches separated by spatial and temporal characteristics of the mechanical loading. Compression-based OCE approaches with quasi-static or harmonics loading schemes have been proposed using either wide-area tools [216–219] or specific needle probes for indentation on the surface [220–222] or within the tissue [223]. Moreover, intraluminal pressures are applied to facilitate quasi-static compression for OCE of vascular or airway structures [224–226]. Quasi-static [227], harmonic [228–232], multi-frequency [232, 233] and impulse [232, 234] loading profiles have also been applied using PZT, i.e., in ring actuator shape. Stimulation of shear waves with ARF has been presented in various setups on the tissue surface utilizing air-coupled setups [211, 235, 236], or water coupling [213, 237–241], or from within the tissue [242–244] with impulse, harmonic or multi-frequency actuation schemes. Air-puff excitation techniques enable non-contact impulse excitation on the tissue surface [245, 246]. Laser-pulse stimulation of shear waves has been proposed for application at the tissue surface [247–249] and has been extended with an injection of nano bombs for wave excitation inside the tissue [214, 250]. For each study, a colored dot representing the loading principle is shown. Circled dots indicate that miniaturized OCE imaging probes have been applied.

For all loading schemes, spatial and temporal sampling schemes need to be optimized to achieve a precise assessment of shear wave velocity. For transient OCE approaches, the distance between excitation and imaging Δs should be adequately defined and remain constant during signal acquisition. Additionally, the temporal sampling should be maximized to accurately determine the run time Δt_s between shear wave excitation and imaging. In the case of wavelength elastography approaches, imaging setups must effectively sample the spatial propagation of the shear wave, which involves capturing a sufficient number of sampling points along its cosine waveform. For benchtop OCE setups, consistent spatial sampling is enabled with precisely adjusted optical scanning setups that offer high lateral resolution. In Section 2.1, two imaging modes are introduced: BM-scans and MB-scans. In BM-scan mode, entire B-scans are acquired sequentially as a shear wave moves through the imaging field. In MB-scan mode, A-scans are captured rapidly at a fixed position while a wave is excited, and this is repeated across different spatial scanning positions. This mode enables higher temporal sampling rates but involves complex and repetitive excitation and imaging processes. The collected A-scans are then rearranged into two-dimensional image sequences.

In summary, accurate spatial and temporal sampling is crucial for optimizing quantitative elastography with these different OCE approaches. Most importantly, to assess small tissue displacements over a short time period. For example, the spatial distance Δs between wave excitation and imaging must be calibrated carefully to extract the shear wave velocity using Equation 3.3. Especially for wave-based elastography approaches involving harmonic or multi-frequency mechanical loading schemes, the OCT image data must be acquired with high temporal sampling rates.

3.2.2 Miniaturized Elastography Probes

While various OCE setups have been demonstrated for ex-vivo or enface tissue analysis [216, 237, 251–253], translation to miniaturized imaging probes is still being explored. Several challenges arise when designing OCE probes for minimally-invasive applications. Relevant OCE probe designs studied for compression and shear wave elastography are summarized in the following. In Figure 3.4 miniaturized probe concepts for compression-based or shear wave elastography are exemplarily shown.

At first, compression-based OCE probes have been proposed with single-fiber optics embedded in the tip [220, 221]. These designs enable the measurement of axial tissue displacements by evaluating the OCT image data acquired. Compression-based elastography requires a reference sensing of the applied stress to ensure quantitative analysis as intro-

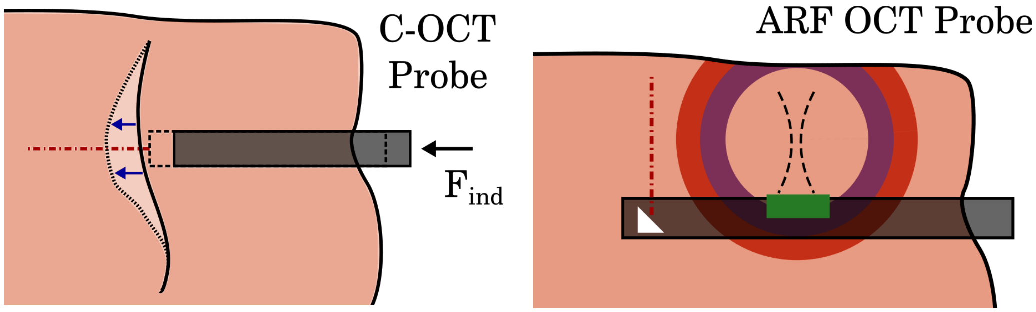

Figure 3.4 Exemplary probe designs for compression-based and wave-based OCE.

duced in Equation 3.1. Therefore, additional sensors [222] or imaging optics [223] have been incorporated in recent OCE probe designs, enabling a reference measurement based on the principle of Fabry-Perot interferometry. Similarly, a multi-purpose needle design has been presented that combines force sensing based on Fiber-Bragg Grating (FBG) with OCT imaging at the needle tip [254]. However, these probe concepts only allow for one-dimensional imaging, and thus, a tissue displacement analysis is limited to a single spatial axis. In conventional benchtop compression-based OCE approaches, the lateral tissue displacements have been considered involving two-dimensional imaging acquisition [218]. Embedding imaging optics for two-dimensional image acquisition in medical instruments is complicated in terms of fabrication and miniaturization. However, a concept for intravascular compression-based OCE has been presented, requiring high A-scan rates of up to 3 MHz and a stable OCE probe position [225] to enable the acquisition of BM-scans. Here, intraluminal pressure has been applied to induce tissue displacements. The compensation of NURD using deep learning has been addressed in related studies to ensure proper overlap of successive A-scans for an optimized compression-based elastography [255]. Previously, a similar compression-based OCE probe has been proposed for elasticity estimation in the airway wall [226, 256]. These concepts are also partly based on probe designs that have been presented for intravascular Ultrasound Elastography (USE) [208, 257–260] or intravascular OCE [224, 225, 261]. For hand-held probes designed for use on the skin surface, the miniaturization requirements are less relevant, so several designs have been proposed for compression-based OCE [219, 262, 263]. Here, the compression is applied manually, and dedicated stress sensors at the probe surface measure the applied loading.

Miniaturized probes for shear wave elastography have been developed with different excitation and imaging strategies. On the one hand, probe designs with combined wave excitation and imaging have been presented. Combining shear wave excitation and imaging requires a compact probe design that does not sacrifice imaging quality. Additionally, sufficient energy transfer must be ensured to excite a mechanical wave from the miniaturized probes. In particular, piezoelectric elements for ARF typically need to be several millimeters in size to deliver enough energy and therefore generate reasonable motion amplitudes [238–242, 244, 264–266]. Suitable acoustic coupling is necessary for excitation of shear waves with these elements. A novel probe concept has been presented that combines two US elements for shear wave excitation and one optic for high-resolution OCT imaging to track shear waves [244]. The synchronization of excitation and imaging is improved using this design, but with the drawback of increased probe dimensions. To facilitate a beam steering for ARF shear wave excitation from miniaturized probes, a cylindrical transducer array has recently been combined with a IVUS imaging probe [267]. Embedding optical fibers for photoacoustic stimulation [247, 248, 268] saves space but requires precise excitation schemes to avoid tissue heating or damage. In addition, the necessary wiring or fibers are expensive to manufacture and prone to failure. Alternatively, shear wave OCE probe concepts with an external device for shear wave excitation have been demonstrated, which promise significantly smaller probe dimensions [269, 270]. In addition, external excitation of shear waves is more effective, mainly when relevant relative tissue movements occur and mechanical coupling is not reliable, e.g., in vascular tissue [271].

Most miniaturized probes for wave-based OCE are again equipped with single-fiber optics to minimize the probe size. Being limited to one-dimensional image acquisition at one spatial position, the shear wave velocity is estimated based on the transient OCE approach introduced in Equation 3.3. Similar to IVOCT imaging probes, two- or three-dimensional image acquisition may be possible with the addition of translation or rotation of the probe. For wave-based OCE methods, this movement should either be performed at high speed, ensuring a spatial overlap of A-scans acquired sequentially, or repeated successively for an MB-scan acquisition in which one excitation and imaging cycle per position is evaluated. However, performing these probe motion profiles within the tissue in a reproducible manner is challenging. The resulting uncertainty in the spatial sample might affect the accuracy of the estimated elasticity. Consequently, concepts for actuating the optical fiber have been demonstrated, enabling two- or three-dimensional imaging without the need to move the entire imaging probe. The vibration of piezoelectric actuators or the application of magnetic coils allows fiber movement along an axis or in a circular shape. This is a promising alternative for superficial tissue analysis, especially for laparoscopic interventions [239, 272]. Recently, a fiber-based OCE probe has been proposed for application in minimally invasive surgery [273]. However, embedding additional actuators leads to larger probe dimensions, and the transmission of high voltages creates a relevant risk with direct tissue contact.

In summary, the design of miniaturized OCE probes poses several challenges, particularly when estimating elasticity from within tissue rather than just at the surface. Most current advancements focus on ex-vivo or enface tissue analysis, but reducing the size of probes for minimally invasive applications is an ongoing challenge. Many miniaturized OCE probes rely on single-fiber optics, restricting them to one-dimensional imaging and limiting the analysis to surface or very shallow measurements. This poses a significant challenge for accurately estimating elasticity within tissue. Attempts to overcome this include actuating optical fibers using piezoelectric or magnetic mechanisms for two- or three-dimensional imaging, but these solutions inherently increase the probe's dimensions and complexity. Moreover, external devices for shear wave excitation offer an alternative for reducing probe size, but they come with additional complexity regarding effective mechanical coupling, especially in dynamic body environments such as vascular tissues. Consequently, achieving consistent and reproducible measurements within the tissue remains a significant limitation for miniaturized OCE probes, emphasizing the need for further innovations in probe design as well as excitation and synchronization techniques. Investigating simplified OCE probes designs for assessing the elasticity of soft tissue from the inside, e.g., in vascular structures or when inserting medical needles, is therefore an essential focus of this work.

3.2.3 Image Processing Methods for Elastography

Image processing methods for both probe concepts, i.e., compression-based or shear wave elastography, focus on deriving tissue displacements from the complex OCT image data. In particular, either the intensity or phase information has been studied. Furthermore, hybrid methods have been demonstrated to use both signals [251, 274]. The OCT intensity data have been studied to assess tissue displacements, especially for compression-based elastography approaches with comparatively large displacements. Equivalent to the Loupas algorithm that has been demonstrated for the quantification of motion in two- or three-dimensional US images [96], image processing methods have been established for OCT image analysis from benchtop setups [275]. These approaches focus on estimating the tissue displacements in multi-dimensional image sequences by calculating the correlations between OCT intensity images acquired in different displacement states [276]. Secondly, the quantification of tissue displacements during palpation by evaluating the OCT phase difference has been demonstrated for compression-based OCE needle probes [220, 277]. Here, the phase difference $\frac{\delta\Phi}{\delta t}$ of subsequently acquired axial scans (see Equation 2.12) is used as a measure of tissue motion [278].

Shear waves usually generate relatively small amplitudes of soft tissue motion that are difficult to resolve within the OCT intensity data. Thus, mainly the OCT phase information has been elaborated to quantify shear wave motion with subpixel resolution. In particular, wave-based OCE approaches from miniaturized probes involve analyzing the phase difference of the OCT signals acquired sequentially at the same spatial position. One important step in phase signal processing is compensating for phase jumps. Therefore, phase unwrapping methods have been studied, e.g., focusing on computational approaches [279–281].

Depending on the imaging setup and elastography approach, different image representations are introduced in Section 2.1, including BM-scans, MB-scans, M-scans, and pseudo M-scans. Computational image processing methods for the described two- or three-dimensional image representations focus on extracting the shear characteristics, namely the wavelength λ_s or frequency f_s. Quantifying the shear wavelength λ_s requires at least two-dimensional sampling of the wave propagation, as introduced in Section 3.2.1. In addition, the shear wave frequency f_s must be known. An alternative approach to investigate the spatial wave characteristics is to combine the estimation of temporal and spatial wave characteristics. Here, transient OCE approaches focus on tracking the shear wave front by constructing space-time diagrams from BM- or MB-scans [212, 282]. Using this space-time diagram, the slope of the visible shear wave front has been analyzed, e.g., by applying a Fourier transformation and extracting the dominant pixel with maximum intensity in the resulting frequency-wavenumber diagram. The shear wave velocity v_s follows as

$$v_\mathrm{s} = \frac{f_\mathrm{s}}{k_\mathrm{s}}, \tag{3.5}$$

with f_s and k_s describing the shear wave frequency and wavenumber, respectively.

In various OCE studies, the influence of dispersion effects on elasticity quantification has been discussed [283]. Considering shear wave propagation in soft tissue, dispersion effects are described as the variance of shear wave velocities with frequency. Based on the general wave equation 3.4, a constant wave frequency is assumed for lossless propagation in isotropic media. The frequency stays constant for all tissue properties such that only the wavelength varies, e.g., due to stiffness. However, the shear wave speed changes with frequency for anisotropic media, such as soft tissue. Thus, an evaluation of wave velocities over a broad frequency bandwidth has been proposed to elucidate tissue characteristics more extensively [284]. Here, the phase velocities $v_\mathrm{s,ph}$ are obtained after Fourier transformation of the space-time diagram using the point with maximum intensity $k_\mathrm{s,max}$ over a certain frequency band $f_{\mathrm{s,min}} < f_{\mathrm{s},i} < f_{\mathrm{s,max}}$ with

$$v_{\mathrm{s,ph}}(f_{\mathrm{s},i}) = \frac{f_{\mathrm{s},i}}{k_{\mathrm{s,max}}}. \tag{3.6}$$

Particularly in tissue structures with an anisotropic or layered structure, the related dispersion effects also studied in USE [285] cause the shear wave velocities to increase with frequency. Analyzing the phase velocity curves for multi-frequency excitation schemes enables an analysis of the tissue viscosity. One crucial approach focuses on quantifying local phase velocity by evaluating small image crops separately in the frequency domain [286]. Furthermore, the methods define the group velocity as the slope of the phase velocity curve. The group and phase velocities should be equal whenever single-frequency wave excitations are applied [287]. However, the reliability of group velocity estimation has been questioned in recent studies, particularly when artifacts in the Fourier-transformed images hinder the detection of actual heterogeneous and homogeneous structures.

The described computational image processing methods require proper parameter tuning to accurately extract the wave peak or wavefront over time or choose the optimal maximum intensity point in the space-time diagrams. This leads to a particular bias when estimating threshold values. Thus, deep learning methods have recently been applied to extract the wave characteristics [288] or to assess the elasticity in an end-to-end fashion [289, 290]. Additionally, the uncertainty in a shear wave speed prediction has been explored using a neural network with space-time diagrams as input [291]. Another study demonstrates the advantages of deep learning methods for estimating shear wave speeds in limited field of view (FOV) sizes, where conventional computational methods are unsuccessful due to the limited number of spatial sampling points along the wavelength [292].

In summary, image processing methods for extracting spatial wavelength characteristics are not applicable when miniaturized OCE probes are limited to one-dimensional signal acquisition. As a result, transient elastography approaches are often employed to estimate the run time Δt_{s} between the excitation and imaging points, as described in Equation 3.3. This method requires a known distance Δs, and peak detection methods to extract the shear wave front from M-scans [293]. While benchtop OCE setups provide stable spatial and temporal sampling of two- or three-dimensional images, miniaturized OCE probes face challenges due to relative motion in tissue. Variability in probe positioning and unstable mechanical coupling can affect the accuracy of elasticity measurements. Additionally, optical tissue properties such as attenuation affect OCT signal quality and sampling accuracy. This thesis systematically examines these limitations and their effects on the spatial and temporal sampling of shear wave parameters.

3.3 Quantification of Soft Tissue Interactions

In various medical interventions, needles are inserted in soft tissues and navigated to a target position. In the field of anesthesiology, needles are used to apply anesthetic drugs in vessel structures or next to nerve structures [294]. For tumor tissue diagnosis or therapy, needles are navigated toward the lesions to either perform a biopsy or for seed placements for brachytherapy [295]. External imaging modalities, such as US imaging, are applied to assist in needle navigation [296]. However, several imaging artifacts arise when observing the insertion of metallic needles, impeding the detection of the needle tip in the image data [297].

On the other hand, even if US imaging is available in most clinical settings, navigation requires proper interpretation of the image data and spatial registration of the needle tip and target region, which often occurs in the doctor's mind. Finally, the puncture success rate depends on the physician's experience and training. In addition to external imaging, the physician commonly uses the forces felt at the needle shaft to differentiate tissue structures [298]. The felt resistance, the number of Loss-Of-Resistance (LOR) events [299], and the increasing or possibly varying friction are used as surrogates for needle navigation. Hence, several approaches have been derived to simulate, predict, or quantify the forces acting at the needle tip and shaft during needle insertion [300]. Preserving this analysis of needle and tissue interactions is essential for minimally invasive or robot-assisted interventions. Here, direct tissue palpation or instrument contact, as is common in open surgery or manual puncture, is no longer possible. Therefore, more recent studies aim to quantify the properties of needle puncture, making them tangible for the physician. As one possible application scenario, in robotic systems with haptic feedback control [301], these force estimates could be used to mimic the natural interactions between the needle and tissue, enabling intuitive needle navigation. For example, minimally invasive robotic systems that ensure haptic feedback control [302–305] have been presented, where improved sensing of tissue and instrument interactions is essential.

3.3.1 Mechanical Characteristics of Needle Insertion

The mechanical characteristics of needle insertions have been analyzed in various studies. On the one hand, mathematical models are derived to describe the needle insertion mechanics in soft tissue phantoms [300, 306], e.g., using gelatin or plastisol phantoms. These phantoms provide a homogeneous structure and mechanical properties similar to those of soft tissue. In addition, mechanical modeling such as Finite Element Modeling (FEM) or simulations have been performed [307–310]. However, soft tissue's fiber or collagen structures are not

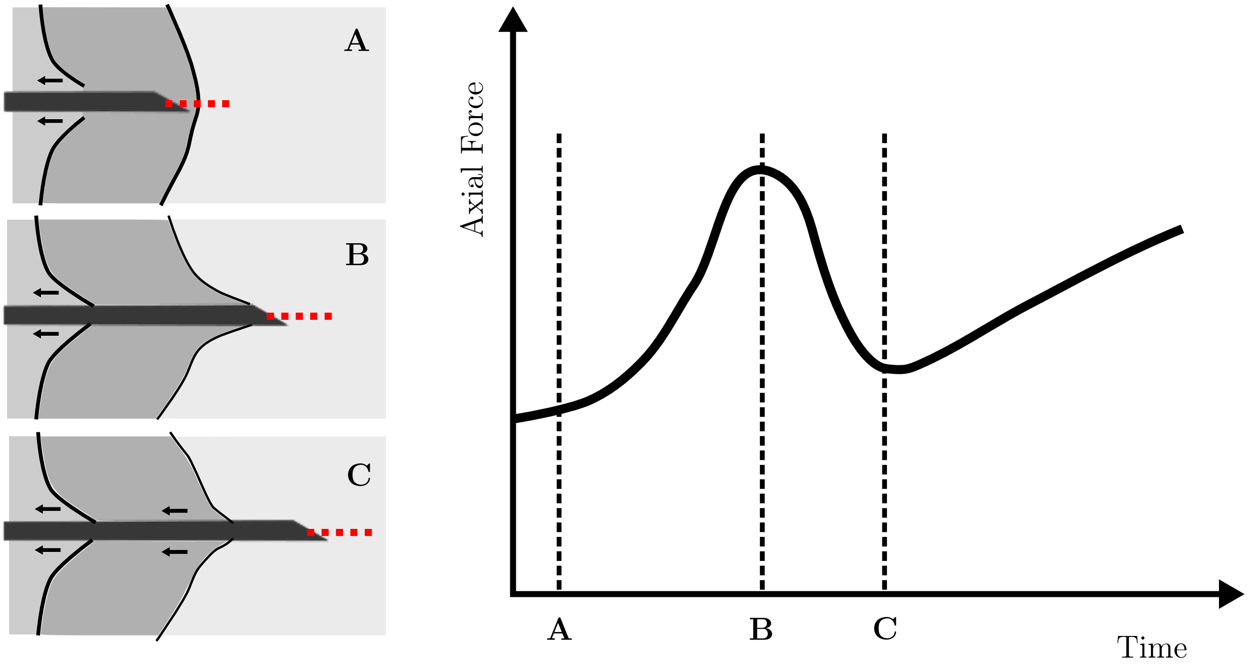

Figure 3.5 Mechanical interactions between the needle and soft tissue for a puncture through several soft tissue layers. The axial forces measured at the needle shaft are sketched over time. The force values increase with tissue deformation and compression in front of the needle (A to B). Once the tissue layer ruptures (B), tissue relaxation leads to a decrease in force until the stiffness and friction of the next tissue layer increase again (C).

reproduced in tissue phantoms or simulations [311]. Thus, on the other hand, several studies also analyze the mechanical characteristics of ex-vivo tissue samples, considering different effects, such as deformation or cutting processes [312]. For example, uniaxial compression or tensile experiments have been performed on tissue samples to study the corresponding mechanics [313]. However, a correlation to in-vivo measurements is still limited as several simplifications are made. Therefore, experimental studies have been proposed, where different sensing approaches have been investigated during needle insertion in soft tissue phantoms or ex-vivo tissue samples [38, 311, 314]. In most studies, the forces acting on the needle have been used as surrogates to describe the mechanical events during insertion. Analogously, the main phases and events during needle insertion studied in this thesis are depicted in Figure 3.5 and correlated to the sensed axial forces.

We assume a sharp needle tip, i.e., bevel or trocar shape, to describe mechanical interactions in a layered tissue during needle insertion. We hypothesize that the following effects occur for each tissue boundary on the needle path. First, the needle cuts through the current tissue layer until the tissue stiffness in front is too high, and tissue displacement and deformation follow. This increases the axial forces felt at the needle shaft (A to B in Figure 3.5). Once the compressed and deformed layer is punctured, a LOR event occurs [315, 316]. Such an event is usually associated with a spontaneous decrease of the axial forces (B to C in Figure 3.5). At the same time, the deformed and punctured tissue relaxes. A new resistance then acts on the needle tip, as the following soft tissue structures in front of the needle tip are deformed (after C in Figure 3.5). The magnitudes of deformation and displacement before a rupture are related to the tissue structure in front of and around the needle [317]. In addition, the structure of the connective tissue, as well as surrounding bone structures, influences the mechanics during insertion. Similarly, the magnitude of a LOR event is dependent not only on the tissue structures around but also on the needle's shape and sharpness [308, 318]. Additionally, the mechanical characteristics sensed during needle puncture can vary depending on the selected trajectories and the individual anatomies of patients. For this reason, physicians often do not rely on absolute measured values during handheld needle navigation, but rather on the relative differences in resistance felt. For a specific target region, e.g., the epidural space for anesthetic treatment, the physician knows which structures lie on the planned needle path and can therefore count the number of LOR events or the number of felt tissue differences to estimate the current needle position [299].

Overall, the four events of tissue cutting, displacement, deformation, and rupture are considered in this thesis to describe the insertion process. When analyzing force values sensed during insertion, deformations are associated with rising force values, e.g., due to a resistance on the needle trajectory [300, 319, 320]. Almost constant force values are associated with tissue cutting. Displacement events might lead to increasing force values, but nearly constant force values are also possible. The elastic properties of the tissue structures around the needle influence these displacements and related force sensing. Thus, deformation and displacement events that have also been reported for needle placement in brachytherapy [321, 322] are not always clearly distinguishable. Rupture events are associated with the cutting of tissue structures and the spontaneous retraction or relaxation of the surrounding tissue. Additionally, substantial deformation and displacement occur before the tissue ruptures. The related LOR is also visible in the decreasing force values (see Figure 3.5). These rupture events are often associated with transitions of the needle from one tissue to another, such as when puncturing tissue surfaces or penetrating deep tissue structures. However, smaller rupture events can also occur within a specific tissue structure, e.g., when collagen fibers are punctured perpendicularly. Differentiating between these ruptures within a tissue and at a particular boundary is crucial when navigating a needle to a specific region.

3.3.2 Miniaturized Needle Probes

In this Section, we differentiate between miniaturized probe designs that either directly assess the forces acting on the needle, e.g., using force sensor designs, or estimate tissue properties from image data acquired at the tip.

The mechanics of tissue and instrument interaction have been studied using various sensing methods applied at either the proximal or distal end of the instrument. First, force sensing setups have been proposed where Force-Torque (FT) sensors are mounted to the proximal end of an instrument [40, 323, 324]. The proximal end refers to an attachment at the rear end of the instrument, e.g., the mounting of a needle shaft. In addition, the instrument tissue forces have been estimated by proximal measurement of the cable tensions of micromanipulators [325]. Moreover, an audio-based force sensing concept has been proposed that measures the vibrations acting on the needle shaft [326]. These proximal setups have the benefit of fewer requirements for sterilization. However, proximal force sensing is hindered by possible friction forces acting on the instrument shaft [308, 327]. Thus, additional shielding instruments, e.g., needle tubes, have been applied to eliminate the influences of frictional forces on the proximal sensing [328, 329].

Second, distal sensing has been proposed to improve tactile sensing, which refers to all measurements performed directly at the instrument tip. While miniaturized multi-axis force sensors have been presented [330] with much effort in terms of fabrication, also substituting sensing setups have been developed. The proposed sensing approaches include piezoresistive [331], piezoelectric, capacitive sensing [332, 333], impendence sensing [334], and optical sensing technologies. For example, strain-sensing methods have been developed by integrating strain gauges in MIS instrument tips [335, 336]. Analogously, these sensors have been incorporated into needles [337].

In addition to optical sensing approaches incorporating strain-sensing, instrument designs with integrated FBG sensors have been proposed [338]. The applied optical fibers with installed gratings impress with their small size and simple integration possibilities. In addition to proximal and distal sensing approaches, FBGs have also been applied to sense the instrument shape during minimally invasive interventions. For example, when assessing the bending of an endovascular imaging probe to assist the minimally invasive instrument navigation [339, 340]. Optical force sensing approaches also involve optical imaging methods, such as OCT. Placing the optical fiber in front of a cavity whose size varies with the forces acting at the instrument tip enables force sensing based on the concept of Fabry-Perot interferometry [341–344]. During versatile calibration processes, an assignment of a measured cavity size to a force is enabled. The application of deep learning methods has shown potential in calibrating these sensing approaches, i.e., estimating the forces directly from the OCT intensity data [329, 345]. Moreover, a miniaturized optoelectronic sensor measuring the cavity size with an infrared transmitter and an emitter placed opposing each other has been studied [346].

Needle navigation based on external imaging has been presented for several applications. Especially, US guided needle placement is the gold standard in clinical practice and supplements traditional techniques, such as LOR [316]. However, imaging from the outside is hampered by several imaging artifacts, motivating the acquisition of images directly at the needle tip. In contrast to force-sensing approaches that attempt to correlate variations in acquired force curves with specific tissue structures, analyzing image data promises a more comprehensive tissue characterization.

Acquiring OCT image data at the needle tip is possible with the integration of imaging optics. As the cavity in medical needles is limited, imaging optics should be minimized and simplified. Thus, mainly single-fiber optics have been embedded in recent OCT needle designs. The applied imaging optics vary in terms of complexity and image orientation. Either forward-viewing [347] or side-viewing imaging optics have been presented. Common-path imaging was initially developed to enhance signal stability, primarily focusing on OCT phase signals [348]. Imaging optics are constructed by orthogonally cleaving the fiber tip, which creates a partially reflective surface for light waves. These reflected waves serve as reference signals at the OCT detector, while the remaining light continues to the tissue sample for signal acquisition. This setup eliminates the need for an external reference arm, providing a stable reference intensity. Maintaining a constant reference intensity is challenging for external reference arm setups, particularly in flexible applications with significant fiber movement [349]. To optimize reference intensity characteristics during tissue contact, half-ball or ball lenses have been spliced to the common-path fiber end [350–353]. The simplified reference signal acquisition of common-path approaches comes with the cost of an unfocused imaging beam. Thus, GRIN fiber optics have alternatively been spliced to the fiber end to achieve appropriate beam focusing and adjustment of the working distance [319, 354–356], requiring an external reference arm setup. Moreover, focus adjustment of a miniaturized probe has been proposed by moving the fiber with piezoelectric elements in front of a GRIN optic [357]. Image quality is improved with these GRIN probes with the necessity of external reference arm setups. All of these forward-viewing imaging optics have been designed to acquire single-column depth images over time, also referred to as OCT M-scan or pseudo M-scan, as soon as the needle probe is moved.

Miniaturized imaging optics have been further developed to acquire multi-dimensional image data. As proposed for IVOCT catheters, needle probes with imaging directed perpendicular to the needle axis have been demonstrated. Here, GRIN fiber optics have been polished to create an angled fiber end to diffract the light beams [358, 359]. Alternatively, optical prisms are positioned in front of a GRIN focused fiber optic [360, 361]. Similar to IVOCT imaging profiles, rotation and translation of the needle probe enable the acquisition of two- or three-dimensional image data [362–367]. Alternatively, miniaturized scanning setups have been investigated to facilitate two- or three-dimensional imaging without requiring the actuation of the probe itself. The integration of oscillating mirrors in the tip, as proposed for benchtop OCT setups, is limited due to the restricted space available in medical needles or instruments. Therefore, imaging probes with embedded micro-motors have been studied [368]. However, these designs are still comparatively huge, and their repeatability is limited due to mechanical constraints. Thus, further approaches with a proximally positioned scanning setup have been presented, where the needle acts as a light tunnel [369, 370]. Other relevant studies on designing minaturized scanning probes are based on methods for actuating the imaging fiber itself [371]. An oscillating motion of the fiber end is aimed to achieve two-dimensional scan patterns. Thus, fiber actuation has been proposed by placing the fiber in between two oscillating piezoelectric elements [372–375]. The endoscopic probe designs were further refined so that miniaturizations with an outer diameter of up to 1.6 mm were achieved [376]. Embedding up to four piezoelectric elements around the fiber and actuating them with interlaced sinusoidal profiles enables a helical motion of the imaging fiber and thereby the acquisition of three-dimensional image data. Moreover, Lissajous scanning profiles have been studied to improve the illumination uniformity with the drawback of an extensive pre-calibration requirement [377]. As an alternative to piezoelectric stimulation, magnetic stimulation setups have been proposed [378, 379]. However, even though these actively scanning probes achieve impressive two- or three-dimensional imaging capabilities, they are not intended for use in direct tissue contact. In particular, the scan patterns would be severely distorted by the varying refractive indices of the tissue on contact. In addition, the acquisition of multidimensional image data also limits the sampling frequency and, consequently, the sensitivity in detecting spontaneous motion patterns, such as those occurring during tissue rupture events.

3.3.3 Image Processing Methods for Soft Tissue Interactions

While directly estimating forces acting on the needle is possible with incorporated sensors, processing of OCT signals acquired from miniaturized imaging probes is not trivial. On the one hand, the image data contains information to characterize tissue using the morphology information contained as discussed in Section 4.2.2. On the other hand, evaluating the optical tissue characteristics and motion information from needle insertion promises value for tissue characterization. This thesis focuses on extracting morphological and motion information from image data acquired at the needle tip to characterize the punctured tissue structures. Thus, we mainly introduce related image processing methods in the following.

Conventional image processing methods and deep learning approaches have been developed that enable tissue characterization by evaluating the OCT intensity signals [380]. At first, computational analysis of A-scan signal characteristics has been proposed by determining the number of high-intensity peaks, the intensity decay, or the area under the A-scan curve [381]. Moreover, attenuation and backscattering coefficients have been derived based on quantitative models to describe the tissue properties from OCT signals [382–385]. These methods to extract specific optical tissue features have also been referred to as parametric imaging [386, 387]. In addition to these computational signal analyses, deep learning methods have been proposed for classifying tissue structures. While learning approaches with an end-to-end design [388], i.e., processing the original image data and directly extracting classification labels, have been proposed to extract any feature information independently, learning approaches exist that use extracted optical feature values as input, e.g., attenuation coefficients and backscattering intensities [193, 195, 389, 390]. Motivation for the latter feature-based learning approach is, on the one hand, the limited data set sizes that additionally should contain enough variability for training a neural network that is capable of generalizing on unseen data sets. On the other hand, comprehensible classification of neural networks is essential for application in clinical scenarios [390]. Relying on strictly defined features will limit the possibilities of unrealistic classifications. However, the disadvantage remains that crucial image features, which are not directly accessible to the human mind, may be unused and could be recognized by a neural network. As an alternative, deep learning methods that incorporate a separate feature extraction component have been proposed [194]. This approach makes the training process more comprehensible by cascading a feature extraction network with a separated classification layer, e.g., using a Support Vector Machine (SVM).

The assessment of motion in OCT image data has been presented in different studies. Apart from elastography studies, where motion has been analyzed to study the compression profiles of tissue or propagating shear waves (see Section 3.2), optimization of imaging characteristics has been proposed by motion compensation [391]. Moreover, a few studies focus on OCT-based motion estimation to study the interaction of soft tissue and instruments, e.g., to estimate the acting forces [303, 392–394]. By utilizing benchtop OCT setups, two- or three-dimensional OCT sequences are acquired and analyzed in these studies. Dependent on the motion amplitudes studied, either the OCT intensity or phase signals have been evaluated. Similarly, OCT-based motion estimation has been applied for soft tissue tracking, using either correlation-based filter methods [395] or deep learning approaches [396, 397]. Analogously, OCT-guided robotic needle insertion, instrument motion has been analyzed from the volumetric image data [398, 399]. Image data acquired with the miniaturized probe designs described above also contain motion information. However, as the needle probes are usually in direct contact with the tissue or hand-held, the relative motion is usually caused by both the probe and the tissue. Moreover, a spatial arrangement of the acquired one-dimensional OCT depth scans might be limited. Therefore, the previously described methods for motion estimation from two- or three-dimensional OCT image sequences are not directly transferable. Related studies focused, therefore, on methods to process these pseudo OCT M-scans by analyzing the intensity signals, e.g., for proximity sensing [400]. In recent studies, deep learning approaches have been presented to segment boundaries in the intensity data, e.g., using neural networks [352]., In addition, the phase signals have been considered, e.g., for evaluating the relative motion of tissue and probe [319]. Alternatively, the phase signals acquired during needle insertion have been evaluated to detect blood flow based on the Doppler effect and thereby vessel structures ahead of the needle tip [354].

As previously described, either the OCT intensity or phase signals contain relevant information to analyze relative motion, depending on the temporal characteristics and amplitude of the motion sensed. During the insertion of needle probes in soft tissue structures, the motion patterns and related force values vary. To characterize tissue from this varying measure, a systematic analysis of tissue punctures is necessary. One crucial event during needle insertion is the LOR, which can also be described as a tissue rupture event. In this thesis, we aim to describe the image characteristics due to rupture events systematically. We study the detection of rupture events from different modalities and investigate whether OCT imaging in front of the needle tip delivers suitable information for tissue characterization, leveraging both the OCT intensity and phase information.

3.4 Summary of Research Questions

Modern medical technologies aim to optimize the clinical outcome through minimally invasive interventions or surgeries. Reduced invasiveness results in a shorter healing time, less pain for the patient, and optimized treatment outcomes for the physician. However, a substantial drawback of minimally invasive interventions is the lack of haptic and visual feedback. Even if external imaging or instrument tracking approaches are available, transferring the information recorded externally or pre-operatively to the intraoperative scenario inside the patient is not easy. This motivates the need for approaches to assess the soft tissue morphological, elasticity, and instrument interaction properties directly at the instrument tips from inside the patient.

Although several modern and miniaturized sensor designs have been presented, their application in clinical practice remains limited. One important issue is the necessity of sterilization when instruments or needles are used multiple times on different patients. Thus, low-cost probe designs are preferred for medical applications that are either sterilizable or disposable. OCT imaging probes with embedded single-fiber optics are investigated as one such solution in this work. Embedding optical fibers in medical instruments, such as needle probes or catheters, offers substantial benefits over conventional sensing technologies, e.g., FBG and piezoelectric sensors, as the fibers and imaging optics are small and easy to manufacture. In addition, OCT imaging offers a high spatial resolution, and novel high-speed imaging systems enable the acquisition of several million A-scans per second. However, extracting physical parameters from the complex OCT image data is not trivial, which is a major focus of this thesis. We aim to study the application of OCT imaging as a sensor for tissue characterization with high spatial and temporal resolution. We aim to minimize the effort required for probe manufacturing by utilizing simplified imaging optics. Through advanced image processing, we aim to extract significant tissue characteristics even from blurred image data. In particular, we investigate the OCT intensity and phase signals to extract relevant features for analzying soft tissue morphology, elasticity, and relative motion. In contrast to imaging modalities typically applied from outside the patient body, such as MRI or US, imaging probes with single fiber optics limit the possibilities for capturing tissue properties in two or three dimensions. Moreover, once the imaging probe is applied from within the patient's body, the imaging coordinate system becomes unstable, and its global position is typically unknown. In the following, we introduce the research questions studied in this thesis to assess tissue characteristics from miniaturized OCT probes.

In our first research question, we investigate the accuracy of morphology reconstructions given a clinical IVOCT imaging catheter. A miniature optical fiber is positioned within a catheter shell, with a 45-degree polished prism attached to the distal end of the fiber. A rotation and translation of the fiber result in a helical scan profile, delivering three-dimensional information from within the vascular structure. Usually, the allocated A-scans per revolution are assigned to a cross-sectional image of the artery. These two-dimensional images are further used to analyze and classify the lesion stage. However, this image representation contains imaging artifacts from relative tissue motion due to the pulsation and contraction of the heart. Furthermore, the IVOCT probe follows an unknown spatial trajectory in the curved arteries. However, most three-dimensional IVOCT image reconstruction methods are based on simplified probe geometries and motion trajectories. They, therefore, neglect the specific orientation and position of the A-scan. Thus, imaging artifacts due to uneven and unknown spatial sampling of the A-scans are not compensated during the three-dimensional reconstruction of the image data, leading to inaccuracies in artery reconstruction. Consequently, relevant under- or overestimations of coronary diameters and stenosis expansion. As one approach to assist in three-dimensional IVOCT image reconstruction, bimodal imaging has been applied by imaging the vascular structures using IVOCT and tracking the probe motion with an externally applied second imaging modality. The first aim of this thesis is to systematically analyze and optimize the two- and three-dimensional morphological reconstruction of coronary arteries from IVOCT M-scan data. We compare different reconstruction methods, including vascular centerline analysis or catheter tracking from external imaging. We systematically study the imaging and relative motion artifacts that influence morphological reconstructions and emphasize the importance of compensation.

Summarized, the first research question of this thesis is:

- How to sample the A-scan acquisition, pose, and orientation during pullback and rotation of the IVOCT probe with different external imaging modalities?

Our second research question investigates the quantification of soft tissue elasticity from within the tissue with a miniaturized OCE probe. We aim to measure the propagation characteristics of excited shear waves with a simplified optical probe design. Using this probe, we study two main challenges. Initially, while most OCE approaches focus on acquiring two- or three-dimensional image data, the studied probe design involves a single spatial sampling position with one-dimensional imaging only. Consequently, the shear wave characteristics are evaluated based on the transient OCE approach. Second, in contrast to common benchtop OCE setups and miniaturized wave-based OCE probes that measure the wave propagation on the tissue surface, we aim to investigate the shear wave propagation in deeper tissue. Once the probe is no longer outside but inside the tissue, it is more difficult to determine its spatial position, especially relative to a wave excitation source. In this thesis, we aim to systematically analyze the wave excitation and sensing capabilities for different OCE probe positions relative to the shear wave origin. We investigate calibration approaches to achieve reliable spatial and temporal sampling of the shear wave. Finally, we investigate a dual-fiber probe design to minimize the effort required for temporal synchronization of wave excitation and imaging. We aim to enable reproducible elasticity estimates even for unstable probe positions relative to the excitation source.

This leads to the research questions related to our second application:

- How to quantify soft tissue mechanics from a miniaturized imaging probe independent of the origin and direction of the shear wave?

In our third research milestone, we investigate the soft tissue interactions that occur during needle insertion. We propose a simplified, miniaturized probe design for OCT imaging at the needle tip. The one-dimensional depth-resolved scans captured in front of the OCT needle tip do not offer the usual two- or three-dimensional image representation known from other imaging modalities. However, we aim to study the motion characteristics based on the complex spatio-temporal OCT signals. We hypothesize that both imaging and insertion speed influence the appearance of speckle patterns of tissue structures in successive A-scans. Consequently, we develop specific image reconstruction and interpretation methods in this thesis. We evaluate the spatio-temporal features of the complex OCT data to derive methods quantifying needle and tissue interactions during insertion. First, we quantify the particle slope to distinguish between tissue and relative motion, enabling the detection of ruptures during needle insertion. Second, we apply deep learning methods to classify rupture events in the insertion data. To verify our findings, we compare measures from OCT data with external sensing and imaging.

Consequently, the following third research question is investigated in this thesis:

- How to sample and interpret the sequence of complex OCT depth scans from needle puncture for tissue characterization?

We face the challenge of interpreting image data based on versatile and initially unknown scan patterns for all three application scenarios. Therefore, investigating methods to assess the related relative motion patterns between probe and soft tissue, e.g., by externally applied imaging modalities or from the OCT image data itself, is the primary focus of this thesis. Moreover, we investigate methods for individual or combined analysis of OCT intensity and phase signals. Addressing also the varied spatial and temporal motion patterns studied. In summary, we study various miniaturized OCT imaging probe designs and the capabilities for extracting and interpreting relevant information from complex OCT data to characterize soft tissue structures.

Chapter 4

Material and Methods

4.1 Miniaturized Imaging Probes

In this thesis, different designs of miniaturized OCT probes for soft tissue characterization are investigated. The purpose of these probes is to acquire high-resolution image data from inside the human body. OCT imaging inherently offers the ability to record depth-resolved scans with a resolution of up to a few micrometers. When applied from outside the human body, optical scanning setups are typically used to acquire two- or three-dimensional images of the tissue. However, it is hardly possible to integrate these scanning setups into miniaturized probe designs. This work, therefore, focuses on incorporating imaging optics that are firstly simple to manufacture and secondly as small as possible, resulting in designs that are limited to acquiring one-dimensional OCT depth scans. In particular, probe designs for radial and axial acquisition of one-dimensional depth scans are being investigated. Figure 4.1 visualizes the probe designs studied to assess vascular morphology, soft tissue elasticity, and soft tissue interaction. The infrared imaging beam is aligned perpendicular to the probe axis for studies of morphology and elasticity. A probe design with imaging aligned axially to the probe is proposed to study the interaction with the soft tissue during needle insertion.

The main challenges in applying these probes in the human body are, firstly, the limitation to one-dimensional imaging, and secondly, the unknown and unstable coordinate system of the imaging when they are applied inside the human body. In medical imaging systems, such as US, CT, or MRI, two- or three-dimensional images are acquired using a fixed image coordinate system. Additionally, the distance between individual pixels or voxels is known from the system setup or the applied imaging sequence. For one-dimensional imaging probes, a two- or three-dimensional sampling of tissue structures is possible when the probe or imaging optic itself is moved. When using a probe with a radially oriented imaging axis,

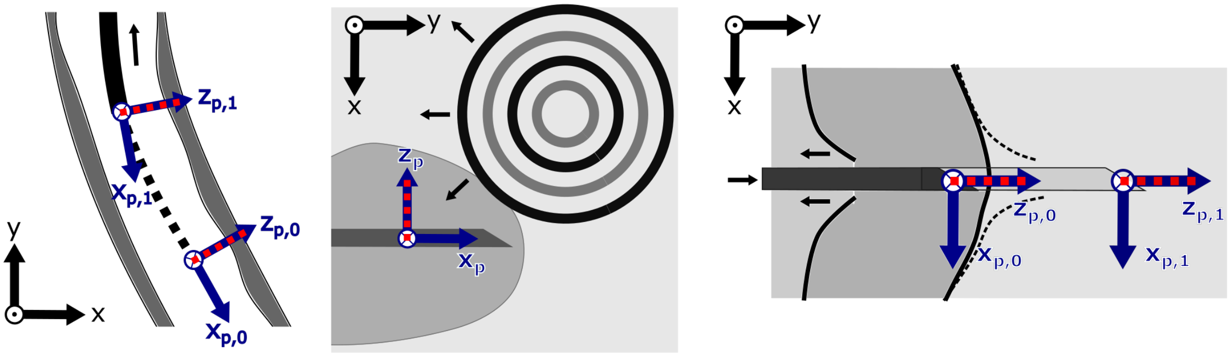

Figure 4.1 Visualization of OCT probes applied for quantification of vascular morphology (left), soft tissue elasticity (middle), and soft tissue interaction (right). The reference coordinate systems of externally applied imaging systems are highlighted in black. The one-dimensional OCT depth scans are acquired along the $z_{\mathrm{p},t}$ axis of the probe coordinate system (blue). Due to probe motion or relative motion of tissue structures, indicated with small black arrows, the position of the probe's coordinate system varies over time $t = 0, 1$. Considering the transient elastography approach investigated, the probe's position is assumed to be constant while a shear wave propagates spherically towards the OCT imaging axis.

rotation enables the acquisition of cross-sectional images around the probe. With additional translation of the probe, a three-dimensional sampling is possible. For imaging probes with axially oriented optics, two-dimensional scanning might be possible for movements perpendicular to the probe axis. However, performing these probe movements within the human body is either not possible or not feasible in a reproducible fashion. Thus, equidistant two- or three-dimensional scanning, as is typically achieved with externally applied imaging systems, cannot be accomplished.

Given the various probe designs, orientations, and movements during OCT signal acquisition, different image processing steps are required to derive soft tissue characteristics. For all probe designs, the one-dimensional OCT depth scans are sequentially acquired and initially arranged side by side, also referred to as an OCT M-scan for a stationary probe, as described in Section 2.1. In this work, the image coordinate systems of the probes are defined so that they are located at the imaging optics, and the $z_{\mathrm{p},t}$-axis points to the one-dimensional scanning axis.

Assuming a stationary probe position, the OCT image data is acquired as a temporal sequence of depth-resolved A-scans, whose complex signal $S(z,t)$ can be specified as follows

$$S(z,t) = I(z,t)e^{i\Phi(z,t)}, \tag{4.1}$$

with $I(z,t)$ and $\Phi(z,t)$ expressing the intensity and phase data resolved over imaging depth

z and time t. Based on Equation 4.1, two-dimensional representations could be derived as long as the transformation from the temporal to a spatial axis is known. Assuming a uniformly rotating probe with a radially orientated imaging axis, the temporal representation in Equation 4.1 could be converted into polar coordinates

$$S(z, \varphi) = I(z, \varphi) e^{i\Phi(z,\varphi)}, \tag{4.2}$$

with $\varphi = \frac{2\pi f_{\mathrm{rot}}}{f_{\mathrm{OCT}}}$ expressing the rotation angle based on the given OCT sampling frequency f_{OCT} and the rotation frequency f_{rot}. After the transformation from Polar to Cartesian coordinates, a two-dimensional representation of the OCT data is possible. Similarly, conversion from temporal to Cartesian axes is possible if the probe is moved perpendicular to the imaging axis with a known constant velocity

$$S(z, x) = I(z, x) e^{i\Phi(z,x)}, \tag{4.3}$$

with $x = \frac{v_{\mathrm{p},x}}{f_{\mathrm{OCT}}}$ stating the position depending on the sampling frequency f_{OCT} and the motion velocity of the probe $v_{\mathrm{p},x}$. A two-dimensional image representation is not possible for probe designs with equally oriented imaging and movement axes (see Figure 4.1, right). The spatio-temporal representation in Equation 4.1 could, therefore, be transformed into a one-dimensional representation only, also referred to as pseudo M-scan in the following,

$$S(z') = I(z') e^{i\Phi(z')}, \tag{4.4}$$

with $z' = \frac{v_{\mathrm{p,z}}}{f_{\mathrm{OCT}}}$ being dependent on the OCT sampling frequency f_{OCT} and the probe's motion $v_{\mathrm{p,z}}$. Please note that subsequently allocated depth scans could overlap in space when the imaging frequency is substantially higher than the probe's velocity.

Based on these general image representations, the image reconstruction and analysis methods in this thesis focus on: First, defining the transformation from the OCT image coordinate systems to the positions of specific tissue structures in the global coordinate system. Second, estimating the probe motion to reconstruct two- or three-dimensional OCT image representations, i.e., transforming the OCT M-scan to a spatial representation. Third, assessing small motion patterns from the OCT signals to analyze the relative motion of the probe and tissue. In all these methods, external imaging systems are used as a reference, for example, to estimate the position of the probe in global coordinates or to understand the physical relationships that lead to variation in the OCT signal properties.

4.2 Quantification of Vascular Morphology

In this chapter, we explore the capabilities of intravascular OCT imaging for tissue characterization. We perform morphological analyses based on IVOCT data considering different methods for the three-dimensional reconstruction of vascular tissue structures from radially acquired OCT depth scans (see Equation 4.2). Further, we analyze to what extent motion hampers these morphological analyses in the two- and three-dimensional representations of IVOCT image data. In experimental studies, we systematically analyze the imaging parameters of IVOCT to enable an optimized two- and three-dimensional reconstruction of vascular structures. We study DSA and MPI as reference modalities to estimate the vascular morphology and the trajectory of the IVOCT probe. First, we assess the vascular morphology by estimating the three-dimensional trajectory of the probe from the vascular centerline. Second, we investigate approaches to account for motion during image acquisition by spatio-temporal tracking of the probe. Third, we study deep learning methods to assess the imaging parameters directly from the IVOCT image data. Please note that the following methodical descriptions are based on publications on bi-modal IVOCT and DSA imaging [401, 402] as well as on bi-modal IVOCT and MPI imaging [403–405]. The latter studies have been conducted in close cooperation with colleagues from the Institute of Biomedical Imaging, in particular, Florian Griese. The described methods referring to MPI image acquisition and analysis have been developed by Florian Griese.

4.2.1 Vascular Imaging Systems

We apply and combine different imaging systems described in the following sections for our intravascular imaging studies. First, we introduce the clinical and the custom-built IVOCT imaging setup. Second, we describe the system properties of DSA and MPI, applied for external visualization and tracking of the imaging probe.

Imaging systems for IVOCT commonly comprise an OCT imaging unit, a motion driver, and an imaging catheter. Depending on the catheter design with proximal or distal actuation, the motion driver includes a unit for translation and optional rotation of the imaging probe. The imaging probe is rotated and pulled through arteries using this system setup while image data is acquired. In this thesis, we use a clinical IVOCT imaging system or a customized imaging setup described below. The IVOCT imaging setup developed in this thesis is sketched in Figure 4.2. It consists of an SD-OCT system (Telesto I, Thorlabs GmbH, Germany) and a custom motion unit with an adapter for optical and mechanical connection

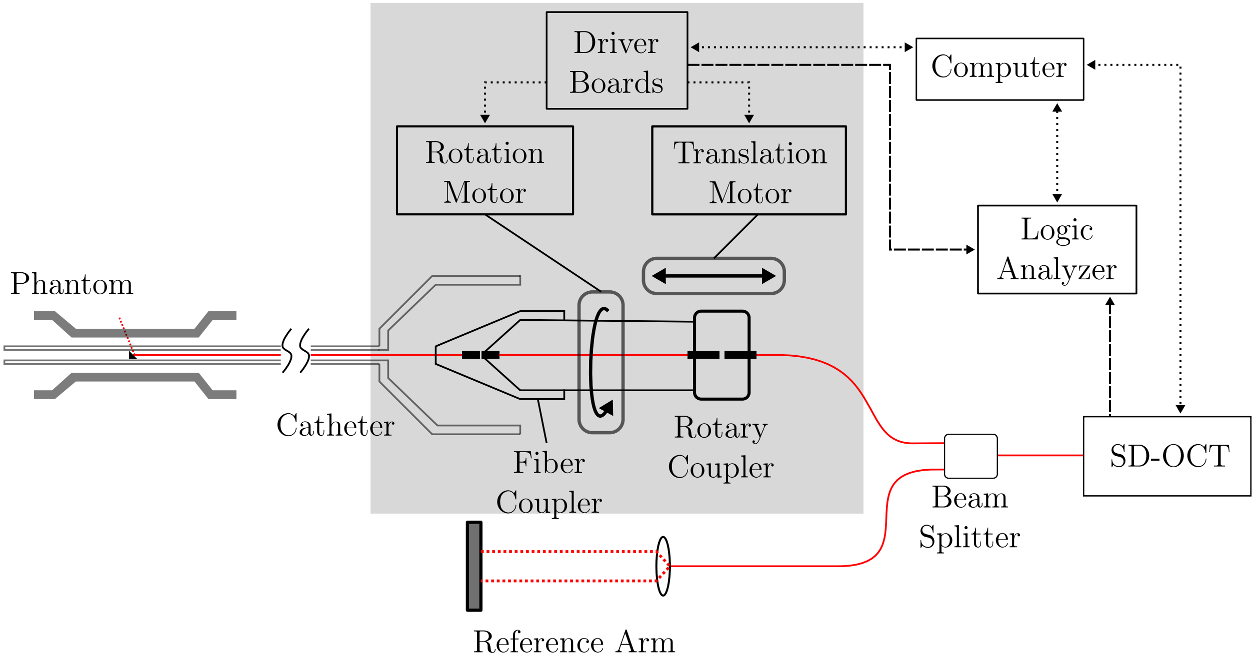

Figure 4.2 Custom IVOCT imaging setup composed of a SD-OCT imaging system and a motion unit (gray background). Catheter translation and rotation are performed with two separate motors. The infrared light (dashed red) is coupled from the SD-OCT system through the fiber coupler into the imaging probe or reference arm via a beam splitter. Installing the rotary coupler prevents the twisting of the optical fiber (red) connected to the motion unit. A computer controls the motion actuation, OCT image acquisition, and trigger recording at the logic analyzer.

of various IVOCT imaging probes. The spectral-domain OCT system uses a central wavelength of 1315 nm and provides an A-scan rate of $f_{\mathrm{OCT}} = 91\,\mathrm{kHz}$. The axial FoV in air is approximately $FOV_{\mathrm{OCT},z} = 2.66\,\mathrm{mm}$ and each A-scan contains $P = 512$ pixels.

The assembly of the motion unit is shown in Figure 4.3 and described below. We use two separate motors to enable translation and rotation of an attached imaging probe. First, we utilize a brushless DC motor with an optical encoder (DB28L01, WEDS5541-B14-KIT, Nanotec Electronic GmbH, Germany) to drive a shaft with a 6:1 gear ratio. Second, a linear stepper motor (LP3575S0504, Nanotec Electronic GmbH, Germany) enables precise shaft translation. For the optical connection, a 2x2 beam splitter (TN1310R5A1, Thorlabs GmbH, Germany) is connected to the light output of the OCT system. The beam is split into an external reference arm setup and the motion unit. The motion unit contains an optical adapter for IVOCT probes and a fiber optic rotary joint (FO285, Moog Inc., USA) that is placed between the beam splitter and the rotating shaft. This rotary coupler prevents twisting of the fiber connected to the beam splitter when moving the imaging probe.

We use different software interfaces to automate the IVOCT image acquisition. We use

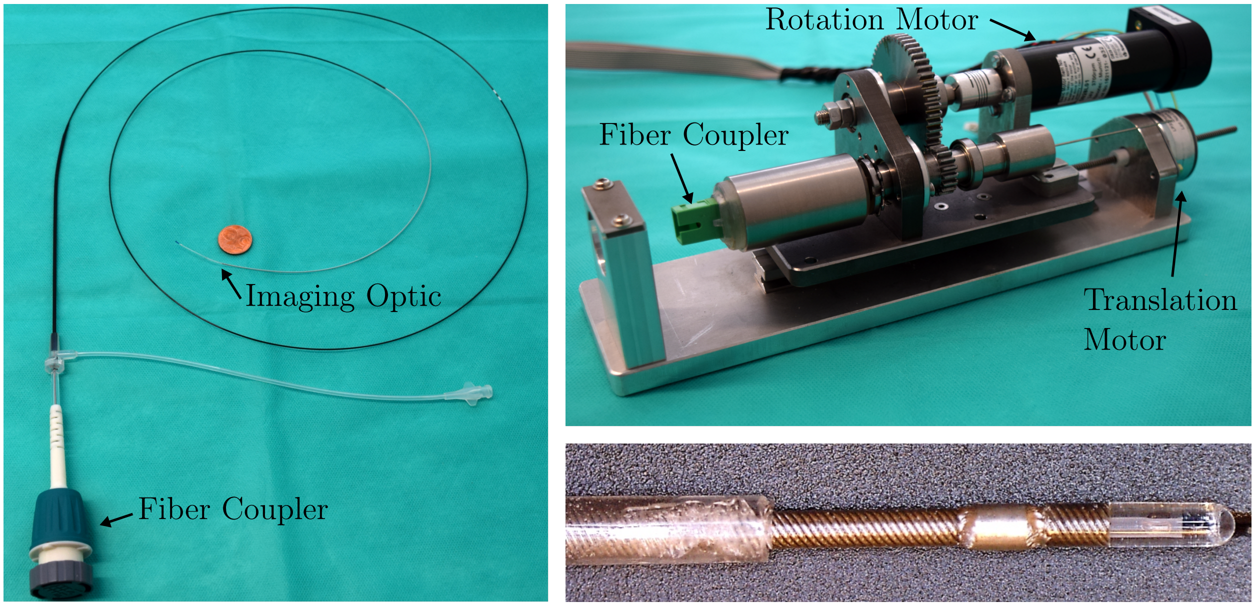

Figure 4.3 Pictures of IVOCT imaging catheter with highlighted fiber coupler and the customized motion unit, enabling translation and rotation of the imaging probe. In the lower right, an enlargement of the imaging optic is shown.

two driver boards to control the motion interface components. We attach an Arduino Uno board with MotorShield to actuate the linear motor and read input trigger signals. We achieve a probe pullback speed of up to 1 mm s^{-1} with different step modes. Using a motor driver board (SMCP33, Nanotec Electronic GmbH, Germany), we execute specific rotational motion profiles. The motor control is written in C++. The following requirements are important when actuating the rotation. A slow start of the rotation movement is required to avoid damage to the imaging probe. To enable constant rotational speeds and prevent too high loads during OCT image acquisition, we limit the maximum probe rotation to 13 Hz. We control the simultaneous OCT image acquisition and probe motion with a user interface written in Python. An imaging server written in C++ receives commands for setting the OCT imaging parameters and enabling or disabling a measurement. Additionally, we utilize a digital oscilloscope (Saleae Logic-8, Saleae, Inc., USA) to capture the trigger signals of OCT imaging and motor actuation.

In this thesis, we apply the clinical DragenFly Duo imaging catheter composed of a flexible catheter shell with 0.9 mm outer diameter and an imaging probe fed through this catheter (see Figure 4.3). The overall catheter length is given as 1.5 m. At the proximal probe end, an optical prism is attached to refract the laser beam with an angle of approximately 78°. An optical snap-in connector and mechanical junction are combined at the distal end to connect to the ILUMIEN Optis motion unit. A schematic of this imaging probe is shown in

Table 4.1 Comparison of clinical and custom IVOCT system specifications. The parameters listed refer to the maximum values that can be set.

Parameters	ILUMIEN Optis	Custom IVOCT setup
Axial resolution	$5.2\,\mu m$	$6.7\,\mu m$
A-scan rate	89 kHz	91 kHz
Rotation rate	180 Hz	13 Hz
Pullback speed	$17\,mm\,s^{-1}$	$1\,mm\,s^{-1}$
Pullback length	54 mm	20 mm

Figure 4.2. Three metallic rings embedded at the optical fiber shaft of the IVOCT catheter are used to assess the probe position in externally acquired DSA images. For MPI-based probe tracking approaches, we additionally apply a magnetic lacquer to the tip of the imaging optics.

In clinical practice, the ILUMIEN OPTIS system (Abbott, USA), together with the associated DragonFly imaging catheter (Abbott, USA) and the motion unit, is most used for IVOCT imaging. The motion unit allows proximal rotation and translation of the imaging probe. The imaging specifications are compared to the customized setup developed in this thesis in Table 4.1. Simultaneous acquisition of IVOCT and DSA image data is enabled using a separate interface.

For our bi-modal IVOCT and DSA imaging studies, we use a bi-plane angiography system (Allura Xper FD10, Philips GmbH, Germany). This system allows simultaneous acquisition of 2D images while both arms are positioned in different orientations relative to the target structure. As soon as an imaging procedure is started, a series of images is recorded with a frequency f_C of up to 30 Hz. We vary the C-arm orientation angles γ_C in our experimental studies to study the influence of different projective views on the quantitative volume reconstruction. We combine the bi-plane angiography system with the clinical ILUMIEN Optis IVOCT system and DragonFly Duo imaging catheter. For synchronous IVOCT and DSA image acquisition, we use the Optis Integrated system software interface. The DragonFly Duo imaging catheter consists of three imaging markers that are used in the clinical system for Co-registration.

For bimodal IVOCT and MPI imaging, we perform experimental studies with a preclinical MPI scanner (MPI PreClinical, Bruker Corporation, USA). The scanner has a bore diameter of 118 mm with a couch for positioning small animals, e.g., rats or mice. A motion stage is also built in the MPI scanner to run calibration scans with SPIONs or other particle samples. Using the animal couch, we place vascular tissue phantoms of different morphologies with the inserted DragonFly Duo IVOCT imaging catheter in the MPI device. The custom IVOCT imaging system enables translation and rotation of the imaging catheter. We synchronize IVOCT and MPI image acquisition using an electrical trigger connection. The control software of the IVOCT imaging setup, which is implemented in C++ and running on a dedicated controller PC, reads the MPI trigger and, in turn, controls the catheter motion and the OCT image acquisition.

4.2.2 Reconstruction of Vascular Morphology

Three main challenges arise in the correct spatial reconstruction of IVOCT image data. Due to the flexible IVOCT imaging catheter design, the IVOCT probe will follow different paths for each pullback, even with similar positioning and actuation profiles. Thus, without external imaging information, the actual three-dimensional path of the imaging probe is unknown. Furthermore, the assumed translation of the imaging probe is affected by catheter bending or heartbeat motion. In particular, heartbeat motion will result in unknown relative motion between the imaging optic and the vascular structures. Lastly, unknown non-uniform rotations of the imaging optic, e.g., due to torsion of distally rotated imaging probes, will result in NURD artifacts.

This chapter investigates different methods for three-dimensional reconstruction of IVOCT image data. We first evaluate an approach using only the set IVOCT imaging parameters. Second, we study volume reconstruction methods based on bimodal imaging setups. We differentiate between methods estimating the three-dimensional vascular shape, the three-dimensional path of the IVOCT probe, or the 4D imaging probe trajectory assessed from tracking with an external imaging modality. Third, we examine deep learning methods to extract the motion information directly from the IVOCT image data.

For all of these investigations, it is important to consider that we define an IVOCT imaging coordinate system that is oriented at the origin of the imaging optics (see Section 4.1). The z_p-axis of this coordinate system is pointing in the direction of the imaging beam. The x_p-axis is aligned perpendicular to this along the catheter shaft, and the y_p-axis is, in turn, perpendicular to x_p and z_p as shown in Figure 4.1. In the following sections, we estimate the spatio-temporal displacement of this coordinate system during image acquisition to arrange the IVOCT image data spatially.

In the following, we describe the lumen segmentation methods and the two- and three-dimensional morphology reconstruction without information from external imaging, solely based on the set IVOCT imaging parameters. We focus on assessing the vascular morphology and first apply image processing methods to extract the luminal boundary. We define a three-dimensional representation of the vessel lumen using this boundary information and the assumed three-dimensional position and orientation of the IVOCT imaging probe.

We use different representations of the vascular image data to achieve lumen segmentation. At first, we neglect the set parameters for the pullback and rotation of the IVOCT imaging probe. The image data is initially available as a matrix whose axes refer to the image depth and time as introduced in Equation 4.1 and shown in Figure 4.4. Hence, we use this IVOCT M-scan to extract threshold values for image filtering and binarization. In addition, constant imaging artifacts, e.g., due to reflections from the catheter sheath, are extracted from the image data. Secondly, we apply edge detection methods to segment the luminal boundary. We use morphological operations to reduce noise signals and apply a moving average filter over the temporal image dimension. Subsequently, we extract the first pixel positions with maximum intensity along the depth axis as a luminal boundary point. To account for outliers, we smooth the resulting boundary profile over time.

After extracting the luminal boundary, we aim to reconstruct cross-sectional images of the vascular tissue. Therefore, we use the set rotation parameters f_{rot} of the IVOCT imaging probe. We assume a uniform rotation profile and, based on the OCT sampling frequency f_{OCT} and assign a fixed number $H = f_{\mathrm{rot}}/f_{\mathrm{OCT}}$ of depth-resolved IVOCT scans to a single cross-sectional image as shown in Figure 4.4. The helical trajectory of the OCT probe is neglected, and cross-sectional images of the phantom result after transformation from polar in Cartesian coordinates. We can assess the center of mass per lumen based on the two-dimensional representation of the IVOCT images. For this purpose, we transform the luminal contour extracted from Polar to Cartesian space. Assuming a circular lumen shape, we can directly estimate the center of mass as the midpoint of the segmented lumen area. For later described three-dimensional reconstruction methods, it is essential to clarify that the IVOCT imaging probe is not necessarily positioned within this center of mass.

Next, we consider a method to arrange the reconstructed two-dimensional images using the set pullback speed v_{pull}. Thus, we define the transformation of the imaging coordinate system between two consecutive cross-sectional images S_i as

$$
{}_{\mathrm{S}_i}T^{\mathrm{S}_{i+1}} = \begin{pmatrix} 1 & 0 & 0 & \Delta x \\ 0 & 1 & 0 & 0 \\ 0 & 0 & 1 & 0 \\ 0 & 0 & 0 & 1 \end{pmatrix}, \tag{4.5}
$$

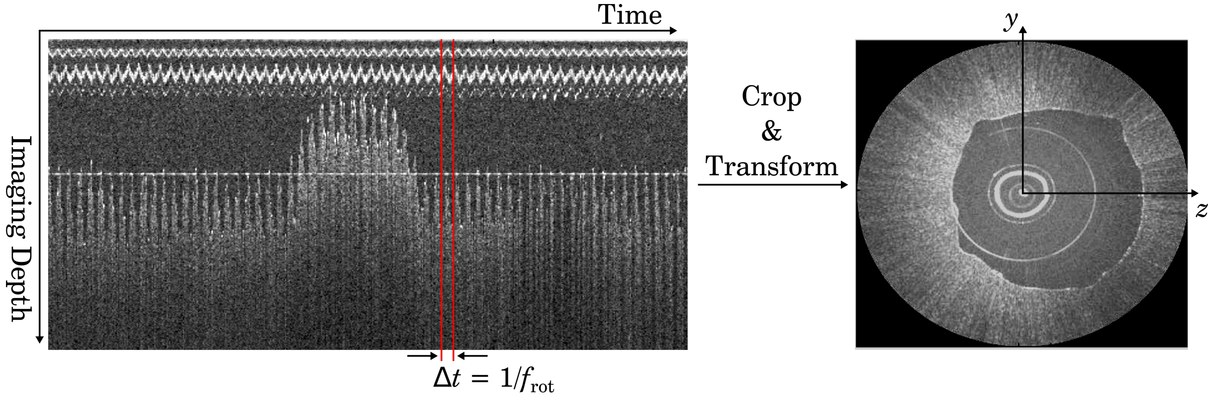

Figure 4.4 Reconstruction of IVOCT cross-sectional images from the acquired M-scan. Given the probe rotation parameters f_{rot} and the OCT A-scan rate, A-scans are cropped from the M-scan and transformed from polar to Cartesian space.

with the displacement along the x_{p}-axis defined as $\Delta x_{\text{p}} = v_{\text{pull}}/(2\pi f_{\text{rot}})$. We assume uniform rotation and translation of the probe and do not assume additional rotation around the image coordinate axes x_{p}, y_{p}, and z_{p} with the angles α_{p}, β_{p}, and γ_{p}, respectively. The cross-sectional images are arranged equidistantly on the x_{p}-axis in this representation. These assumptions of a straight probe trajectory and a uniform pullback velocity with a constant pitch Δx_{p} are also most commonly used for IVOCT image reconstruction in clinical systems.

As an alternative to the spatial arrangement of cross-sectional IVOCT images, we investigate a method for helical volume reconstruction. Here, we estimate the transformations between each successive IVOCT A-scan A_i as

$$
{}_{\text{A}_i}T^{\text{A}_{i+1}} = \begin{pmatrix} 1 & 0 & 0 & \Delta x \\ 0 & \cos\Delta\alpha_{\text{p}} & -\sin\Delta\alpha_{\text{p}} & 0 \\ 0 & \sin\Delta\alpha_{\text{p}} & \cos\Delta\alpha_{\text{p}} & 0 \\ 0 & 0 & 0 & 1 \end{pmatrix}, \tag{4.6}
$$

assuming uniform rotation around and translation along the x-axis with $\Delta\alpha_{\text{p}} = f_{\text{oct}}/f_{\text{rot}}$ and $\Delta x_{\text{p}} = v_{\text{pull}}/f_{\text{rot}}$, respectively. Using this helical reconstruction approach, we account for deviations in spatial sampling due to large pullback speed compared to the IVOCT A-scan sampling frequency.

Uniform imaging parameters and reconstruction assumptions, as introduced in Section 4.2.2, are unrealistic for in-vivo measurements. Non-uniform motion profiles of the imaging probe will lead to unknown translational $(\Delta x_{\text{p}}, \Delta y_{\text{p}}, \Delta z_{\text{p}})$ and rotational parameters $(\Delta\alpha_{\text{p}}, \Delta\beta_{\text{p}}, \Delta\gamma_{\text{p}})$ of the matrices describing the transformation between cross-sectional IVOCT images or consecutive A-scans. Thus, we demonstrate different approaches for spatial regis-

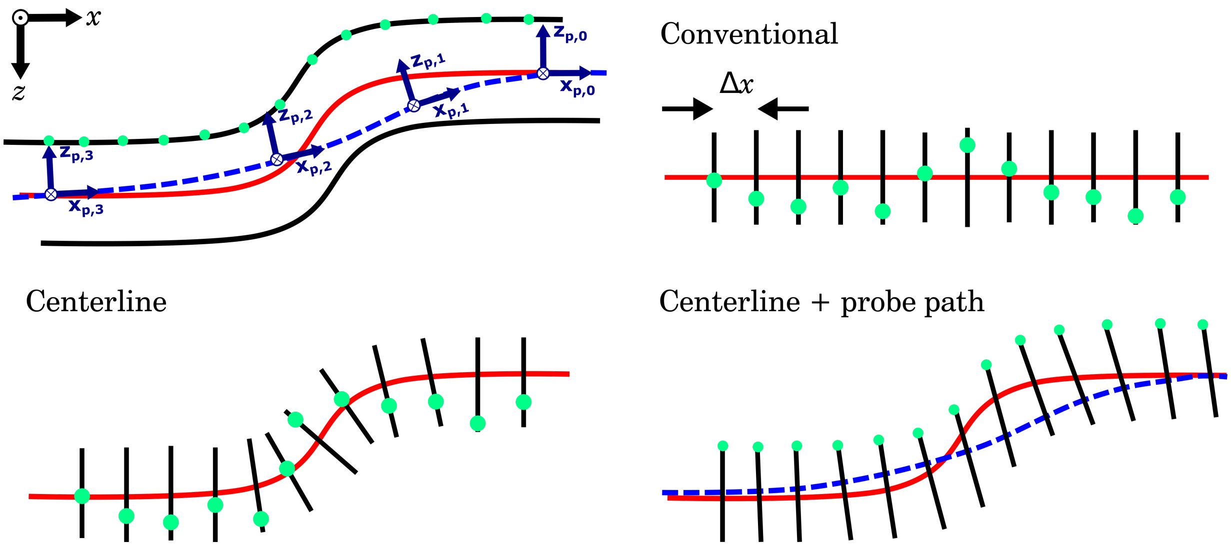

Figure 4.5 Overview of slice-wise IVOCT volume reconstruction methods investigated in this thesis. In contrast to the conventional approach visualized on the top right, methods for bi-modal volume reconstruction are studied involving an estimation of the vascular centerline (red) and probe path (blue) from external imaging. The green dots highlight vascular boundary points originally imaged in the same plane. NURD artifacts or wrong spatial rotation of cross-sectional images result in deviations of these points that are compensated in the combined centerline and probe trajectory approach.

tration of IVOCT image data based on external imaging, assessing either the three-dimensional vascular centerline or the spatio-temporal probe trajectory. The methods described in the following Sections have been presented in studies focusing on volume reconstruction from DSA [401] and MPI [403, 404] as well as imaging probe tracking with MPI [405].

The conventional volume reconstruction method described before is based on two simplifications: first, the IVOCT imaging probe follows a straight trajectory, and second, the imaging probe is centered in the vascular cross-section. However, due to the curved anatomic structure of coronary arteries, the catheter does not follow a straight line and, in most cases, is not positioned centrally in the vessel lumen. Therefore, we want to investigate methods for volume reconstruction that consider the three-dimensional luminal centerline as registration points of external and intravascular images, as depicted in Figure 4.5. For optimized reconstruction of the vascular morphology, we first analyze the external image data from DSA and MPI to extract the vascular centerline. The necessary image processing steps are described below.

For our bi-modal IVOCT and DSA studies, we first extract the vascular centerline from each individual C-arm configuration. We fill the vessel phantom with a contrast agent and apply a threshold-based segmentation approach to extract the outer luminal contours

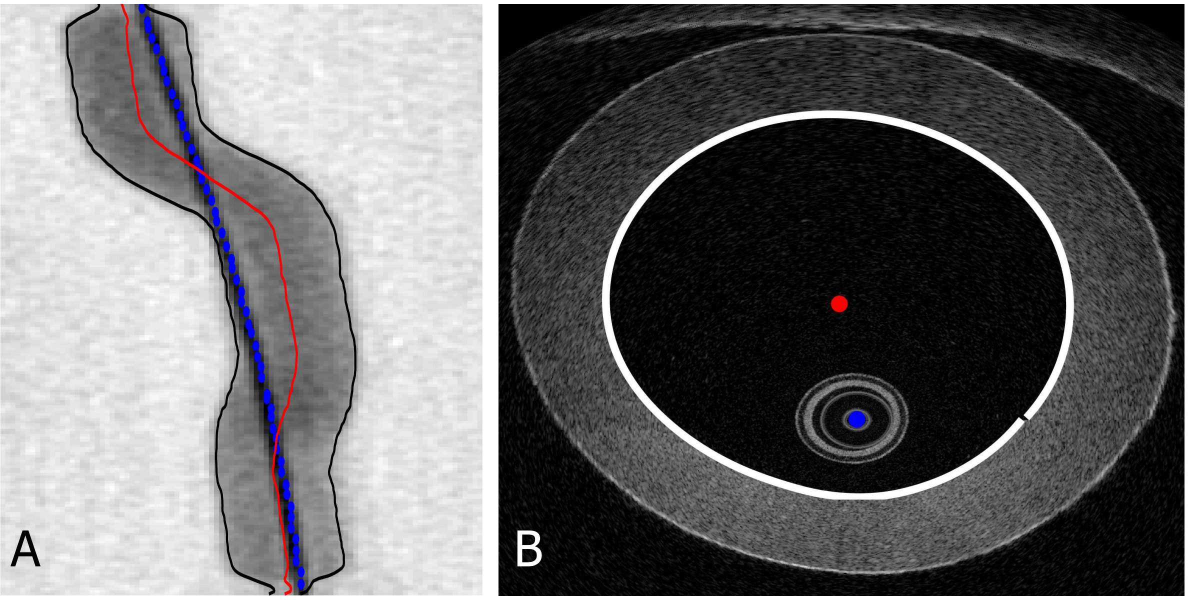

Figure 4.6 A) X-ray image of configuration C_1. Segmented catheter trajectory points are highlighted with blue dots. The contours of the phantom are highlighted with black lines. The related 2D phantom centerline is depicted in red. B) Cropped intravascular OCT frame with segmented luminal boundary in white. The respective catheter (blue) and luminal center of mass (red) positions are highlighted. Figure adapted from [401].

from the X-ray images. For each projective view, the vascular centerline follows between these segmented contours as shown in Figure 4.6. We transfer this projective information to the three-dimensional space in the second step. To extract three-dimensional position information from the X-ray image pairs, we apply a stereoscopic localization approach based on [110]. A necessary condition for this approach is a known relative pose of the two C-arms. Thus, we conduct an image calibration using a phantom with embedded steel balls whose relative positions are known. Using a Point-n-Point algorithm (*Posit* [406]), we estimate the transformations from the calibration phantom reference frame to the respective imaging coordinate systems ${}^{I_i}T_{\mathrm{ph}}$. Consequently, the transformation between the C-arms follows as

$${}^{I_2}T_{I_1} = {}^{I_1}T_{\mathrm{ph}}({}^{I_2}T_{\mathrm{ph}})^{-1}. \tag{4.7}$$

Finally, using mid-point triangulation, we can determine the corresponding three-dimensional position in the object coordinate system for a point in the X-ray image.

In the bi-modal IVOCT and MPI studies, we fill the vascular phantom with SPIONss to visualize the vascular shape. In contrast to bi-plane DSA, we directly receive three-dimensional images of the vascular structures. We extract the centerline by evaluating the MPI images slice-wise along the system's x_{p}-axis. Here, we estimate the center position of the luminal cross-sections with sub-millimeter accuracy [116]. Due to imaging effects, we can only evaluate 24 slices of the MPI imaging FOV. We then use the estimated three-dimensional centerline as a surrogate for the vessel shape to achieve a realistic three-dimensional arrangement of the IVOCT image data. Therefore, we assign a constant number of IVOCT A-scans to a cross-sectional image and estimate the luminal center of mass highlighted with a red dot in Figure 4.6. We discretize or interpolate the centerline assessed from external imaging and apply spatial registration to the center of mass extracted from each two-dimensional IVOCT image. We assume that the IVOCT images are orthogonally oriented to the externally assessed centerline.

Alternatively to the reconstruction based on the vascular centerline, we study volume reconstruction methods by estimating the trajectory of the IVOCT imaging probe. First, we combine the three-dimensional probe trajectory estimated from DSA [401] with the centerline estimated. Second, we apply MPI to track the IVOCT imaging probe in three dimensions over time [405].

Similar to the DSA image processing steps for centerline extraction, we estimate the three-dimensional IVOCT probe trajectory. We first segment the visible probe tip marker for all successive DSA images and second estimate the respective three-dimensional positions after triangulation from the two projective views. Subsequently, we combine the estimated trajectories of the vascular centerline and the imaging probe. Unlike the reconstruction approach using the estimated vascular centerline, we align the IVOCT cross-sectional images orthogonal to the probe trajectory and use the centerline to adjust the angle orientation of the images resulting from non-uniform rotation profiles with angle α_{p}. More precisely, we rotate the IVOCT images around the probe origin, minimizing the distance between the center of mass estimated from IVOCT and the centerline estimated from DSA.

In comparison, we aim to acquire three-dimensional MPI images over time to assess the spatio-temporal motion of the IVOCT probe. As introduced before, specific magnetic particles are required to generate a signal echo that can be measured with the MPI system. Thus, we use a magnetic lacquer to coat the IVOCT probe tip without covering the imaging optic. Image processing steps applied in this thesis to extract the 3D+t probe trajectory are similar to the methods described in [116] and structured as follows. First, a threshold-based image binarization is performed to highlight the MPI signals induced by the marker from the noise. Second, we use this binarization mask to find the largest contiguous region with the highest maximum intensity values. Third, the center of mass of the found region is determined with submillimeter accuracy as IVOCT probe position per volume over time. These processing steps produce optimal results when evaluating an effective MPI imaging FOV. Furthermore, we apply outlier extraction methods to correct for falsely detected marker positions due to massive noise signals. Lastly, we smooth the extracted 4D motion trajectory and interpolate the extracted position to respective IVOCT sampling positions. Using this 4D probe motion trajectory for the three-dimensional arrangement of the IVOCT image requires an accurate temporal synchronization of the IVOCT and MPI image data sets. We arrange the IVOCT A-scans on a helical trajectory as proposed when using the set IVOCT imaging parameters for reconstruction. Here, we use the pitch of the motion difference in pullback direction Δx_p estimated from MPI imaging per IVOCT probe rotation. We assume a uniform IVOCT probe rotation and arrange the image data with a fixed angular difference $\Delta \alpha_\mathrm{p}$ around the catheter trajectory.

The accuracy of the methods for reconstructing the vascular morphology is compared to the ground truth shapes from the CAD sketches of the phantoms using the Dice Coefficient (DICE) that has been proposed for segmentation analysis [407]. In particular, the DICE is calculated using the longitudinal or cross sections of the reconstructed volumes as

$$\mathrm{DICE} = \frac{2 \mid \mathbf{p}_\mathrm{CAD} \cap \mathbf{p}_\mathrm{L} \mid}{\mid \mathbf{p}_\mathrm{CAD} \mid + \mid \mathbf{p}_\mathrm{L} \mid}, \tag{4.8}$$

with $\mathbf{p}_\mathrm{L}$ and $\mathbf{p}_\mathrm{CAD}$ expressing the respective points of the segmented longitudinal boundaries or the ground truth points of the CAD sketch. Using $\mathbf{p}_\mathrm{C}$ in Equation 4.8 instead of $\mathbf{p}_\mathrm{L}$ results in the DICE for comparison with the luminal cross sections.

4.3 Quantification of Soft Tissue Elasticity

In this chapter, we investigate different experimental setups and signal processing methods to achieve a quantitative estimate of soft tissue elasticity from a miniaturized imaging probe. In particular, we aim to explore different temporal and spatial sampling schemes to assess the propagation of excited shear waves accurately. We study different probe designs and shear wave excitation approaches. In our experimental studies, we systematically vary the setup parameters to study the influence on the quantification results. For example, we vary the distance between the excitation and imaging probe. The methods described in the following Sections are based on experimental studies published [270, 408].

4.3.1 Shear Wave Excitation and Imaging Systems

The shear wave tracking approaches presented in this thesis are based on the concept of transient elastography. Hence, we excite a single shear wave and investigate its propagation through the tissue by evaluating OCT signals at distinct positions. Basically, the shear wave velocity can be estimated from the spatial distance Δs and the sensed run time t_s as introduced in Equation 3.3. These approaches require precise spatial calibration, meaning that the position of the excitation and imaging needs to be known. Additionally, accurate temporal sampling is necessary.

In the following sections, we introduce our transient shear wave elastography concept from miniaturized imaging probes. Particularly, we study how a shear wave can be excited and measured while the OCE probe is inserted into the tissue. First, we examine a Single-Fiber OCE (SF-OCE) probe design to track shear waves. In contrast to multi-dimensional image acquisition setups, we only acquire one-dimensional depth scans to sense the incoming wave. Addressing the high demands of transient elastography on spatial and temporal calibration, we additionally propose a Dual-Fiber OCE (DF-OCE) probe design. In our experimental studies, we compare these approaches to elasticity measurements applied from outside the tissue, i.e., in benchtop OCE and USE.

In Section 3.2.1, we compared various concepts for shear wave excitation. Analogously, methods to excite a single shear wave pulse at the tissue surface are investigated in this thesis either using a stacked piezoelectric actuator or with ARF from US probes shown in Figure 4.7. In the first case, we mount a needle on the piezoelectric stack actuator and place it on the surface. We use a sinusoidal pulse actuation, which leads to a rapid back-and-forth movement of the needle tip. This enables the point excitation of a single shear wave that

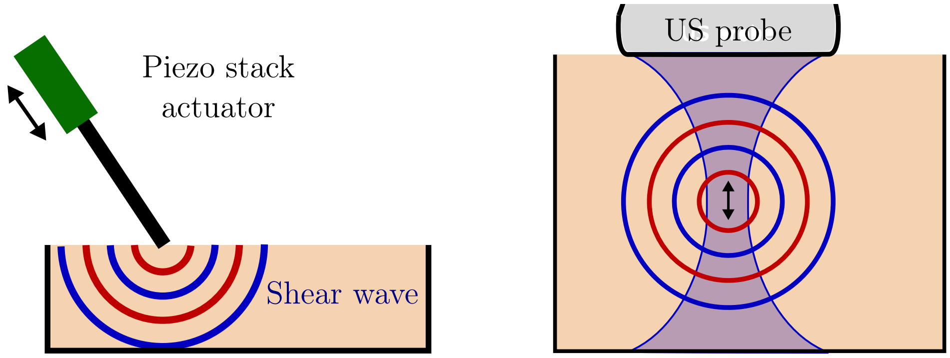

Figure 4.7 Visualization of shear wave excitation setups investigated in this thesis. (Left) We position a piezo stack actuator with a connected rod on the tissue surface and excite shear waves when actuating vibrations with an amplitude of 10 µm. (Right) Alternatively, we use a US transducer to excite a ARF. Consequently, a small axial motion is applied inside the soft tissue (black arrows), followed by a spherically translating shear wave.

propagates as a surface wave with a corresponding spherical wave inside the tissue. Consequently, we can assess the shear wave properties either at the surface with a benchtop OCE setup or from within the tissue with our miniaturized OCE probe. In the second case, we position a US linear array probe on the tissue surface. We specify a transmit beam-forming profile to actuate the probe elements from the outside to the inside successively to focus the acoustic energy on a specific point in the tissue. Thereby, the sequentially actuated acoustic waves accumulate in the desired focus point, leading to a small tissue motion. This requires applying a high actuation voltage and optimal transmit beam forming conditions. The excited longitudinal motion wave has an orientation perpendicular to the US probe. Assuming a perfect beam forming and point excitation, we can assume a spherical wave propagating outwards.

Based on the excitation principles described, concepts for the quantification of soft tissue elasticity from miniaturized OCE imaging probes are developed in this thesis. The OCE probe designs demonstrated in this thesis are composed of imaging optics that enable one-dimensional depth scanning perpendicular to the instrument axis. Meanwhile, the overall probe diameter should be minimized. Similar to IVOCT imaging probes, this design should be capable of assessing tissue characteristics radially around the instrument. In Figure 4.8, the design of the applied imaging optics is shown, encompassing a GRIN fiber and a fiber prism that are spliced to the end of a single-mode fiber to focus and deflect the beam. First, the GRIN fiber acts as a lens that collimates the light beam while the outer diameter of the optics remains small. By integrating a step-index multi-mode or coreless fiber between

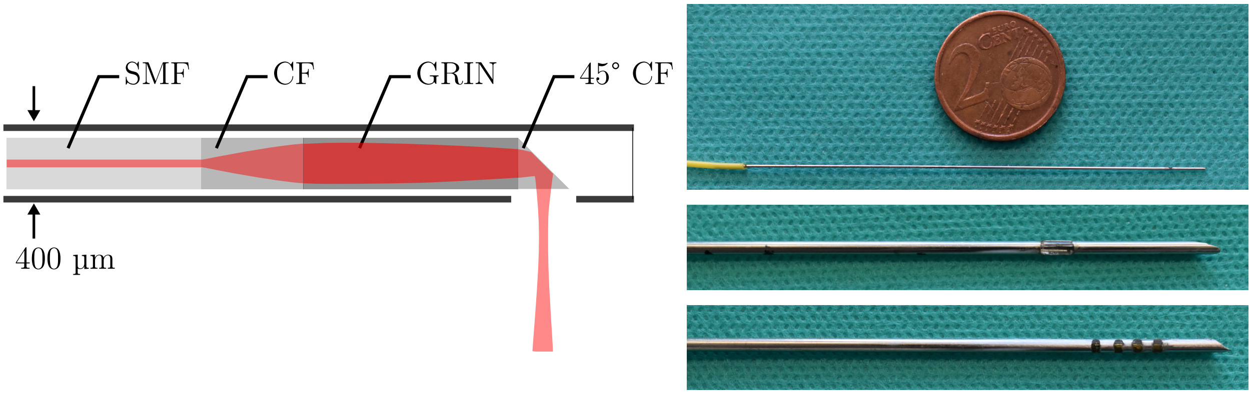

Figure 4.8 (Left) Optical design of our developed OCE probe. A single-mode fiber (SMF) is used as the foundation of the probe. Next, a coreless fiber (CF) is spliced between SMF and a GRIN fiber to widen and collimate the beam. Finally, a 45° polished coreless fiber is used to deflect the optical beam. (Right) Pictures of different OCE probe designs. Finally, a SF-OCE probe with a minimized diameter of up to 400 µm is shown as sketched on the left. Below, two probe designs with three or four embedded imaging optics are shown with diameters of up to 2 mm.

single-mode and GRIN fiber, also referred to as optical spacer, we widen the beam and achieve long working distances. Second, we build a fiber prism by polishing a terminating fiber to an angle of approximately 45°. By varying the lengths of fiber components used, we define the respective working distances and axial resolutions.

In this thesis, we investigate a single-fiber and DF-OCE probe design. For the first design [270], we splice a step-index multi-mode fiber (FG200LEA, Thorlabs GmbH, Germany) of length 0.6 mm together with a GRIN fiber (G200/220, Fiberware GmbH, Germany) of length 0.8 mm to a single-mode fiber (SMF-28, Thorlabs GmbH, Germany). Next, we splice a second multi-mode fiber (FG200LEA, Thorlabs GmbH, Germany) and construct our fiber prism by polishing the end at an angle of 45°. Using this design, we achieve an outer diameter of 220 µm for our optics. We embed the described imaging optics in a capillary tube with an outer diameter of 810 µm and a drilled imaging window. We use UV-curing adhesives to fix the optical components inside the tube. Lastly, we apply a low-viscosity optical adhesive to close the imaging window and polish the surface to minimize astigmatism effects. To enable punctures in tissue, we equip the SF-OCE probe with a conically shaped tip.

With our DF-OCE probe design [408], we aim to sample a propagating shear wave at two positions along the probe shaft. As an essential prerequisite for our transient shear wave approach, we specify that the deflected light beams should be aligned parallel. Developing a DF-OCE probe requires further miniaturization of the embedded imaging optics. Thus, we splice a GRIN fiber [409] of length 0.95 mm and diameter of 125 µm with an embedded coreless fiber acting as an optical spacer to a single-mode fiber (SMF-28, Thorlabs GmbH, Germany). As a fiber prism, we use a coreless fiber (FG125LA, Thorlabs GmbH, Germany) of length 140 µm and polish its end at an angle of 47°. We define the lengths for the applied fiber components to achieve a beam diameter of 60 µm, a working distance of approximately 1.5 mm, and an axial resolution of 7 µm. We use capillary tubes of 410 µm outer diameter to stabilize the imaging optics. We align the optics so that the light beams are deflected through a drilled imaging window. Again, we fix the optical components with UV-curing adhesives and seal the imaging window with a low-viscosity epoxy adhesive (NOA86H, Norland Products Inc., USA). The flat polishing of the imaging window ensures an almost astigmatism-free beam focusing outside the probe.

In the final design step, we investigate different alignments of these single-fiber probes in another capillary tube to obtain multi-fiber OCE probes. First, we designed a probe with multiple imaging probes oriented around a stabilizing rod. We align the imaging optics at a certain distance from each other along the probe shaft. At the same time, we want to ensure that the individual light beams emerge in parallel from the probe. However, this alignment imaging optics was restricted in manufacturing. In Figure 4.8, two different OCE probes are shown with light beams deflected in various directions around the probe. To ensure a parallel beam deflection in our final DF-OCE probe design, we embed two single-fiber imaging optics that are aligned not next to each other but in a line in a capillary tube of 1 mm outer diameter. We developed a specific clamping device to adapt and fix the rotational orientation of the deflected light beams. Please note that the processing of optical fiber components for the presented OCE probes was carried out by our project partner at the University of Lübeck. A filament splicer (GPX3800, Thorlabs, Germany) was used to splice the glass fibers. The fiber prisms were processed using a polishing machine (Trig™ Bare Fiber Polisher, Krelltech, USA) for optical fibers.

With our developed OCE probes, we acquire one-dimensional depth-resolved scans using a spectral-domain OCT imaging system (Telesto I, Thorlabs GmbH, Germany). The imaging system contains a broadband laser source and a detector composed of a spectrometer with a line scan camera as introduced in Section 2.1. For signal acquisitions with our SF-OCE probe, we connect the probe and an external reference arm over a 2x2 beam splitter (TN1310R5A1, Thorlabs GmbH, Germany) to the SD-OCT system as depicted on the left in Figure 4.9. Before signal acquisition, we manually adjust the reference arm length to ensure optimal positioning of the imaging focus in the acquired depth scan. During this alignment, we also try to minimize the influence of multiple reflections occurring on surfaces in the OCE probes design, e.g., imaging windows, and glass fiber end.

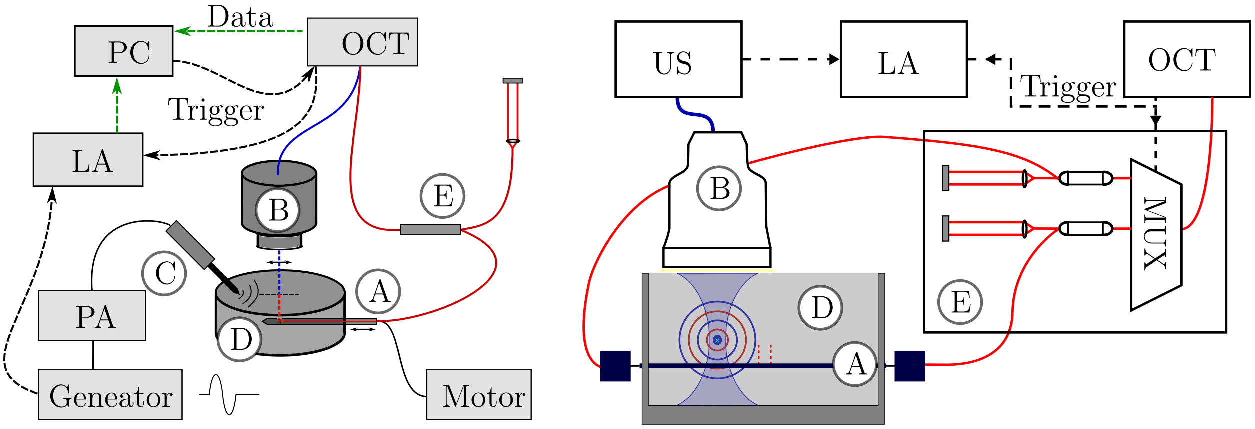

Figure 4.9 Imaging Setups to acquire OCT image data from single-fiber (left) or dual-fiber OCE probe (right). We insert our OCE probe (A) in a soft tissue phantom (D) and acquire image data with the OCT system. Depending on the OCE probe design, different reference arm setups (E) are used. A multiplexer enables high-speed switching between the imaging optics for our dual-fiber probe. Additionally, an OCT scan head or US transducer are applied to acquire reference elasticity measurements (B). Shear waves are generated with a piezoelectric stack (C) or with ARF using the US transducer.

For signal acquisition with our dual fiber OCE probe, we complement the previous setup with a second reference arm setup and an optical multiplexer (NSSW-3111033, Agiltron Inc., USA). Different reference arm lengths are required because the individual imaging probes are not necessarily of the same length. In addition, signals from both optics cannot be captured simultaneously with the OCT system. Therefore, we connect each imaging optic with a dedicated reference arm to a separate beam splitter and use the optical multiplexer to switch between the two imaging optics. We apply an Arduino Uno microcontroller to activate the switching based on the trigger signals of the OCT system. Please note that the used OCT imaging system sends a trigger signal for each depth scan measured at the detector. Our overall signal acquisition setups designed for OCE from our miniaturized probes are depicted in Figure 4.9.

During our experimental studies, we aim to obtain reference elastography measures from conventional imaging setups applied from outside the tissue. Therefore, we complement our probe-based elastography setups with external OCE or USE imaging setups described in the following. First, we designed a transient OCE imaging setup using the scan head (LSM03, Thorlabs GmbH, Germany) and a SD-OCT system. Using the scan head's built-in reference arm, we adapt the axial height of the imaging FOV and focus point. Given the shear wave excitation with a piezoelectric actuator on the tissue surface, we vary the lateral orientation of excitation and imaging by adapting the scanning position with the scan head. After shear wave excitation, we sequentially acquire one-dimensional depth scans for a stationary position of the scan head's galvanometers. We record the trigger signals of the SD-OCT system and the signals generated for actuation of the piezoelectric element with a digital oscilloscope (STEMlab 125-14, Red Pitaya, Slovenia).

To obtain a global elastography reference map in deeper layers of the tissue, we alternatively complement our setup with a high-speed US system (128 Channel Cicada, Cephasonics Ultrasound, USA) for USE. In particular, we position a linear US transducer (CPLA12875, Cephasonics Ultrasound, USA) on the tissue surface. Using this transducer, we first excite a shear wave in a specific position within the tissue by applying ARF and second track the propagating wave during two-dimensional plane wave image acquisition. The US system enables the excitation of piezoelectric actuators with frequencies of up to 40 MHz. For ARF shear wave excitation, we actuate the piezoelectric elements of the transducer one after the other from the outside to the inside. We repeat this excitation of elements with the maximum system frequency several times. Consequently, the acoustic waves overlap at one point in the depth of the tissue, resulting in a small tissue motion perpendicular to the US probe. Assuming perfectly directed acoustic beams, a spherical shear wave propagates as depicted in Figure 4.7.

4.3.2 Calibration and Synchronisation

An important prerequisite for transient OCE approaches is an accurate spatial calibration and temporal synchronization of shear wave excitation and imaging. In the following, we describe our derived methods for calibration and synchronization. We differentiate between two imaging setups developed for OCE from our single-fiber or dual-fiber probe.

The first setup for OCE from our single-fiber probe is shown in Figure 4.9. We calibrate our experimental setup to ensure that the external OCE signal acquisition and the acquisition from within the tissue are aligned normal to the tissue surface and along the same vertical line. For shear wave excitation, we position a needle attached to a piezoelectric actuator on the surface of a gelatin phantom. We insert the OCE probe into the phantom facing upwards and position a scan head above, which records A-scans in the opposite direction. Consequently, we can sample the shear wave, which propagates as a transverse wave on the tissue surface and propagates with corresponding spherical components in the tissue. For setup calibration and alignment of the OCT imaging FOVs, we design and print a calibration phantom with a three-dimensional cross. First, we orient the cross centrically in the scan head's FOV. We then position the OCE probe over the cross and ensure that the polished

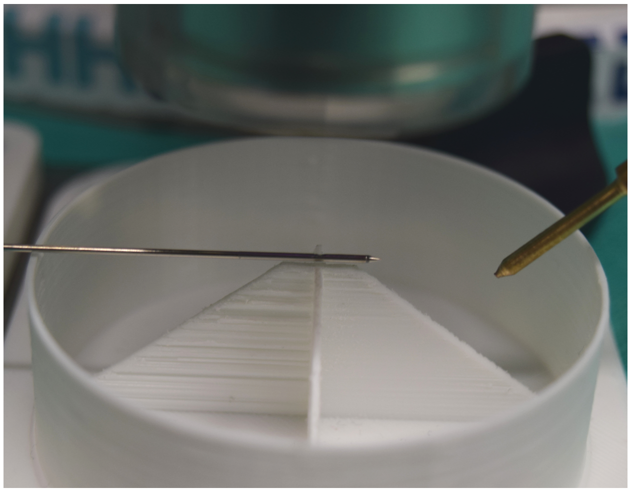

Figure 4.10 Calibration approach for single-fiber study. We position a three-dimensional cross underneath the OCT scan head and position the OCE probe imaging window in plane with the scan head's FOV. Next, we position the rod for shear wave excitation in the calibration center as a reference to determine the distance between the excitation and imaging positions.

fiber prism is in the center of the scan head's FOV as shown in Figure 4.10. During calibration and signal acquisition, we vary the imaging position of the OCE probe and the OCT scan head with a linear motion stage or hexapod robot, respectively. Additionally, we vary the insertion height of our OCE probe by manually adjusting a micrometer screw.

The second setup for the quantification of shear wave velocities from our DF-OCE probe is shown in Figure 4.9. We align the imaging FOVs of the USE and OCE probes so that the same areas in the tissue are examined. Moreover, we calibrate our setup, which consists of our imaging probes and a hexapod robot, so that reproducible measurements are possible with various orientations of shear wave excitation and OCE imaging positions. In particular, we use a linear transducer for shear wave excitation and acquire USE image data as a reference. Therefore, we position the US transducer directly on the phantom surface and aim to insert our OCE probe in-plane with the US imaging FOV. Please note that our OCE probe is positioned in a phantom container that is mounted to a hexapod robot. Thus, we vary the position and orientation of our OCE probe by moving the hexapod. Meanwhile, our US probe remains in a rigid position above the hexapod. As the first step of our calibration approach, we position our OCE probe in the water-filled phantom container so that the maximum reflections occur in the US image. Second, we determine the positions of our imaging optics relative to the US FOV. To do this, we attach a thin needle with a diameter of 0.2 mm to the center of our US probe and move the OCE probe relative to it while acquiring OCT image data. We assign hexapod positions with maximum reflections in the OCT images to

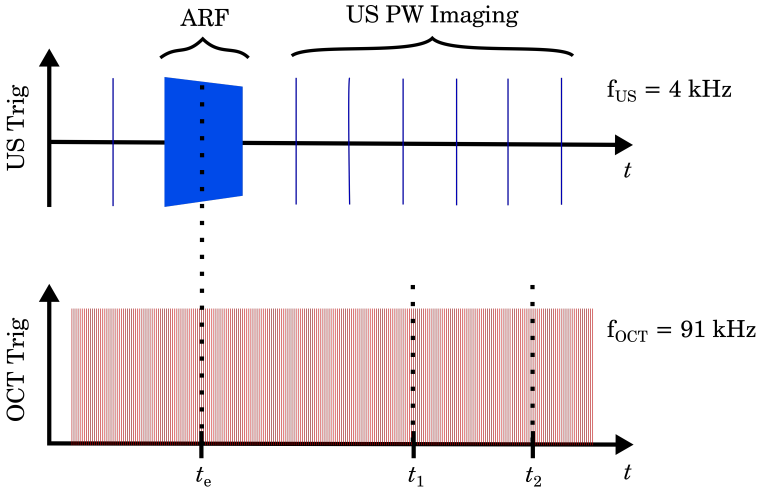

Figure 4.11 Exemplary visualization of trigger signals acquired during synchronous OCE and USE measurements. The OCT A-scan acquisition with a frequency of 91 kHz is started, afterwards the ARF pulse is emitted at time point t_e. Subsequently, the acquisition of US plane wave images with a frame rate of 4 kHz is started. The time points (t_1, t_2) at which the shear wave reaches the two imaging optics are highlighted.

the US images in which the respective imaging optics are centered. Finally, we obtain the three-dimensional OCE probe position relative to our US probe in hexapod coordinates and the distance $\Delta p_{1,2}$ of our two imaging optics. Using this spatial information, we choose an ARF focus point above the OCE probe to minimize acoustic artifacts. When calculating the related beam-forming profiles, we account for the different speeds of sound of the investigated tissue phantoms. In our experimental studies, we systematically vary the distances between the imaging optics and the excitation source. Since shear waves are not necessarily excited in-plane with the imaging optics and are usually located above the probe, we consider the angles α_x and α_y to compensate for an underestimation of the distance $\Delta p_{1,2}$. For temporal synchronization, we use a digital oscilloscope to record the trigger signals of both shear wave excitation and imaging.

In the case of our SF-OCE probe and external OCE setup, we use this information to estimate the wave's run time t_s toward a certain imaging position. With the respective spatial distance given from setup calibration, we can estimate the shear wave velocity as introduced in Section 3.2.1. In this way, however, only an average elasticity value can be determined for all tissue structures located between excitation and imaging. Minimizing this distance would be preferable for improved quantification of elasticity. However, it is only possible to a limited extent, ensuring proper sampling of the wavefront.

In contrast, our DF-OCE probe concept promises a more accurate quantification of soft tissue elasticity. We again record the trigger signals from excitation and imaging, but do not necessarily use this for velocity quantification. Most importantly, we examine the wave's run time between both OCE imaging optics. To infer the shear wave velocity, we use the distance between imaging optics $\Delta p_{1,2}$ determined from OCE probe calibration. This distance remains constant for all orientations of our excitation source. For USE analysis, we additionally record the trigger signals sent for each US frame. As the ARF excitation is also defined as US frame, we retrieve the trigger signals shown in Figure 4.11. To track the propagating shear wave, we acquire a sequence of US plane wave images with a frame rate of 4 kHz. During image acquisition, a steering angle of 10° minimizes reflection artifacts from the phantom container walls. Consequently, the acquired US image FOV consists of 400×420 pixels which correspond to approximately $37.5\times$ 30 mm in homogeneous gelatin.

4.3.3 Image Processing for Quantitative Elastography

In transient shear wave elastography approaches, the main idea is to estimate the time difference t_{s} between exciting a wave and sensing it at a certain imaging position as depicted in Figure 4.12. In particular, we focus on actuating single-pulse shear waves, where we assume spherical propagation in the tissue. Assessing soft tissue elasticity from a miniaturized probe reveals problems not described for analogous benchtop OCE setups. First, the imaging probe and, therefore, the respective coordinate frame do not remain constant during signal acquisition as usual for external optical scanning setups. Determining the respective distance between the imaging probe and shear wave excitation is therefore more difficult. Secondly, the part of the mechanical wave tends to propagate differently in the depth of the tissue than surface acoustic waves, which are usually tracked. Consequently, the alignment of the imaging axis relative to the oscillation direction of the shear wave becomes more complicated. In the following, we will summarize the derived image processing methods to observe elasticity estimates from the miniaturized probes and the respective measures from externally OCE or USE imaging.

The OCT signals acquired from our OCE probes and also from our external imaging setup are composed of sequentially acquired A-scans, also referred to as M-scan and introduced in Section 2.1. For shear waves traveling through the imaging FOV, variations in the sensed complex signals are observed. As the motion amplitudes of these shear waves are relatively small, the motion is mainly contained in the phase component, while the magnitude or intensity data show disturbances. Considering the design of our experimental setups, we can assume that the excited shear waves travel almost perpendicular through the one-dimensional depth scan, with the motion oscillating in the depth direction. In the phase signals of a temporal sequence of A-scans, these oscillations are visible, varying between $-\pi$ and π.

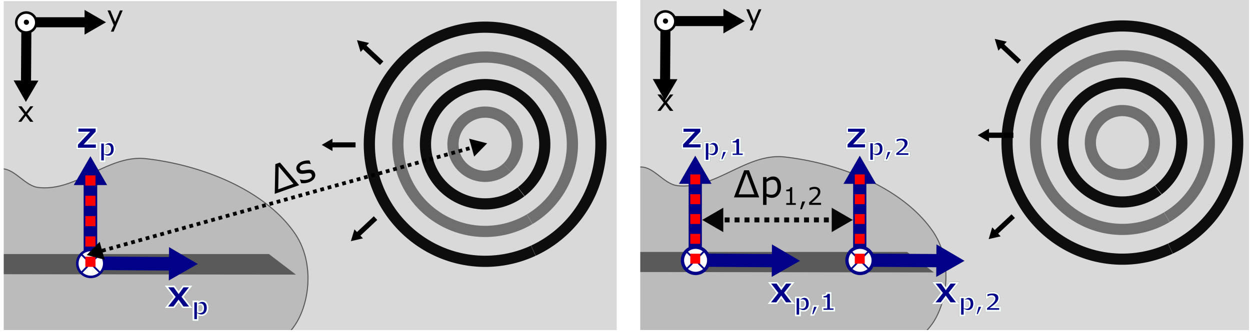

Figure 4.12 Visualization of transient OCE approach from minaturized imaging probes. In particular, the spatial distances between excitation and imaging Δs for the single-fiber probe and the distance between imaging optics $\Delta p_{1,2}$ in the dual-fiber probe are highlighted.

In this thesis, we investigate image processing methods to derive the elasticity of soft tissue by extracting the shear wave parameters from the complex OCT signal. Given the transient OCE approach, we first focus on estimating the runtime Δt_s and spatial distance Δs between excitation and imaging. On the other hand, we study methods to correlate the image data from both imaging optics of our DF-OCE probe. In particular, this method relies on a fixed distance $\Delta p_{1,2}$ between the imaging optics. The spatial orientation of shear wave excitation and imaging positions is depicted for both OCE probe concepts in Figure 4.12. The necessary image processing steps described in the following are structured as 1) pre-processing of complex OCT signals, 2) extraction of individual shear wave components, and 3) a combined spatio-temporal analysis of a number of excited and imaged shear wave pulses.

First, several signal pre-processing steps are necessary. Given the design of our imaging optics, several reflections occur from surfaces in the probe. Even if we use the reference arm to minimize these artifacts, we need to extract the left ones for improved image interpretation. In general, we arrange our reference arm so that reflections from optical components are only visible in the first pixels of the axial scan. As reflections from the imaging window are the most prominent ones, we average the first 1000 A-scans and search for the highest intensity values in the first 100 pixels. Next, we can use this depth information to cut off the first pixels of our one-dimensional depth scan. For observing motion information from our cropped complex OCT signals, we mainly use the phase difference derived in Equation 2.12. The phase signal describes the orientation of a certain scatterer relative to the imaging beam expressed as values between $-\pi$ and π. Consequently, the absolute pixel values of these phase images cannot be interpreted directly. Thus, according to the Doppler OCT principle introduced in Section 2.1, we calculate the phase difference of successive axial scans. The resulting image contains information on the motion differences per imaging depth.

Given the temporal A-scan sampling rate of 91 kHz, fast motion can be resolved quite well. However, there is a trade-off between the temporal sampling rate, motion frequency, and amplitude. In addition, phase wrapping or drift effects described in Section 2.1 need to be compensated during preprocessing of the image data. We use the unwrapping function contained in MATLAB, which searches for abrupt phase jumps and attempts to correct them by subtracting multiples of 2π. Compensation is not trivial, as phase drift effects occur with different magnitudes and consistency during signal acquisitions. However, when calculating the phase differences, these drifts are most commonly small compared to the real tissue motion and can be ignored, especially for image acquisition schemes with relatively short acquisition periods.

Next, our investigated methods to extract specific shear wave characteristics from OCT signals acquired at one stationary position are described. We use the preprocessed phase signals after cropping, unwrapping, and calculating phase differences. We observe the same image representation, independent of the imaging setup, i.e., SF-OCE probe or external scan head. In the spatio-temporal images, the shear waves are visible as sinusoidal, altering angular orientations. The sampling frequency and the shear wave velocity determine the visibility of the entire waveform. For example, a slow temporal sampling of OCT A-scans and a high wave speed lead to a limited number of sampling points of the waveform and thus to a spontaneous change in the positive and negative motion amplitudes visible in the phase signals. In Figure 4.13, exemplary signals are shown for fast shear waves traveling. Considering the soft tissue's scattering and refraction characteristics, a decreased imaging depth of approximately 1 to 1.5 mm results. Together with the orientation of excitation and imaging, we assume that the shear waves are traveling perpendicular to the imaging FOV. Therefore, the motion patterns contained in the phase differences should be equally visible across the entire image depth. Even if the wave arrives at an angle relative to the imaging FOV, the differences in the direction of movement over the small image depth might be negligible. We rely on these physical assumptions and average our phase difference over the whole imaging depth. Thus, we observe a motion amplitude signal over time that we use to analyze the wave characteristics as described below.

Referring to our transient OCE approach, we first aim to extract the time t_I when a shear wave arrives at the imaging position. With our introduced excitation and imaging scheme, we ensure that only one shear wave is excited per repetition and reflected waves from previous excitations are already completely attenuated. We therefore search for the first prominent peak in the extracted motion curves from one excitation and imaging sequence and assign this as the maximum of the excited shear wave. First, we consider peak extraction methods

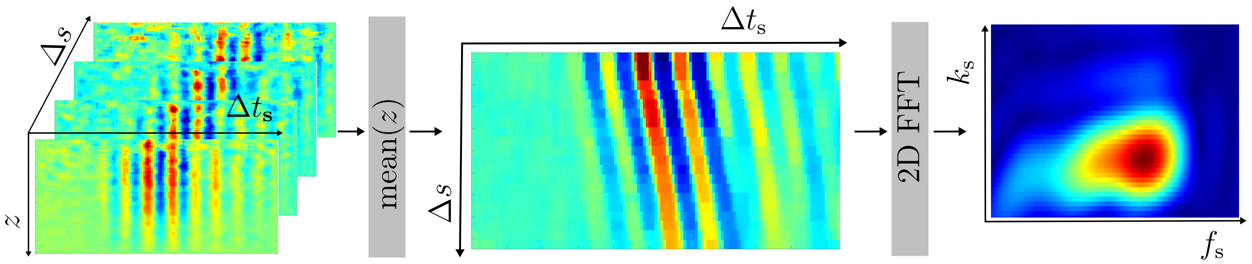

Figure 4.13 Image processing for SF-OCE approach using the distance between excitation and imaging Δs and time difference Δt_s from setup calibration. (Left) For each distance between excitation and imaging Δs_i, a sequence of OCT phase scans is acquired. The respective unwrapped phase M-scans are stacked over Δs. (Middle) A space-time diagram is generated after averaging the phase values over the imaging depth. (Right) Performing a 2D Fast Fourier Transformation results in the respective kf-diagram. The shear wave velocity is extracted from the maximum intensity point of this diagram.

by defining a threshold value c_{th}. Second, we fit a sinusoidal curve to the extracted motion curves and define $c_{th} = sin(\pi)$ as the peak. Subtracting the corresponding time t_{I} from the time point of shear wave excitation t_{E} returns the wave's run time Δt_{s} between excitation and imaging. With the spatial distance Δs known from calibration, we can define the average shear wave velocity as

$$v_{\mathrm{s,SF}} = \frac{\Delta s}{\Delta t_{\mathrm{s}}}. \tag{4.9}$$

In contrast to an individual shear wave analysis for a specific excitation and imaging direction, we also investigate the propagation for several different orientations. In our experimental studies, we either vary the position of the excitation source or imaging probe to simulate different spatial distances or analyze different tissue sections. For example, we insert our SF-OCE probe in a tissue phantom and excite shear waves for different probe positions i. Using the information on spatial distance $\Delta d_{\mathrm{s},i}$, we can arrange the motion curves in a space-time map. An exemplary visualization is shown in Figure 4.13, where the distance and time difference between excitation and imaging are shown on the axes, respectively. Next, we apply a two-dimensional Fast Fourier Transformation (FFT) to get from the space-time map in the Fourier domain. With the frequency f_{s} and wavenumber k_{s}, we can extract the shear wave velocity v_{s} by searching for a maximum intensity position ($f_{\mathrm{s,max}}$, $k_{\mathrm{s,max}}$) within a certain frequency band

$$v_{\mathrm{s,ST}} = \frac{f_{\mathrm{s,max}}}{k_{\mathrm{s,max}}}, \quad \text{with} \quad f_0 < f_{\mathrm{s,max}} < f_1. \tag{4.10}$$

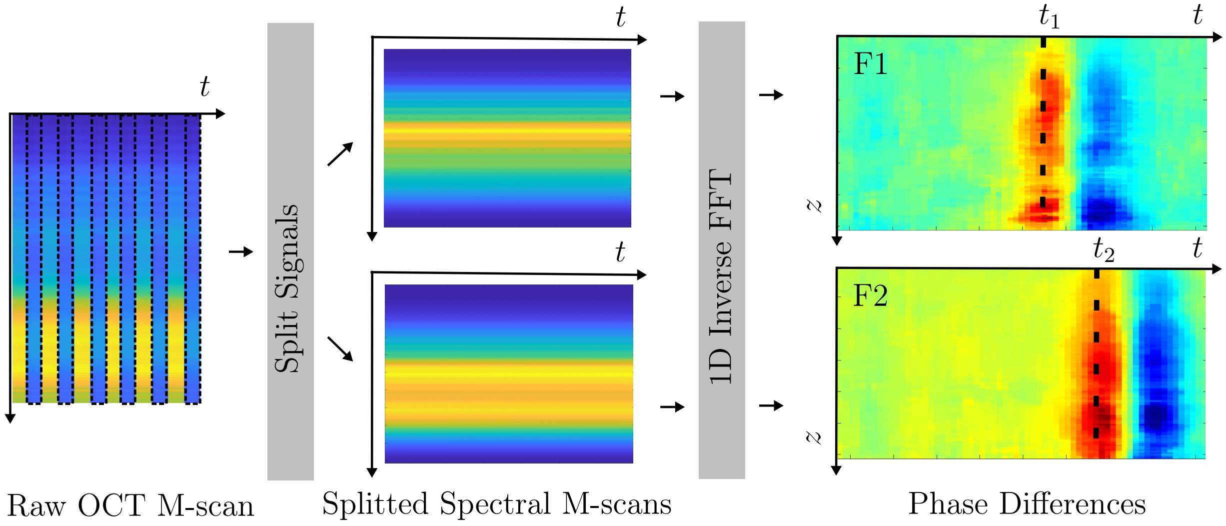

Figure 4.14 Visualization of OCE image pre-processing steps for dual-fiber probe design. (Left) Given the system setup in Figure 4.9, the raw OCT signals are acquired as a sequence of spectral A-scans acquired alternately from the two imaging optics (F1 and F2). (Middle) Afterwards, these signals are split into two individual spectral M-scans. (Rihgt) The respective phase M-scans per imaging optic are extracted from these spectral scans after applying 1D Inverse Fourier Transformation and performing relevant phase pre-processing steps. The time points at which the shear wave arrives at the individual imaging optics are highlighted (t_1, t_2) and used to assess the time difference $\Delta t_{1,2}$.

The previously described methods analyze the complex OCT signals from a single imaging optic. In the following, we introduce our concept for evaluating the shear wave velocity from the OCT signals acquired simultaneously at two imaging positions with our DF-OCE probe. The respective image processing steps are also shown in Figure 4.14. Given the system setup in Figure 4.9 with the applied optical multiplexer, the raw OCT signals are available as a sequence of spectral A-scans acquired alternately from the two imaging optics (F1 and F2). Using the OCT trigger signal, the sequence of A-scans can be split for each imaging optic. The spectral M-scans of each imaging optic are then pre-processed as described for the SF-OCE approach. After phase unwrapping and calculation of phase differences over time, the representations on the right in Figure 4.14 follow. Here, the time point of shear wave arrival t_i at the respective imaging optics is highlighted.

Our subsequent method focuses on extracting the time difference $\Delta t_{1,2}$, which represents the time it takes for the shear wave to travel between the two imaging optics. Therefore, we use the two-dimensional representations of the preprocessed phase difference signals per imaging position and calculate a two-dimensional cross-correlation. In this correlation image, we extract the time difference $\Delta t_{1,2}$ at the position of maximum intensity. With the distance

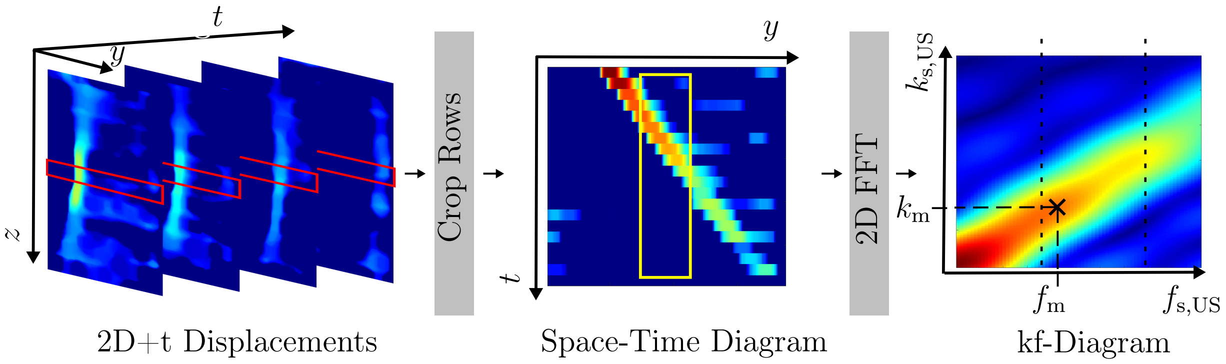

Figure 4.15 Visualization of USE image processing steps. (Left) The two-dimensional US displacement fields are stacked over time and cropped in a specific image height z_i (red boxes). (Middle) The image crops are arranged in a space-time map indicating the shear wave propagation. (Right) After applying 2D Fast Fourier Transformation, a kf-diagram follows. Here, the shear wave velocity is extracted from the maximum intensity peak within a certain frequency band.

$\Delta p_{1,2}$ between imaging optics, we can directly assess the shear wave velocity as

$$v_{\mathrm{s,DF}} = \frac{\Delta d_{1,2} \cos\alpha_x \cos\alpha_z}{\Delta t_{1,2}}. \tag{4.11}$$

The angles α_x, α_z are known from the arrangement of imaging optics relative to the wave excitation source. In contrast to the transient OCE approach presented for a single-fiber probe, we do not need to know the actual time point of wave excitation. In addition, the spatial distance to the excitation source is negligible for small angles between the excitation and imaging positions, meaning a wave propagation perpendicular to the imaging FOVs.

The assessment of the elastic properties from USE image data is described in the following and visualized in Figure 4.15. The sequence of US plane wave images acquired after ARF shear wave excitation is available as raw spectral data. In the first step, we perform beamforming to construct a spatially correct IQ data representation. Using this complex data, the Loupas algorithm [96] is applied to extract two-dimensional displacement fields over time. At the height of the OCE probe, we evaluate these USE displacement fields by converting them into a space-time diagram. As highlighted in Figure 4.15, we extract a certain number of rows (red box) per 2D displacement field, average them, and arrange them over time. Applying a two-dimensional Fourier transformation yields a kf-diagram specifying the motion velocities. We extract the shear wave velocity from this diagram and for the maximum intensity position within a frequency band with

$$v_{\mathrm{s,US}} = \frac{f_{\max}}{k_{\max}}, \quad 180 < f_{\max} < 350\,\mathrm{Hz}. \tag{4.12}$$

4.4 Quantification of Soft Tissue Interactions

In various medical interventions, needles are inserted into soft tissues and navigated toward a specific target position. In the field of anesthesiology, needles are used to apply anesthetic drugs in vascular structures or next to nerve structures. For tumor tissue diagnosis or therapy, needles are navigated toward the lesions to perform either a biopsy or brachytherapy. For all these applications, needle navigation based on external imaging modalities, such as US, is possible but limited due to shadowing and imaging artifacts, especially in deep tissue structures. Furthermore, the puncture success rate strongly depends on the physician's experience and training. The physician commonly uses the forces felt at the needle shaft to differentiate tissue structures. The felt resistance, the number of LOR events, and the increasing or possibly varying friction forces are used as a surrogate for needle navigation. Hence, several methods are derived to simulate, predict, or quantify the forces acting at the needle tip and shaft during needle insertion. Especially in robotic systems with haptic feedback, these force estimates enable intuitive needle navigation.

In this thesis, we aim to investigate whether the complex information from one-dimensional OCT imaging at the needle tip can be used to quantify the needle-tissue interactions during insertion. The methods described in the following are based on previous publications on detecting soft tissue deformation and rupture events during insertion [410] and identifying specific tissue structures [411, 412].

4.4.1 Sensing and Imaging Systems

In the following sections, we introduce the experimental setups that combine different imaging and sensing modalities to assess the soft tissue response during needle insertion. First, we describe the design of the developed OCT needle probe for forward-viewing acquisition of one-dimensional depth scans. Second, we present US imaging and force sensing approaches that act as externally applied reference modalities.

The OCT needle probe designed and studied in this thesis is shown in Figure 4.16. The imaging optics are produced by vertically cleaving the end of a Single Mode Fiber (SMF). Consequently, the light waves are either reflected at the fiber surface or emitted outwards in the direction of the fiber axis. This results in a common-path imaging design that eliminates the need for an external reference arm. Common-path imaging designs have been proposed for various hand-held applications as they are less sensitive to fiber vibration or elongation [240, 413]. As shown in Figure 4.16, we embed the imaging fiber in a medical Thouhy needle that is usually applied for epidural punctures. We use optical adhesive (NoA

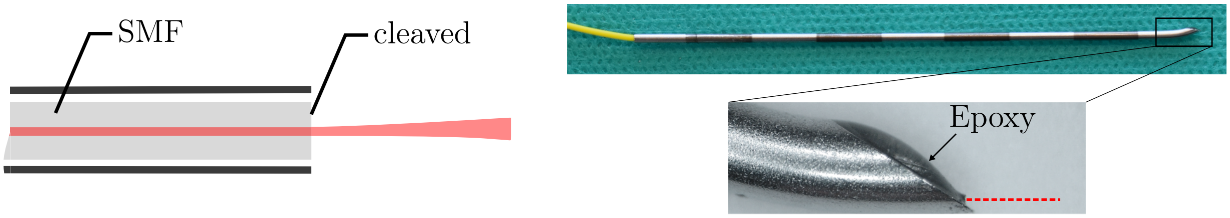

Figure 4.16 Sketch and pictures of the developed OCT probe for sensing soft tissue interaction in front of the needle tip. A SMF with cleaved fiber end is embedded in a medical Thouhy needle for common-path OCT signal acquisition.

63, Norland Products, USA) to fix the imaging optic in the needle tip. Connected to the SD-OCT imaging system (Telesto I, Thorlabs, Germany), we can acquire one-dimensional depth scans in front of the needle tip, facing the direction of insertion.

In Figure 4.17, our experimental setup for multi-modal analysis of needle insertions is shown. We designed a motion stage featuring a stepper motor (LP3575S0504-TR3.5×1, Nanotec Electronic GmbH, Germany) and Arduino MEGA board to automate needle insertions. We apply a linear US transducer (CPLA128, Cephasonics Ultrasound, USA) attached to an US system (128 channel Cicada, Cephasonics Ultrasound, USA) for image-based needle and soft tissue motion assessment. In addition, we attach a FT sensor (SRI M3703A, Sunrise Instruments, USA) at the proximal needle shaft to analyze the forces acting during insertion.

4.4.2 Signal and Image Processing for Insertion Analysis

Studying the soft tissue response during needle insertion requires analyzing different motion components. First, the needle motion in global coordinates needs to be defined. Second, the tissue motion around the needle tip needs to be considered. Finally, these analyses need to be related to appropriate mechanical models.

During insertion with a sharp needle tip, several types of mechanical tissue response have been introduced [311, 324, 327], such as cutting, deformation, displacement, as well as spontaneous ruptures. The mechanical responses generally relate to the stress-strain curves analyzed during pressure or tensile material tests. In this thesis, we consider the following tissue responses. During needle insertion in soft tissue structures, on the one hand, the tissue is cut with the sharp needle tip with no relevant friction and resistance forces acting on the needle. On the other hand, the tissue gets deformed or displaced in front of the needle tip, resulting in increasing forces acting on the needle. Alternatively, the compressed tissue ruptures spontaneously. All the described tissue deformations and displacements exhibit non-linear behavior, and the forces acting between the tissue and the needle cannot be

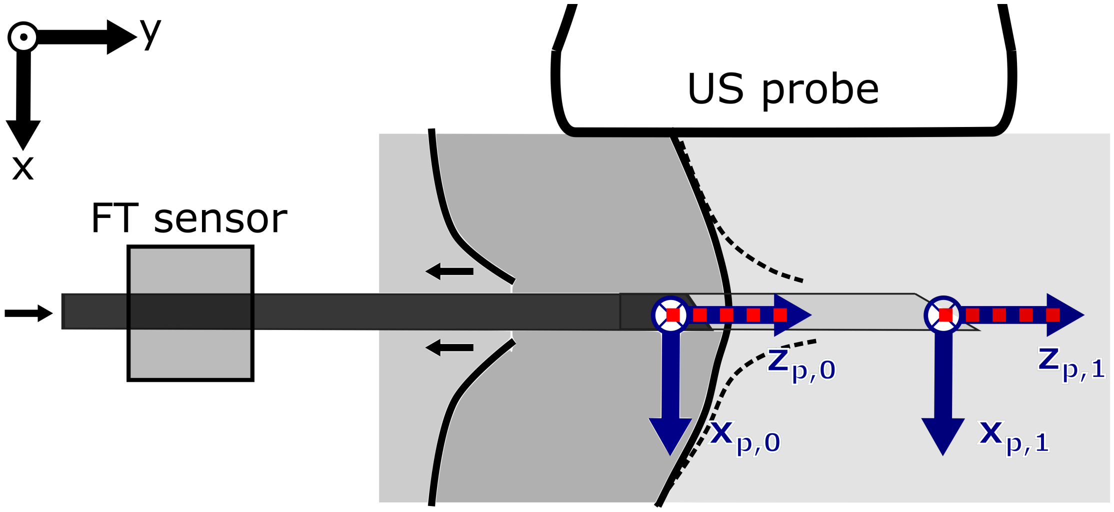

Figure 4.17 Illustration of multi-modal sensing approach for analyzing soft tissue interactions during needle insertion. The developed OCT probe is inserted in a stacked tissue phantom. Simultaneously, force values and US images are acquired with externally attached sensors.

defined clearly. However, we hypothesize that the magnitude of deformation, displacement, and rupture varies depending on the tissue's structure, stiffness, and strength. For example, stiff tissue structures, such as muscle tissue or tendons, are more challenging to penetrate and exhibit greater deformation than fatty soft tissue structures. We also assume that almost no tissue deformation can be detected in soft tissue, resulting in smooth cutting.

The following methods are described for analyzing tissue and needle interactions based on the OCT, FT, US, and motion data sets. Specifically, methods for deriving tissue deformation curves from various modalities and extracting rupture events are presented.

The OCT image data acquired during insertion in front of the needle tip can be represented as a spatio-temporal sequence or pseudo M-scan introduced in Section 2.1. As indicated, assigning spatial axes of the tissue to the M-scan is not directly possible. Since the imaging axis is aligned with the axis of movement and the image acquisition is usually much faster than the movement being performed, the successive axial scans partially show the same sections of tissue. However, a two-dimensional representation, commonly achieved with optical scanning setups, is impossible as the needle and the imaging optics move in a straight line.

Therefore, extracting tissue-specific features from the OCT image data is not trivial. In this thesis, we investigate the OCT intensity and phase signals to analyze tissue by extracting different mechanical responses, namely soft tissue displacement, deformations, and rupture events. We hypothesize that we can use the OCT data to analyze the tissue motion in front of the needle tip. Therefore, we assume constant needle insertion velocities and use the temporal sequence of OCT A-scans to characterize tissue and its mechanic response.

In the intensity signal of the OCT pseudo M-scans, tissue boundaries are visible whose positions and reflectivity along the scan axis vary with the insertion depth. Assuming pure cutting processes during needle insertion, without deformation and displacement of the tissue in front, a tissue boundary should be visible as a straight line with a constant slope a in the OCT M-scan. Here, the slope of the boundary structure a depends on the needle insertion speed. Whenever soft tissue deformation or displacements occur, the tissue boundaries will appear with a varying slope in the OCT M-scan. For example, tissue deformation leads to a parabolic shape of the boundary of a layer in the OCT intensity signals as shown in Figure 4.18. Therefore, we hypothesize that the slope a of the tissue boundaries running through the OCT M-scan resolves characteristics of the tissue deformation and displacements in front of the needle.

We use the OCT intensity data to assess the boundary slope a with the following image processing steps. First, we apply a background subtraction algorithm and Gaussian filtering to emphasize boundary signals. Next, we extract edges in the intensity scans using a Sobel filter. Isolated pixels are subsequently eliminated. We search for objects with more than g connected pixels in the remaining binarized image. Using these object branch points, we estimate the respective boundary slopes. Finally, the relevant boundaries and slope estimates are saved with the according time point in the OCT M-scan, resulting in $a(t)$.

Analyzing the OCT intensity signals enables relative motion tracking, i.e., soft tissue deformations and displacements, within the axial resolution of the OCT system. However, tissue motion amplitudes smaller than the axial resolution are not resolvable. Therefore, an additional analysis of the motion information contained in the OCT phase signals is conducted. Calculating the phase difference of successive axial scans enables quantification of the relative movement or relative particle velocity $v_{\text{rel},z}$ in sub-pixel resolution as introduced in Equation 2.12 and referred to as deformation analysis in the literature [312, 319, 327]. As previously introduced, a crucial prerequisite for this approach is that the OCT imaging frequency is significantly higher than the relative needle movement, ensuring that the same tissue structures are imaged in successive A-scans. We hypothesize that this occurs whenever the tissue is compressed and deformed before the needle tip reaches it. Thus, in addition to analyzing the OCT intensity signals, we assess this relative motion from the OCT phase signals. Given the sequence of OCT phase signals, we calculate the relative particle velocity

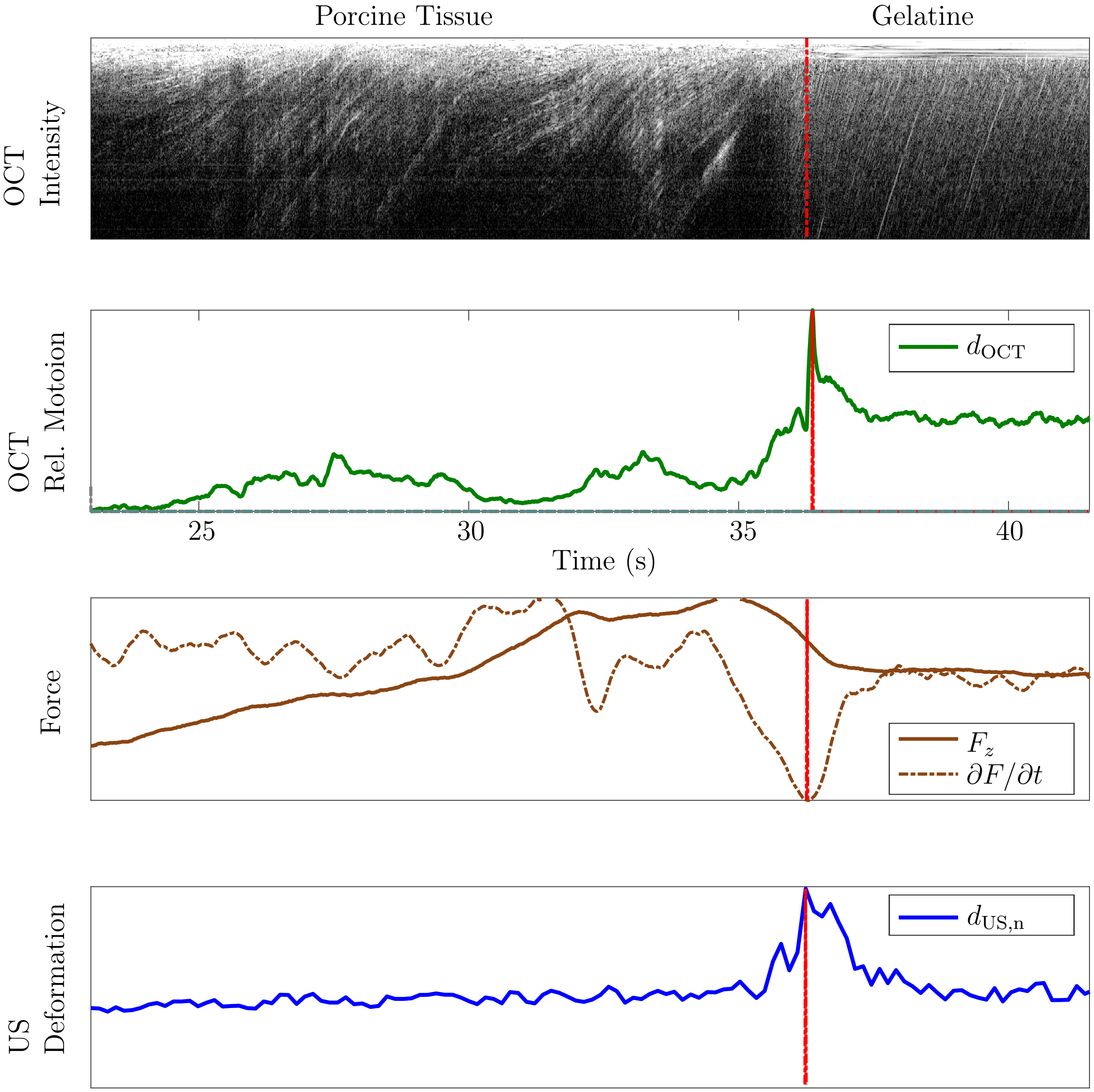

Figure 4.18 Analysis multi-modal signals during needle insertion, i.e., from OCT, FT, and US. One rupture event is detected from each modality and highlighted with a red bar, respectively.

$v_{\mathrm{rel},z}$ for each pixel of the subsequently acquired A-scans as

$$v_{\mathrm{rel}}(z,t) = \frac{\Delta\Phi(z,t))\lambda}{4\pi n T_{\mathrm{oct}}}, \tag{4.13}$$

with $\Delta\Phi(z,t)$ resulting from differentiating successive unwrapped OCT phase signals per imaging depth z. Please note that phase unwrapping is necessary to eliminate phase jumps over time. To reduce signal noise, we additionally apply a moving median filter of length $n = 10$ on the temporal axis of the particle velocity M-scan. The time difference between A-scans T_{oct} is estimated by reading the OCT system trigger signals, and the center wavelength $\lambda_{\mathrm{o},0} = 1300\,\mathrm{nm}$ is given from the system specifications.

We aim to extract cumulative deformation information per time point $\Delta d_{\mathrm{OCT}}(t)$ of the acquired OCT M-scan. We therefore add up the absolute particle velocity over the A-scan depth as

$$\Delta d_{\mathrm{OCT}}(t) = \sum_{p=1}^{P} |v_{\mathrm{rel}}(z,t)|. \tag{4.14}$$

Please note that we ignore the direction of the relative movement by adding the absolute velocity values over the A-scan depth.

As the final part of the OCT signal analysis, we aim to extract meaningful features to detect a rupture event in the M-scans. Given the analysis of boundary slopes $a(t)$ and the quantification of soft tissue deformation $\Delta d(t)$ over time, we define a rupture event correlated with the spontaneous end of a tissue displacement or deformation process. Therefore, we search for time points with maximum peaks of the extracted deformation profiles. We extract rupture events t_{oct} as peaks with $\Delta d > d_{\mathrm{m}}$, where d_{m} is defined as the maximum deformation peak height per insertion. We determine the prominence for all local maxima in the displacement profiles, whereas the greatest prominence is defined as the maximum peak height per insertion.

Using the FT sensor, we measure forces and moments acting on the needle shaft. To assess the needle tissue interactions during insertion, we mainly analyze the axial forces, resolved on the z_{FT}-axis of the FT sensor. The forces that act when the needle is inserted have already been investigated for soft tissue interpretation [125, 327]. In general, an increase in force with insertion depth is reported, which is related to friction at the shaft and resistance of the tissue. Similar to the boundary slope analysis of OCT signals, we assume the force slopes are related to the tissue properties. However, the relationship between force and tissue boundary slopes must be studied for different insertion scenarios.

We extract two features from the measured FT data to quantify the tissue insertion characteristics. First, we assess the average force sensed during needle insertion with

$$F_{\mathrm{avg}} = \sum_{i=1}^{N} F_{z,i}. \tag{4.15}$$

Second, we estimate the absolute force difference ΔF_z per needle insertion, considering the maximum $F_{z,\mathrm{max}}$ and minimum force values $F_{z,\mathrm{min}}$ per insertion with

$$\Delta F_z = F_{z,\mathrm{max}} - F_{z,\mathrm{min}}. \tag{4.16}$$

We use the acquired sequences of US images to analyze the needle and the soft tissue motion during insertion as a global reference. First, we estimate the needle position per US image and time point using the calibration data acquired in a solid gelatin phantom. Column by column, we search for the needle in the images using a threshold-based approach. As the needle moves from left to right through the imaging FOV, we define the rightmost column per image with the visible needle as the needle tip position. We assign this image position to the respective position of the stepper motor. Second, we use the US image sequences acquired in our soft tissue phantoms to derive a reference measure of tissue deformation during insertion. Therefore, we cropped the images with 20 pixels above and below the estimated needle tip height. Next, we apply the Lucas Kanade optical flow algorithm [414] that is implemented in MATLAB 2019b to estimate the motion of tissue particles in successive US image crops by solving the optical flow constraint equation

$$\Delta I_{\mathrm{US},x}\mathbf{u} + \Delta I_{\mathrm{US},y}\mathbf{m} + \Delta I_{\mathrm{US},t} = 0. \tag{4.17}$$

In this equation, the intensity brightness derivatives ΔI_{US} over space (x, y) and time (t) are considered to estimate the horizontal $\mathbf{u}$ and vertical $\mathbf{m}$ motion vectors. We split the horizontal motion vectors $\mathbf{u}_i$ into two groups, considering the orientation relative to the needle motion, and calculated the sum over all vector magnitudes. In this way, we obtain positive $d_{\mathrm{US,p}}$ and negative $d_{\mathrm{US,n}}$ tissue motion profiles corresponding to movements with and against the direction of the needle motion, respectively. For example, the positive tissue motion is calculated as follows

$$d_{\mathrm{US,p}} = \sum_{i=1}^{N} \left|\mathbf{u}_i\right|, \quad \mathbf{u}_i > 0. \tag{4.18}$$

Third, we estimate the position of visible tissue boundaries from the first US image acquired before needle insertion. We apply an edge detection algorithm to segment the boundaries after noise reduction. The boundary position is transferred in motor positions and compared with the rupture position resulting from US and OCT image processing and force signal analysis.

4.4.3 Detection of Rupture Events

In addition to the hand-crafted tissue feature extraction methods, we investigate deep learning methods to directly predict a specific insertion state (rupture, no rupture). Given a large number of insertion datasets and reliable ground truth information, we hypothesize that a neural network could be trained to independently extract relevant signal features from the complex OCT data for rupture classification. In particular, we study the separated and combined analysis of the OCT intensity and phase signals. Furthermore, we investigate what externally applied imaging and sensing methods are suitable to detect a rupture event as ground truth. Relevant data pre-processing steps, the investigated neural network architecture, and evaluation metrics are described in the following. Please note that the methods and results related to deep learning-based rupture detection presented in the following are based on a publication [410] published with equal contributions from Sarah Latus and Johanna Sprenger. The implementations of network architectures and described ablation studies were mainly conducted by Johanna Sprenger.

Training of a neural network architecture requires a sophisticated pre-processing of the multi-modal signals acquired during needle insertion. The first part of the data pre-processing focuses on extracting time points t_{R} of a rupture event from all available data sets. Considering the FT measurements, we hypothesize that a spontaneous decrease in the measured force is related to the rupture of a boundary layer. Analogously, we calculate the gradient of the axial forces and search for time points t_{F} with local maxima that can be assigned to tissue ruptures with

$$\nabla F_z > b_{\mathrm{F}} \max_t \nabla F_z(t). \tag{4.19}$$

Here, a scaling factor b_{F} is used to set the threshold for peak detection, considering the maximum peak height per insertion. Following the described US image processing steps, we define a rupture event based on the extracted tissue motion profiles. Given the main hypothesis of tissue relative motion during needle insertion, we first assume tissue deformation in front of the needle tip. This deformation should be visible as positive tissue motion in the profiles extracted from US images with a maximum right before the rupture. Once the tissue boundary is ruptured, the relaxation processes will lead to a negative tissue motion (see

Figure 3.5, B to C). Thus, we search for time points with a maximum in the negative motion profile $d_{\mathrm{US,n}}$ and assign this to a rupture. Again, a scaling factor is applied to estimate the optimal threshold value based on the maximum peak height per insertion with

$$d_{\mathrm{US,n}} > b_{\mathrm{US}} \max_{t} d_{\mathrm{n}}(t). \tag{4.20}$$

The optimal scaling factors b_{US} and b_{F} are set after performing a grid search and analyzing the Receiver Operating Characteristic (ROC) for an interval $b_{\mathrm{F}} \in [0.2, 0.8]$. To ensure a reliable detection of a rupture event, we study different combinations of the externally applied FT sensing and US imaging to extract a ground truth label. We define a rupture event by either using only one external modality alone as a ground truth or by combining US and force logically, i.e., noting a point in time as a rupture t_{R} if either both (AND) or one of these external modalities (OR) recognize a rupture.

After defining reliable ground truth labels, the sequence of one-dimensional depth scans acquired with the OCT system during needle insertion is converted into an M-scan representation in which the individual scans are displayed side by side. Next, we split the complex OCT signals into intensity and phase components. The first and last pixels per A-scan are cropped to minimize image artifacts and remove areas without information. In the lower scan range, there is usually only noise, as the light is increasingly absorbed and not much reflected with increasing tissue depth. This cropping results in M-scans with a scan depth composed of 224 pixels. To neglect phase wrapping effects, unwrapping is applied over the temporal axis of the phase M-scans. We then calculate the phase difference for each pixel of the consecutive scans. For processing with our neural network architectures, we subsample the pre-processed intensity and unwrapped phase difference M-scans by extracting every 1000th scan only. Here we assume that subsequent A-scans contain similar information, as the insertion speed is slow compared to the high temporal A-scan sampling.

Around the time points t_{R} extracted from FT and US data, we create intensity and phase crops of 224×224 pixels that can be used as training images with annotation as rupture. Please note that the input width of 224 pixels corresponds to an acquisition time of approximately 2.46 s. Similarly, we randomly extract image crops from the intensity and phase data for time points without rupture events. Therefore, we do not use a specific point in time to locate the rupture but detect the occurrence in a time interval. The data is sampled around the detected rupture event so that minor differences in the multi-modal ground-truth generation measurements do not affect the ground-truth markers themselves.

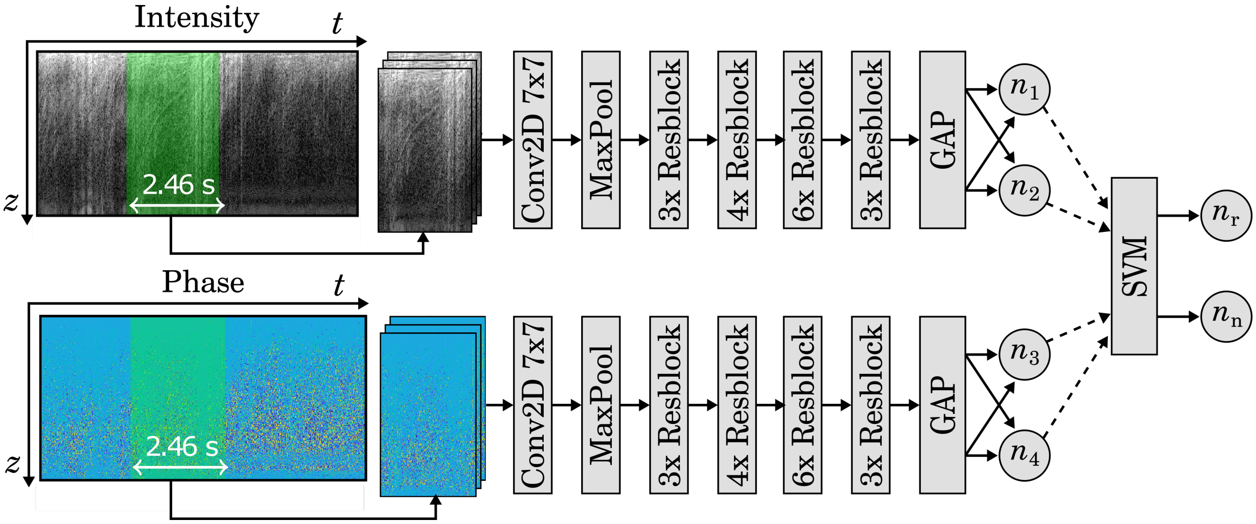

Figure 4.19 Siamese CNN network architecture for combined analysis of OCT intensity and phase data for rupture detection. Image crops from the OCT M-scans with and without rupture are extracted from both signal entities and copied into the input channel of the respective ResNet-50 architecture. After training the rupture detection n_i from intensity and phase signals separately, a SVM is utilized to combine the outputs.

To classify rupture events, we evaluate two individual neural network architectures that use either the OCT intensity or phase signal as input. In comparison, we study a Siamese network architecture shown in Figure 4.19 that enables parallel processing of intensity and phase signals. Here, a SVM combines the respective outputs of the trained individual networks.

We design our network architectures using a ResNet-50 model [415] as a basis. Being pre-trained on the ImageNet dataset [416], the ResNet-50 architecture is designed to process RGB images with three input channels. Thus, the OCT intensity and phase matrices are duplicated in each of the three input channels. The network architecture comprises a first two-dimensional convolution layer that applies a 7×7 convolutional kernel to the 224×224 pixels input images. A max pooling layer follows this first layer. Next, four residual blocks with different layers and convolutional sizes are applied. Together with an activation layer at the end, 50 individual layers are combined in this ResNet-50 architecture. During training, we update the weights for the last few network layers to fit the model to the OCT data. Usually, the activation layer is then connected with a final fully connected layer. We replace this fully connected layer with a binary rupture classification.

We train our intensity and phase networks individually using the image crops with and without rupture extracted from the pre-processed intensity and phase signals of the OCT M scans, respectively. For the ground truth annotation of the respective image crops, we use either the force measurements on the needle shaft or the external US imaging or combine both information. In the Siamese classification approach the outputs of the individually trained intensity and phase networks are combined using a SVM.

Finally, we aim to predict a rupture event continuously during needle insertion. Therefore, move with a sliding window over our complex OCT M-scan to evaluate short sequences of one-dimensional depth scans of 224×224 pixels with the trained networks. Consequently, we evaluate a single one-dimensional depth scan with different numbers of previous and subsequent depth scans, leading to rupture predictions over a certain time.

We evaluate the performance of the different learning approaches by comparing the network classifications with the ground truth information gathered by either US or force or a combination of both. More specifically, we compute the accuracy, precision, recall and F1-scores introduced in [417]. Apart from using the different external imaging and acquisition modalities as a reference, we also evaluate the impact of different input images, i.e., the OCT intensity or phase signal separately or in the Siamese network combined.

Chapter 5

Experimental Evaluations

5.1 Quantification of Vascular Morphology

In the following Sections, we will introduce the vessel phantom designs and imaging procedures and sequences used to study the quantification of vascular morphology.

5.1.1 Vessel Phantoms

We investigate the quantification of morphology using 3D-printed vascular phantoms of different shapes. For our bi-modal volume reconstruction studies, we design straight phantoms with stenosis and curved phantoms with U- and Z-shapes to simulate catheter bending. Along the luminal centerline, all phantoms have a constant diameter and shape, except the sections with stenosis. For the co-registration of the bimodal image data, we add landmarks on each side of the phantom. Additionally, we utilize these landmarks to crop the resulting volumes. Due to the different imaging depths of the applied clinical and custom IVOCT imaging system, we chose different luminal diameters for the DSA and MPI studies, respectively. In Figure 5.1, the phantoms applied for bi-modal IVOCT and MPI imaging are shown on the left. We design the MPI phantom with a total phantom length of 25 mm and an inner diameter of 2.5 mm (stenosis narrow part 1.5 mm). As the clinical IVOCT imaging system enables imaging depths of up to 5 mm in air, we enlarge the diameter of the DSA phantom design to 4 mm. Furthermore, we increase the phantom length to 32.25 mm. Again, co-registration landmarks are embedded in the vessel phantom design with a downsized luminal diameter of 1.5 mm. The respective phantoms are shown on the right in Figure 5.1.

We produce all phantoms with a 3D printer based on stereolithography (Form 1+, Formlabs Inc., USA), which offers a high accuracy of 0.05 mm in all axes. We investigated different mixtures of white and gray colored resin (FLGPWH01, Formlabs Inc., USA) for printing,

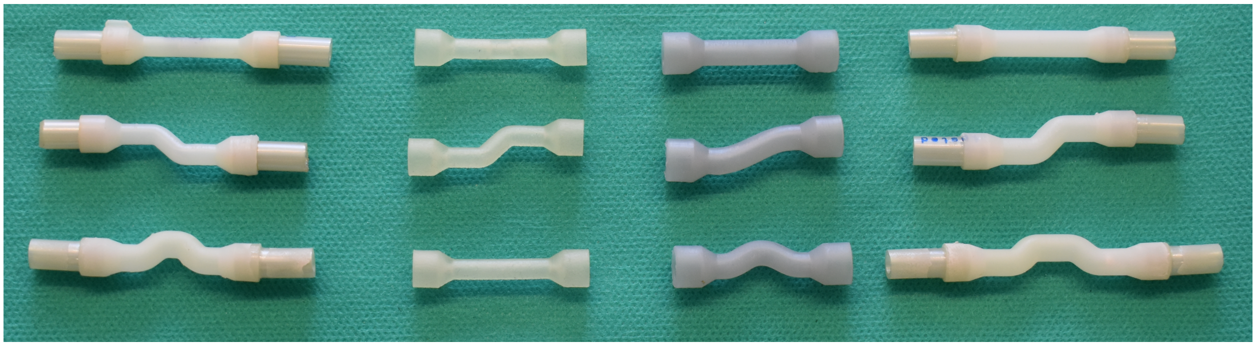

Figure 5.1 Picture of 3D-printed vessel phantoms used for experimental studies on volume reconstruction. Different materials have been investigated, influencing the optical scattering characteristics.

resulting in various colors shown in Figure 5.1. Aiming the color particles to serve as optical scatterers for IVOCT image acquisition, we chose the white mixtures shown on the very left and right side for our experimental studies. Finally, solid phantoms with 65 MPa ultimate tensile strength and a Young's Modulus of 2.8 GPa result after curing.

5.1.2 Bi-modal Vascular Imaging Studies

In our bi-modal DSA and IVOCT studies, we first calibrate the imaging setup shown in Figure 5.2. As described in Section 4.2.1, a specific calibration phantom is imaged for two different C-arm configurations, namely the right anterior oblique (RAO) and left anterior oblique (LAO). The respective configuration angles $\gamma_{\mathrm{C},i}$ are chosen as $\gamma_{\mathrm{C,1,RAO}} = 45°$ and $\gamma_{\mathrm{C,1,LAO}} = 45°$ and $\gamma_{\mathrm{C,2,RAO}} = 30°$ and $\gamma_{\mathrm{C,2,LAO}} = 30°$. The configurations are related to clinically relevant orientations applied for imaging vessel structures of the right coronary artery (RCA), as our phantom is positioned in a similar orientation with respect to the angiography system.

After calibration, we perform bi-modal imaging experiments with the sequences described below. Initially, we position the vessel phantom on the patient couch and fill it with a 1:4 mixture of distilled water and contrast medium (Imeron 350, Bracco Imaging Deutschland GmbH, Germany), which enhances the DSA image contrast while maintaining proper IVOCT imaging properties. Subsequently, we acquire a sequence of DSA images from both C-arms, which act as reference scans for image processing. Afterward, the IVOCT imaging probe is positioned in the vessel phantom. Using the clinical co-registration software, we start the acquisition of IVOCT and DSA images. During image acquisition, the imaging probe is simultaneously retracted and rotated. We choose a pullback distance of 54 mm with a speed of $18\,\mathrm{mm\,s^{-1}}$. The cross-sectional IVOCT images and bi-plane DSA images are acquired with

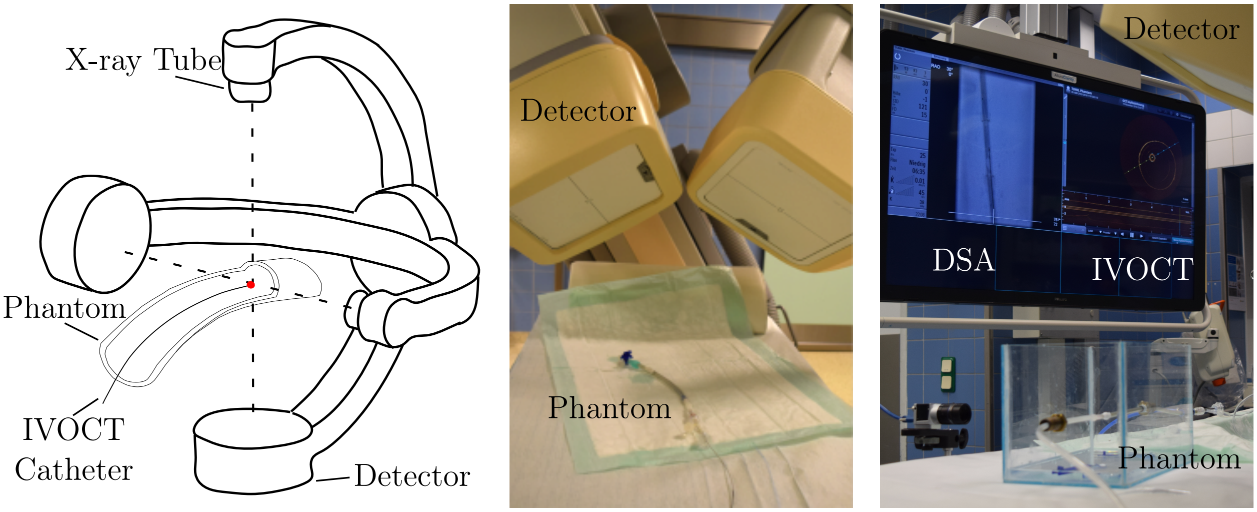

Figure 5.2 (Left) Schematic of bi-modal imaging studies combining IVOCT and bi-plane DSA. A phantom is positioned on the patient couch with an inserted IVOCT catheter and two C-arms are oriented relative to the phantom. (Middle) Experimental setup for bi-plane angiography imaging. (Right) Co-registration view provided by the Optis Integrated system.

sampling rates of 180 Hz and 30 Hz, respectively. Referring to these imaging parameters, each cross-sectional IVOCT image is composed of 496 A-scans with 960 pixels on the z-axis. These image acquisition sequences are repeated four times for each C-arm configuration.

In this thesis, we investigate bi-modal MPI and IVOCT imaging procedures for centerline estimation or tracking of the IVOCT imaging probe. The overall bimodal imaging setup is sketched in Figure 5.3. For the MPI data acquisition, we use the software Paravision from Bruker. In all experiments, we acquire MPI volumes using the orthogonal sinusoidal excitation fields with an amplitude of 12 mT and frequencies of $f_{\mathrm{MPI},x} = 2.5/102\,\mathrm{MHz}$, $f_{\mathrm{MPI},y} = 2.5/96\,\mathrm{MHz}$, $f_{\mathrm{MPI},z} = 2.5/99\,\mathrm{MHz}$ in the respective imaging axis. We receive the signal echoes with the radiometric coil and select a cycle time of 21.54 ms. We enable spatial encoding by applying a gradient of the selection field with $2.0\,\mathrm{T\,m^{-1}}$ in z-direction and $1.0\,\mathrm{T\,m^{-1}}$ in the x- and y-directions. Consequently, we achieve an effective MPI volume rate of 46.43 Hz for a FOV size of 24x24x12 mm.

Calibration scans are performed ahead of the phantom studies with a delta sample that is moved through the MPI scanning FOV. The reference sample of the particle material and concentration that is imaged during later experimental studies is filled in a holder of a size of 1x1x1 mm. To achieve calibration scans for our centerline studies, we use 1 µL Perimag (micromod Partikeltechnologie GmbH, Germany) with an iron concentration of $10\,\mathrm{mmol\,L^{-1}}$ as SPIONs. We investigate the influence of the magnetic particles on the OCT image quality and choose a concentration of $2.5\,\mathrm{mmol\,L^{-1}}$ to achieve optimal imaging conditions for both

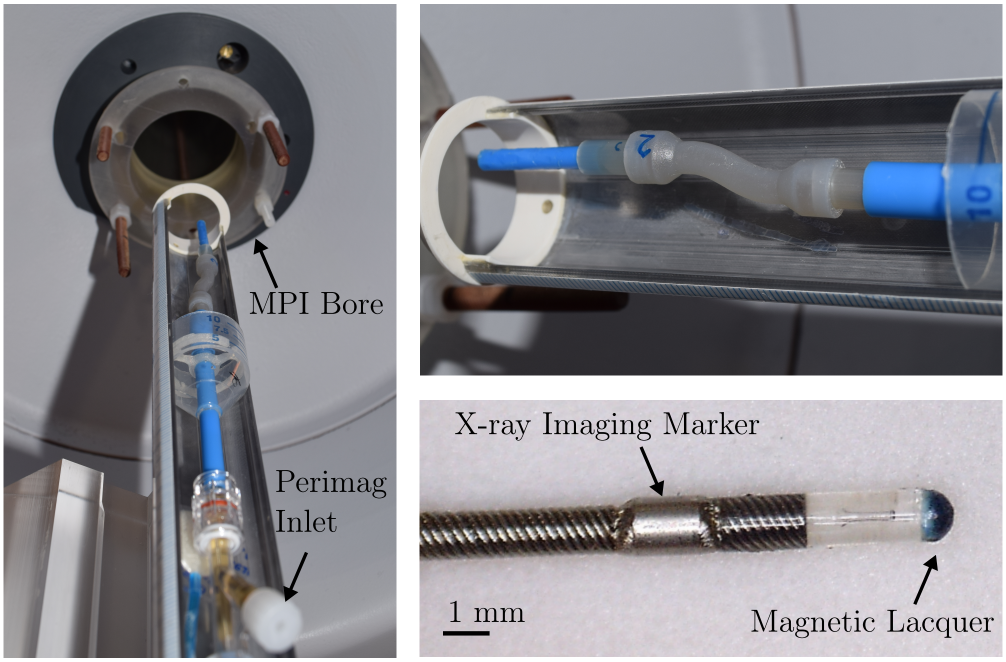

Figure 5.3 Bimodal imaging setup visualizing the vessel phantom with inserted IVOCT catheter positioned on the MPI couch. A magnetic lacquer is attached to enable probe tracking of the IVOCT imaging tip.

modalities [404]. Similarly, 1 µL of the magnetic lacquer applied in the probe tracking study is filled in the sample holder. For each sample position in the calibration FOV, we acquire a separate MPI volume. Note that the calibration FOV is chosen slightly larger than the later applied imaging FOV to circumvent artifacts at the FOV boundaries [418]. Thus, we can generate a system matrix correlating the measured maximum intensities to the set excitation voltages for all sample positions.

For our volume reconstruction methods relying on the imaged vessel centerline, we perform the following imaging sequence. First, we acquire a reference MPI volume of the vessel shape with SPIONs particles filled inside. We acquire a sequence of MPI volumes and average these for centerline estimation described in Section 4.2.2. Afterward, we insert the intravascular probe and acquire IVOCT image data. We use the customized IVOCT imaging adapter to rotate the imaging probe with a velocity of 16.6 Hz and set a pullback speed of $0.75\,\mathrm{mm\,s^{-1}}$. During the acquisition of OCT A-scans with a sampling rate of 91 kHz, the probe is retracted over a total distance of 25 mm. Lastly, we acquire another MPI volume using the same imaging parameters described above with the inserted IVOCT imaging probe. We repeat this imaging procedure three times for all phantom shapes.

The experiments and related MPI imaging sequences applied for tracking the intravascular probe are structured as follows. We fill the stenosis vessel phantom with water and insert the IVOCT imaging probe. We start the acquisition of MPI volumes and simultaneously send an electrical trigger signal to the customized probe adapter to start synchronous IVOCT imaging. We run three different motion profiles of the intravascular probe to simulate relative motion artifacts that occur during in-vivo imaging. After completion of the respective probe motion, both imaging systems are stopped.

The translational motion profiles varied for probe tracking studies, are described in the following. First, we conduct a conventional IVOCT imaging profile with the motion parameters described for the centerline estimation, referred to as a continuous motion profile. Second, we simulate a deceleration of the imaging probe due to a bending of the imaging catheter. Thus, we apply a deceleration of the imaging probe for a certain period followed by a spontaneous acceleration until the initial pullback speed is reached. Third, we apply a motion profile with translational variations to simulate relative motion between the probe and tissue associated with the heartbeat. Here, we move the imaging probe back and forth with a speed of $\pm 1.25\,\mathrm{mm}$. We conduct these experiments on a stenosis phantom and evaluate the variation in the estimated stenosis length.

5.2 Quantification of Soft Tissue Elasticity

The subsequent sections summarize the experimental studies conducted to demonstrate the quantification of soft tissue elasticity using the developed miniaturized OCE probes. First, we present the systematic preparation of soft tissue phantoms to provide a ground truth of the measured elasticities. Second, we introduce the experimental setups to study the shear wave imaging from single-fiber or DF-OCE probes.

5.2.1 Elastography Phantoms

We prepare gelatin phantoms to mimic different soft tissue stiffnesses. We can achieve dedicated soft tissue elasticity values by varying the mixture of water and gelatin. The phantoms are prepared according to a strict recipe. First, we mix the gelatin powder (Gelita Ballastic 3, Gelita AG, Germany) and water and leave it to soak for two hours. If necessary, a certain amount of titanium dioxide particles (Titandioxid Rutil, Johannes Gerstaecker GmbH, Germany) and graphite powder (Graphit 450187, Emil Lux GmbH, Germany) are added to the mixture to act as optical or acoustic scatterers. Afterward, we heat the mixture to around 40 degrees and stir continuously. Once all gelatin particles have dissolved, we can fill the mixture in a specific mold shown in Figure 5.4. Optionally, we first wait for the mixture to cool down to a temperature of about 25 °C to minimize the sinking of the added particles. On the one hand, we prepare homogeneous tissue phantoms with constant concentrations of gelatin and water. On the other hand, we produce stacked tissue phantoms composed of tissue layers with different stiffness. Therefore, we pour a layer and leave it to cool completely, then pour a second layer on top.

To observe reference values of the phantom's Young's modulus E, we conduct indentation tests with an experimental setup described in [202]. Given the stress-strain curves allocated during phantom indentation and based on [419], we can estimate the modulus as

$$E = \frac{\sigma}{\varepsilon} = \frac{F_{\mathrm{ind}}}{\pi r_{\mathrm{ph}}^2} \frac{h_{\mathrm{ph},0}}{\Delta h_{\mathrm{ph}}}, \tag{5.1}$$

with the applied load F_{ind}, original phantom radius r_{ph}, original phantom height $h_{\mathrm{ph},0}$ and current phantom height Δh_{ph}. Please note that in our setup, F_{ind} and Δh_{ph} are measured continuously during the indentation of the phantom.

In the case of our comparative elastography studies involving OCE and USE, we need to optimize the proportion of optical and acoustic scatterers added to the gelatin mixtures. While graphite powder is essential to create acoustic signals from the tissue phantoms in the

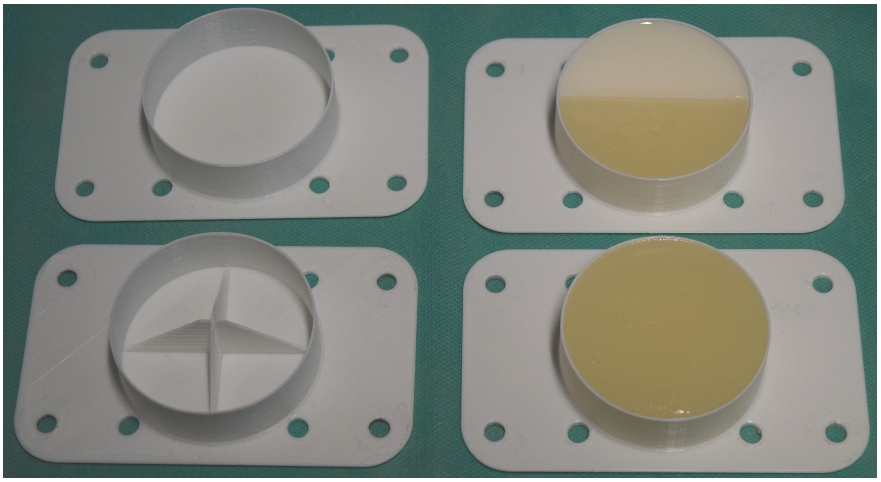

Figure 5.4 (Left) Molds for preparation of soft tissue phantoms and setup calibration. (Right) A split phantom with different amounts of optical scatterers and a homogeneous soft tissue phantom without optical scatterers.

US images, the OCT imaging conditions decrease. Thus, we added a preliminary study on varying the concentrations of titanium dioxide and graphite. We quantify the signal-to-noise ratios per imaging modality and mixture. Finally, we observe the optimal imaging conditions for both imaging modalities with a 2:3 mixture of graphite and titanium dioxide.

5.2.2 Probe-based Elastography Studies

Using the setup sketched in Figure 5.5a, the image data from the SF-OCE probe and the OCT scan head are recorded simultaneously. We insert the OCE probe in the gelatin phantoms and acquire image data for 21 different needle insertion depths $15.75 <= x_i <= 24.25\,\mathrm{mm}$ and three different heights $z_i = 4, 6, 10\,\mathrm{mm}$. We also move the OCT scan head with the Hexapod robot according to the position of the OCE probe. The piezoelectric actuator is kept stationary for all image positions and is controlled with a modulation frequency of 9 Hz. Based on the trigger signals of the piezoelectric actuator, the OCT signal acquisition with an A-scan frequency of 5 kHz is started. Six repetitions of the shear wave excitation and imaging sequences are recorded per needle position. We study the shear wave propagation in homogeneous phantoms of four different gelatin-water concentrations (4 %, 5 %, 6.5 %, and 10 %). Additionally, we investigate the measurements for a split phantom composed of 7.5 % and 10 % gelatin. Please note that the shear wave was excited in the softer gelatin and propagated toward the harder gelatin. Here, we distinguish the quantification of shear wave velocity for all imaging positions or the respective imaging positions per density.

The experimental setup for evaluating elasticity quantification from a DF-OCE probe is

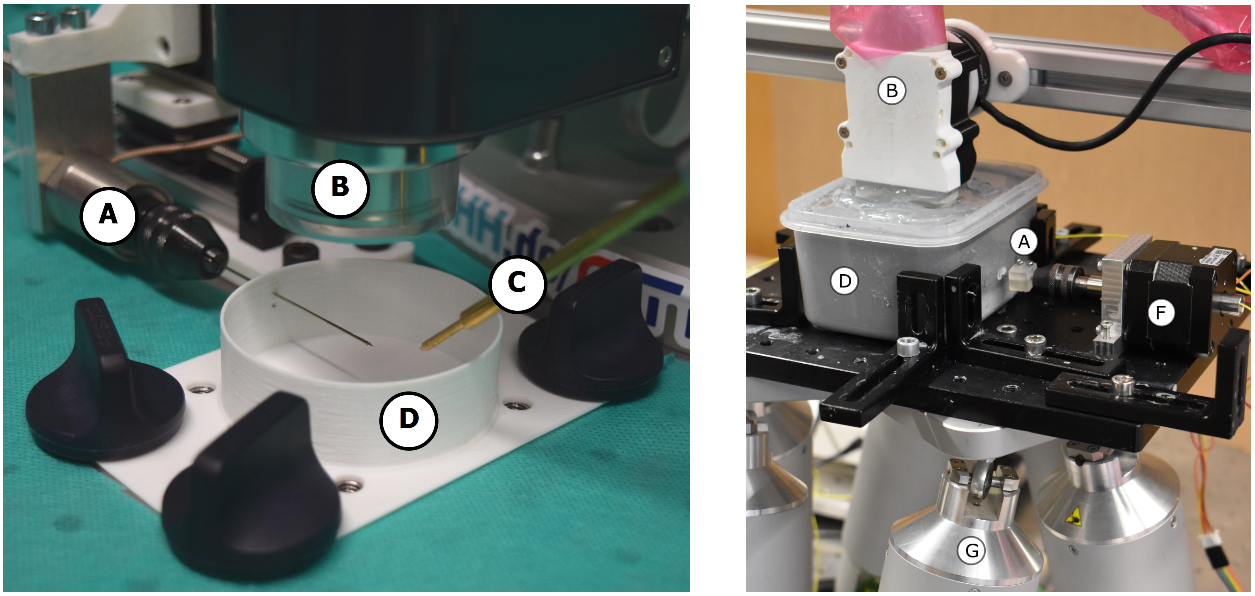

(a) (b)

Figure 5.5 Experimental setups for OCE from miniaturized probes. (a) The SF-OCE probe (A), OCT scan head (B) for reference measures, piezoelectric actuator (C), and empty phantom container (D) are shown. (b) The DF-OCE probe (A) is inserted in the soft tissue phantom (D). The US transducer (B) is used for wave excitation and reference measurements. A hollow shaft motor (F) is used to adapt the rotational orientation of the OCE probe. In both setups, a hexapod robot (G) is used to vary the orientation of excitation and imaging. Figure adapted from [408].

shown in Figure 5.5b. The US probe is rigidly mounted above the phantom container and a hexapod robot is used to position the phantom with the inserted DF-OCE probe differently relative to the US FOV. We apply ARF for shear wave excitation and subsequently acquire OCT signals from both imaging fibers and the USE plane wave images. In detail, we perform 2000 excitation cycles of the piezoelectric elements of the US probe with a center frequency of 5 MHz. After a cooling time of 10 ms, the acquisition of US plane wave images starts with an imaging frequency of 15 kHz. The resprective trigger signals are exemplary shown in Figure 4.11. Using the OCT system A-scans are subsequently acquired with a frequency of 91 kHz. The resprective imaging trigger signals are exemplary shown in Figure 4.11. With the multiplexing activated after every second A-scans, we achieve an effective imaging frequency $f_{\mathrm{OCT},i} = 22.75\,\mathrm{kHz}$ per imaging optic. The respective OCT M-scan is composed of A-scans arranged next to each other, which were taken with different imaging optics. We record the trigger signals from all systems at a digital oscilloscope for synchronization.

We conduct experiments on four homogeneous gelatin phantoms and one split gelatin phantom composed of two different gelatin concentrations. For all experiments, we chose a stationary position of the DF-OCE probe within the respective phantom. We vary the distance between shear wave excitation and imaging by positioning the OCE probe and phantom with the hexapod robot at different locations relative to the US probe and execute the ARF. Specifically, 65 ARF positions $\mathbf{e}$ were chosen, which are arranged in a square with different distances in x, y, and z relative to the OCE probe as shown in Figure 5.6. Five repetitions of wave excitation and imaging are performed for each excitation position $\mathbf{e}$.

In addition to the experimental evaluation on gelatin tissue phantoms, we apply the DF-OCE probe to assess the shear wave velocities of ex-vivo porcine heart tissue as shown in Figure 5.7. In particular, we insert the OCE probe in a coronary artery and aim to estimate the shear wave velocity of the vascular wall. We first examine the tissue by palpating and determining two stiffer regions. Based on the palpation, we define four different OCE probe positions within the artery that should be examined.

We embed the porcine heart tissue in gelatin to ensure proper mechanical coupling and realistic morphological conditions during shear wave excitation with the US transducer. For each OCE probe position, we execute wave excitation and imaging for ARF excitation positions arranged similarly as shown in Figure 5.6. Three repetitions of wave excitation and imaging are performed for each excitation position. Consequently, the mean and standard deviations for shear wave velocity are estimated based on all wave excitation positions.

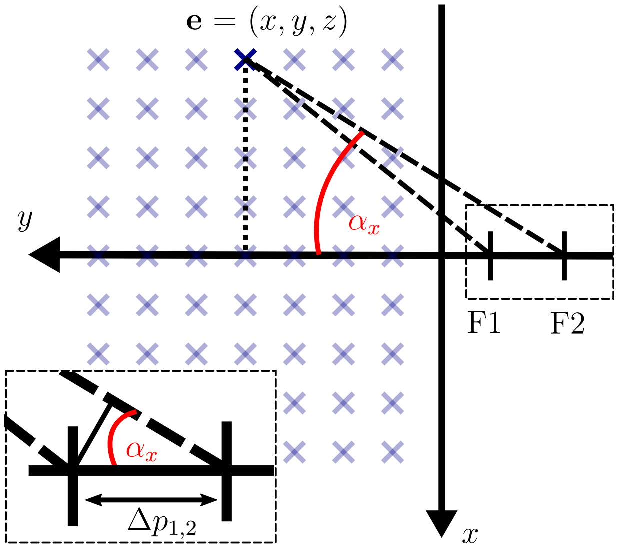

Figure 5.6 Top view of ARF shear wave excitation positions $\mathbf{e}$ in x, y coordinates relative to the OCE probe's imaging optics (F1, F2). The orientation angle α_x between excitation and imaging results after setup calibration.

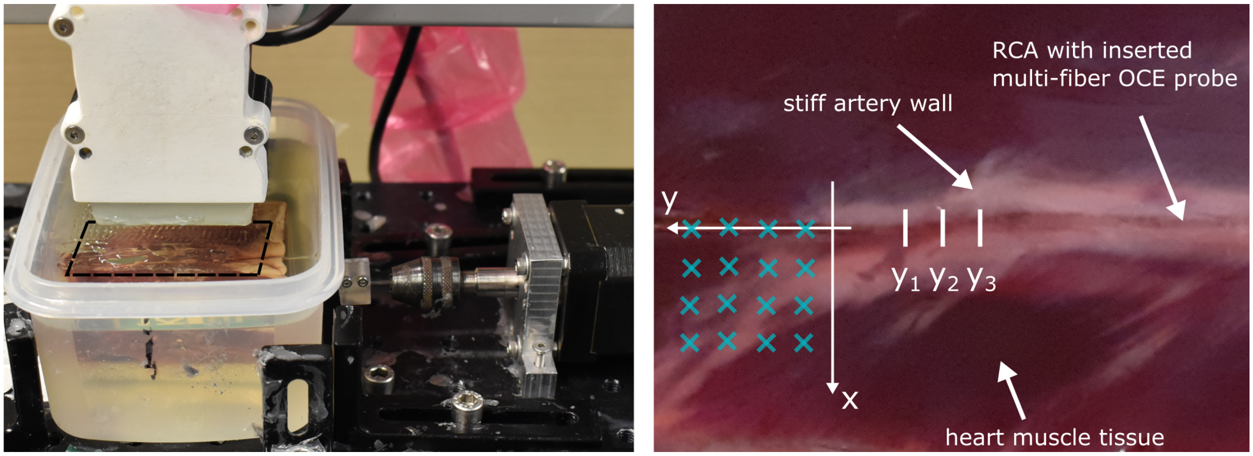

Figure 5.7 Experimental setup elasticity quantification of the vascular walls of coronary arteries using the DF-OCE probe. Shear waves are actuated for several US probe positions indicated with blue crosses. The position of the DF-OCE probe was varied along the vascular structure (see positions y_i.). Figure adapted from [408].

5.3 Quantification of Soft Tissue Interactions

The details of the experimental setups, the phantoms, and the conducted experiments for analyzing the soft tissue interactions during needle insertion are described in the following.

5.3.1 Multi-layer Soft Tissue Phantoms

We investigate the tissue interactions during needle insertion on soft tissue phantoms composed of several layers. To simulate epidural punctures, various tissue layer structures are mimicked with porcine and bovine tissue embedded in gelatin of different densities. The phantoms are prepared following the recipe as described before, using gelatin powder (Gelita Ballastic 3, Gelita AG, Germany) with added titanium dioxide particles (Titandioxid Rutil, Johannes Gerstaecker GmbH, Germany) as scatterers. The phantoms are poured into a container with a side opening. The tissues are layered in the containers so that the needle penetrates the interfaces vertically when inserted through the side opening. The phantoms have a size of 40 × 80 × 200 mm in height, width, and length. Table 5.1 summarizes the composition of tissue layers and gelatin densities per phantom type and states the number of conducted insertions per phantom. In addition to the layered tissue phantoms, we embed bovine tissue with tendons and capsules in transparent gelatin.

Table 5.1 Properties of multi-layered soft tissue phantoms for analyzing interactions during needle insertion.

Phantom	Layer 1	Layer 2	Layer 3	punctures
A	6.25 % Gelatin	hom. Porcine	6.25 % Gelatin	33
B	6.25 % Gelatin	hom. Porcine	20 % Gelatin	33
C	20 % Gelatin	hom. Porcine	6.25 % Gelatin	33
D	20 % Gelatin	inhom. Porcine	20 % Gelatin	51

5.3.2 Automatic Needle Insertion Studies

Our experimental setup for analysis of automatic needle insertions is shown in Figure 5.7 and consists of our OCT needle probe, two motors for executing the needle insertion and for changing the phantom position, the US imaging transducer, a FT sensor, and a control unit, as described in Section 4.4.1. We position the US transducer on the phantom surface so the needle runs horizontally through the image from left to right. We apply transmit and receive beamforming to acquire two-dimensional US B-mode images with an average frequency of 30 Hz during insertion. We use the first motion stage to insert the OCT needle at a constant

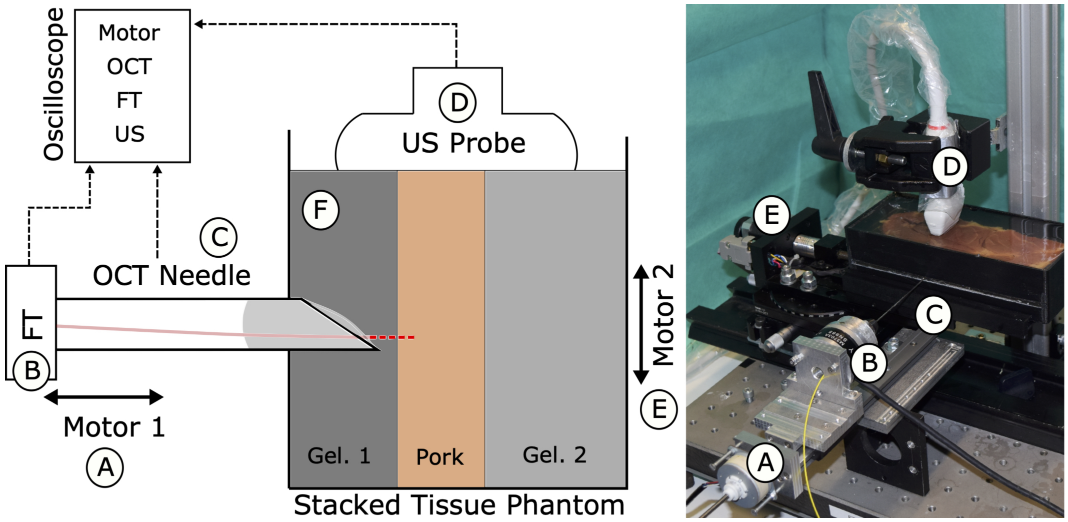

Figure 5.8 Experimental setup composed of our miniaturized OCT needle (C), a FT sensor, an US transducer, two motors for needle insertion (A) and phantom translation (E), and versatile soft tissue phantoms (F). Figure adapted from [410].

speed of 1 mm s^{-1}. Meanwhile, OCT A-scans are acquired with a frequency of 91 kHz, and the FT values are recorded with a frequency of Hz. Given the US image width of mm, we limit the needle insertion depth to 40 mm. After each insertion, we use the second motion stage to move the phantom, enabling parallel needle paths in the phantom with a distance of 8 mm to each other.

For multi-modal analysis of rupture events, ensuring appropriate temporal synchronization of image and signal acquisition is essential. Hence, the trigger signals and time stamps of all systems are recorded at a control unit. Moreover, the spatial information retrieved from US and OCT imaging as well as the motion unit needs to be transformed into a global coordinate system. Thus, several setup calibration steps are performed after optimal spatial alignment of the US imaging probe and needle insertion path. First, the depth of the US imaging FOV is estimated using a calibration phantom. Second, we perform a calibration to estimate the transformation of the needle tip position estimated from US images to the motion unit position. For this purpose, we perform several needle insertions in a transparent gelatin phantom and simultaneously record the motion unit positions and US images. Third, we estimate the position and intensity of the infrared light beam relative to the needle tip. This information is used to estimate the position of the OCT A-scan in the US image.

After conducting insertion studies on soft tissue phantoms, we also investigate the signal characteristics when puncturing ex-situ tissue samples extracted from human corpses. In particular, we use the motion unit to insert our OCT needle probe into liver and prostate tissue samples. Given the small size of the tissue samples, US imaging was not possible.

Therefore, we use the FT signals acquired at the needle shaft to reference the tissue interactions during insertion. Similar to the automatic insertion study, we apply a constant insertion speed of $1\,\mathrm{mm\,s^{-1}}$ as well as OCT and FT acquisition frequencies of 91 kHz and Hz, respectively. The tissue samples are embedded in a container that enables cutting through the insertion channel after puncture. Subsequently, we fixed the tissues with formalin and followed up with a histopathological analysis. As the tissue was cut along the insertion channel we can assess the surrounding tissue composition from the histological images.

Chapter 6

Results

6.1 Quantification of Vascular Morphology

The results of the experimental studies on quantifying vascular morphology from IVOCT image data with and without external imaging are summarized in the following Sections. First, the reconstruction performances are evaluated based on the three-dimensional vascular centerline registered from the IVOCT image data to the external imaging with DSA and MPI. Second, methods for volume reconstructions combining the estimation of vascular centerline and imaging probe trajectory are evaluated. Third, a spatio-temporal tracking of the imaging probe with MPI is evaluated for different motion artifacts.

6.1.1 Centerline Estimation

First, a qualitative analysis of the investigated volume reconstruction methods is conducted based on the reconstructed volumes' xy- and xz-views. Considering the DSA as the external imaging modality and the C-arms aligned perpendicular to the luminal centerline, the visualizations in Figure 6.1 demonstrate substantial deviations in the phantom shape when using the IVOCT image data alone. The reconstructions considering the luminal centerline from DSA and IVOCT imaging and optionally combining this with the probe trajectory show improved results. However, when examining the quantitative results for different C-arm configurations, the DICE values shown in Figure 6.3 for the respective volume reconstruction methods considering both DSA and IVOCT images decrease. For our studies using MPI as the external imaging modality, the benefit of combining both MPI and IVOCT image data is clearly shown in Figure 6.2. Here, the actual imaging probe trajectory deviates more clearly from the assumption of a straight trajectory.

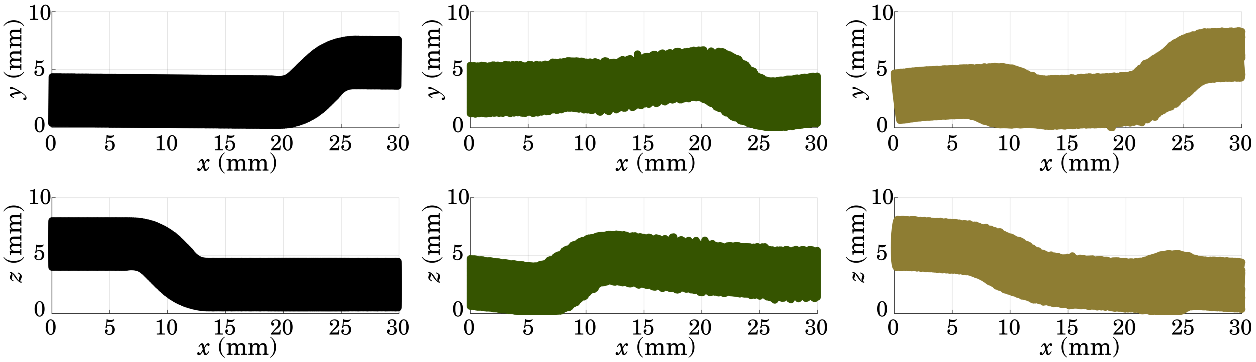

Figure 6.1 xy- and xz-view of the reconstructed volumes with catheter trajectory estimation from DSA with $\alpha = 45°, \beta = 0°$ compared to the ground truth shape. The OCT image frames are oriented differently. The conventional method (green) shows obvious deviations in phantom shape. For the centerline method (olive), the first phantom curve was wrongly reconstructed as shown in the respective xy-view.

Results of DICE quantification for vascular volume reconstruction from bimodal IVOCT imaging in combination with DSA or MPI are shown in Figure 6.3. The DICE boxplots are created for 18 projective views of the reconstructed volumes with the projection calculated for rotation around the x-axis. The conventional volume reconstruction approach, using only the IVOCT image data, results in the worst DICE coefficients for both external imaging modalities. This approach includes arranging the IVOCT cross-sections after calculating the luminal center of mass from the IVOCT images. Using the vessel centerlines extracted from the external imaging (DSA or MPI) and registering them with the centerlines extracted from the IVOCT images, referred to as the three-dimensional centerline approach, further improves the results.

6.1.2 Combination of Centerline and Probe Path

We analyze the volume reconstruction with reference from DSA combining information from the luminal centerline and probe path for continuous probe motion profiles. Here, we assess both information centerline and probe path from the same image data. As visualized in Figure 6.3 this approach further improved volume reconstructions. This is especially true for curved vessel structures where the IVOCT imaging probe does not run along the centerline. However, again, the C-arm configuration relative to the phantom centerline and probe path influences the volume reconstruction accuracy. The combination of centerline estimation and probe path leads to even worse results in configuration $\gamma_C = 45\circ$, $\gamma_C = 30\circ$ than the conventional approach without external imaging.

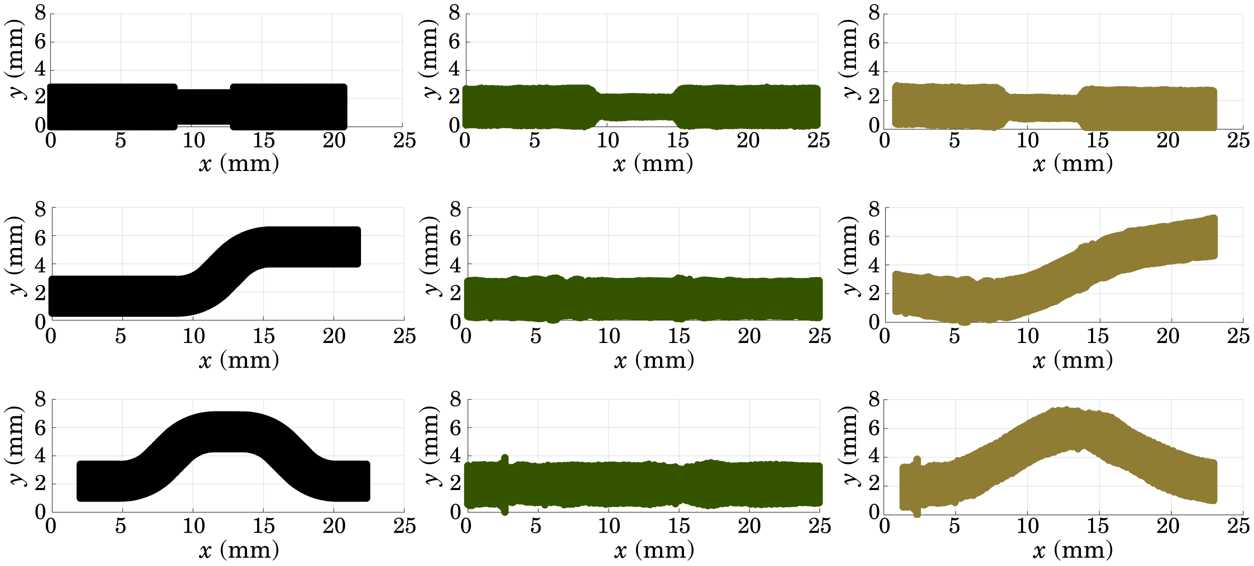

Figure 6.2 IVOCT volume reconstructions for the three phantoms (stenosis, Z-shape, U-shape) of conventional (green) and centerline method (olive) shown for external MPI imaging.

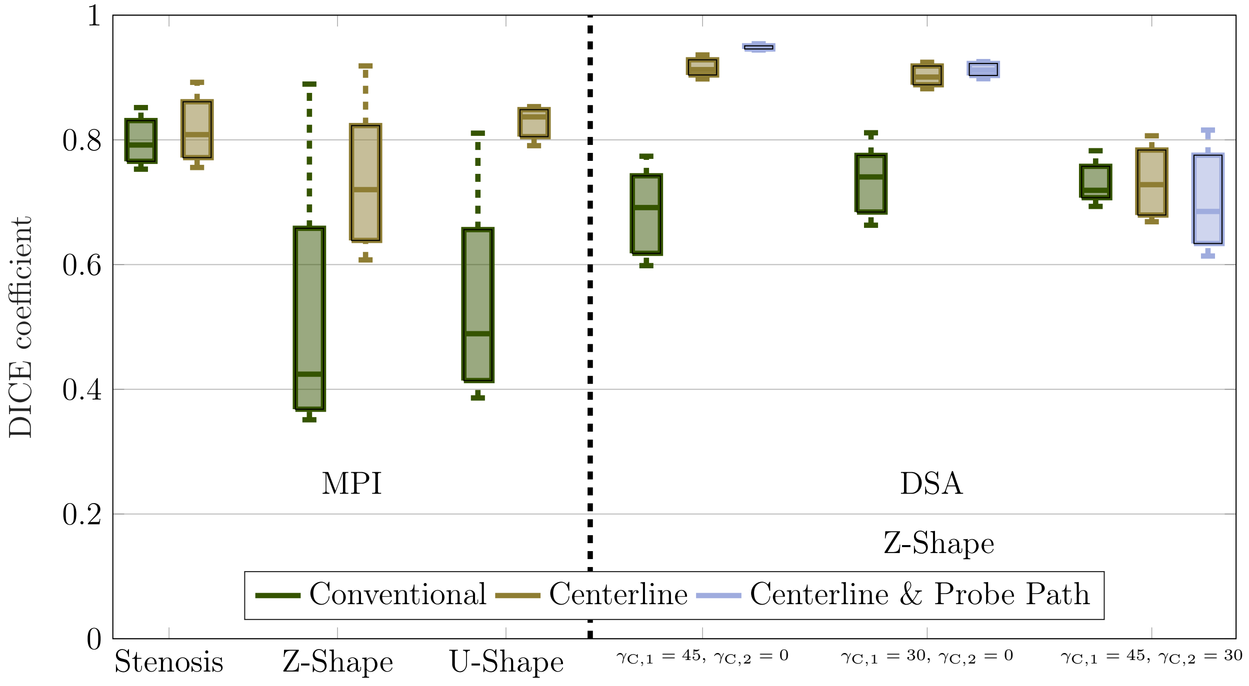

Figure 6.3 Quantitative results of volume reconstruction from MPI and DSA imaging shown as DICE coefficient for different phantom shapes and C-arm configurations.

6.1.3 Spatio-temporal Tracking of Imaging Probe

Since external imaging with MPI promises tracking of probe motion independent of the orientation relative to the imaging system, studies with simulated motion artifacts are eval-

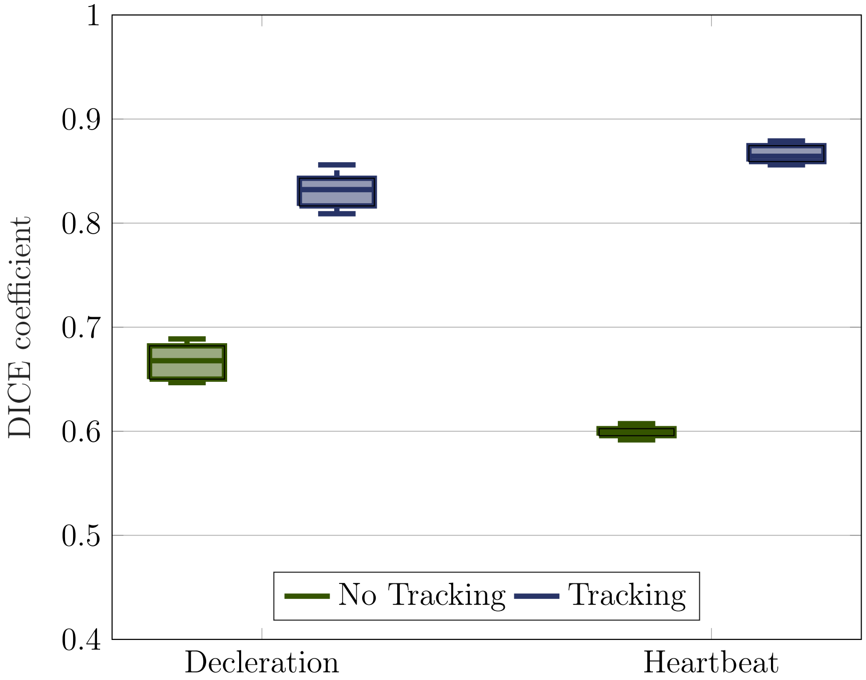

Figure 6.4 DICE for volume reconstructions with and without MPI-based probe tracking.

uated. The respective vascular volumes are constructed considering the helical trajectory of the imaging optic. We evaluate the volume reconstruction performance based on the resulting stenosis length and the DICE. First, we consider the deviation in estimating the stenosis length for different motion profiles with and without probe tracking. From the Computer Aided Design (CAD) sketch, a ground truth stenosis length of 1.5 mm is given. Reconstructing the vascular volume without MPI-based probe tracking for the probe deceleration and heartbeat motion profile, an overestimation of the stenosis length of 164 % and 137 % follows, respectively. It should be noted that for the heartbeat motion profile, the imaging probe translated twice through the stenosis section. Consequently, the vascular shape extracted without probe tracking shows substantial deviations. Considering the probe trajectory with MPI-based tracking, the stenosis length gets slightly underestimated with 4 % and 33 % for deceleration and heartbeat motion, respectively. Second, the DICE coefficients are calculated and shown in Figure 6.4 to evaluate the overall volume with the ground truth from the CAD sketch. The results are shown for conventional reconstruction (no tracking) and for the approach using the MPI-based tracking. Similar to stenosis length evaluation, the DICE coefficients are significantly improved for the spatio-temporal probe tracking.

6.2 Quantification of Soft Tissue Elasticity

6.2.1 Single-Fiber Elastography

In our experimental studies with a SF-OCE probe, we vary the distance between the imaging optics and the position of the shear wave excitation by moving either the OCE probe itself or the wave excitation source. The respective quantitative results are presented subsequently.

First, we analyze the impact of varied imaging positions on the elasiticty quantification. As visualized in Figure 5.5a, the OCE probe is inserted step by step in a phantom container using a linear motion stage (A). This results in different distances Δs_{n} between the excitation and imaging sites, which were determined during setup calibration. First, the estimation of shear wave velocity is analyzed for homogeneous tissue structures. In Figure 6.5, the quantitative results for shear wave velocity estimation from the SF-OCE needle are compared to the estimates from external OCE imaging. For both imaging setups, we construct the space-time maps and quantify the velocities based on the Equation 4.10. Here, we use a frequency interval $f_{\mathrm{s},i} \in [180, 230]$Hz and search for the maximum intensity points per frequency f_i. Given the 10 wave excitation and imaging repetitions per probe position and the evaluated frequency band, the boxplots shown in Figure 6.5 are created per phantom density.

Second, the split tissue phantom shown in Figure 5.4, which consists of two different densities, is used to analyze the quantification of the shear wave velocity. Similar to the study on homogeneous tissue, the quantifications of the SF-OCE probe are compared with the estimates of the external OCE imaging system. Based on the equation 4.10, the shear wave velocity is either estimated using all probe positions in the soft and harder tissue or evaluated separately for probe positions in the hard or soft gelatin. The quantitative results are shown as boxplots over the excitation and imaging sequences per probe position and the evaluated frequency band in Figure 6.6. Again, a frequency interval $f_{\mathrm{s},i} \in [180, 230]$Hz is used. A shear wave velocity $v_{\mathrm{s,ST}} = 2.5\,\mathrm{m\,s^{-1}}$ follows when evaluating the signals across all probe positions. When analyzing the velocity separately over the positions in soft and harder gelatin, velocities of $v_{\mathrm{s,SF}} = 1.9\,\mathrm{m\,s^{-1}}$ and $v_{\mathrm{s,ST}} = 2.9\,\mathrm{m\,s^{-1}}$ follow respectively. Please note that the shear wave is excited in the softer gelatin of 7.5 % and then propagates towards the harder gelatin. The total distance between excitation and imaging is considered to quantify the shear wave velocity in the harder gelatin based on equation 4.10. Compared to the shear wave evaluation for homogeneous tissue phantoms, considerably more outliers appear.

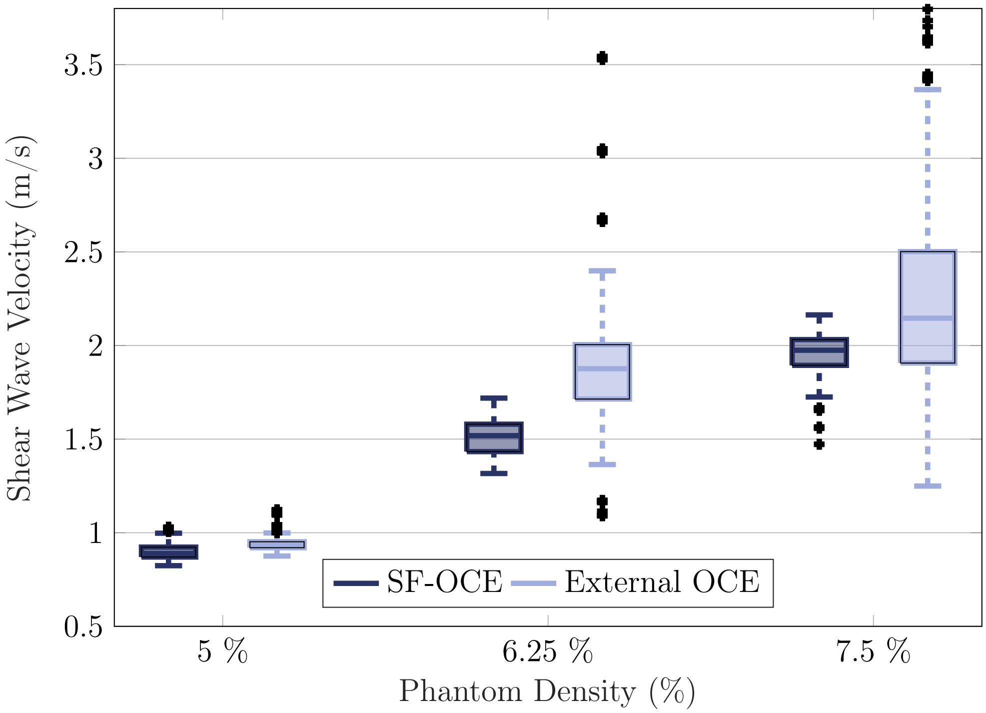

Figure 6.5 Quantitative elasticity estimates from SF-OCE needle compared to external OCE using a scan head for homogeneous phantom of different densities.

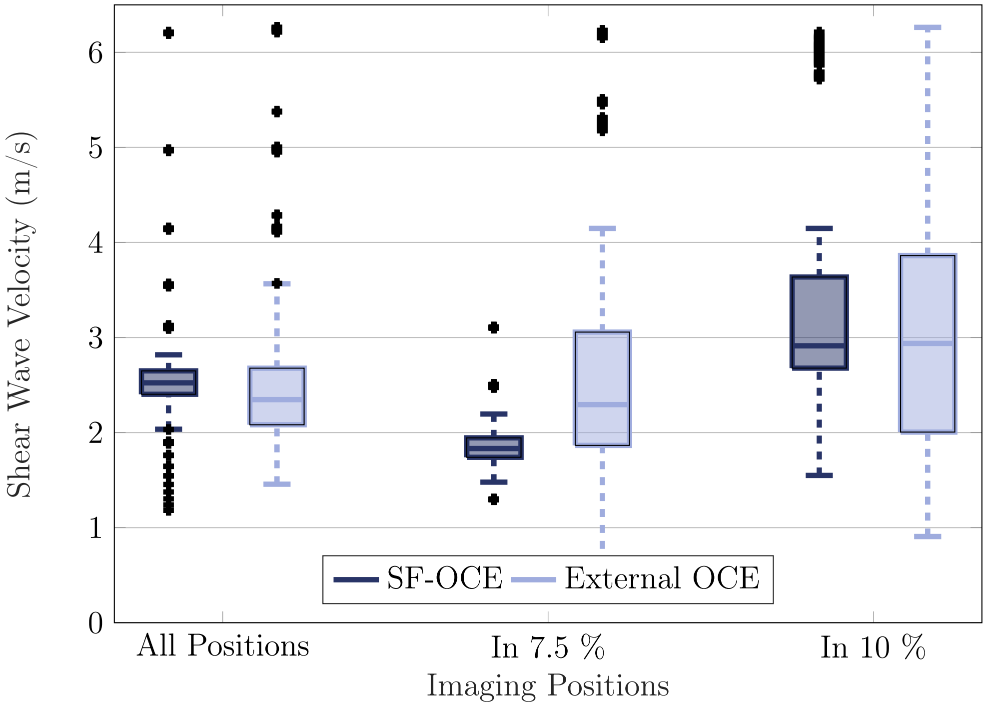

Figure 6.6 Quantitative elasticity estimates from SF-OCE needle compared external OCE using a scan head for the inhomogeneous phantom shown in Figure 5.4 composed of 7.5% and 10% gelatin density.

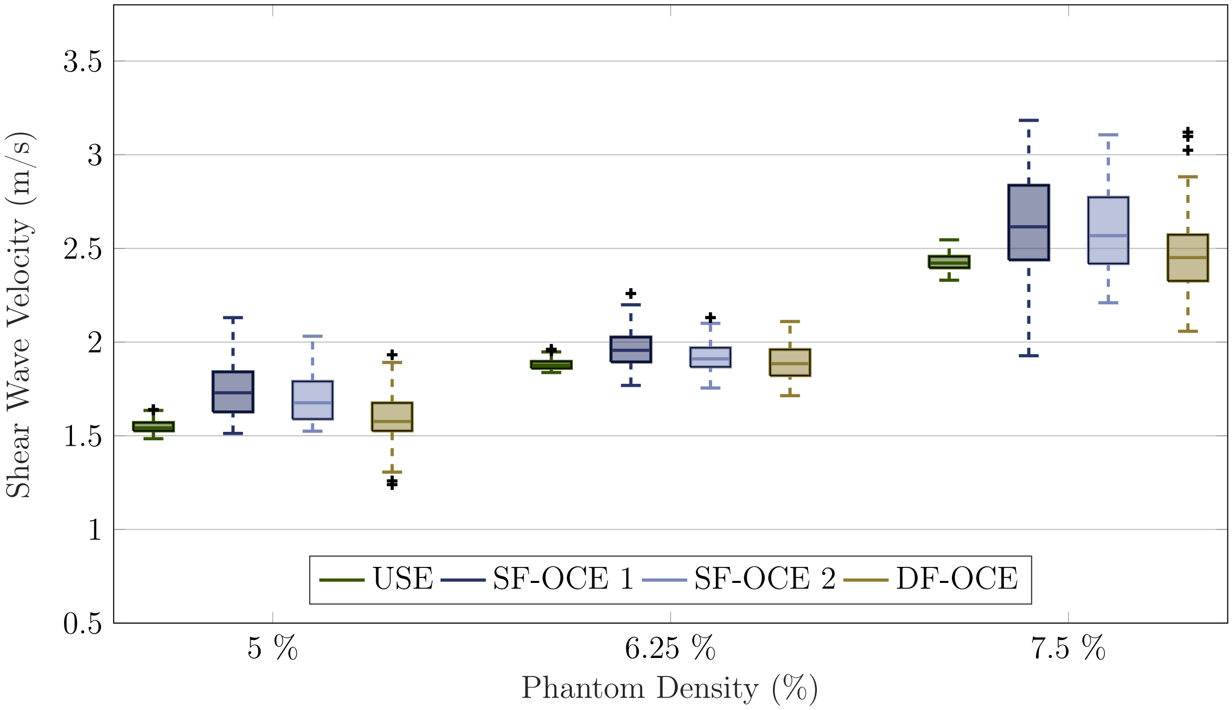

Figure 6.7 Quantitative elasticity estimates from single- and DF-OCE compared to external USE using a linear imaging probe for homogeneous phantoms of different densities.

6.2.2 Dual-Fiber Elastography

In this Section, we evaluate the quantification of shear wave velocity OCT phase signals acquired with the DF-OCE probe. This evaluation is conducted for various distances between the imaging probe and the position of shear wave excitation. Here, the probe position is kept constant, and the shear wave excitation positions are varied. The excitation positions relative to the OCE probe are visualized in Figure 5.6. Six excitation and imaging sequences are carried out for the 99 shear wave excitation positions. In contrast to the variation of the imaging position studied before, excitation positions are defined that are not necessarily in line with the OCE imaging probe. Analyzing the effect of different shear wave and imaging orientations. The results for studies on homogeneous tissue phantoms are shown in the figure as boxplots for all excitation positions and repetitions 6.7. In comparison to the DF-OCE results, we also present the estimations from SF-OCE and compare both to the externally applied USE. Please note that we derive the velocities for SF-OCE from Equation 4.10. The quantifications from USE result after image processing and evaluating Equation 4.12. The quantifications from SF-OCE show a slight increase in standard deviation, compared to measurements from USE and DF-OCE, especially in the harder phantom density.

The results for the inhomogeneous phantom are shown as boxplots in Figure 6.8. Please

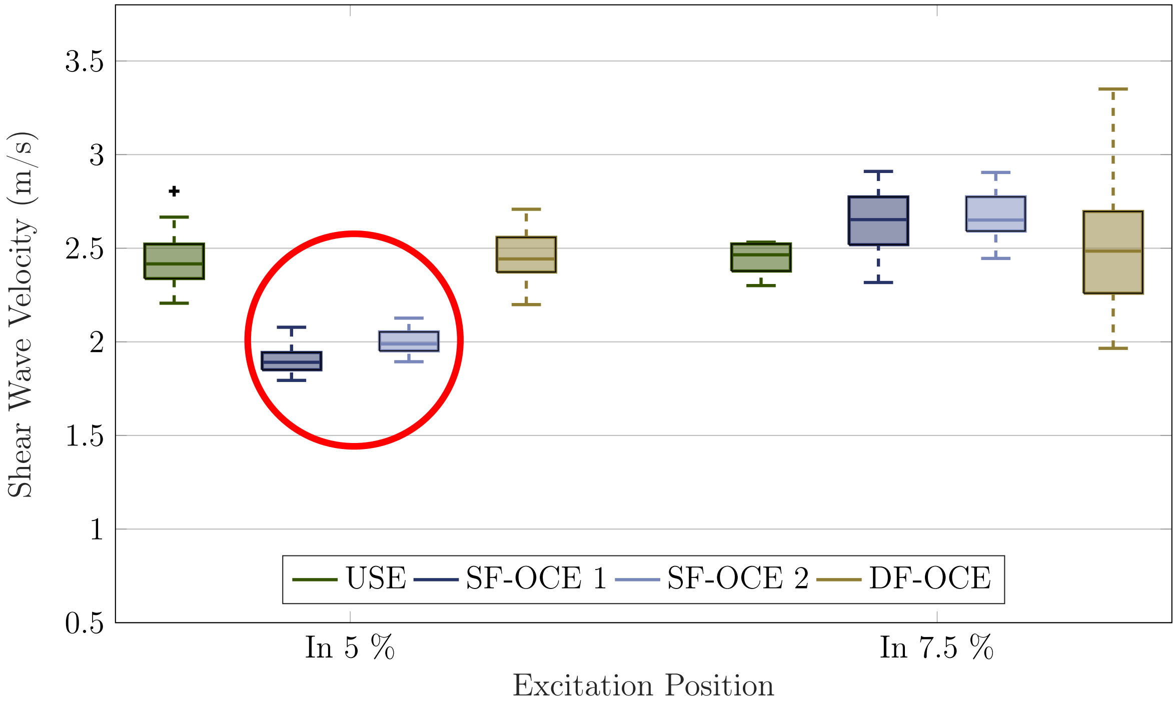

Figure 6.8 Quantitative elasticity estimates from single-fiber and DF-OCE compared to external USE for the inhomogeneous phantom composed of 5 % and 7.5 % gelatin density and OCE imaging probe positioned in 7.5 % gelatin.

note that the OCE imaging probe is positioned in the harder 7.5 % gelatin density, and the shear wave is excited at different positions relative to this probe. For excitation positions in the softer density of 5 %, the estimations from SF-OCE results in significant underestimations compared to the estimations from externally applied USE. These deviations are not given for excitation positions in the harder density. Except for an increase in the confidence interval in the case of excitation positions in the harder gelatin, the estimates from DF-OCE are comparable to USE. Also for excitation position in the softer gelatin, where the OCE probe is not positioned, the median agrees with the USE estimates. The respective results in inhomogeneous tissue phantoms, obtained from six repetitions per excitation position, are also visualized in Figure 6.9. Here, the deviations to estimations from USE are displayed with colors. For SF-OCE, greater deviations are shown for excitation positions in the softer gelatin. This correlates to the underestimated average shear wave velocity in Figure 6.8. In contrast, no significant deviations between the estimates from DF-OCE and USE are visible.

Finally, we summarize our elasticity quantification results from measurements with our DF-OCE probe inserted in porcine vascular tissue. In Table 6.1, the respective shear wave velocities are listed for measurements based on USE, SF-OCE, and DF-OCE. We determine the values after removing outliers using the interquartile range method. The estimates from

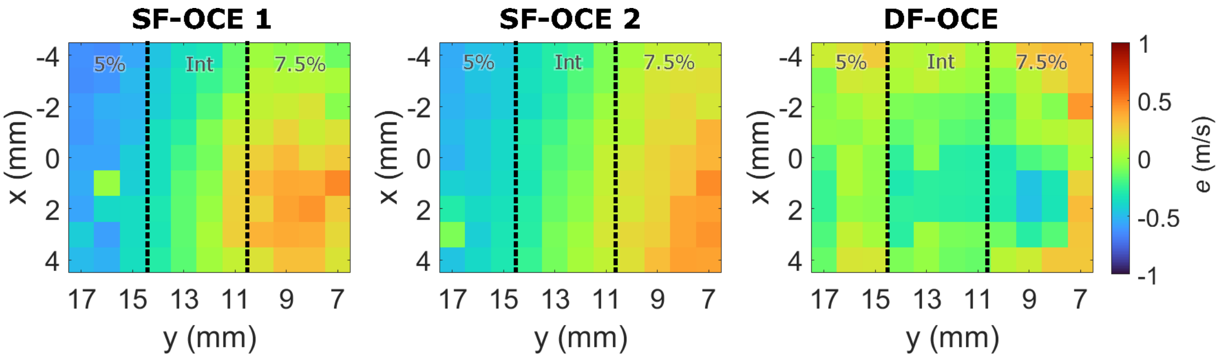

Figure 6.9 Errors in shear wave velocity visualized over the different excitation positions relative to the OCE imaging probe. Figure adapted from [408].

USE exhibit significantly higher standard deviations than those from the phantom study. An increase in standard deviation is also noted for both single-fiber and DF-OCE, but the deviations at all positions $y_{\mathrm{p},i}$ are lowest with the DF-OCE approach.

Table 6.1 Shear wave velocities in $\mathrm{m\,s^{-1}}$ estimated for heart tissue study. The mean and standard deviations are estimated over all shear wave excitation repetitions and positions depicted in Figure 5.7. Please note that the OCE probe positions y_i are correlated to different stiffnesses observed by palpation.

Position	USE	SF-OCE 1	SF-OCE 2	DF-OCE
y_1 (soft)	2.78 ± 1.45	2.74 ± 1.05	2.23 ± 0.61	2.50 ± 0.89
y_2 (stiff)	2.57 ± 1.58	2.47 ± 0.16	3.46 ± 1.59	3.20 ± 0.78
y_3 (stiff)	2.65 ± 1.53	3.05 ± 1.22	2.56 ± 0.40	3.19 ± 0.75

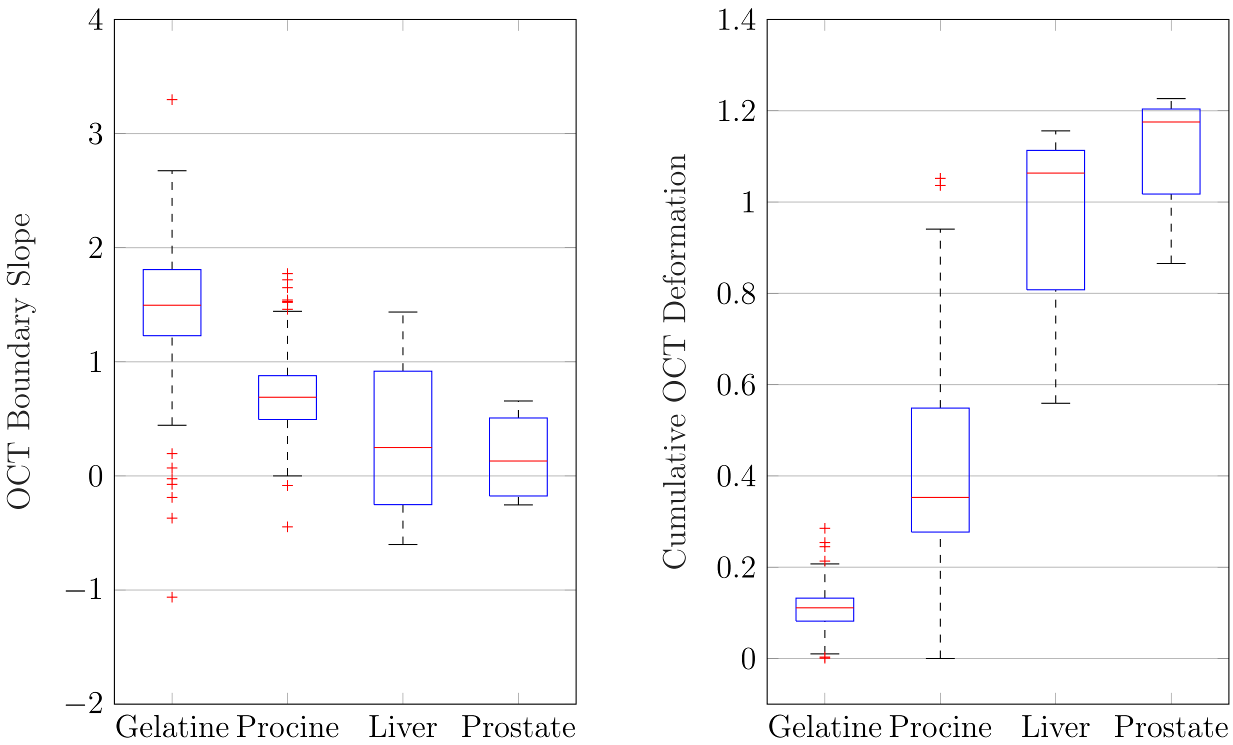

Figure 6.10 Comparison of tissue parameters, namely boundary slope and cumulative deformation, derived from OCT intensity and phase signals during needle insertion. The mean estimates per insertion are shown as boxplots and displayed separately per studied tissue, i.e., gelatin phantom, porcine tissue, ex-vivo liver, and ex-vivo prostate.

6.3 Quantification of Soft Tissue Interactions

6.3.1 Feature Extraction for Soft Tissue Analysis

Based on the three sensing modalities, namely OCT, FT, and US, and the proposed processing methods, the differentiation of tissue structures is investigated for the automatic needle insertion study. First, we consider the boundary slope $a(t)$ and cumulative deformation $d(t)$ extracted from the complex OCT data. For each insertion, we estimate the average slope and deformation values. In Figure 6.10, we compare the averaged slope and deformation magnitudes for all insertions per tissue type. Insertions in homogeneous gelatin phantoms show high boundary slopes while the measured deformations are minimal. For punctures in tissues, i.e., ex-vivo porcine tissue or liver and prostate tissue removed from cadavers, the slopes are significantly smaller, and there is a significant increase in the measured deformations. The largest average deformation derived from the OCT phase signals is reported for the prostate tissue samples. In addition, comparatively small boundary slopes are determined for these tissues.

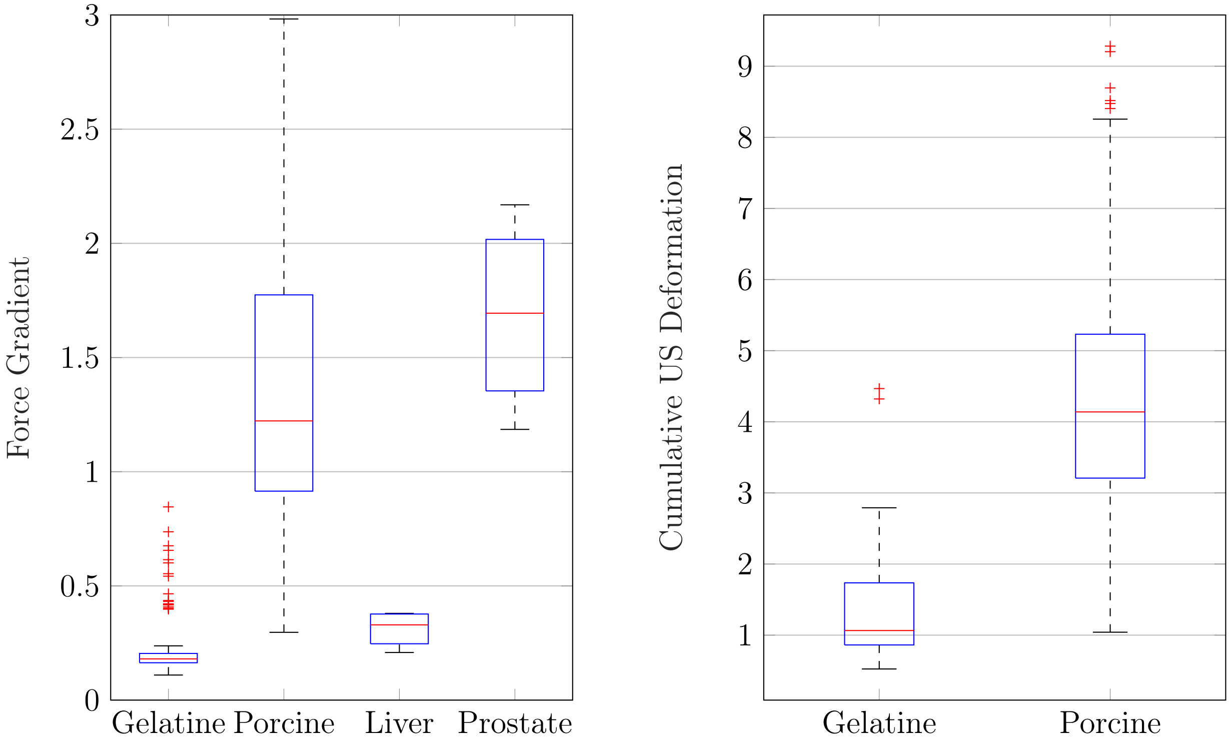

Figure 6.11 Comparison of tissue parameters, namely the cumulative force and cumulative deformation, derived from FT and US during needle insertion. The mean estimates per insertion are shown as boxplots and displayed separately per studied tissue, i.e., gelatin phantom, porcine tissue, ex-vivo liver, and ex-vivo prostate.

The features extracted from the externally applied sensing modalities, i.e., FT and US, are compared in Figure 6.11. Force measurements for needle insertions in gelatin phantoms show significant deviations from porcine and prostate tissue punctures. The punctures in liver tissue also show substantial differences from experiments on gelatine phantoms. However, their absolute average values are much lower than the values reported for punctured porcine and prostate tissue. The cumulative US deformations for gelatine and porcine tissue needle insertions also show significant deviations.

6.3.2 Detection of Rupture Events

First, we compare the threshold-based rupture detection from US, FT or OCT phase signals. We define minor and major rupture events as introduced in Section 4.4.3 and compare the number of detected events for our needle insertions in gelatin phantoms, homogeneous and inhomogeneous porcine tissue, as well as ex-vivo liver and prostate tissue samples. The average number of minor and major rupture events detected for the different modalities and

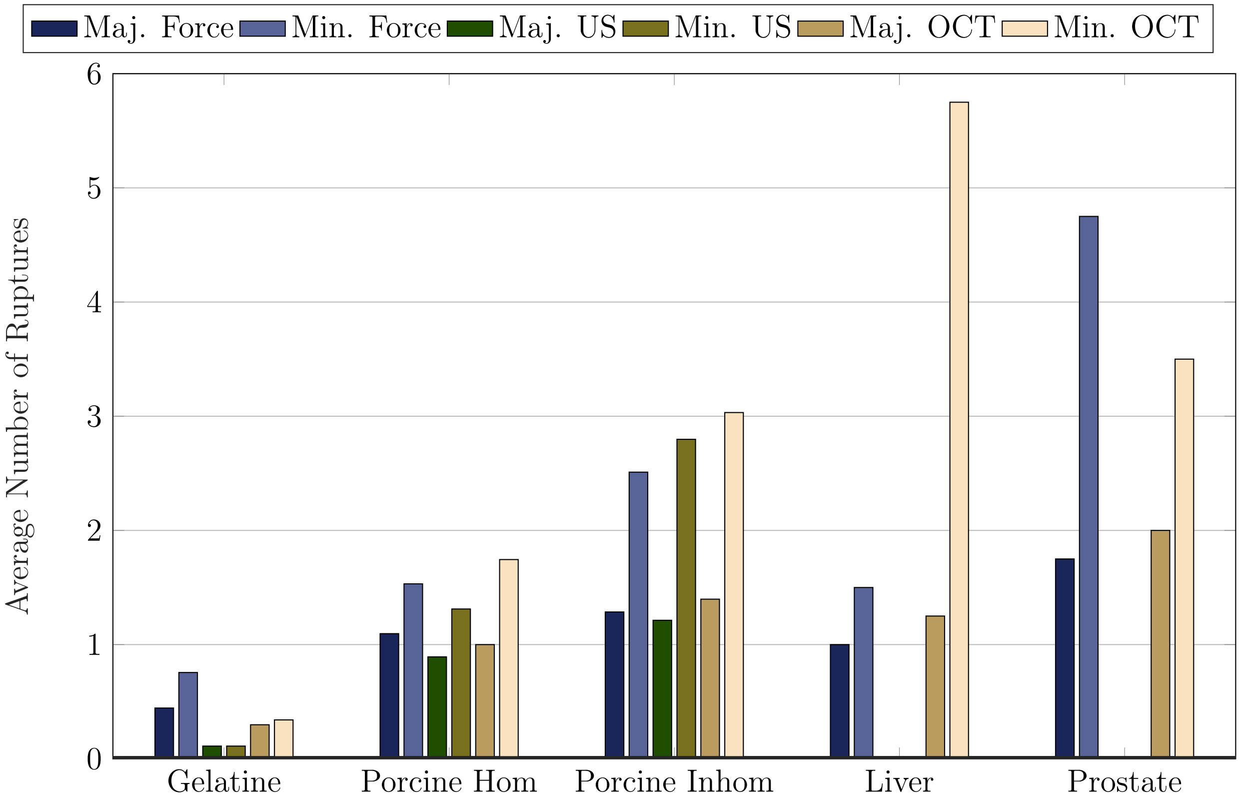

Figure 6.12 Number of minor and major rupture events extracted from FT, US, and OCT during needle insertion. The average number of ruptures over all insertions is shown per modality and punctured tissue, i.e., gelatin phantom, homogeneous and inhomogeneous porcine tissue, ex-vivo liver, and ex-vivo prostate.

tissue samples are shown in Figure 6.12. While the insertions in gelatin tissue show almost no rupture events, the experiments in porcine tissue show at least one major rupture event per insertion. An increase in detected minor rupture events is depicted for the insertions in inhomogeneous porcine tissue. Please note, as US measurements were not possible during the ex-vivo study, only FT and OCT signals are compared for the insertions in liver and prostate tissue.

In addition to this analysis, we evaluate whether the external measurements show the same temporal occurrence of rupture events. Therefore, we crop the insertion data sets on the temporal axes. We chose a window size of 224 A-scans corresponding to 2.46 s. We extract an equal number of time intervals with and without detected rupture events and evaluate the conformity of the external sensing modalities. In Table 6.2, the accuracy, precision, recall, and f1-score are given for all phantom insertions and separated by the tissue phantoms (A-

Table 6.2 Evaluation of threshold-based rupture detection compared for using both US $t_{\mathrm{R,US}}$ and force $t_{\mathrm{R,FT}}$ as ground truth for all tissue phantoms (all) and separated phantom types (A-D). Accuracy, precision, recall, and f1-Score are given.

Phantoms	Acc.	Prec.	Rec.	F1-Score
all	0.849	0.722	0.871	0.789
A	0.866	0.958	0.770	0.854
B	0.845	0.582	0.880	0.700
C	0.828	0.630	0.940	0.755
D	0.859	0.756	0.880	0.813

Table 6.3 Evaluation of the CNN-based rupture detection trained on the whole data set. Different inputs and ground-truth annotations are evaluated. Also, the ground-truth labels are fused as AND (t_{us} *and* t_{f}) and OR (t_{us} *or* t_{f}).

Input	GT	Acc.	Prec.	Rec.	F1-Score
int	t_{us}	0.722	0.684	0.653	0.660
phase	t_{us}	0.919	0.901	0.929	0.911
comb.	t_{us}	0.923	0.913	0.914	0.914
int	t_{f}	0.699	0.659	0.651	0.654
phase	t_{f}	0.923	0.908	0.927	0.916
comb.	t_{f}	0.926	0.913	0.923	0.918
int	OR	0.683	0.662	0.660	0.661
phase	OR	0.909	0.901	0.912	0.905
comb.	OR	0.893	0.885	0.891	0.888
int	AND	0.748	0.687	0.652	0.662
phase	AND	**0.944**	**0.920**	**0.953**	**0.934**
comb.	AND	0.937	0.912	0.946	0.926

D). Here, a ground truth combined from US and FT measures is used. In particular, we define time points as rupture event t_{R}, whenever $t_{\mathrm{R,US}}$ and $t_{\mathrm{R,FT}}$ are overlapping.

To evaluate the deep learning based rupture detection approach, we use the OCT intensity and phase signals from phantom insertions separated per phantom type or combined (comb.) as input images for training the proposed network architectures. In addition, we vary the ground truth (GT) labels used from externally applied US and FT sensing. The respective evaluation metrics are depicted in Table 6.3. The best results were achieved when using the combined ground truth from US and FT sensing (AND). Comparing the separated training with using either OCT intensity or phase signals as input demonstrates a substantial prediction improvement when using the OCT phase signals.

Considering the different phantom compositions, we additionally evaluate prediction performances for training and tests using only one phantom type (separated) and perform a

Table 6.4 Validation of CNN trained on the four phantom types separately (sep.) and cross-validation between the phantom types (cross) using the Siamese network and ground truth label AND.

Phantom	Acc.	Prec.	Rec.	F1-Score
A	0.689	0.842	0.526	0.456
B	0.777	0.594	0.583	0.587
C	0.621	0.481	0.480	0.480
D	0.585	0.499	0.499	0.499

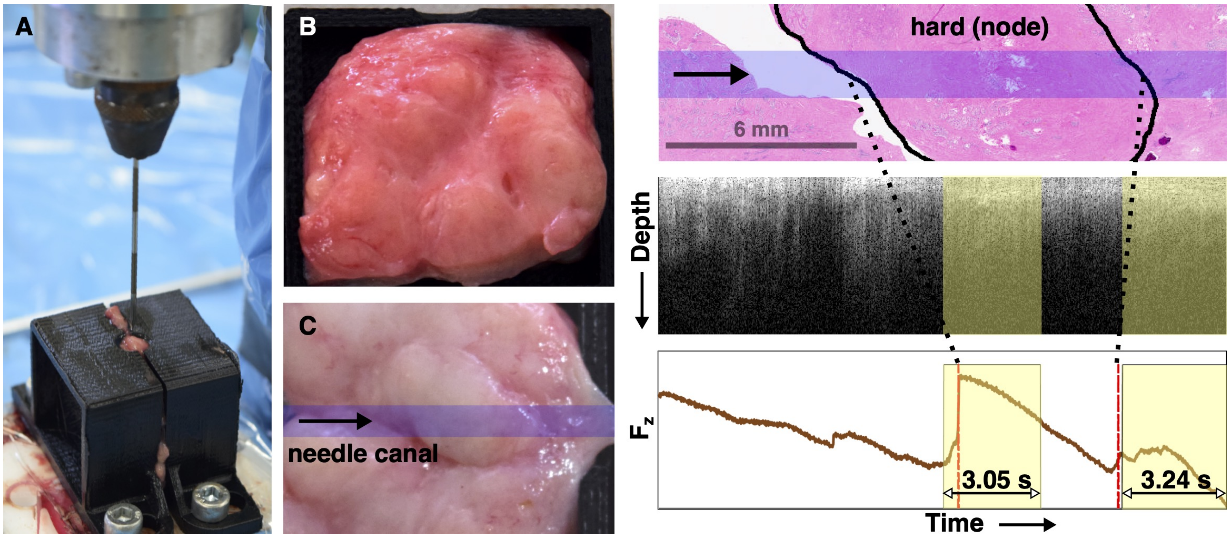

Figure 6.13 Experimental setup for needle insertion in ex-vivo prostate tissue sample. The tissue is shown in the container before puncture and afterwards with a highlighted insertion canal. On the right, the histopathological image of the tissue sample is shown with a highlighted node. According to this node, two ruptures are detected in the OCT signals and shown with respective force measurements. Figure adapted from [410].

cross-validation study excluding a specific phantom type from training. The respective performance metrics are listed in Table 6.4. While training and evaluation on the same phantom type show high prediction performances, the cross-validation study demonstrates decreased performances. In particular, the experiments with phantom C, listed as phantoms with soft gelatine behind the porcine tissue, and phantom D, referring to phantoms with inhomogeneous porcine tissue embedded in gelatin, show worse performances.

Finally, we use the trained CNN to predict ruptures in the OCT M-scans from ex-situ experiments. In Figure 6.13, the experimental setup for a needle insertion in an ex-vivo prostate tissue sample is shown. Moreover, the detected rupture events are highlighted in the OCT and FT signals.

The prediction performances for punctures in liver and prostate tissue are listed in Ta-

Table 6.5 Performance of the trained CNN on OCT inputs (intensity, phase, comb.) from insertions in liver and prostate tissue with t_f used as ground truth. The mean values and standard deviations for the different samples are shown.

liver

Input	Acc.	Prec.	Rec.	F1-Score
int	0.68 ± 0.13	0.14 ± 0.29	0.44 ± 0.11	0.48 ± 0.11
phase	0.73 ± 0.15	0.41 ± 0.48	0.63 ± 0.17	0.55 ± 0.20
comb.	0.73 ± 0.15	0.63 ± 0.17	0.41 ± 0.48	0.55 ± 0.20

prostate

input	Acc.	Prec.	Rec.	f1-Score
int	0.60 ± 0.17	0.48 ± 0.02	0.19 ± 0.24	0.39 ± 0.06
phase	0.46 ± 0.10	0.51 ± 0.06	0.33 ± 0.26	0.34 ± 0.04
comb.	0.47 ± 0.07	0.52 ± 0.08	0.34 ± 0.26	0.36 ± 0.04

ble 6.5. In general, the punctures in liver tissue show performances that are comparable to those achieved in the cross-validation study on tissue phantoms. Again, using the OCT phase signals as input image improves the prediction performance. Furthermore, combining the OCT intensity and phase signals using the Siamese network architecture shows the best results. Considering the punctures in prostate tissue, the prediction performances decrease, especially when comparing the reported accuracies.

Chapter 7

Discussion

7.1 Quantification of Vascular Morphology

With our experimental setup, particularly the motion unit, artificial vascular phantoms, and external imaging systems, a systematic analysis of various volume reconstruction methods is possible. Given the external image data from bi-planar DSA and MPI, we first investigated methods to register the three-dimensional vascular centerline extracted from the IVOCT data. In Figure 6.1, two projective views are shown for the volume reconstructions using DSA as reference modality. Using the centerline method, the volume reconstructions show substantial improvements compared to the conventional approach. This improvement is also visible in the quantitative analysis in Figure 6.3. Especially for C-arm configurations with $\gamma_{\mathrm{C}} = 0$, the performance improves significantly when comparing conventional IVOCT image reconstruction with the centerline approach. In particular, evaluating the first C-arm configurations the best performance increase with a mean of 91 % compared to 69 % using the conventional reconstruction approach is reported. Considering the third C-arm configuration with $\gamma_{\mathrm{C}} = 30$, the improvement using the centerline approach no longer exists. Even if the mean value increases, no significant deviation is visible in Figure 6.3. Hence, it is reasonable to assume that the luminal centerline estimated from DSA becomes inaccurate. These results demonstrate the importance of correct three-dimensional vascular centerline estimation when reconstructing IVOCT image data. However, when using DSA as reference modality, C-arm configurations relative to the artery structure should be used where projective errors are minimized. As shown for experiments with C-arm configuration $\gamma_{\mathrm{C}} = 30$ the centerline estimation deviates substantially from the ground truth and therefore the volume reconstruction performance decreases.

Our centerline approach, considering MPI as the reference modality, yields similar results. As depicted in Figure 6.2, the vascular morphology is much better reconstructed using the centerline method. Especially for curved phantom geometries, i.e., the Z-shape and U-shape, the morphology is well reconstructed compared to ground truth. For these phantoms, the quantitative results in Figure 6.3 also show substantial improvements for the centerline method compared to the conventional IVOCT volume reconstruction approach. The experiments in the U-shaped phantom, in particular, demonstrate a significant improvement in reconstruction. As the IVOCT imaging probe follows a trajectory with essential catheter bending, related imaging artifacts are much better compensated using the centerline approach. The quantitative results in the stenosis phantom do not indicate an obvious improvement in reconstruction. Here, the IVOCT follows a straight trajectory through the phantom that is equal to the assumption of a straight vascular centerline used in the conventional IVOCT volume reconstruction. When estimating the stenosis length, however, the advantage of the centerline approach becomes visible again. As the IVOCT imaging parameters set at the proximally attached motion unit do not necessarily reflect the motion profile of the IVOCT imaging optic at the distal end, the distance between luminal cross-sections is in case of the conventional reconstruction method overestimated. This leads to an increase in stenosis length of about 2 mm for the conventional approach compared to an increase of 0.8 mm with the centerline approach.

When comparing the quantitative results shown in Figure 6.3, using either DSA or MPI reference modality, the different imaging resolutions, and FOV sizes but also the acquisition modes should be considered. While MPI has comparatively low image resolutions and small FOV, the possibility of direct three-dimensional image acquisition is advantageous. In comparison, DSA enables increased image resolution and FOV size but has the drawback of complex image acquisition and three-dimensional reconstruction cycles. Arranging the C-arms properly relative to the vascular structures presents a major challenge. Finding reliable configurations for all patient-specific vascular geometries might be difficult in clinical practice. This effect has already been discussed in the literature [420–422]. Most importantly, the applied ionization of DSA is a relevant drawback compared to MPI, especially when conducting bi-planar image acquisition. However, clinical MPI scanner systems for human-sized evaluations are still being explored. A research prototype of a MPI head scanner has already been proposed [118] and recent image analysis methods promise a fast three-dimensional image acquisition [119]. Making an important milestone for the future analysis of vascular lesions [423, 424].

In the next step, we evaluate the vascular volume reconstruction using the vascular centerline and the IVOCT probe path extracted from external DSA. The quantitative results in Figure 6.3 demonstrate further improvements in the volume reconstruction, especially for curved vascular morphologies. Here, two major effects are described in the literature that may cause inaccuracies in volume reconstruction [425, 426]. First, the catheter bending in the curved section leads to NURD artifacts with a resulting rotation of the IVOCT cross-sectional images. Second, the two-dimensional IVOCT images, constructed after assigning a certain number of A-scans to a full rotation of the imaging optic, do not necessarily reflect a physical cross-section of the vascular morphology. In the case of vascular curvatures, the imaging optic may not move perfectly along the vascular centerline. Instead, the probe moves along the shortest path along a curve. Therefore, the two-dimensional IVOCT images are acquired for probe orientations that are not perpendicular to the estimated centerline. Considering both, the vascular centerline and the probe path for arranging the IVOCT images in three dimensions compensates for these artifacts. Consequently, we achieve an average DICE coefficient of 95 % for the first C-arm configuration. Again, a decrease in accuracy is reported for non-parallel configurations of the C-arms. For a C-arm configuration with $\beta = 30$ this volume reconstruction even deteriorates compared to the conventional method. One relevant drawback of the DSA-based probe path estimation is the limited temporal sampling of images. The DSA imaging frequency is slow compared to the IVOCT pullback speed applied in the clinics. Thus, temporal tracking of the imaging probe motion is limited as fast motion artifacts might not be sampled. Also, for reducing the ionization during PCI, an increase in the frame rate should be neglected.

Lastly, we evaluate the spatio-temporal tracking of the IVOCT imaging probe using MPI as reference modality. Here, we consider the helical vascular volume reconstruction approach. Two motion artifacts occurring during IVOCT image acquisition are studied. First, a deceleration of the imaging probe is simulated, reflecting imaging artifacts due to catheter bending. Second, a heartbeat motion is simulated with a back-and-forth motion of the IVOCT imaging probe. The volume reconstructions for both motion profiles are compared. Overall, the volume reconstructions lead to significantly larger phantom lengths if the IVOCT probe tracking is neglected. Considering the heartbeat motion profile, the phantom length is estimated to be twice as large as the ground truth. Next, the estimated stenosis length is quantitatively compared for both reconstruction approaches and motion profiles. For the deceleration profile, the stenosis appears larger with an overestimation of 230 %. The heartbeat profile results in the stenosis being sampled twice during one pullback. Applying the MPI-based IVOCT probe tracking and reconstructing the vascular phantom volumes accordingly results in much better results. The spatial position of the stenosis within the vessel phantom is correctly reconstructed for both motion profiles. The deceleration profile was compensated with slightly underestimating the stenosis length of 4 %. The heartbeat motion profile was also compensated so that only one stenosis section is visible in the reconstructed volume. In addition, the color map indicating the temporal information of the IVOCT image data shows that the same vascular structures are sampled for different times of the pullback. However, the quantitative analysis of the stenosis lengths results in an underestimation of 32 %. Here, the MPI-based tracking exhibits inaccuracies in the tracking of the reversing movement. Especially due to the limited spatial resolution of MPI, estimating variations in the IVOCT probe position for slight motion amplitudes or back-and-forth movement might be difficult. Finally, the DICE coefficients are compared for the reconstructed volumes and results are shown in Figure 6.4. A significant improvement is visible for both motion profiles when using the MPI-based tracking approach.

The MPI-based probe tracking shows promising improvements in vascular reconstruction but still, some limitations should be considered in future applications. First, increasing the image resolution will be one important step, for example, with further optimized calibration of the imaging FOV. Furthermore, an approach to extract both the vascular centerline and the probe trajectory from the same sequence of MPI volumes would be promising. At the time of the studies presented, no approach was available with which two different SPIONss concentrations could be equally well represented in the MPI volumes. A related study [405] demonstrating a concept for sequential acquisition of the vascular volume and the probe tracking has been presented to overcome the drawback that it is not possible to clearly distinguish between SPIONss used to mark the imaging probe and the SPIONss used to visualize the vessel shape. Another relevant limitation of bi-modal IVOCT and MPI imaging is the influence of the IVOCT probe rotation on the MPI imaging quality. During the experimental studies, significant influences were visible whenever the metallic markers used for probe tracking in DSA were inside the MPI FOV. To reduce these artifacts, the IVOCT catheter was adapted and the MPI imaging FOV was cropped during the studies. Outside of this cropped MPI FOV the catheter position could not be determined as robust since more image artifacts are introduced by the rotation of the catheter. Designing a MPI compatible imaging probe would be preferable for the future. This includes also a study on suitable material parameters and SPIONs concentrations to embed tracking markers on the IVOCT imaging probe. The application of magnetic liquor already shows promising results. However, applying a marker with a reasonable three-dimensional shape might ensure improved tracking accuracies. Recent studies on estimating the orientation of magnetic particles with parallel-aligned imaging axis [427, 428] motivate estimating not only the three-dimensional position of the intravascular imaging probe but also the rotational orientation. With this rotational information also NURD artifacts could be compensated during volume reconstruction.

The presented experimental studies demonstrate the importance of proper three- dimensional IVOCT volume reconstruction for PCI. The results motivate the potential for improved image analysis using the reconstructed IVOCT volumes. Compared to the co-registration software already established in clinical practice, the three-dimensional information could be interpreted directly in a single visualization. Two main scenarios need to be underlined that may impede the interpretation of intravascular image data with conventional three-dimensional reconstruction. On the one hand, the analysis of curved vascular structures might show relevant under- or overestimations of the vascular dimensions. Here, the catheter bending or non-centric translation of the imaging probe through curvatures might influence the conventional volume reconstruction. The presented approaches for improved volume reconstruction using the 3D centerline or considering the probe position relative to the vascular structures show the potential to compensate for these effects. The catheter bending is often combined with the presence of NURD artifacts that influence the volume reconstruction. But more importantly, these artifacts impede the two-dimensional cross-sections extracted from the temporal sequence of acquired IVOCT A-scans. These images are still mainly analyzed by physicians to estimate the stenosis diameter and select the stent size accordingly during PCI. Therefore, recent studies also focused on the deep learning-based estimation of the imaging probe motion to compensate for these NURD artifacts [402, 429–431]. However, also the longitudinal evaluation of vascular lesions becomes more important in clinical practice [192]. In clinical studies, the negative impact of so-called over-stenting has been discussed, where IVOCT promises high potential to find optimal values for defining minimum stent areas [432, 433]. This motivates to assess not only the two-dimensional IVOCT cross-sections but also the volumetric morphology in advanced diagnosis and treatment. On the other hand, the volume reconstruction may be influenced by relative motion artifacts during image acquisition. For this purpose, spatiotemporal probe tracking has been investigated in this thesis. The results demonstrate a significant impact on volume reconstruction results whenever relative motion artifacts are not compensated, such as probe deceleration or heartbeat contractions. To overcome the influences of heartbeat contraction, research studies on optimized intravascular imaging propose to apply SS-OCT systems that enable a high-speed acquisition of A-scans [183]. The authors promise to acquire a full IVOCT volume in less than 1 s and an Electrocardiography (ECG) triggered pullback start. Consequently, no heartbeat motion might influence image acquisition. The deceleration of the imaging probe due to catheter bending or other physical effects might still affect the image reconstruction. Therefore, approaches for spatial and temporal tracking of the imaging probe might be helpful.

IVOCT imaging enables the analysis of vascular structures with high spatial resolution. Within a few seconds, a volume of several centimeters in length can be acquired. However, this results in several hundred cross-sectional images or billion-pixel values that need to be interpreted by physicians. Thus, the future perspectives of IVOCT in clinical practice [192] include, in addition to an improved reconstruction of the vascular morphology, the application of deep learning to automatically analyze and classify the reconstructed image data. This includes, on the one hand, an online highlighting of relevant stenosis and an assessment of its diameter and length. On the other hand, an automated classification of stenosis lesions. Various studies have already presented the potential of deep learning to automatically distinguish different lesion states [33, 434, 435], i.e., calcified or lipid lesions. Furthermore, the automated segmentation of stent struts has been proposed to assist in assessing stent apposition [135, 436, 437]. Moreover, the high-resolution information on vascular structure contained in the IVOCT image data can also be used for the treatment and diagnosis of diseases that are accompanied by cardiovascular disease. For example, the connection between diabetes and changes in vascular structures was recently investigated in more detail with the help of IVOCT [438].

7.2 Quantification of Soft Tissue Elasticity

Our experimental studies, using a SF-OCE probe to estimate the shear wave velocity of soft tissue phantoms, demonstrate promising results. Using the precise calibration of imaging setup enables transient OCE. Thus, the distances between excitation and imaging Δd are known and allow the construction of space-time diagrams introduced in Equation 4.10. Here, the temporal axis Δt is defined from the temporal sampling of the OCT A-scan acquisition and shear wave excitation.

We evaluate the assessment of shear wave velocity by systematically varying both the position of the shear wave imaging and excitation. First, we discuss the experiments with varied imaging positions. Here, the estimates from SF-OCE from within the tissue are compared to OCE evaluated on the tissue surface with a conventional scan head setup. In general, the quantitative results for studies on homogeneous tissue phantoms in Figure 6.5 prove the linear relationship between phantom stiffness and shear wave velocity. Considering the estimates from SF-OCE, the evaluated phantom densities show significant differences in their velocity. In contrast, results from externally applied OCE depict increasing deviations for stiffer tissue phantoms and overlapping confidence intervals. Two physical effects might influence these quantifications. First, the surface acoustic waves propagating on the phantom surface show higher signal-to-noise ratios. This might be related to the higher motion amplitudes and has the consequence that multiple wave reflections with various distances traveled are detected at the imaging position. In addition to the multiple reflections, phase-wrapping effects might occur due to the high motion amplitudes. Second, the distance Δd estimated between excitation and imaging might not be valid for all imaging positions.

The shear wave velocity quantification using a split phantom with two different stiffnesses is evaluated. Please note, that the shear wave travels from the softer tissue (7.5 %) towards the stiffer area. The boxplots in Figure 6.6 depict the velocity estimates considering all imaging positions or imaging in the respective individual densities (in 7.5 % or in 10 %). Extrapolating the results in homogeneous tissue phantoms results in an estimated shear wave velocity of approximately $3\,\mathrm{m\,s^{-1}}$ for the area with 10 % gelatin concentration. However, the results from SF-OCE using all imaging positions show an average velocity of $2.5\,\mathrm{m\,s^{-1}}$. In contrast, evaluating the imaging position per density separately, average velocity values of $2\,\mathrm{m\,s^{-1}}$ and $3\,\mathrm{m\,s^{-1}}$ follow for 7.5 % and 10 % density, respectively. The results for imaging position in the stiffer phantom show higher deviations with a large confidence interval and a higher number of outliers compared to the softer tissue. As the shear wave travels first through the soft tissue, reaches the boundary between both, got partially reflected but also transmitted, we assume that the wave motion amplitude decreases when entering the harder tissue. This can be correlated to the decreasing signal-to-noise ratios and also the increasing number of outliers shown. In contrast to the SF-OCE results described before, the results from external OCE show larger deviations. The average velocity values are showing the same trend as described for the SF-OCE. However, the large confidence intervals impede a clear distinction of phantom stiffnesses.

For these studies comparing the SF-OCE probe measurements from within the tissue with the externally applied OCE, it should be noted that different wave components are measured. Given the external OCE setup, mainly surface acoustic waves are imaged. In contrast, the wave propagation in deeper tissue structures is analyzed using the miniaturized OCE probe that is inserted in the soft tissue phantom. Therefore the quantitative estimates are not directly comparable to each other. As motivated in a review on wave-based elastography [212], the different shear wave components do not necessarily reflect the same propagation characteristics.

Second, we evaluate the quantification of shear wave velocity when varying wave excitation positions. We use USE as reference modality in these experiments, in contrast to external OCE applied in the previous analyses. This enables an analysis of shear wave propagation in deeper tissue layers, not just on the surface. Thereby, the same shear wave components are analyzed with the SF-OCE probe and the reference measurements from USE. For three homogeneous tissue phantoms, the shear wave velocity is estimated, and the results are shown in Figure 6.7. The absolute velocity values show deviations from the studies with varied imaging positions in Figure 6.5. These deviations can be explained by the temperature variation of gelatin elasticities that has already been discussed in the literature [439]. Comparing the reference values from USE (green) with those from SF-OCE (blue), increases in the confidence intervals are visible for the latter. Nevertheless, a distinction between the different phantom stiffnesses is possible for both modalities. The average shear wave velocity values estimated from SF-OCE show slight increases compared to USE.

Next, we evaluate the shear wave propagation through a split phantom composed of soft to hard gelatine concentration when varying the wave excitation position. The quantitative results from SF-OCE in Figure 6.6 show relevant deviations in estimating the shear wave velocity for excitation positions in the soft tissue. Here, it should be noted that the SF-OCE probe was placed in the same position in the hard phantom part of 7.25 % for all variations of the excitation position. A decrease of about 25 % follows for the average shear wave elasticity estimates compared to the experiments in the homogeneous phantom. The reported values are comparable to those estimated for homogeneous phantoms of 6.25 %. In contrast, the USE results show similar average shear wave velocity for excitation positions in both the hard and soft gelatin. These average values of approximately $2.5\,\mathrm{m\,s^{-1}}$ correspond to the experiments in homogeneous phantoms with the same gelatin concentration of $7.5\,\%$. However, an increase in confidence intervals is noticeable when evaluating the shear wave velocity with USE in the split phantom. There a no relevant deviations visible for excitation and imaging position in the harder phantom part.

The described experimental studies in split phantoms demonstrate the drawback of transient OCE with a single-fiber probe. Whenever the shear wave travels through inhomogeneous tissue, its velocity can only be estimated as an average value for the current distance between excitation and imaging Δd. The results in Figure 6.6 underline this effect. Evaluating all imaging positions for shear wave velocity quantification results in an average velocity between the respective values for the two individual phantom densities. If the tissue boundary is known, e.g., due to speckle variations or from segmentations, the shear wave velocities can also be calculated separately per phantom density. However, the high variance of the results for imaging positions in the harder part demonstrates the uncertainty of velocity estimates. For these imaging positions, the respective distances Δd_i correspond to different proportions of propagation in the soft and hard phantom. Similar conclusions can be drawn from the experiments with varied excitation positions in Figure 6.8. The shear wave travels through two different densities when being excited in the softer phantom part. Consequently, the shear wave velocity estimates were underestimated.

In summary, with transient SF-OCE homogenous tissues can be analyzed properly using precisely known calibration parameters. In inhomogeneous tissue, the precise calibration is not enough to accurately resolve the shear wave velocity. Depending on the distance between excitation and imaging and the proportion of tissue densities on the wave propagation path only average elasticity estimates are possible. Thus, when using a SF-OCE probe in unknown tissue an under or overestimation of elasticity might occur. Besides potential soft tissue inhomogeneities, a proper experimental calibration might limited, i.e., defining the distance between excitation and imaging.

Using the novel DF-OCE probe design, we are facing the described limitations of SF-OCE. We aim to enable reliable and precise estimation of shear wave speeds by eliminating the need for extensive experimental calibration. In particular, a local quantification of shear wave velocities should be achieved while being independent of the wave excitation position. In contrast to estimating the shear wave velocity over the whole propagation distance between excitation and imaging, we aim to measure the velocity locally around the miniaturized OCE probe. Two integrated fiber optics with rigid spatial orientation to each other are embedded in the probe. The distance between these optics Δx and the time difference between wave arrival at the two positions is used to estimate the shear wave velocity. The quantitative results in homogeneous tissue phantoms in Figure 6.7 demonstrate the potential of distinguishing different phantom stiffnesses but also the improvement of measurement precision when compared to the SF-OCE results. This is visible in the decreased confidence intervals for DF-OCE and the average shear wave velocity values showing minor deviations to the reference from USE.

In addition, the studies in the split phantom underline the capabilities of sensing local elasticity properties independent of the shear wave origin. As depicted in Figure 6.8 the estimated shear wave velocity shows comparable values to the experiments in homogeneous tissue, even for wave excitation positions within the soft tissue of 5 %.

The spatial relationship of the estimated shear wave velocity and wave excitation position is investigated using Figure 6.9. The deviations to the reference from USE are displayed for all excitation positions. Please note, that the excitation positions are given with the respective spatial distances in x- and y-direction relative to the respective imaging optic. These excitation maps are shown for the single-fiber and DF-OCE approach. The underestimation of shear wave speeds for excitation positions in the soft phantom part is visible in the SF-OCE maps. The smallest deviations are visible in the transition area between soft and hard phantom parts (Int). Consistent estimates of shear wave velocity are obtained for most positions when the DF-OCE approach is used. However, for increased compensation angles α_x, α_z, the shear wave velocity quantification shows slight overestimations to the reference from USE. These compensation angles correspond to excitation positions with $y <= 7\,\text{mm}$ and $x > 2\,\text{mm}$.

This novel OCE probe design with two integrated imaging optics enables simple manufacturing with small probe dimensions. Two important requirements should be considered for quantification of shear wave velocities. First, an exact calibration of the distance between the imaging optics Δx. Second, externally excited shear waves should propagate along the needle shaft. In clinical practice, this requirement could, for example, be met by aligning a US transducer in-plane with the probe shaft, a standard in US based needle navigation. Subsequently, ARF shear wave excitation could be applied. Therefore, an exact estimation of the distance between the excitation and the imaging position, as necessary for SF-OCE, is no longer required. Moreover, the local quantification of shear wave velocities ensures reliability independent of the tissue structures between excitation and the dual-fiber imaging position. This makes the presented DF-OCE probe design promising for application in clinical practice.

Our study on heart tissue demonstrates that it is feasible to quantify local stiffness in coronary arteries using our DF-OCE probe. Compared to phantom studies, we generally notice increased standard deviations in single-fiber and dual-fiber OCE. This may be related to non-uniform push excitations and wave disturbances within the myocardial tissue. In these heterogeneous tissue structures, multiple wave refractions and reflections occur, causing deviations in the push sequence and the estimated spatiotemporal wave propagation. This is particularly true for the SF-OCE estimates, which can be influenced by the non-uniform tissue structures between the excitation and imaging positions. As a result, we cannot clearly distinguish the transition from soft to stiff artery tissue using SF-OCE, and the standard deviation also increases. In contrast, the transition is detectable using DF-OCE as shown in Figure 6.9. As the wave propagates through thin tissue structures, its movement is barely detectable with USE, as demonstrated in Figure 7.1. This leads to increased standard deviations for USE compared to phantom experiments. Considering the reported significance levels and standard deviations, the application of USE as a reference modality in these heart tissue experiments is limited.

Using the DF-OCE probe design, we propose a temporal correlation approach to extract the wave run time $\Delta t_{1,2}$ between the two optical sampling positions. Computing the two-dimensional cross-correlation of the two sequences of OCT phase signals results in the run time. In contrast to SF-OCE with evaluating space-time diagrams, the dual-fiber correlation approach leads to more reliable estimates even when the signal quality decreases. As visualized in Figure 7.1, the signal-to-noise ratios in the USE space-time or and SF-OCE phase scans decrease substantially for shear waves traveling through inhomogeneous phantoms or ex-vivo tissue samples. However, cross-correlated signals displayed for DF-OCE show good signal qualities.

The variations in the analyzed signal-to-noise ratios of our OCE probes, USE, or the externally applied OCE can be explained with the different shear wave components measured within a respective imaging axis. For both wave excitation approaches we assume a spherical propagation of the shear wave. In the case of piezoelectric excitation at the surface, the shear wave thus propagates on the one hand as an surface acoustic wave with the wave amplitude perpendicular to the tissue surface. On the other hand, the shear wave propagates spherically in deeper tissue layers. A similar spherical propagation is assumed for the ARF excitation with origin in the focus point. As the distance between excitation and imaging increases, the deformation of this spherical wave into a plane wave increases. For some scenarios, the shear wave motion may not be parallel to the imaging axis, resulting in an underestimated motion amplitude. These signal variations might also impede the handcrafted feature extraction

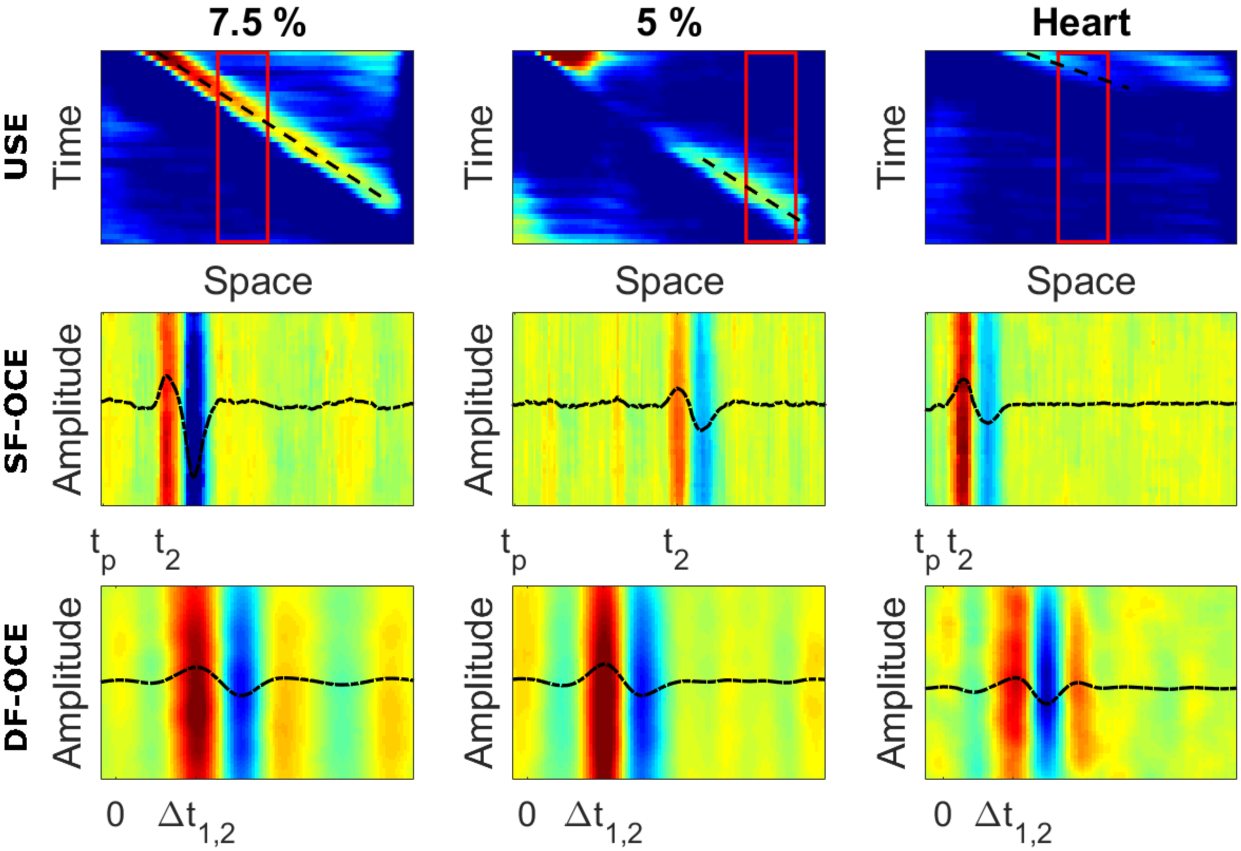

Figure 7.1 Comparison of signal qualities for experimental studies on the inhomogeneous phantom and ex-vivo tissue samples. Figure adapted from [408].

methods presented. Therefore, in future studies, the application of machine or deep learning methods for signal analysis should be studied. The necessary calibration of the probe properties could, for example, be learned directly through end-to-end learning processes, as proposed in related studies [289, 290].

Recent miniaturized OCE probe designs integrate the wave excitation source [440]. This creates an alternative approach to simplify the spatio-temporal calibration of excitation and imaging. However, the standard approach of embedding only one imaging optic limits the precision of shear wave analysis. As investigated in related studies, the distance between shear wave excitation and imaging should not be too close [441]. Therefore, the resolution of the spatial wave sampling decreases. Hence, only average shear wave velocity values are reported, which depend on all tissue structures between excitation and imaging. In addition to the constraints related to spatial sampling, the embedded excitation sources should enable reproducible excitation schemes. Here, piezoelectric actuators, which are typically used, require proper and consistent mechanical coupling. Ensuring this is complicated, especially when positioning and moving these probes in soft tissue of varying densities. Since, in recent studies, probes have been mainly placed at the tissue surface, where excitation and coupling effects can be optimized, the question arises about possible uncertainties in the application when the probes are inserted into the tissue. Especially for the intraluminal application, such as in coronary arteries or bronchial structures, ensuring this mechanical coupling is not trivial. To overcome these issues of shear wave excitation, an approach for imaging naturally induced shear waves, e.g., by heart contraction [442], has been presented in the context of USE. This approach would also be promising for OCE probes but has not yet been presented. As an alternative to the presented ARF-based excitation, future studies should therefore investigate the sampling of natural shear waves with a DF-OCE probe design.

In inhomogeneous anisotropic tissue structures, the shear wave coupling and propagation characteristics, i.e., the resulting wave frequency, might vary due to dispersion effects [285]. Therefore, ensuring reliable shear wave velocity analysis from OCE probes requires a reproducible wave excitation and a consistent spatial sampling. Using our proposed DF-OCE probe, the same external excitation position and coupling could be applied for various probe positions inside the tissue. This promises more reproducible shear wave excitation with limited variations in shear wave sampling. Still, the wave propagation might be influenced by dispersion effects. However, when evaluating the runtime with our cross-correlation approach, we primarily focus on the temporal correlation of the local maximum of the sampled wave. Given the small spatial distance $\Delta p_{1,2} = 2\,\mathrm{mm}$ between the imaging optics, we assume that dispersion effects influencing the wave characteristics between the sampling points are minimal. With the application of even faster OCT systems, i.e., SS-OCT systems, this distance between the imaging optics could be further decreased, ensuring more precise local sampling.

One significant limitation of our OCE probe design is that the shear wave frequency characteristics and amplitude variations are mainly sampled using one-dimensional imaging per optic. A recent OCE fiber endoscope design [273] demonstrates the ability of sampling the shear wave propagating using a line or circular scanning shape. This miniaturized probe design enables the analysis of wavelength variations in two- or three-dimensional representations, similar to benchtop OCT setups. However, even with this probe design, only a superficial shear wave analysis is possible as it is proposed for MIS. The high voltages applied for piezoelectric actuation and the optical setup require contactless imaging. Therefore, needle-based OCE with direct tissue contact might be challenging with this fiber endoscopic probe design.

7.3 Quantification of Soft Tissue Interactions

This thesis studies the analysis of OCT signals in front of the needle tip and investigates whether tissue characterization or differentiation is possible using this modality. These findings are also compared to FT and US measurements that are usually applied externally.

First, the feature extraction methods for analyzing needle tissue interactions from OCT are discussed. Features derived from OCT, FT, and US demonstrate that the tissue response during insertion varies for the tissue structures studied. First, we evaluated the features in the sequence of complex OCT scans. In particular, the slope of tissue boundaries visible in the OCT intensity signals and the tissue deformation derived from the OCT phase signals are studied. While the average boundary slope in gelatin tissue in Figure 6.10 shows significant deviation from those of porcine or human ex-vivo tissue, the liver and prostate tissue samples are not distinguishable. Considering the deformation profiles extracted from the OCT phase signals, the porcine and human tissue samples show substantial differences. Thus, considering the tissue deformation and displacements during needle insertion solely based on the tissue boundaries visible in the OCT intensity signals might not be able to distinguish tissue. In contrast, evaluations from OCT phase signals motivate a more sophisticated analysis of deformations. Here, we assume that bulk displacements occur with a comparatively large motion amplitude and therefore are not contained in the relative motion analyzed when evaluating the OCT phase signal.

Second, we investigate the information from FT and external US imaging and extract features for tissue distinction. The average force gradients depicted in Figure 6.11 enable a distinction between gelatin and ex-vivo tissue. However, porcine and human ex-vivo samples are not distinguishable. Even if the gradients measured for punctured liver tissue samples show significant deviations, the corresponding values in the human prostate and porcine tissue are not distinguishable. The evaluation of the deformation profiles for gelatin and porcine tissue extracted from US imaging shows significant variations. Comparing the deformation profiles from OCT and US imaging, the distribution of the cumulative deformation in the different gelatin tissues appears similar. Still, the increasing confidence interval for porcine tissues indicates greater differences in the deformation processes. This applies also to the deformation processes determined from the OCT phase signals in ex-vivo tissue.

In summary, the presented feature extraction study shows the potential to analyze tissue or respective properties during needle insertion. However, assessing feature values from the different modalities that highlight the same tissue properties is not directly possible. In addition, the individual modalities and investigated feature extraction approaches do not necessarily reflect clear metrics for differentiating between tissues. While the evaluation of force gradients might be applied to divide tissue structures related to the mechanical response, the absolute values could vary, e.g., due to inhomogeneities of the tissue itself or the surrounding tissue. Accordingly, the evaluated force gradients for punctures in porcine tissue show higher confidence intervals when distinguishing between homogenous and inhomogeneous tissue.

In addition to analyzing specific features extracted from the insertion data sets, we study the detection of rupture events. Given the definition of a rupture in Section 4.4.3, we search for time windows when a specific tissue boundary has recently been punctured. We distinguish between major and minor ruptures according to the respective amplitude of tissue relaxation processes.

The number of minor and major rupture events averaged per tissue type and extracted from OCT, US, and FT signals are compared in Figure 6.12. Please note that all needle punctures in gelatin and porcine tissue were conducted with the same insertion depths of approximately 54 mm. The insertions in ex-vivo tissue from corpses were conducted in specific tissue holders of 30 mm length. In gelatin phantoms, the number of ruptures is less than one per puncture for all modalities. The FT based rupture detection reveals a slight increase in the reported average number of rupture events. This might be related to force differences due to varied friction along the needle shaft. Next, the punctures in homogeneous and inhomogeneous porcine tissue are analyzed. While experiments in all porcine tissues show one major rupture per puncture, the number of minor ruptures increases in the case of inhomogeneous tissue. Considering the specific transitions in the inhomogeneous tissue, e.g., from tendon to muscle, the increase in minor ruptures could be explained.

For punctures in ex-vivo tissue OCT and FT signals are evaluated. In particular, the punctures in liver tissue result in one major rupture. The evaluation of the OCT signals shows a significant increase in minor rupture events. This number of rupture events is not comparable to those obtained from the FT signals. Given the comparatively soft liver tissue with tiny liver lobules, each about a few millimeters in size [443], the needle probe might puncture several internal tissue boundaries. However, these internal boundaries might exhibit only small variances in the force values measured at the needle shaft, impeding the rupture detection. In contrast, the OCT signals recorded directly in front of the needle tip appear to show the corresponding deformation and rupture processes on the lobules more precisely. Combining the rupture detection analysis with the feature values extracted from OCT signals (Figure 6.10) underlines the differences in internal rupture processes and those at the tissue surface for the liver tissue. The boundary slope shows a high confidence interval for punctures in the liver. We hypothesize that the lobules can be assigned to increased boundary slopes where the deformation ahead of a rupture event is comparatively small. In contrast, the ruptures that belong to the exit of the tissue sample show decreased boundary slopes that can be explained by a longer period of tissue deformation in front of the tissue until the tissue ruptures. The punctures in prostate tissue show an increase in the number of minor and major rupture events for both OCT and FT signals. Investigating the temporal appearance of the major ruptures for the other tissue types, these events can mostly be associated with the exit from the respective tissue. Small nodules often form in the prostate with relevant influence on the tissue collagen structure [444]. These nodules can be easily detected during palpation of the tissue. We hypothesize that these nodules also influence the number of ruptures detected during needle insertion. Therefore, an increase in major but also minor rupture events is reported in Figure 6.12. Given the comparatively large tissue stiffness, the deformation and rupture processes show larger amplitudes than the ex-situ liver and porcine tissue punctures.

Next, we analyze the detection performance of rupture events with the threshold-based detection approach from OCT phase signals in different phantom types. In particular, we distinguish tissue phantoms with either soft (6.25 %) or hard (20 %) gelatin embedded around the porcine tissue. We analyze the detection performance using the events extracted from FT sensing as ground truth and perform a grid search to estimate the optimal threshold values. Given the temporal crops of OCT and FT data we create a balanced data set with the same amount of time windows with and without rupture event. The accuracy varies between 0.83 and 0.87 when all phantom types are evaluated together or separately (see Table 6.2). The best results are obtained for data sets from a phantom with the same gelatin density around homogeneous porcine tissue (A). Similar performances were achieved for punctures in inhomogeneous porcine structures (D). Here the porcine tissue was also embedded in the same gelatin density. Punctures in phantoms with two different gelatin densities around the porcine tissue (B and C) demonstrate a relevant decrease in precision values. This indicates a relevant amount of data set crops that were incorrectly labeled. Considering also the comparison in Figure 6.12 this variation in detecting rupture events from FT and OCT data might be related to the different sensing capabilities. While OCT signals acquired at the needle tip enable more sensitive detection of minor rupture events, the FT measurements at the needle shaft are impeded by friction forces.

In conclusion, the threshold-based rupture detection from OCT signals promises to be a sensitive approach. Analyzing the insertion processes is feasible using the OCT intensity and phase signals acquired in front of the needle tip. Especially for small tissue deformations and minor tissue ruptures, the OCT signals outperform the external measurements from

FT or US. However, the threshold-based rupture detection approach is limited considering the necessary fine-tuning of threshold values. Especially for unknown tissue structures, determining a suitable threshold is challenging.

In addition to the threshold-based rupture detection approach, we investigate deep learning for extracting time windows with rupture events from needle insertion data sets. We first analyze the rupture detection performance for different data sets from needle insertion in gelatin and porcine tissue. While the threshold-based approach mainly analyzed the OCT phase signals, processing both OCT intensity and phase signals is considered with the deep learning approach. In particular, the influence of different input signals is examined, using either phase and intensity signals separated or a combination of both. We train a Convolutional Neural Network (CNN) for rupture detection with ground truth labels extracted from US imaging and FT sensing. Table 6.3 lists the respective rupture detection performances using different combinations of input data sets and ground truth labels. Please note that no tissue-dependent data set splits are performed here, i.e., using all data sets from insertions in gelatin porcine phantoms in a random split. For all ground truth labels, the worst performances are shown when OCT intensity signals are used as input. An increase in performance is visible when either the OCT phase signals are used separately or in combination with the OCT intensity signals as input.

These results underline the importance of phase signals for interpreting relative motion patterns during needle insertion. Even though the OCT intensity signals allow an analysis of the boundary slopes during insertion, these parameters do not necessarily reflect consistent features for rupture detection. Depending on the tissue structure and stiffness, the deformation processes ahead of a rupture event might result in varying boundary slopes in the OCT intensity signals and inconsistent temporal patterns.

The variation of ground truth labels for training results in the best rupture detection performances when the labels from US and FT are combined (AND). Following the feature extraction analysis we observe different appearances of rupture events based on the modality that is used for sensing. While OCT imaging at the needle tip ensures the highest spatial sampling of tissue structures and motion patterns in a comparatively small FOV, US imaging benefits from the increased FOV but with lower spatial resolution. In addition, the FT sensing at the needle shaft is impeded by friction forces. Using the rupture events where FT and US labels match (AND) the evaluation metrics are maximized. However, the slightly lower precision values indicate that still some rupture events might be contained in the OCT signals that are not resolvable with US and FT. In the case of FT sensing, friction forces might be higher than the force differences sensed during ruptures, especially for deep insertion positions. For the analysis of US images, the processing algorithms might not be perfect and may be affected by imaging artifacts. For example, the detection of the needle tip in the US images is limited and extensively discussed in the literature [445]. In addition, defining threshold values for rupture detection from FT and US might be prone to errors.

In addition to the influence of ground truth modalities and input data sets on the detection performance, we conduct a cross-validation study with data set splits considering the different phantom types. Table 6.4 lists the metrics for insertions in the respective phantoms (A, B. C, D) excluded from the training datasets. For these evaluations, we used a Siamese network architecture that processes OCT intensity and phase signals as input signals and uses the combined ground truth label (AND). A substantial decrease in rupture detection performance is detectable for all data set splits. Especially insertions in phantoms of type C and D show a deterioration of results. This might be because these phantoms show relevant variations in tissue dynamics before and during a boundary puncture compared to phantoms A and B. Given the phantom structure, we assume several minor rupture events appear when entering the boundary from porcine tissue to softer gelatin or within the inhomogeneous tissue.

Finally, we evaluate the rupture detection performance for needle insertions in ex-situ tissue samples, i.e., liver and prostate tissue. The detection performances in Table 6.5 are separated again for different inputs (intensity, phased, or combined) and derived for using the FT signals as ground truth. Overall, the results for insertions in liver tissue are similar to those listed for the cross-validation study in Table 6.4. Moreover, processing the OCT phase signals alone or in combination with the intensity signals outperforms the predictions from using OCT intensity signals only. However, the decreased precision values again indicate a different sensitivity in rupture detection using either OCT or FT signals. This correlates to the observations when comparing the detection of major and minor rupture events in Figure 6.12 with a substantial increase in minor rupture events detected from OCT phase signals. The rupture detection performance metrics for insertion in prostate tissue vary substantially from those discussed before. In contrast to previous observations, using OCT intensity signals alone as input shows the best results. Considering the other input variations, poorer performance metrics are listed, indicating that the OCT phase signals contain less useful information for rupture detection in these prostate tissue samples. Together with the analysis of the number of ruptures extracted from OCT and FT signals in Figure 6.12, the sensitivity of OCT-based rupture detection is questionable for these tissue structures with comparatively large variations in tissue stiffness and related large force gradients. Whenever larger motion amplitudes appear between successive OCT A-scans, the evaluated phase difference might be influenced by phase wrapping effects, that have already been discussed for blood flow [446] or elastography [274] analysis with OCT. Therefore, future studies should also investigate an end-to-end learning strategy that uses not only the preprocessed OCT signals but also the raw spectral data as input. In addition, the number of data sets used for training the network architectures should be increased. Most importantly, the variation in feature patterns contained in the data sets should be high to enable a reasonable generalization capability.

Our approach to using externally applied sensing modalities as ground truth for detecting rupture events enables an analysis of how far the different modalities are exchangeable. Our results demonstrate that due to the different spatial and temporal sampling capabilities, minor and major rupture events are not necessarily detected with the same pattern from all modalities. While externally applied FT sensing is accurate in detecting major rupture events with large force gradients, the complex OCT signals at the needle tip are more sensitive in detecting minor rupture events. These minor ruptures might be correlated to small force gradients that could potentially also be impeded by friction and therefore not resolvable.

In the literature, several approaches to derive mechanical models of tissue from force data during insertion have been presented [300, 306]. However, the derivation of suitable physical models or formulae for differentiating tissue structures is often accompanied by simplifications that harm the quality of insertion analysis. Most models include simplifications that ignore specific tissue properties and impede the identification of tissue structures, e.g., for improved needle navigation.

In this thesis, we studied the capabilities of OCT imaging in front of the needle tip to distinguish tissue structures and detect rupture events during insertion. The feature extraction analysis demonstrates the correlation between specific dynamics during needle insertion and the variation in OCT intensity and phase signals. Different tissue structures are distinguishable by estimating the boundary slopes appearing in the OCT intensity data or extracting the tissue deformation from the OCT phase signal before a rupture event. These features show correlations with measurements extracted from externally applied FT sensing and US imaging. Moreover, the presented deep learning-based approach enables the detection of rupture events in various tissues. In addition to the hand-crafted feature extraction methods, deep learning has proven to be an appropriate method to extract relevant features from complex image data for rupture detection. However, the studied external modalities do not necessarily serve as reliable ground truth labels for training these architectures. This applies, in particular, to the generalization capabilities when applying the trained networks to unseen data sets. As shown for needle insertions in comparatively stiff prostate tissue, the OCT signals contain feature information that differs substantially from those insertions in porcine phantoms. Furthermore, the sensitivity of OCT-based rupture detection could be questioned for insertion in tissue with large stiffness variations. The analysis in softer tissue, e.g., ex-situ liver tissue samples, demonstrates the potential of OCT imaging at the needle tip for local fine navigation. When combined with another external sensing modality, such as FT sensing or US imaging, OCT imaging and the proposed rupture detection method could supplement and improve the navigation.

The studied rupture detection approach forms an alternative to state-of-the-art force sensing modalities applied at the needle tip, such as FBG probes [343] or probe design employing the concept of Fabry-Perot interferometry. For Fabry-Perot interferometry, OCT probes have been proposed that enable force measurements by using compressions at the needle tip as a surrogate [344, 447–449]. While these force sensing probe designs rely on measuring variations in needle geometry or compression within the probe, the OCT probe design investigated in this work uses image information from the tissue itself to estimate the mechanical properties during needle insertion. In contrast to estimating specific force values acting within the needle tip, an end-to-end detection of rupture event is proposed with no need for manual interpretation of force values. In related studies, the probe design studied in this thesis has also been used in collaborative robotic needle insertion to provide haptic feedback [400]. Moreover, a semi-supervised tissue classification approach has been studied using the complex OCT signals acquired in front of the needle tip [412].

The presented OCT probe design has the main limitation of being restricted to one-dimensional imaging in front of the needle tip during insertion. In contrast, OCT probe designs with distally attached scanning setups for two-dimensional image acquisition [355, 370] or with proximal attached and radially oriented imaging optics for the acquisition of three-dimensional image data sets [353] have been proposed. However, these probe designs come on the one hand with the limitation of either substantially increased dimension impeding hand-held applications. On the other hand, interpreting the image data of probe designs with radially oriented imaging optics for an analysis of instrument tissue interactions might be difficult. Especially when focusing on small tissue deformations. Our concept of fast acquisition of one-dimensional depth scans with a common-path optical design promises a more sensitive analysis of relative motion, especially when analyzing the OCT phase signals [450]. For probes enabling two- or three-dimensional imaging the prerequisites for interpretable phase signals introduced in Section 2.1 are not met, in particular, requiring a spatial overlap of successively acquired A-scans.

Our investigations on different image processing methods, including deep learning approaches, build an essential basis for interpreting A-scan sequences acquired during needle insertion. Deep learning approaches have also been considered to analyze boundary segmentation in OCT image data. While most studies investigated the segmentation of soft tissue layers in two- or three-dimensional images [451, 452], the analysis of tissue boundaries in a spatio-temporal representation introduced in Equation 4.4 is only investigated by a few groups [352, 412, 453]. In particular, one study focusing on boundary segmentation in A-scan sequences acquired with a similar OCT probe design has been published [352]. This study aims to localize a specific tissue membrane to navigate a needle probe.

Our approach of training a Siamese network architecture for detecting rupture events by feeding in both the OCT intensity and phase shows substantial performance improvements. Combining the information from both signal entities is particularly beneficial when analyzing tissue motion of varying amplitudes. Building on this idea, similar Siamese network architectures have also been studied for force sensing at the needle tip [454]. Moreover, complex network architectures have been applied for OCT image analysis where the intensity and phase signals are not processed as individual input but as the original complex number [455]. Also for other imaging modalities complex neural networks have been investigated to optimize the signal analysis, i.e., observed from MRI [456]. Moreover, transformer network architectures have been proposed for processing complex-valued sequences [457]. However, these network architectures require a vast amount of data sets and a more extensive training to appropriately optimize the weights. Another approach for learning-based analysis of our OCT signals could be addressed by the application of anomaly detection methods. In particular, the limited possibilities for observing ground truth annotation for a rupture event during in-vivo needle insertion could be addressed with these methods.

Chapter 8

Conclusion

This thesis investigates the characterization of soft tissue using miniaturized OCT imaging probes. Applying OCT imaging with a high spatial and temporal resolution from inside the human body promises a precise analysis of tissue properties at hand. In response to the need for both cost-effective and simple probe designs, simplified imaging optics are being studied that enable the acquisition of high-resolution one-dimensional depth scans. In particular, OCT probe designs with different orientations of the imaging axis relative to the probe shaft have been investigated in this thesis. For all these probe designs, three main challenges have been observed when acquiring sequences of one-dimensional depth scans inside the human body. First, the probe position and orientation with respect to relevant tissue structures and other instruments should be known. This is important because a spatio-temporal rigid imaging coordinate system, as is typically provided for externally applied imaging modalities, is not given. The imaging probe follows either a completely undefined motion profile within the human body or a predefined motion profile that may be impeded by anatomical or physiological constraints, such as probe or tissue motion. Second, methods for transforming sequences of one-dimensional scans into a two-, three-dimensional, or pseudo-spatial representation are needed. Therefore, approaches for deriving the spatio-temporal motion and image sampling schemes are required. This also includes considering the relative motion between the probe and the tissue. Third, data processing methods are essential for an appropriate analysis of both the OCT intensity and phase signals. Depending on the application scenarios, the information of one or both OCT signal entities might be relevant for soft tissue characterization.

The analysis of soft tissue characteristics from miniaturized imaging probes is split into estimating its morphology, elasticity, and interaction. For all application scenarios, the results of this thesis demonstrate that an extraction of tissue-specific features from OCT

A-scan sequences is possible. However, this requires precise calibration and synchronization of imaging setups. Most importantly, it is necessary to achieve a spatial localization of the imaging probe and to interpret the temporal sampling schemes.

All in all, the methods investigated in this thesis focus on estimating and analyzing motion with different imaging and sensing modalities. First, the motion of the OCT imaging probe itself is estimated. Here, external imaging modalities are applied. Additionally, image and signal processing methods are elaborated on, aiming to assess the motion of surrounding tissue structures. The studied motion patterns vary in terms of the spatial amplitudes and temporal frequencies. On the one hand, externally induced motion patterns are analyzed, such as shear waves that travel through the tissue structures. Here, comparatively small motion amplitudes appear with high temporal frequencies. Therefore, these motion patterns are mainly resolvable and analyzed in the OCT phase signals. On the other hand, relative tissue motion patterns are studied when inserting an OCT needle probe. In the literature, motion patterns occurring during needle insertion are categorized into cutting, bulk displacements, tissue deformations, and spontaneous tissue ruptures. The amplitudes and temporal schemes vary substantially for these different motion patterns. Therefore, the presented results demonstrate that a combined analysis of OCT intensity and phase signals is beneficial. Considering motion analysis, the temporal sampling frequency and motion amplitude influence each other. In general, a higher A-scan sampling frequency may be ambitious for increasing temporal sensitivity. Here, SS-OCT systems with sampling rates of up to 6 MHz are beneficial [18]. However, the increased sampling rate and also the sweeping through wavelengths might influence the OCT signal stability and Signal-to-Noise Ratio (SNR), especially when aiming for phase signal analysis [458]. Considering this trade-off in future developments of miniaturized OCT probes might be of interest.

Addressing the first research question of this thesis, MPI and DSA are studied as externally applied imaging modalities to resolve the global position of the imaging probe. Even if all of these methods deliver lower imaging resolutions than OCT, they are applicable for estimating the probe position in two or three dimensions. MPI, being an imaging modality whose translation to clinical practice is still being explored, demonstrates benefits in estimating both the probe trajectory and the vascular morphology in three dimensions. With volume rates of Hz, this modality promises capabilities as an alternative to DSA that requires bi-planar imaging sequences. However, also MRI and CT imaging evolve to enable real-time acquisition of three-dimensional image data. Aiming for functional image analysis [459, 460] but also interventional instrument navigation [461, 462]. In the future, MPI promises to be a non-invasive and fast alternative with reasonable results in instrument tracking [463–465].

In addition, the recent approaches to analyze the orientation of SPIONss [466] or actuate nanoparticles by variation of the magnetic fields are of importance for innovative methods for targeted drug delivery [467] or instrument navigation tasks [468, 469]. The experimental studies on bi-modal IVOCT and MPI imaging carried out in this thesis underline the potential benefits of interventional image analysis. Quantifying the three-dimensional vascular morphology with the investigated spatio-temporal OCT probe tracking approach might be crucial in future clinical practice, especially for analyzing vascular structures with bifurcations or tight bends. Together with deep learning based OCT image analysis, e.g., for the classification of vascular plaques [33] or the correction of NURD artifacts [402, 429], the studied approaches will further enhance interventional diagnosis and treatment planning.

Quantifying soft tissue elasticities from a miniaturized OCE probe by evaluating shear wave propagation builds the second milestone of this thesis. The challenges addressed when focusing on this second research question are twofold. First, aim for a simple probe design that limits the image acquisition to one dimension. Thus, only a sampling of the temporal shear wave characteristics is possible. Second, estimating elasticity from an OCE probe that is inserted and in direct contact with the tissue. While other OCE probe concepts are designed for contactless examination of tissue [273], this thesis aims for a reproducible elasticity quantification for various probe positions inside the tissue. Different experimental setups have been presented in the literature, utilizing shear wave excitation and imaging with a rigid position and orientation relative to each other. For these setups, it has been assumed that the spatial and temporal shear wave sampling schemes are constant. However, when applying OCE probes inside the tissue, these assumptions are no longer valid. The experimental studies in this thesis highlight the significant impact of an unknown and potentially unstable distance between wave excitation and imaging position, as well as the limitation to one-dimensional imaging, on elasticity quantification. Therefore, a novel DF-OCE probe concept was proposed in this thesis. This probe design enables a reproducible quantification of soft tissue elasticity. Most importantly, there are no requirements for calibrating the distance between excitation and imaging. As long as the shear wave travels almost parallel to the probe shaft and the distance between the two embedded imaging optics is known, the shear wave velocity can be estimated for various excitation positions. In particular, this approach offers a significant benefit for estimating local elasticity values. Using the proposed dual-fiber design, the wave velocity is estimated solely based on the local tissue properties. In contrast, for SF-OCE probe designs, only an average elasticity estimation evaluating the shear wave propagation over the whole distance between excitation and imaging is possible. This is especially relevant and creates a bias in SF-OCE elasticity quantification for inhomogeneous tissue structures, where the shear wave travels at different velocities. Although this thesis primarily employs conventional image processing methods for quantifying shear wave velocities, the application of deep learning methods may be promising for future work. Especially approaches focusing on end-to-end learning of elasticity values [289] are beneficial in reducing bias from the assumed linear relationship between elasticity and the shear wave velocity introduced in Equation 3.2. Beyond two-dimensional convolutional network architectures, recurrent or transformer architectures [470] are of particular interest due to their potential to efficiently process and learn the temporal patterns contained in the OCT image data.

The third research question of this thesis focused on characterizing tissue structures during epidural punctures. For the studied common-path OCT probe design, the effort in optimizing the optical beam is minimized by simply cleaving the end of the optical fiber and embedding this in a medical needle. With this design, one-dimensional OCT depth scans are sequentially acquired in front of the needle tip during needle insertion. Consequently, OCT signals in a spatio-temporal fashion follow that are not directly transformable into a two- or even three-dimensional representation. While different approaches for the interpretation of external sensing methods have been proposed in the literature [38, 310], the interpretation of OCT data sets is rarely discussed. The analysis of complex OCT data sets has, in this thesis, therefore been split into two parts. First, a correlation analysis of OCT signals to externally applied sensing modalities, i.e., US imaging and FT sensing, is conducted. Here, various features extracted from the OCT intensity and phase signals were studied to interpret the data and characterize the mechanics during needle insertion. Second, a deep learning approach was examined to extract rupture events. These events were associated with the boundaries of subsequent tissue structures. An analysis of the number of minor and major rupture events during needle insertion also demonstrated the possibilities for tissue characterization. The experimental studies highlight the different ranges of the applied sensing modalities. While external force sensing may be applicable for detecting major rupture events in cases of significant force differences, OCT signals captured at the needle tip are sensitive to both major ruptures, based on intensity, and minor ruptures, based on phase signals. The performance of the presented Siamese network architecture for detecting rupture events, which leverages both OCT signal entities, underlines these findings.

Concluding the findings of this thesis, the application of miniaturized OCT imaging probes inside the human body creates a promising approach to characterizing the properties of soft tissue. While studies on morphological tissue reconstruction and interpretation from OCT image data have been discussed for various application scenarios, the innovative

OCT probe designs and image processing methods for estimating soft tissue elasticity and instrument interactions studied represent an essential milestone for future research. Utilizing miniaturized OCT probes and analyzing the spatio-temporal patterns of both intensity and phase signals from high-resolution depth scans demonstrates a precise approach for localizing and characterizing soft tissue in a minimally invasive manner.

Bibliography

[1] R. Akhtar, M. J. Sherratt, J. K. Cruickshank, and B. Derby, "Characterizing the elastic properties of tissues," *Materials Today*, vol. 14, no. 3, pp. 96–105, 2011.

[2] R. Chivers, "Tissue characterization," *Ultrasound in Medicine & Biology*, vol. 7, no. 1, pp. 1–20, 1981.

[3] H. Shimano, J. D. Horton, R. E. Hammer, I. Shimomura, M. S. Brown, and J. L. Goldstein, "Overproduction of cholesterol and fatty acids causes massive liver enlargement in transgenic mice expressing truncated srebp-1a," *The Journal of Clinical Investigation*, vol. 98, no. 7, pp. 1575–1584, 1996.

[4] A. B., S. Rao, and H. J. Pandya, "Engineering approaches for characterizing soft tissue mechanical properties: A review," *Clinical Biomechanics*, vol. 69, pp. 127–140, 2019.

[5] J. Konstantinova, M. Li, G. Mehra, P. Dasgupta, K. Althoefer, and T. Nanayakkara, "Behavioral characteristics of manual palpation to localize hard nodules in soft tissues," *IEEE Transactions on Biomedical Engineering*, vol. 61, no. 6, pp. 1651–1659, 2014.

[6] M. L. Varela, M. Mogildea, I. Moreno, and A. Lopes, "Acute inflammation and metabolism," *Inflammation*, vol. 41, no. 4, pp. 1115–1127, 2018.

[7] G. M. Fomovsky and J. W. Holmes, "Evolution of scar structure, mechanics, and ventricular function after myocardial infarction in the rat," *American Journal of Physiology-Heart and Circulatory Physiology*, vol. 298, no. 1, H221–H228, 2010, PMID: 19897714.

[8] S. Surti, V. Viswanath, M. E. Daube-Witherspoon, M. Conti, M. E. Casey, and J. S. Karp, "Benefit of improved performance with state-of-the art digital pet/ct for lesion detection in oncology," *Journal of Nuclear Medicine*, vol. 61, no. 11, pp. 1684–1690, 2020.

[9] T. Wan, H. Feng, C. Tong, D. Li, and Z. Qin, "Automated identification and grading of coronary artery stenoses with x-ray angiography," *Computer Methods and Programs in Biomedicine*, vol. 167, pp. 13–22, 2018.

[10] D. Ardila, A. P. Kiraly, S. Bharadwaj, B. Choi, J. J. Reicher, L. Peng, D. Tse, M. Etemadi, W. Ye, G. Corrado, D. P. Naidich, and S. Shetty, "End-to-end lung cancer screening with three-dimensional deep learning on low-dose chest computed tomography," *Nature Medicine*, vol. 25, no. 6, pp. 954–961, 2019.

[11] P. Pattanayak and D. A. Bleumke, "Tissue characterization of the myocardium: State of the art characterization by magnetic resonance and computed tomography imaging," *Radiologic Clinics*, vol. 53, no. 2, pp. 413–423, 2021/08/31 2015.

[12] C. Schichor, N. Terpolilli, J. Thorsteinsdottir, and J.-C. Tonn, "Intraoperative computed tomography in cranial neurosurgery," *Neurosurgery Clinics*, vol. 28, no. 4, pp. 595–602, 2017.

[13] T. M. Moriarty, R. Kikinis, F. A. Jolesz, P. M. Black, and E. Alexander, "Magnetic resonance imaging therapy: Intraoperative mr imaging," *Neurosurgery Clinics of North America*, vol. 7, no. 2, pp. 323–331, 1996.

[14] C. Roder, P. Haas, M. Tatagiba, U. Ernemann, and B. Bender, "Technical limitations and pitfalls of diffusion-weighted imaging in intraoperative high-field mri," *Neurosurgical Review*, vol. 44, no. 1, pp. 327–334, 2021.

[15] J. Chevrie, A. Krupa, and M. Babel, "Real-time teleoperation of flexible beveled-tip needle insertion using haptic force feedback and 3d ultrasound guidance," in *2019 international conference on robotics and automation (ICRA)*, IEEE, 2019, pp. 2700–2706.

[16] O. Carrasco-Zevallos, B. Keller, C. Viehland, L. Shen, G. Waterman, B. Todorich, C. Shieh, P. Hahn, S. Farsiu, A. Kuo, et al., "Live volumetric (4d) visualization and guidance of in vivo human ophthalmic surgery with intraoperative optical coherence tomography," *Scientific reports*, vol. 6, no. 1, p. 31 689, 2016.

[17] C. Kut, K. L. Chaichana, J. Xi, S. M. Raza, X. Ye, E. R. McVeigh, F. J. Rodriguez, A. Quiñones-Hinojosa, and X. Li, "Detection of human brain cancer infiltration ex vivo and in vivo using quantitative optical coherence tomography," *Science translational medicine*, vol. 7, no. 292, 292ra100–292ra100, 2015.

[18] T. Klein and R. Huber, "High-speed oct light sources and systems," *Biomedical optics express*, vol. 8, no. 2, pp. 828–859, 2017.

[19] J. A. Linehan, E. R. Bracamonte, L. P. Hariri, M. H. Sokoloff, P. S. Rice, J. K. Barton, and M. M. Nguyen, "Feasibility of optical coherence tomography imaging to characterize renal neoplasms: Limitations in resolution and depth of penetration," *BJU international*, vol. 108, no. 11, pp. 1820–1824, 2011.

[20] C. Shi, X. Luo, P. Qi, T. Li, S. Song, Z. Najdovski, T. Fukuda, and H. Ren, "Shape sensing techniques for continuum robots in minimally invasive surgery: A survey," *IEEE Transactions on Biomedical Engineering*, vol. 64, no. 8, pp. 1665–1678, 2016.

[21] N. Bandari, J. Dargahi, and M. Packirisamy, “Miniaturized optical force sensor for minimally invasive surgery with learning-based nonlinear calibration,” *IEEE Sensors Journal*, vol. 20, no. 7, pp. 3579–3592, 2019.

[22] Z. Fu, Z. Jin, C. Zhang, Z. He, Z. Zha, C. Hu, T. Gan, Q. Yan, P. Wang, and X. Ye, “The future of endoscopic navigation: A review of advanced endoscopic vision technology,” *IEEE Access*, vol. 9, pp. 41 144–41 167, 2021.

[23] D. P. Steinfort, Y. H. Khor, R. L. Manser, and L. B. Irving, “Radial probe endobronchial ultrasound for the diagnosis of peripheral lung cancer: Systematic review and meta-analysis,” *European Respiratory Journal*, vol. 37, no. 4, pp. 902–910, 2011.

[24] D. B. Ellebrecht, S. Latus, A. Schlaefer, T. Keck, and N. Gessert, “Towards an optical biopsy during visceral surgical interventions,” *Visceral medicine*, vol. 36, no. 2, pp. 70–79, 2020.

[25] C. W. Tsao, A. W. Aday, Z. I. Almarzooq, C. A. Anderson, P. Arora, C. L. Avery, C. M. Baker-Smith, A. Z. Beaton, A. K. Boehme, A. E. Buxton, et al., “Heart disease and stroke statistics—2023 update: A report from the american heart association,” *Circulation*, vol. 147, no. 8, e93–e621, 2023.

[26] A. V. Finn, F. D. Kolodgie, J. Harnek, L. J. Guerrero, E. Acampado, K. Tefera, K. Skorija, D. K. Weber, H. K. Gold, and R. Virmani, “Differential response of delayed healing and persistent inflammation at sites of overlapping sirolimus- or paclitaxel-eluting stents,” *Circulation*, vol. 112, no. 2, pp. 270–278, 2005.

[27] C. W. Hwang, D. Wu, and E. R. Edelman, “Physiological transport forces govern drug distribution for stent-based delivery,” *Circulation*, vol. 104, no. 5, pp. 600–605, 2001.

[28] A. Kastrati, A. Dibra, S. Eberle, J. Mehilli, J. Suárez de Lezo, J.-J. Goy, K. Ulm, and A. Schömig, “Sirolimus-eluting stents vs paclitaxel-eluting stents in patients with coronary artery disease: Meta-analysis of randomized trials,” *JAMA*, vol. 294, no. 7, pp. 819–825, 2005.

[29] M. V. Peycheva, Z. I. Zahariev, K. G. Velkova, and L. Chervenkov, “Characteristics of unstable carotid plaques - new image modalities,” *Folia Medica*, vol. 61, no. 1, pp. 26–33, 2019.

[30] P. A. McCullough, “Contrast-induced acute kidney injury,” *Journal of the American College of Cardiology*, vol. 51, no. 15, pp. 1419–1428, 2008.

[31] R. W. Katzberg and C. Haller, “Contrast-induced nephrotoxicity: Clinical landscape,” *Kidney international. Supplement*, vol. 69, no. 100, S3–7, 2006.

[32] J. M. Lee et al., “Intravascular imaging-guided or angiography-guided complex pci,” *The New England journal of medicine*, 2023.

[33] N. Gessert, M. Lutz, M. Heyder, S. Latus, D. M. Leistner, Y. S. Abdelwahed, and A. Schlaefer, "Automatic plaque detection in ivoct pullbacks using convolutional neural networks," *IEEE transactions on medical imaging*, vol. 38, no. 2, pp. 426–434, 2018.

[34] N. R. Pillalamarri, S. S. Patnaik, S. Piskin, P. Gueldner, and E. A. Finol, "Ex vivo regional mechanical characterization of porcine pulmonary arteries," *Experimental Mechanics*, vol. 61, no. 1, pp. 285–303, 2021.

[35] G. Sommer, P. Regitnig, L. Költringer, and G. A. Holzapfel, "Biaxial mechanical properties of intact and layer-dissected human carotid arteries at physiological and supraphysiological loadings," *American Journal of Physiology-Heart and Circulatory Physiology*, vol. 298, no. 3, H898–912, 2010.

[36] J. Ormachea and K. J. Parker, "Elastography imaging: The 30 year perspective," *Physics in Medicine & Biology*, Nov. 2020.

[37] C. Sun, B. Standish, and V. X. D. Yang, "Optical coherence elastography: Current status and future applications," *Journal of Biomedical Optics*, vol. 16, no. 4, p. 043 001, 2011.

[38] Z. Cheng, M. Koskinopoulou, S. Bano, D. Stoyanov, T. R. Savarimuthu, and L. S. Mattos, "Sensing technologies for guidance during needle-based interventions," *IEEE Transactions on Instrumentation and Measurement*, 2024.

[39] M. Nagel, M. Hoheisel, R. Petzold, W. A. Kalender, and U. H. Krause, "Needle and catheter navigation using electromagnetic tracking for computer-assisted c-arm ct interventions," in *Medical Imaging 2007: Visualization and Image-Guided Procedures*, SPIE, vol. 6509, 2007, pp. 184–192.

[40] N. Abolhassani and R. V. Patel, "Teleoperated master-slave needle insertion," *The International Journal of Medical Robotics and Computer Assisted Surgery*, vol. 5, no. 4, pp. 398–405, 2009.

[41] S. Aumann, S. Donner, J. Fischer, and F. Müller, "Optical coherence tomography (oct): Principle and technical realization," *High resolution imaging in microscopy and ophthalmology: new frontiers in biomedical optics*, pp. 59–85, 2019.

[42] J. Fujimoto and W. Drexler, "Introduction to optical coherence tomography," in *Optical coherence tomography: Technology and applications*, Springer, 2008, pp. 1–45.

[43] J. A. Izatt and M. A. Choma, "Theory of optical coherence tomography," *Optical Coherence Tomography: Technology and Applications*, pp. 47–72, 2008.

[44] B. Liu and M. E. Brezinski, "Theoretical and practical considerations on detection performance of time domain, fourier domain, and swept source optical coherence tomography," *Journal of biomedical optics*, vol. 12, no. 4, pp. 044 007–044 007, 2007.

[45] J. Qiu, T. Han, Z. Liu, J. Meng, and Z. Ding, "Uniform focusing with an extended depth range and increased working distance for optical coherence tomography by an ultrathin monolith fiber probe," *Optics Letters*, vol. 45, no. 4, pp. 976–979, 2020.

[46] J. A. Izatt, M. D. Kulkarni, H.-W. Wang, K. Kobayashi, and M. V. Sivak, "Optical coherence tomography and microscopy in gastrointestinal tissues," *IEEE Journal of Selected topics in quantum electronics*, vol. 2, no. 4, pp. 1017–1028, 1996.

[47] J. G. Fujimoto, "Optical coherence tomography for ultrahigh resolution in vivo imaging," *Nature biotechnology*, vol. 21, no. 11, pp. 1361–1367, 2003.

[48] T. Wang, W. Wieser, G. Springeling, R. Beurskens, C. T. Lancee, T. Pfeiffer, A. F. Van Der Steen, R. Huber, and G. v. Soest, "Intravascular optical coherence tomography imaging at 3200 frames per second," *Optics letters*, vol. 38, no. 10, pp. 1715–1717, 2013.

[49] K. Wiesauer, M. Pircher, E. Götzinger, S. Bauer, R. Engelke, G. Ahrens, G. Grützner, C. K. Hitzenberger, and D. Stifter, "En-face scanning optical coherence tomography with ultra-high resolution for material investigation," *Optics Express*, vol. 13, no. 3, pp. 1015–1024, 2005.

[50] B. Wolff, A. Matet, V. Vasseur, J.-A. Sahel, and M. Mauget-Faÿsse, "En face oct imaging for the diagnosis of outer retinal tubulations in age-related macular degeneration," *Journal of ophthalmology*, vol. 2012, no. 1, p. 542 417, 2012.

[51] N. Iftimia, S. Cizginer, V. Deshpande, M. Pitman, S. Tatli, N.-A. Iftimia, D. X. Hammer, M. Mujat, T. Ustun, R. D. Ferguson, et al., "Differentiation of pancreatic cysts with optical coherence tomography (oct) imaging: An ex vivo pilot study," *Biomedical optics express*, vol. 2, no. 8, pp. 2372–2382, 2011.

[52] J. G. Fujimoto, W. Drexler, J. S. Schuman, and C. K. Hitzenberger, "Optical coherence tomography (oct) in ophthalmology: Introduction," *Optics express*, vol. 17, no. 5, pp. 3978–3979, 2009.

[53] A. M. Hagag, S. S. Gao, Y. Jia, and D. Huang, "Optical coherence tomography angiography: Technical principles and clinical applications in ophthalmology," *Taiwan journal of ophthalmology*, vol. 7, no. 3, pp. 115–129, 2017.

[54] Y. Wu, J. Xi, L. Huo, J. Padvorac, E. J. Shin, S. A. Giday, A. A. Lennon, M. I. F. Canto, J. H. Hwang, and X. Li, "Robust high-resolution fine oct needle for side-viewing interstitial tissue imaging," *IEEE Journal of Selected Topics in Quantum Electronics*, vol. 16, no. 4, pp. 863–869, 2010.

[55] G. Guagliumi and V. Sirbu, "Optical coherence tomography: High resolution intravascular imaging to evaluate vascular healing after coronary stenting," *Catheterization and Cardiovascular Interventions*, vol. 72, no. 2, pp. 237–247, 2008.

[56] K. Beaudette, J. Li, J. Lamarre, L. Majeau, and C. Boudoux, "Double-clad fiber-based multifunctional biosensors and multimodal bioimaging systems: Technology and applications," *Biosensors*, vol. 12, no. 2, p. 90, 2022.

[57] J. Amorebieta, J. Pereira, G. Durana, C. Franciscangelis, A. Ortega-Gomez, J. Zubia, J. Villatoro, and W. Margulis, "Twin-core fiber sensor integrated in laser cavity," *Scientific Reports*, vol. 12, no. 1, p. 11 797, 2022.

[58] J. Wang, M. Hosoda, D. M. Tshikudi, Z. Hajjarian, and S. K. Nadkarni, "Intraluminal laser speckle rheology using an omni-directional viewing catheter," *Biomedical Optics Express*, vol. 8, no. 1, pp. 137–150, 2017.

[59] J. Xu, S. Song, Y. Li, and R. K. Wang, "Complex-based oct angiography algorithm recovers microvascular information better than amplitude-or phase-based algorithms in phase-stable systems," *Physics in Medicine & Biology*, vol. 63, no. 1, p. 015 023, 2017.

[60] W. Wieser, B. R. Biedermann, T. Klein, C. M. Eigenwillig, and R. Huber, "Multi-megahertz oct: High quality 3d imaging at 20 million a-scans and 4.5 gvoxels per second," *Optics express*, vol. 18, no. 14, pp. 14 685–14 704, 2010.

[61] C. Li, G. Guan, R. Reif, Z. Huang, and R. K. Wang, "Determining elastic properties of skin by measuring surface waves from an impulse mechanical stimulus using phase-sensitive optical coherence tomography," *Journal of The Royal Society Interface*, vol. 9, no. 70, pp. 831–841, 2012.

[62] M. S. Hepburn, P. Wijesinghe, L. Chin, and B. F. Kennedy, "Analysis of spatial resolution in phase-sensitive compression optical coherence elastography," *Biomedical optics express*, vol. 10, no. 3, pp. 1496–1513, 2019.

[63] Y. Zhang, B. Dong, Y. Bai, S. Ye, Z. Lei, and Y. Zhou, "Measurement of depth-resolved thermal deformation distribution using phase-contrast spectral optical coherence tomography," *Optics express*, vol. 23, no. 21, pp. 28 067–28 075, 2015.

[64] Y. Zhao, Z. Chen, C. Saxer, S. Xiang, J. F. de Boer, and J. S. Nelson, "Phase-resolved optical coherence tomography and optical doppler tomography for imaging blood flow in human skin with fast scanning speed and high velocity sensitivity," *Optics letters*, vol. 25, no. 2, pp. 114–116, 2000.

[65] J. Walther, G. Mueller, H. Morawietz, and E. Koch, "Analysis of in vitro and in vivo bidirectional flow velocities by phase-resolved doppler fourier-domain oct," *Sensors and Actuators A: Physical*, vol. 156, no. 1, pp. 14–21, 2009.

[66] B. F. Kennedy, K. M. Kennedy, A. L. Oldenburg, S. G. Adie, S. A. Boppart, and D. D. Sampson, "Optical coherence tomography: Technology and applications," in Springer, 2015, ch. Optical coherence elastography.

[67] B. J. Vakoc, G. J. Tearney, and B. E. Bouma, "Statistical properties of phase-decorrelation in phase-resolved doppler optical coherence tomography," *IEEE Transactions on Medical Imaging*, vol. 28, no. 6, pp. 814–821, 2009.

[68] S. Song, W. Wei, B.-Y. Hsieh, I. Pelivanov, T. T. Shen, M. O'Donnell, and R. K. Wang, "Strategies to improve phase-stability of ultrafast swept source optical coherence tomography for single shot imaging of transient mechanical waves at 16kHz frame rate," *Applied Physics Letters*, vol. 108, no. 19, p. 191 104, May 2016.

[69] M. S. Hepburn, K. Y. Foo, P. Wijesinghe, P. R. T. Munro, L. Chin, and B. F. Kennedy, "Speckle-dependent accuracy in phase-sensitive optical coherence tomography," *Optics Express*, vol. 29, no. 11, pp. 16 950–16 968, May 2021.

[70] A. Szkulmowska, M. Szkulmowski, A. Kowalczyk, and M. Wojtkowski, "Phase-resolved doppler optical coherence tomography—limitations and improvements," *Optics letters*, vol. 33, no. 13, pp. 1425–1427, 2008.

[71] Y.-J. Hong, S. Makita, F. Jaillon, M. J. Ju, E. J. Min, B. H. Lee, M. Itoh, M. Miura, and Y. Yasuno, "High-penetration swept source doppler optical coherence angiography by fully numerical phase stabilization," *Optics Express*, vol. 20, no. 3, pp. 2740–2760, 2012.

[72] Y. Ma, X. Chen, W. Zhu, X. Cheng, D. Xiang, and F. Shi, "Speckle noise reduction in optical coherence tomography images based on edge-sensitive cgan," *Biomedical optics express*, vol. 9, no. 11, pp. 5129–5146, 2018.

[73] Y. Zhou, K. Yu, M. Wang, Y. Ma, Y. Peng, Z. Chen, W. Zhu, F. Shi, and X. Chen, "Speckle noise reduction for oct images based on image style transfer and conditional gan," *IEEE Journal of Biomedical and Health Informatics*, vol. 26, no. 1, pp. 139–150, 2022.

[74] S. Ma, R. Wang, S. Qiu, R. Li, Q. Yue, Q. Sun, L. Chen, F. Yan, G.-Z. Yang, and Y. Feng, "Mr elastography with optimization-based phase unwrapping and traveling wave expansion-based neural network (twenn)," *IEEE Transactions on Medical Imaging*, vol. 42, no. 9, pp. 2631–2642, 2023.

[75] T. L. Szabo, *Diagnostic ultrasound imaging: inside out*. Academic press, 2013.

[76] V. Chan and A. Perlas, "Basics of ultrasound imaging," *Atlas of ultrasound-guided procedures in interventional pain management*, pp. 13–19, 2011.

[77] K.-V. Jenderka and S. Delorme, "Diagnostischer ultraschall," *Medizinische Physik: Grundlagen–Bildgebung–Therapie–Technik*, pp. 285–305, 2018.

[78] O. Dössel, *Bildgebende Verfahren in der Medizin*. Springer, 2000.

[79] A. Manbachi and R. S. Cobbold, "Development and application of piezoelectric materials for ultrasound generation and detection," *Ultrasound*, vol. 19, no. 4, pp. 187–196, 2011.

[80] R. Lerch, G. Sessler, and D. Wolf, *Technische Akustik: Grundlagen und Anwendungen.* Springer-Verlag, 2009.

[81] H. Kim, J. Yoo, D. Heo, Y.-S. Seo, H. G. Lim, and H. H. Kim, "High-attenuation backing layer for miniaturized ultrasound imaging transducer," *IEEE transactions on ultrasonics, ferroelectrics, and frequency control*, vol. 69, no. 6, pp. 1960–1969, 2022.

[82] C. Hou, C. Fei, Z. Li, S. Zhang, J. Man, D. Chen, R. Wu, Di Li, Y. Yang, and W. Feng, "Optimized backing layers design for high frequency broad bandwidth ultrasonic transducer," *IEEE Transactions on Biomedical Engineering*, vol. 69, no. 1, pp. 475–481, 2022.

[83] A. Ng and J. Swanevelder, "Resolution in ultrasound imaging," *Continuing Education in Anaesthesia, Critical Care & Pain*, vol. 11, no. 5, pp. 186–192, 2011.

[84] S. Smith, G. Trahey, and O. Von Ramm, "Phased array ultrasound imaging through planar tissue layers," *Ultrasound in medicine & biology*, vol. 12, no. 3, pp. 229–243, 1986.

[85] K. Hynynen and R. M. Jones, "Image-guided ultrasound phased arrays are a disruptive technology for non-invasive therapy," *Physics in Medicine & Biology*, vol. 61, no. 17, R206, 2016.

[86] L. E. Derchi, G. Serafini, N. Gandolfo, N. G. Gandolfo, and C. Martinoli, "Ultrasound in gynecology," *European radiology*, vol. 11, pp. 2137–2155, 2001.

[87] K. Hammond, J. Mampilly, F. A. Laghi, A. Goyal, E. G. Collins, C. McBurney, A. Jubran, and M. J. Tobin, "Validity and reliability of rectus femoris ultrasound measurements: Comparison of curved-array and linear-array transducers," *Journal of Rehabilitation Research and Development*, vol. 51, no. 7, p. 1155, 2014.

[88] Z. Zhang, M. Su, F. Li, R. Liu, R. Cai, G. Li, Q. Jiang, H. Zhong, T. R. Shrout, S. Zhang, H. Zheng, and W. Qiu, "New sm-pmn-pt ceramic-based 2-d array for low-intensity ultrasound therapy application," *IEEE transactions on ultrasonics, ferroelectrics, and frequency control*, vol. 67, no. 10, pp. 2085–2094, 2020.

[89] K. Yasufuku, M. Chiyo, E. Koh, Y. Moriya, A. Iyoda, Y. Sekine, K. Shibuya, T. Iizasa, and T. Fujisawa, "Endobronchial ultrasound guided transbronchial needle aspiration for staging of lung cancer," *Lung cancer*, vol. 50, no. 3, pp. 347–354, 2005.

[90] Y. Qiu, J. V. Gigliotti, M. Wallace, F. Griggio, C. E. M. Demore, S. Cochran, and S. Trolier-McKinstry, "Piezoelectric micromachined ultrasound transducer (pmut) ar-

rays for integrated sensing, actuation and imaging," *Sensors (Basel, Switzerland)*, vol. 15, no. 4, pp. 8020–8041, 2015.

[91] P. Lin, Y. Zhu, C. Fei, D. Chen, Z. Chen, C. Zheng, S. Zhang, Di Li, W. Feng, Y. Yang, and C. Chai, "Multilayer stairstep piezoelectric structure design for ultrabroad-bandwidth ultrasonic transducer," *IEEE Sensors Journal*, vol. 21, no. 18, pp. 19 889–19 895, 2021.

[92] H. S. Lay, B. F. Cox, V. Seetohul, C. E. M. Demore, and S. Cochran, "Design and simulation of a ring-shaped linear array for microultrasound capsule endoscopy," *IEEE transactions on ultrasonics, ferroelectrics, and frequency control*, vol. 65, no. 4, pp. 589–599, 2018.

[93] H.-W. Kim, H. Wu, and X. Jiang, "Miniaturized sub-megahertz focused ultrasound transducer composed of multilayer hard pzt ceramics," in *2018 IEEE International Ultrasonics Symposium (IUS)*, IEEE, 2018, pp. 1–4.

[94] A. A. Oglat, M. Matjafri, N. Suardi, M. A. Oqlat, M. A. Abdelrahman, and A. A. Oqlat, "A review of medical doppler ultrasonography of blood flow in general and especially in common carotid artery," *Journal of medical ultrasound*, vol. 26, no. 1, pp. 3–13, 2018.

[95] G. F. Pinton, J. J. Dahl, and G. E. Trahey, "Rapid tracking of small displacements with ultrasound," *IEEE transactions on ultrasonics, ferroelectrics, and frequency control*, vol. 53, no. 6, pp. 1103–1117, 2006.

[96] T. Loupas, J. Powers, and R. Gill, "An axial velocity estimator for ultrasound blood flow imaging, based on a full evaluation of the doppler equation by means of a two-dimensional autocorrelation approach," *IEEE Transactions on Ultrasonics, Ferroelectrics, and Frequency Control*, vol. 42, no. 4, pp. 672–688, 1995.

[97] N. T. Schiefler JR, J. M. Maia, F. K. Schneider, A. J. Zimbico, A. A. Assef, and E. T. Costa, "Generation and analysis of ultrasound images using plane wave and sparse arrays techniques," *Sensors (Basel, Switzerland)*, vol. 18, no. 11, 2018.

[98] B. Abhisheka, S. K. Biswas, B. Purkayastha, D. Das, and A. Escargueil, "Recent trend in medical imaging modalities and their applications in disease diagnosis: A review," *Multimedia Tools and Applications*, vol. 83, no. 14, pp. 43 035–43 070, 2024.

[99] S. R. Karanam, Y. Srinivas, and S. Chakravarty, "A systematic review on approach and analysis of bone fracture classification," *Materials Today: Proceedings*, vol. 80, pp. 2557–2562, 2023.

[100] G. Gavelli and E. Giampalma, "Sensitivity and specificity of chest x-ray screening for lung cancer," *Cancer*, vol. 89, no. S11, pp. 2453–2456, 2000.

[101] H. Chen, M. M. Rogalski, and J. N. Anker, “Advances in functional x-ray imaging techniques and contrast agents,” *Physical Chemistry Chemical Physics*, vol. 14, no. 39, pp. 13 469–13 486, 2012.

[102] R. Tanaka, “Dynamic chest radiography: Flat-panel detector (fpd) based functional x-ray imaging,” *Radiological physics and technology*, vol. 9, no. 2, pp. 139–153, 2016.

[103] C. J. Allen, K. Guha, and R. Sharma, “How to improve time to diagnosis in acute heart failure–clinical signs and chest x-ray,” *Cardiac failure review*, vol. 1, no. 2, p. 69, 2015.

[104] J. A. Seibert, “X-ray imaging physics for nuclear medicine technologists. part 1: Basic principles of x-ray production,” *Journal of nuclear medicine technology*, vol. 32, no. 3, pp. 139–147, 2004.

[105] J. T. Bushberg and J. M. Boone, *The essential physics of medical imaging.* Lippincott Williams & Wilkins, 2011.

[106] D. F. Jackson and D. J. Hawkes, “X-ray attenuation coefficients of elements and mixtures,” *Physics Reports*, vol. 70, no. 3, pp. 169–233, 1981.

[107] M. Daly, J. Siewerdsen, Y. Cho, D. Jaffray, and J. Irish, “Geometric calibration of a mobile c-arm for intraoperative cone-beam ct,” *Medical physics*, vol. 35, no. 5, pp. 2124–2136, 2008.

[108] S. Celi, N. Martini, L. Emilio Pastormerlo, V. Positano, and S. Berti, “Multimodality imaging for interventional cardiology,” *Current pharmaceutical design*, vol. 23, no. 22, pp. 3285–3300, 2017.

[109] C. P. Derdeyn, C. J. Moran, D. Cross, R. Grubb, and R. Dacey, “Intraoperative digital subtraction angiography: A review of 112 consecutive examinations.,” *American journal of neuroradiology*, vol. 16, no. 2, pp. 307–318, 1995.

[110] A. Brost, N. Strobel, L. Yatziv, W. Gilson, B. Meyer, J. Hornegger, J. Lewin, and F. Wacker, “Accuracy of x-ray image-based 3d localization from two c-arm views: A comparison between an ideal system and a real device,” in *Medical Imaging 2009: Visualization, Image-Guided Procedures, and Modeling*, SPIE, vol. 7261, 2009, pp. 650–659.

[111] E. J. Duffis, P. Jethwa, G. Gupta, K. Bonello, C. D. Gandhi, and C. J. Prestigiacomo, “Accuracy of computed tomographic angiography compared to digital subtraction angiography in the diagnosis of intracranial stenosis and its impact on clinical decision-making,” *Journal of Stroke and Cerebrovascular Diseases*, vol. 22, no. 7, pp. 1013–1017, 2013.

[112] M. Andreucci, R. Solomon, and A. Tasanarong, “Side effects of radiographic contrast media: Pathogenesis, risk factors, and prevention,” *BioMed Research International*, vol. 2014, p. 741 018, 2014.

[113] J. W. M. Bulte, “Superparamagnetic iron oxides as mpi tracers: A primer and review of early applications,” *Advanced Drug Delivery Reviews*, vol. 138, pp. 293–301, 2019.

[114] E. A. Neuwelt, B. E. Hamilton, C. G. Varallyay, W. R. Rooney, R. D. Edelman, P. M. Jacobs, and S. G. Watnick, “Ultrasmall superparamagnetic iron oxides (USPIOs): A future alternative magnetic resonance (MR) contrast agent for patients at risk for nephrogenic systemic fibrosis (NSF)?” *Kidney International*, vol. 75, no. 5, pp. 465–474, 2009.

[115] J. Franke, N. Baxan, H. Lehr, U. Heinen, S. Reinartz, J. Schnorr, M. Heidenreich, F. Kiessling, and V. Schulz, “Hybrid mpi-mri system for dual-modal in situ cardiovascular assessments of real-time 3d blood flow quantification—a pre-clinical in vivo feasibility investigation,” *IEEE Transactions on Medical Imaging*, vol. 39, no. 12, pp. 4335–4345, 2020.

[116] F. Griese, T. Knopp, R. Werner, A. Schlaefer, and M. Möddel, “Submillimeter-accurate marker localization within low gradient magnetic particle imaging tomograms,” *International journal on magnetic particle imaging*, vol. 3, no. 1, 2017.

[117] E. E. Mason, E. Barcikowski, J. Carl, M. Chandeeing, B. Davison, B. Fellows, W. Fetsch, K. Fields, J. Greve, J. J. Konkle, et al., “Preliminary results: Large bore clinical mpi system imaging human head-sized fovs,” *International Journal on Magnetic Particle Imaging*, vol. 10, no. 1 Suppl 1, 2024.

[118] M. Gräser, F. Thieben, P. Szwargulski, F. Werner, N. Gdaniec, M. Boberg, F. Griese, M. Möddel, P. Ludewig, D. Van De Ven, et al., “Human-sized magnetic particle imaging for brain applications,” *Nature communications*, vol. 10, no. 1, p. 1936, 2019.

[119] F. Thieben, F. Mohn, F. Foerger, N. Hackelberg, J.-P. Scheel, M. Graeser, and T. Knopp, “Safe and rapid 3d imaging: Upgrade of a human-sized brain mpi system,” *International journal on magnetic particle imaging*, vol. 9, no. 1, 2023.

[120] P. Vogel, M. Rückert, C. Greiner, J. Günther, T. Reichl, T. Kampf, T. Bley, V. Behr, and S. Herz, “Impi: Portable human-sized magnetic particle imaging scanner for real-time endovascular interventions,” *Scientific Reports*, vol. 13, no. 1, p. 10 472, 2023.

[121] M. H. Pablico-Lansigan, S. F. Situ, and A. C. S. Samia, “Magnetic particle imaging: Advancements and perspectives for real-time in vivo monitoring and image-guided therapy,” *Nanoscale*, vol. 5, no. 10, pp. 4040–4055, 2013.

[122] M. P. Bui, T.-A. Le, and J. Yoon, “A magnetic particle imaging-based navigation platform for magnetic nanoparticles using interactive manipulation of a virtual field free

point to ensure targeted drug delivery," *IEEE Transactions on Industrial Electronics*, vol. 68, no. 12, pp. 12 493–12 503, 2020.

[123] F. Griese, T. Knopp, C. Gruettner, F. Thieben, K. Müller, S. Loges, P. Ludewig, and N. Gdaniec, "Simultaneous magnetic particle imaging and navigation of large superparamagnetic nanoparticles in bifurcation flow experiments," *Journal of Magnetism and magnetic Materials*, vol. 498, p. 166 206, 2020.

[124] M. P. Bui, M. Park, T.-A. Le, and J. Yoon, "Real-time 3d mpi-based navigation scheme for microrobots with flexible field free point trajectories and virtual ffp intuitive manipulation," *IEEE Robotics and Automation Letters*, 2024.

[125] C. Zhou, Z. Lin, S. Huang, B. Li, and A. Gao, "Progress in probe-based sensing techniques for in vivo diagnosis," *Biosensors*, vol. 12, no. 11, p. 943, 2022.

[126] K. Beaudette, J. Li, J. Lamarre, L. Majeau, and C. Boudoux, "Double-clad fiber-based multifunctional biosensors and multimodal bioimaging systems: Technology and applications," *Biosensors*, vol. 12, no. 2, p. 90, 2022.

[127] Y. Saito, Y. Kobayashi, K. Fujii, S. Sonoda, K. Tsujita, K. Hibi, Y. Morino, H. Okura, Y. Ikari, and J. Honye, "Clinical expert consensus document on intravascular ultrasound from the japanese association of cardiovascular intervention and therapeutics (2021)," *Cardiovascular Intervention and Therapeutics*, vol. 37, no. 1, pp. 40–51, 2022.

[128] A. S. El-Baz and J. S. Suri, Eds., *Cardiovascular and Coronary Artery Imaging.* Academic Press, 2021.

[129] B. D. MacNeill, H. C. Lowe, M. Takano, V. Fuster, and I.-K. Jang, "Intravascular modalities for detection of vulnerable plaque: Current status," *Arteriosclerosis, Thrombosis, and Vascular Biology*, vol. 23, no. 8, pp. 1333–1342, 2003.

[130] J. M. Tobis, J. Mallery, D. Mahon, K. Lehmann, P. Zalesky, J. Griffith, J. Gessert, M. Moriuchi, M. McRae, and M. L. Dwyer, "Intravascular ultrasound imaging of human coronary arteries in vivo. analysis of tissue characterizations with comparison to in vitro histological specimens," *Circulation*, vol. 83, no. 3, pp. 913–926, 1991.

[131] G. S. Mintz, S. E. Nissen, W. D. Anderson, S. R. Bailey, R. Erbel, P. J. Fitzgerald, F. J. Pinto, K. Rosenfield, R. J. Siegel, E. Tuzcu, P. G. Yock, R. A. O'Rourke, J. Abrams, E. R. Bates, B. R. Brodie, P. S. Douglas, G. Gregoratos, M. A. Hlatky, J. S. Hochman, S. Kaul, C. M. Tracy, D. D. Waters, and W. L. Winters, "American college of cardiology clinical expert consensus document on standards for acquisition, measurement and reporting of intravascular ultrasound studies (ivus)," *Journal of the American College of Cardiology*, vol. 37, no. 5, pp. 1478–1492, 2001.

[132] T. Yonetsu, B. E. Bouma, K. Kato, J. G. Fujimoto, and I.-K. Jang, "Optical coherence tomography– 15 years in cardiology," *Circulation Journal*, vol. 77, no. 8, pp. 1933–1940, 2013.

[133] H. Yabushita, B. E. Bouma, S. L. Houser, H. T. Aretz, I.-K. Jang, K. H. Schlendorf, C. R. Kauffman, M. Shishkov, D.-H. Kang, E. F. Halpern, and G. J. Tearney, "Characterization of human atherosclerosis by optical coherence tomography," *Circulation*, vol. 106, no. 13, pp. 1640–1645, 2002.

[134] G. J. Tearney, H. Yabushita, S. L. Houser, H. T. Aretz, I.-K. Jang, K. H. Schlendorf, C. R. Kauffman, M. Shishkov, E. F. Halpern, and B. E. Bouma, "Quantification of macrophage content in atherosclerotic plaques by optical coherence tomography," *Circulation*, vol. 107, no. 1, pp. 113–119, 2003.

[135] N. Gessert, S. Latus, Y. S. Abdelwahed, D. M. Leistner, M. Lutz, and A. Schlaefer, "Bioresorbable scaffold visualization in ivoct images using cnns and weakly supervised localization," in *Medical Imaging 2019: Image Processing*, SPIE, vol. 10949, 2019, pp. 606–612.

[136] B. E. Bouma, G. J. Tearney, H. Yabushita, M. Shishkov, C. R. Kauffman, D. DeJoseph Gauthier, B. D. MacNeill, S. L. Houser, H. T. Aretz, E. F. Halpern, and I.-K. Jang, "Evaluation of intracoronary stenting by intravascular optical coherence tomography," *Heart*, vol. 89, no. 3, pp. 317–320, 2003.

[137] H. Takebayashi, Y. Kobayashi, G. S. Mintz, S. G. Carlier, K. Fujii, T. Yasuda, I. Moussa, R. Mehran, G. D. Dangas, M. B. Collins, E. Kreps, A. J. Lansky, G. W. Stone, M. B. Leon, and J. W. Moses, "Intravascular ultrasound assessment of lesions with target vessel failure after sirolimus-eluting stent implantation," *The American Journal of Cardiology*, vol. 95, no. 4, pp. 498–502, 2005.

[138] M. Schartl, W. Bocksch, D. H. Koschyk, W. Voelker, K. R. Karsch, J. Kreuzer, D. Hausmann, S. Beckmann, and M. Gross, "Use of intravascular ultrasound to compare effects of different strategies of lipid-lowering therapy on plaque volume and composition in patients with coronary artery disease," *Circulation*, vol. 104, no. 4, pp. 387–392, 2001.

[139] Y. Suzuki, F. Ikeno, and A. C. Yeung, "Drug-eluting stent strut distribution: A comparison between cypher and taxus by optical coherence tomography.," *The Journal of invasive cardiology*, vol. 18, no. 3, pp. 111–114, 2006.

[140] Y. Zhang, V. Farooq, H. M. Garcia-Garcia, C. V. Bourantas, N. Tian, S. Dong, M. Li, S. Yang, P. W. Serruys, and S.-L. Chen, "Comparison of intravascular ultrasound versus angiography-guided drug-eluting stent implantation: A meta-analysis of one randomised trial and ten observational studies involving 19,619 patients," *EuroIntervention : journal of EuroPCR in collaboration with the Working Group on Interventional Cardiology of the European Society of Cardiology*, vol. 8, no. 7, pp. 855–865, 2012.

[141] C. Peng, H. Wu, S. Kim, X. Dai, and X. Jiang, "Recent advances in transducers for intravascular ultrasound (ivus) imaging," *Sensors*, vol. 21, no. 10, p. 3540, 2021.

[142] B. E. Bouma, M. Villiger, K. Otsuka, and W.-Y. Oh, "Intravascular optical coherence tomography," *Biomedical optics express*, vol. 8, no. 5, pp. 2660–2686, 2017.

[143] J. G. Fujimoto, S. A. Boppart, G. J. Tearney, B. E. Bouma, C. Pitris, and M. E. Brezinski, "High resolution in vivo intra-arterial imaging with optical coherence tomography," *Heart*, vol. 82, no. 2, pp. 128–133, 1999.

[144] L. J. Diaz-Sandoval, B. E. Bouma, G. J. Tearney, and I.-K. Jang, "Optical coherence tomography as a tool for percutaneous coronary interventions," *Catheterization and cardiovascular interventions : official journal of the Society for Cardiac Angiography & Interventions*, vol. 65, no. 4, pp. 492–496, 2005.

[145] Y. Kawase, K. Hoshino, R. Yoneyama, J. McGregor, R. J. Hajjar, I.-K. Jang, and M. Hayase, "In vivo volumetric analysis of coronary stent using optical coherence tomography with a novel balloon occlusion-flushing catheter: A comparison with intravascular ultrasound," *Ultrasound in medicine & biology*, vol. 31, no. 10, pp. 1343–1349, 2005.

[146] C. Gatta, O. Pujol, O. Rodriguez Leor, J. Mauri Ferre, and P. Radeva, "Fast rigid registration of vascular structures in ivus sequences," *IEEE transactions on information technology in biomedicine : a publication of the IEEE Engineering in Medicine and Biology Society*, vol. 13, no. 6, pp. 1006–1011, 2009.

[147] Y. Kawase, Y. Suzuki, F. Ikeno, R. Yoneyama, K. Hoshino, H. Q. Ly, G. T. Lau, M. Hayase, A. C. Yeung, R. J. Hajjar, and I.-K. Jang, "Comparison of nonuniform rotational distortion between mechanical ivus and oct using a phantom model," *Ultrasound in medicine & biology*, vol. 33, no. 1, pp. 67–73, 2007.

[148] B. E. Bouma and G. J. Tearney, "Power-efficient nonreciprocal interferometer and linear-scanning fiber-optic catheter for optical coherence tomography," *Optics Letters*, vol. 24, no. 8, pp. 531–533, 1999.

[149] X. Li, T. H. Ko, and J. G. Fujimoto, "Intraluminal fiber-optic doppler imaging catheter for structural and functional optical coherence tomography," *Optics Letters*, vol. 26, no. 23, pp. 1906–1908, 2001.

[150] J. Y. Kim, M. W. Lee, and H. Yoo, "Diagnostic fiber-based optical imaging catheters," *Biomedical Engineering Letters*, vol. 4, no. 3, pp. 239–249, 2014.

[151] I.-K. Jang, G. J. Tearney, B. MacNeill, M. Takano, F. Moselewski, N. Iftima, M. Shishkov, S. Houser, H. T. Aretz, E. F. Halpern, and B. E. Bouma, "In vivo characterization of coronary atherosclerotic plaque by use of optical coherence tomography," *Circulation*, vol. 111, no. 12, pp. 1551–1555, 2005.

[152] S. H. Yun, G. J. Tearney, B. J. Vakoc, M. Shishkov, W. Y. Oh, A. E. Desjardins, M. J. Suter, R. C. Chan, J. A. Evans, I.-K. Jang, N. S. Nishioka, J. F. de Boer,

and B. E. Bouma, “Comprehensive volumetric optical microscopy in vivo,” *Nature medicine*, vol. 12, no. 12, pp. 1429–1433, 2006.

[153] J.-H. Sung and J.-H. Chang, “Mechanically rotating intravascular ultrasound (ivus) transducer: A review,” *Sensors*, vol. 21, no. 11, p. 3907, 2021.

[154] S. Fort, N. A. Freeman, P. Johnston, E. A. Cohen, and F. S. Foster, “In vitro and in vivo comparison of three different intravascular ultrasound catheter designs,” *Catheterization and cardiovascular interventions : official journal of the Society for Cardiac Angiography & Interventions*, vol. 52, no. 3, pp. 382–392, 2001.

[155] J. M. Tobis, J. Mallery, D. Mahon, K. Lehmann, P. Zalesky, J. Griffith, J. Gessert, M. Moriuchi, M. McRae, and M. L. Dwyer, “Intravascular ultrasound imaging of human coronary arteries in vivo. analysis of tissue characterizations with comparison to in vitro histological specimens,” *Circulation*, vol. 83, no. 3, pp. 913–926, 1991.

[156] A. Vasquez, N. Mistry, and J. Singh, “Impact of intravascular ultrasound in clinical practice,” *Interventional Cardiology Review*, vol. 9, no. 3, pp. 156–163, 2014.

[157] N. Bom, C. T. Lancée, and F. C. van Egmond, “An ultrasonic intracardiac scanner,” *Ultrasonics*, vol. 10, no. 2, pp. 72–76, 1972.

[158] M. L. Dufour, C.-E. Bisaillon, G. Lamouche, S. Vergnole, M. Hewko, F. D’Amours, C. Padioleau, and M. Sowa, “Tools for experimental characterization of the nonuniform rotational distortion in intravascular oct probes,” in *Photonic Therapeutics and Diagnostics VII*, SPIE, vol. 7883, 2011, pp. 402–409.

[159] B. J. Kimura, V. Bhargava, W. Palinski, R. J. Russo, and A. N. DeMaria, “Distortion of intravascular ultrasound images because of nonuniform angular velocity of mechanical-type transducers,” *American Heart Journal*, vol. 132, no. 2, pp. 328–336, 1996.

[160] P. P. Kearney, M. Ramo, T. Spencer, T. Shaw, I. R. Starkey, N. McDicken, and G. R. Sutherland, “A study of the quantitative and qualitative impact of catheter shaft angulation in a mechanical intravascular ultrasound system,” *Ultrasound in medicine & biology*, vol. 23, no. 1, pp. 87–93, 1997.

[161] H. ten Hoff, A. Korbijn, T. H. Smith, J. F. Klinkhamer, and N. Bom, “Imaging artifacts in mechanically driven ultrasound catheters,” *International journal of cardiac imaging*, vol. 4, no. 2-4, pp. 195–199, 1989.

[162] S. Hou, Y. Li, C. Zou, Y. Li, H. Tang, Z. Liu, S. Chen, and J. Peng, “A novel distal micromotor-based side-looking intravascular ultrasound transducer,” *IEEE transactions on ultrasonics, ferroelectrics, and frequency control*, vol. 69, no. 1, pp. 283–290, 2022.

[163] J. Peng, L. Ma, X. Li, H. Tang, Y. Li, and S. Chen, "A novel synchronous micro motor for intravascular ultrasound imaging," *IEEE Transactions on Biomedical Engineering*, vol. 66, no. 3, pp. 802–809, 2019.

[164] W. Liao, T. Chen, C. Wang, W. Zhang, Z. Peng, X. Zhang, S. Ai, D. Fu, T. Zhou, and P. Xue, "Endoscopic optical coherence tomography with a focus-adjustable probe," *Optics Letters*, vol. 42, no. 20, pp. 4040–4043, 2017.

[165] R. Ledworuski, "Entwicklung eines ultraschallkatheters mit integriertem mikroantrieb," 2006.

[166] F. Feroldi, J. Willemse, V. Davidoiu, M. G. O. Gräfe, D. J. van Iperen, A. W. M. Goorsenberg, J. T. Annema, J. M. A. Daniels, P. I. Bonta, and J. F. de Boer, "In vivo multifunctional optical coherence tomography at the periphery of the lungs," *Biomedical optics express*, vol. 10, no. 6, pp. 3070–3091, 2019.

[167] D. Lorenser, X. Yang, R. W. Kirk, B. C. Quirk, R. A. McLaughlin, and D. D. Sampson, "Ultrathin side-viewing needle probe for optical coherence tomography," *Optics Letters*, vol. 36, no. 19, pp. 3894–3896, 2011.

[168] S. Moon, Z. Piao, C.-S. Kim, and Z. Chen, "Lens-free endoscopy probe for optical coherence tomography," *Optics Letters*, vol. 38, no. 12, pp. 2014–2016, 2013.

[169] Z. Ding, J. Qiu, Y. Shen, Z. Chen, and W. Bao, "Lens-free all-fiber probe with an optimized output beam for optical coherence tomography," *Optics Letters*, vol. 42, no. 14, pp. 2814–2817, 2017.

[170] Jiawen Li, Simon Thiele, Rodney W. Kirk, Bryden C. Quirk, Ayla Hoogendoorn, Yung Chih Chen, Karlheinz Peter, Stephen J. Nicholls, Johan W. Verjans, Peter J. Psaltis, Christina Bursill, Alois M. Herkommer, Harald Giessen, and Robert A. McLaughlin, "3d-printed micro lens-in-lens for in vivo multimodal microendoscopy," *Small*, vol. 18, no. 17, p. 2 107 032, 2022.

[171] J. Li, S. Thiele, B. C. Quirk, R. W. Kirk, J. W. Verjans, E. Akers, C. A. Bursill, S. J. Nicholls, A. M. Herkommer, H. Giessen, and R. A. McLaughlin, "Ultrathin monolithic 3d printed optical coherence tomography endoscopy for preclinical and clinical use," *Light: Science & Applications*, vol. 9, no. 1, p. 124, 2020.

[172] T. Wu, Y. Huang, Y. Liu, J. Wang, Y. Shi, X. Gu, H. Shen, C. He, and Y. Lu, "Ultrathin lensed fiber based anastigmatic needle probe for endoscopic swept source optical coherence tomography," *Optics and Lasers in Engineering*, vol. 154, p. 107 043, 2022.

[173] J. Xi, L. Huo, Y. Wu, M. J. Cobb, J. H. Hwang, and X. Li, "High-resolution oct balloon imaging catheter with astigmatism correction," *Optics Letters*, vol. 34, no. 13, pp. 1943–1945, 2009.

[174] V. Farooq, T. Okamura, B. D. Gogas, J. H. Heo, M. Magro, J. Gomez-Lara, S. Brugaletta, Y. Onuma, M. Radu, H. M. Garcìa-Garcìa, and P. W. Serruys, “3d reconstructions of optical frequency domain imaging to improve understanding of conventional pci,” *JACC. Cardiovascular imaging*, vol. 4, no. 9, pp. 1044–1046, 2011.

[175] J. N. van der Sijde, G. Guagliumi, V. Sirbu, K. Shimamura, M. Borghesi, A. Karanasos, and E. Regar, “The optis integrated system: Real-time, co-registration of angiography and optical coherence tomography,” *EuroIntervention : journal of EuroPCR in collaboration with the Working Group on Interventional Cardiology of the European Society of Cardiology*, vol. 12, no. 7, pp. 855–860, 2016.

[176] D. de Cock, S. Tu, G. J. Ughi, and T. Adriaenssens, “Development of 3d ivoct imaging and co-registration of ivoct and angiography in the catheterization laboratory,” *Current Cardiovascular Imaging Reports*, vol. 7, no. 10, pp. 1–14, 2014.

[177] L. Hebsgaard, T. M. Nielsen, S. Tu, L. R. Krusell, M. Maeng, K. T. Veien, B. Raungaard, C. J. Terkelsen, A. Kaltoft, J. H. C. Reiber, J. F. Lassen, E. H. Christiansen, and N. R. Holm, “Co-registration of optical coherence tomography and x-ray angiography in percutaneous coronary intervention. the does optical coherence tomography optimize revascularization (doctor) fusion study,” *International Journal of Cardiology*, vol. 182, pp. 272–278, 2015.

[178] F. Galassi, M. Alkhalil, R. Lee, P. Martindale, R. K. Kharbanda, K. M. Channon, V. Grau, and R. P. Choudhury, “3d reconstruction of coronary arteries from 2d angiographic projections using non-uniform rational basis splines (nurbs) for accurate modelling of coronary stenoses,” *PLOS ONE*, vol. 13, no. 1, e0190650, 2018.

[179] M. I. Papafaklis, C. V. Bourantas, T. Yonetsu, R. Vergallo, A. Kotsia, S. Nakatani, L. S. Lakkas, L. S. Athanasiou, K. K. Naka, D. I. Fotiadis, C. L. Feldman, P. H. Stone, P. W. Serruys, I.-K. Jang, and L. K. Michalis, “Anatomically correct three-dimensional coronary artery reconstruction using frequency domain optical coherence tomographic and angiographic data: Head-to-head comparison with intravascular ultrasound for endothelial shear stress assessment in humans,” *EuroIntervention : journal of EuroPCR in collaboration with the Working Group on Interventional Cardiology of the European Society of Cardiology*, vol. 11, no. 4, pp. 407–415, 2015.

[180] G. P. Prause, S. C. DeJong, C. R. McKay, and M. Sonka, “Towards a geometrically correct 3-d reconstruction of tortuous coronary arteries based on biplane angiography and intravascular ultrasound,” *International journal of cardiac imaging*, vol. 13, no. 6, pp. 451–462, 1997.

[181] K. Tsuchida, W. Van Der Giessen, M. Patterson, S. Tanimoto, H. Garcia-Garcia, E. Regar, J. Ligthart, A.-M. Maugenest, G. Maatrijk, J. J. Wentzel, et al., “In vivo validation of a novel three-dimensional quantitative coronary angiography system (cardiop-b™): Comparison with a conventional two-dimensional system (cass ii™) and with special reference to optical coherence tomography.,” *Drug Eluting Stent Im-*

plantation for High Risk Patients and Novel Technologies in Percutaneous Coronary Intervention, p. 147, 2007.

[182] M. Kunio, C. C. O'Brien, A. C. Lopes, L. Bailey, P. A. Lemos, G. J. Tearney, and E. R. Edelman, "Vessel centerline reconstruction from non-isocentric and non-orthogonal paired monoplane angiographic images," *The international journal of cardiovascular imaging*, vol. 34, pp. 673–682, 2018.

[183] T. Wang, T. Pfeiffer, E. Regar, W. Wieser, H. van Beusekom, C. T. Lancee, G. Springeling, I. Krabbendam, A. F. W. van der Steen, R. Huber, and G. van Soest, "Heartbeat oct: In vivo intravascular megahertz-optical coherence tomography," *Biomedical optics express*, vol. 6, no. 12, pp. 5021–5032, 2015.

[184] A. Brost, N. Strobel, L. Yatziv, W. Gilson, B. Meyer, J. Hornegger, J. Lewin, and F. Wacker, "Accuracy of x-ray image-based 3d localization from two c-arm views: A comparison between an ideal system and a real device," in *Medical Imaging 2009: Visualization, Image-Guided Procedures, and Modeling*, SPIE, vol. 7261, 2009, pp. 650–659.

[185] N. Leßmann, D. Drömann, and A. Schlaefer, "Feasibility of respiratory motion-compensated stereoscopic x-ray tracking for bronchoscopy," *International Journal of Computer Assisted Radiology and Surgery*, vol. 9, no. 2, pp. 199–209, 2014.

[186] W. Peng, W. Wu, J. Zhang, H. Xie, S. Zhang, and L. Gu, "An automatic framework for estimating the pose of the catheter distal section using a coarse-to-fine network," *Computer Methods and Programs in Biomedicine*, vol. 225, p. 107 036, 2022.

[187] G. van Soest, J. G. Bosch, and A. F. W. van der Steen, "Azimuthal registration of image sequences affected by nonuniform rotation distortion," *IEEE Transactions on Information Technology in Biomedicine*, vol. 12, no. 3, pp. 348–355, 2008.

[188] E. Abouei, A. M. Lee, H. Pahlevaninezhad, G. Hohert, M. Cua, P. Lane, S. Lam, and C. MacAulay, "Correction of motion artifacts in endoscopic optical coherence tomography and autofluorescence images based on azimuthal en face image registration," *Journal of biomedical optics*, vol. 23, no. 1, pp. 016 004–016 004, 2018.

[189] G. Cao, S. Li, S. Zhang, Z. Peng, Y. Wu, D. Wang, and C. Dai, "Improved fast algorithm for non-uniform rotational distortion correction in oct endoscopic imaging," *Optics Express*, vol. 31, no. 2, pp. 2754–2767, 2023.

[190] N. Uribe-Patarroyo and B. E. Bouma, "Rotational distortion correction in endoscopic optical coherence tomography based on speckle decorrelation," *Optics Letters*, vol. 40, no. 23, pp. 5518–5521, 2015.

[191] O. O. Ahsen, H.-C. Lee, M. G. Giacomelli, Z. Wang, K. Liang, T.-H. Tsai, B. Potsaid, H. Mashimo, and J. G. Fujimoto, "Correction of rotational distortion for catheter-

based en face oct and oct angiography," *Optics Letters*, vol. 39, no. 20, pp. 5973–5976, 2014.

[192] R. Zhang, Y. Fan, W. Qi, A. Wang, X. Tang, and T. Gao, "Current research and future prospects of ivoct imaging-based detection of the vascular lumen and vulnerable plaque," *Journal of Biophotonics*, vol. 15, no. 5, e202100376, 2022.

[193] G. J. Ughi, T. Adriaenssens, P. Sinnaeve, W. Desmet, and J. D'hooge, "Automated tissue characterization of in vivo atherosclerotic plaques by intravascular optical coherence tomography images," *Biomedical optics express*, vol. 4, no. 7, pp. 1014–1030, 2013.

[194] A. Abdolmanafi, L. Duong, N. Dahdah, and F. Cheriet, "Deep feature learning for automatic tissue classification of coronary artery using optical coherence tomography," *Biomedical optics express*, vol. 8, no. 2, pp. 1203–1220, 2017.

[195] D. Prabhu, H. Bezerra, C. Kolluru, Y. Gharaibeh, E. Mehanna, H. Wu, and D. Wilson, "Automated a-line coronary plaque classification of intravascular optical coherence tomography images using handcrafted features and large datasets," *Journal of Biomedical Optics*, vol. 24, no. 10, pp. 1–15, 2019.

[196] S. Tsantis, G. C. Kagadis, K. Katsanos, D. Karnabatidis, G. Bourantas, and G. C. Nikiforidis, "Automatic vessel lumen segmentation and stent strut detection in intravascular optical coherence tomography," *Medical physics*, vol. 39, no. 1, pp. 503–513, 2012.

[197] D. S. Jodas, A. S. Pereira, and J. M. R. Tavares, "Automatic segmentation of the lumen region in intravascular images of the coronary artery," *Medical image analysis*, vol. 40, pp. 60–79, 2017.

[198] J. Yang, L. Tong, M. Faraji, and A. Basu, "Ivus-net: An intravascular ultrasound segmentation network," in *Smart Multimedia: First International Conference, ICSM 2018, Toulon, France, August 24–26, 2018, Revised Selected Papers 1*, Springer, 2018, pp. 367–377.

[199] L. Dong, W. Jiang, W. Lu, J. Jiang, Y. Zhao, X. Song, X. Leng, H. Zhao, J. Wang, C. Li, et al., "Automatic segmentation of coronary lumen and external elastic membrane in intravascular ultrasound images using 8-layer u-net," *BioMedical Engineering OnLine*, vol. 20, pp. 1–9, 2021.

[200] E. Song, Y. Huang, N. Huang, Y. Mei, X. Yu, and J. A. Rogers, "Recent advances in microsystem approaches for mechanical characterization of soft biological tissues," *Microsystems & Nanoengineering*, vol. 8, no. 1, p. 77, 2022.

[201] R. Akhtar, M. J. Sherratt, J. K. Cruickshank, and B. Derby, "Characterizing the elastic properties of tissues," *Materials Today*, vol. 14, no. 3, pp. 96–105, 2011.

[202] M. Neidhardt, M. Bengs, S. Latus, S. Gerlach, C. J. Cyron, J. Sprenger, and A. Schlaefer, "Ultrasound shear wave elasticity imaging with spatio-temporal deep learning," *IEEE Transactions on Biomedical Engineering*, vol. 69, no. 11, pp. 3356–3364, 2022.

[203] J. A. Mulligan, G. R. Untracht, S. N. Chandrasekaran, C. N. Brown, and S. G. Adie, "Emerging approaches for high-resolution imaging of tissue biomechanics with optical coherence elastography," *IEEE Journal of Selected Topics in Quantum Electronics*, vol. 22, no. 3, pp. 246–265, 2016.

[204] N. Bandari, J. Dargahi, and M. Packirisamy, "Tactile sensors for minimally invasive surgery: A review of the state-of-the-art, applications, and perspectives," *IEEE Access*, vol. 8, pp. 7682–7708, 2019.

[205] K. V. Larin, G. Scarcelli, and V. V. Yakovlev, "Optical elastography and tissue biomechanics," *Journal of Biomedical Optics*, vol. 24, no. 11, pp. 110 901–110 901, 2019.

[206] N. Leartprapun and S. G. Adie, "Recent advances in optical elastography and emerging opportunities in the basic sciences and translational medicine," *Biomedical Optics Express*, vol. 14, no. 1, pp. 208–248, 2023.

[207] G. Bourantas, B. F. Zwick, G. R. Joldes, A. Wittek, and K. Miller, "Simple and robust element-free galerkin method with almost interpolating shape functions for finite deformation elasticity," *Applied Mathematical Modelling*, vol. 96, pp. 284–303, 2021.

[208] J. A. Schaar, C. L. de Korte, F. Mastik, R. Baldewsing, E. Regar, P. de Feyter, C. J. Slager, A. F. W. van der Steen, and P. W. Serruys, "Intravascular palpography for high-risk vulnerable plaque assessment," *Herz*, vol. 28, no. 6, pp. 488–495, 2003.

[209] J. Fu, M. Haghighi-Abayneh, F. Pierron, and P. D. Ruiz, "Depth-resolved full-field measurement of corneal deformation by optical coherence tomography and digital volume correlation," *Experimental Mechanics*, vol. 56, no. 7, pp. 1203–1217, 2016.

[210] M. S. Taljanovic, L. H. Gimber, G. W. Becker, L. D. Latt, A. S. Klauser, D. M. Melville, L. Gao, and R. S. Witte, "Shear-wave elastography: Basic physics and musculoskeletal applications," *Radiographics*, vol. 37, no. 3, pp. 855–870, 2017.

[211] F. Zvietcovich, A. Nair, Y. S. Ambekar, M. Singh, S. R. Aglyamov, M. D. Twa, and K. V. Larin, "Confocal air-coupled ultrasonic optical coherence elastography probe for quantitative biomechanics," *Optics Letters*, vol. 45, no. 23, pp. 6567–6570, 2020.

[212] F. Zvietcovich and K. V. Larin, "Wave-based optical coherence elastography: The 10-year perspective," *Progress in biomedical engineering (Bristol, England)*, vol. 4, no. 1, 2022.

[213] W. Qi, R. Li, T. Ma, K. Kirk Shung, Q. Zhou, and Z. Chen, “Confocal acoustic radiation force optical coherence elastography using a ring ultrasonic transducer,” *Applied Physics Letters*, vol. 104, no. 12, p. 123 702, 2014.

[214] P. Boerner, D. Nevozhay, M. Hatamimoslehabadi, H. S. Chawla, F. Zvietcovich, S. Aglyamov, K. V. Larin, and K. V. Sokolov, “Repetitive optical coherence elastography measurements with blinking nanobombs,” *Biomedical Optics Express*, vol. 11, no. 11, pp. 6659–6673, 2020.

[215] K. Nightingale, “Acoustic radiation force impulse (arfi) imaging: A review,” *Current medical imaging reviews*, vol. 7, no. 4, pp. 328–339, 2011.

[216] A. S. Khalil, R. C. Chan, A. H. Chau, B. E. Bouma, and M. R. K. Mofrad, “Tissue elasticity estimation with optical coherence elastography: Toward mechanical characterization of in vivo soft tissue,” *Annals of biomedical engineering*, vol. 33, no. 11, pp. 1631–1639, 2005.

[217] L. Chin, A. Curatolo, B. F. Kennedy, B. J. Doyle, P. R. T. Munro, R. A. McLaughlin, and D. D. Sampson, “Analysis of image formation in optical coherence elastography using a multiphysics approach,” *Biomedical optics express*, vol. 5, no. 9, pp. 2913–2930, 2014.

[218] E. Li, S. Makita, S. Azuma, A. Miyazawa, and Y. Yasuno, “Compression optical coherence elastography with two-dimensional displacement measurement and local deformation visualization,” *Optics Letters*, vol. 44, no. 4, pp. 787–790, 2019.

[219] X. Wang, Q. Wu, J. Chen, and J. Mo, “Development of a handheld compression optical coherence elastography probe with a disposable stress sensor,” *Optics Letters*, vol. 46, no. 15, pp. 3669–3672, 2021.

[220] K. M. Kennedy, B. F. Kennedy, R. A. McLaughlin, and D. D. Sampson, “Needle optical coherence elastography for tissue boundary detection,” *Optics letters*, vol. 37, no. 12, pp. 2310–2312, 2012.

[221] R. Mieling, J. Sprenger, S. Latus, L. Bargsten, and A. Schlaefer, “A novel optical needle probe for deep learning-based tissue elasticity characterization,” *Current Directions in Biomedical Engineering*, vol. 7, no. 1, pp. 21–25, 2021.

[222] Y. Qiu, Y. Wang, Y. Xu, N. Chandra, J. Haorah, B. Hubbi, B. J. Pfister, and X. Liu, “Quantitative optical coherence elastography based on fiber-optic probe for in situ measurement of tissue mechanical properties,” *Biomedical optics express*, vol. 7, no. 2, pp. 688–700, 2016.

[223] R. Mieling, S. Latus, M. Fischer, F. Behrendt, and A. Schlaefer, “Optical coherence elastography needle for biomechanical characterization of deep tissue,” in *Medical Image Computing and Computer Assisted Intervention - MICCAI 2023*, H. Greenspan, A. Madabhushi, P. Mousavi, S. Salcudean, J. Duncan, T. Syeda-Mahmood, and R.

Taylor, Eds., ser. Lecture Notes in Computer Science, Cham: Springer Nature Switzerland and Imprint: Springer, 2023, pp. 607–617.

[224] G. van Soest, F. Mastik, N. de Jong, and A. F. W. van der Steen, "Robust intravascular optical coherence elastography by line correlations," *Physics in Medicine & Biology*, vol. 52, no. 9, pp. 2445–2458, 2007.

[225] Tianshi Wang, Tom Pfeiffer, Ali Akyildiz, Heleen M. M. van Beusekom, Robert Huber, Antonius F. W. van der Steen, and Gijs van Soest, "Intravascular optical coherence elastography," *Biomed. Opt. Express*, vol. 13, no. 10, pp. 5418–5433, 2022.

[226] R. Bu, S. Balakrishnan, H. Price, C. Zdanski, S. Mitran, and A. L. Oldenburg, "Localized compliance measurement of the airway wall using anatomic optical coherence elastography," *Optics Express*, vol. 27, no. 12, pp. 16 751–16 766, 2019.

[227] A. Nair, M. Singh, S. R. Aglyamov, and K. V. Larin, "Multimodal heartbeat and compression optical coherence elastography for mapping corneal biomechanics," *Frontiers in medicine*, vol. 9, p. 833 597, 2022.

[228] X. Liang and S. A. Boppart, "Biomechanical properties of in vivo human skin from dynamic optical coherence elastography," *IEEE Transactions on Biomedical Engineering*, vol. 57, no. 4, pp. 953–959, 2010.

[229] S. Song, Z. Huang, and R. K. Wang, "Tracking mechanical wave propagation within tissue using phase-sensitive optical coherence tomography: Motion artifact and its compensation," *Journal of Biomedical Optics*, vol. 18, no. 12, p. 121 505, 2013.

[230] K. M. Kennedy, L. Chin, R. A. McLaughlin, B. Latham, C. M. Saunders, D. D. Sampson, and B. F. Kennedy, "Quantitative micro-elastography: Imaging of tissue elasticity using compression optical coherence elastography," *Scientific Reports*, vol. 5, p. 15 538, 2015.

[231] J. Zhu, J. Yu, Y. Qu, Y. He, Y. Li, Q. Yang, T. Huo, X. He, and Z. Chen, "Coaxial excitation longitudinal shear wave measurement for quantitative elasticity assessment using phase-resolved optical coherence elastography," *Optics Letters*, vol. 43, no. 10, pp. 2388–2391, 2018.

[232] A. Ramier, B. Tavakol, and S.-H. Yun, "Measuring mechanical wave speed, dispersion, and viscoelastic modulus of the cornea using optical coherence elastography," *Optics Express*, vol. 27, no. 12, pp. 16 635–16 649, 2019.

[233] S. G. Adie, X. Liang, B. F. Kennedy, R. John, D. D. Sampson, and S. A. Boppart, "Spectroscopic optical coherence elastography," *Optics Express*, vol. 18, no. 25, pp. 25 519–25 534, 2010.

[234] C. Li, G. Guan, R. Reif, Z. Huang, and R. K. Wang, "Determining elastic properties of skin by measuring surface waves from an impulse mechanical stimulus using

phase-sensitive optical coherence tomography," *Journal of The Royal Society Interface*, vol. 9, no. 70, pp. 831–841, 2012.

[235] Ł. Ambroziński, S. Song, S. J. Yoon, I. Pelivanov, D. Li, L. Gao, T. T. Shen, R. K. Wang, and M. O'Donnell, "Acoustic micro-tapping for non-contact 4d imaging of tissue elasticity," *Scientific Reports*, vol. 6, no. 1, p. 38 967, 2016.

[236] Z. Jin, R. Khazaeinezhad, J. Zhu, J. Yu, Y. Qu, Y. He, Y. Li, T. E. Gomez Alvarez-Arenas, F. Lu, and Z. Chen, "In-vivo 3d corneal elasticity using air-coupled ultrasound optical coherence elastography," *Biomedical optics express*, vol. 10, no. 12, pp. 6272–6285, 2019.

[237] W. Qi, R. Chen, L. Chou, G. Liu, J. Zhang, Q. Zhou, and Z. Chen, "Phase-resolved acoustic radiation force optical coherence elastography," *Journal of Biomedical Optics*, vol. 17, no. 11, p. 110 505, 2012.

[238] Y. Qu, T. Ma, Y. He, M. Yu, J. Zhu, Y. Miao, C. Dai, P. Patel, K. K. Shung, Q. Zhou, and Z. Chen, "Miniature probe for mapping mechanical properties of vascular lesions using acoustic radiation force optical coherence elastography," *Scientific Reports*, vol. 7, no. 1, p. 4731, 2017.

[239] K. Nakamura, R. Isago, and D. Koyama, "Endoscopic optical coherence elastography using acoustic radiation force and a vibrating fiber," in *AIP Conference Proceedings*, American Institute of Physics, vol. 1474, 2012, pp. 247–250.

[240] A. Parmar, G. Sharma, S. Sharma, and K. Singh, "Portable optical coherence elastography system with flexible and phase stable common path optical fiber probe," *IEEE Access*, vol. 9, pp. 56 041–56 048, 2021.

[241] A. Parmar, G. Sharma, A. Ramming, and K. Singh, "Deep tissue characterization with optical coherence elastography: A comparison of different methods," *Materials (Basel, Switzerland)*, vol. 15, no. 23, 2022.

[242] O. A. Ejofodomi, V. Zderic, and J. M. Zara, "Development of novel imaging probe for optical/acoustic radiation imaging (oari)," *Medical Physics*, vol. 40, no. 11, p. 111 910, 2013.

[243] J. Zhu, Y. Qu, T. Ma, R. Li, Y. Du, S. Huang, K. K. Shung, Q. Zhou, and Z. Chen, "Imaging and characterizing shear wave and shear modulus under orthogonal acoustic radiation force excitation using oct doppler variance method," *Optics Letters*, vol. 40, no. 9, pp. 2099–2102, 2015.

[244] Andrei B. Karpiouk, Donald J. VanderLaan, Kirill V. Larin, and Stanislav Y. Emelianov, "Integrated optical coherence tomography and multielement ultrasound transducer probe for shear wave elasticity imaging of moving tissues," *Journal of Biomedical Optics*, vol. 23, no. 10, pp. 1–7, 2018.

[245] S. Wang and K. V. Larin, “Shear wave imaging optical coherence tomography (swi-oct) for ocular tissue biomechanics,” *Optics Letters*, vol. 39, no. 1, pp. 41–44, 2014.

[246] D. P. Vekilov, M. Singh, S. R. Aglyamov, K. V. Larin, and K. J. Grande-Allen, “Mapping the spatial variation of mitral valve elastic properties using air-pulse optical coherence elastography,” *Journal of Biomechanics*, vol. 93, pp. 52–59, 2019.

[247] S. Das, A. Schill, C.-H. Liu, S. Aglyamov, and K. V. Larin, “Laser-induced elastic wave classification: Thermoelastic versus ablative regimes for all-optical elastography applications,” *Journal of Biomedical Optics*, vol. 25, no. 3, pp. 1–13, 2020.

[248] L. Zhao, D. Vanderlaan, H. Yoon, J. Liu, C. Li, and S. Y. Emelianov, “Ultrafast ultrasound imaging of surface acoustic waves induced by laser excitation compared with acoustic radiation force,” *Opt. Lett.*, vol. 45, no. 7, pp. 1810–1813, Apr. 2020.

[249] C. Li, G. Guan, Z. Huang, M. Johnstone, and R. K. Wang, “Noncontact all-optical measurement of corneal elasticity,” *Optics Letters*, vol. 37, no. 10, pp. 1625–1627, 2012.

[250] M. Hatami, D. Nevozhay, M. Singh, A. Schill, P. Boerner, S. Aglyamov, K. Sokolov, and K. V. Larin, “Nanobomb optical coherence elastography in multilayered phantoms,” *Biomedical optics express*, vol. 14, no. 11, p. 5670, 2023.

[251] M. Singh, F. Zvietcovich, and K. V. Larin, “Introduction to optical coherence elastography: Tutorial,” *Journal of the Optical Society of America A*, vol. 39, no. 3, pp. 418–430, 2022.

[252] M. Neidhardt, M. Bengs, S. Latus, M. Schlüter, T. Saathoff, and A. Schlaefer, “4d deep learning for real-time volumetric optical coherence elastography,” *International journal of computer assisted radiology and surgery*, vol. 16, pp. 23–27, 2021.

[253] M. Razani, T. W. H. Luk, A. Mariampillai, P. Siegler, T.-R. Kiehl, M. C. Kolios, and V. X. D. Yang, “Optical coherence tomography detection of shear wave propagation in inhomogeneous tissue equivalent phantoms and ex-vivo carotid artery samples,” *Biomedical optics express*, vol. 5, no. 3, pp. 895–906, 2014.

[254] M. Ourak, J. Smits, L. Esteveny, G. Borghesan, A. Gijbels, L. Schoevaerdts, Y. Douven, J. Scholtes, E. Lankenau, T. Eixmann, H. Schulz-Hildebrandt, G. Hüttmann, M. Kozlovszky, G. Kronreif, K. Willekens, P. Stalmans, K. Faridpooya, M. Cereda, A. Giani, G. Staurenghi, D. Reynaerts, and E. B. Vander Poorten, “Combined oct distance and fbg force sensing cannulation needle for retinal vein cannulation: In vivo animal validation,” *International Journal of Computer Assisted Radiology and Surgery*, vol. 14, no. 2, pp. 301–309, 2019.

[255] H. Zhang, C. Gu, Q. Lan, W. Zhang, C. Liu, and J. Yang, “Learning-based distortion correction enables proximal-scanning endoscopic oct elastography,” *Biomedical Optics Express*, vol. 15, no. 7, pp. 4345–4364, 2024.

[256] R. Bu, S. Balakrishnan, N. Iftimia, H. Price, C. Zdanski, and A. L. Oldenburg, "Airway compliance measured by anatomic optical coherence tomography," *Biomedical optics express*, vol. 8, no. 4, pp. 2195–2209, 2017.

[257] C. L. de Korte, A. F. van der Steen, E. I. Cépedes, G. Pasterkamp, S. G. Carlier, F. Mastik, A. H. Schoneveld, P. W. Serruys, and N. Bom, "Characterization of plaque components and vulnerability with intravascular ultrasound elastography," *Physics in Medicine & Biology*, vol. 45, no. 6, pp. 1465–1475, 2000.

[258] C. L. de Korte, S. G. Carlier, F. Mastik, M. M. Doyley, A. F. W. van der Steen, P. W. Serruys, and N. Bom, "Morphological and mechanical information of coronary arteries obtained with intravascular elastography; feasibility study in vivo," *European Heart Journal*, vol. 23, no. 5, pp. 405–413, 2002.

[259] C. L. de Korte and A. F. W. van der Steen, "Intravascular ultrasound elastography: An overview," *Ultrasonics*, vol. 40, no. 1-8, pp. 859–865, 2002.

[260] K. Kim, W. F. Weitzel, J. M. Rubin, H. Xie, X. Chen, and M. O'Donnell, "Vascular intramural strain imaging using arterial pressure equalization," *Ultrasound in medicine & biology*, vol. 30, no. 6, pp. 761–771, 2004.

[261] Z. Hajjarian, J. D. Toussaint, J. L. Guerrero, and S. K. Nadkarni, "In-vivo mechanical characterization of coronary atherosclerotic plaques in living swine using intravascular laser speckle imaging," *Biomedical optics express*, vol. 12, no. 4, pp. 2064–2078, 2021.

[262] Q. Fang, B. Krajancich, L. Chin, R. Zilkens, A. Curatolo, L. Frewer, J. D. Anstie, P. Wijesinghe, C. Hall, B. F. Dessauvagie, et al., "Handheld probe for quantitative micro-elastography," *Biomedical Optics Express*, vol. 10, no. 8, pp. 4034–4049, 2019.

[263] Q. Fang, A. Curatolo, P. Wijesinghe, Y. L. Yeow, J. Hamzah, P. B. Noble, K. Karnowski, D. D. Sampson, R. Ganss, J. K. Kim, et al., "Ultrahigh-resolution optical coherence elastography through a micro-endoscope: Towards in vivo imaging of cellular-scale mechanics," *Biomedical optics express*, vol. 8, no. 11, pp. 5127–5138, 2017.

[264] C.-C. Shih, P.-Y. Chen, T. Ma, Q. Zhou, K. K. Shung, and C.-C. Huang, "Development of an intravascular ultrasound elastography based on a dual-element transducer," *Royal Society open science*, vol. 5, no. 4, p. 180 138, 2018.

[265] C.-C. Shih, T.-Y. Lai, and C.-C. Huang, "Evaluating the intensity of the acoustic radiation force impulse (arfi) in intravascular ultrasound (ivus) imaging: Preliminary in vitro results," *Ultrasonics*, vol. 70, pp. 64–74, 2016.

[266] V. Patel, J. J. Dahl, D. P. Bradway, J. R. Doherty, S. Y. Lee, and S. W. Smith, "Acoustic radiation force impulse imaging (arfi) on an ivus circular array," *Ultrasonic imaging*, vol. 36, no. 2, pp. 98–111, 2014.

[267] A. V. Telichko, J. J. Dahl, and C. D. Herickhoff, “Cylindrical transducer array for intravascular shear wave elasticity imaging: Preliminary development,” *IEEE transactions on ultrasonics, ferroelectrics, and frequency control*, vol. 69, no. 3, pp. 1077–1087, 2022.

[268] T. Wang, T. Pfeiffer, M. Wu, W. Wieser, G. Amenta, W. Draxinger, A. F. Van Der Steen, R. Huber, and G. Van Soest, “Thermo-elastic optical coherence tomography,” *Optics letters*, vol. 42, no. 17, pp. 3466–3469, 2017.

[269] R. W. Sanderson, Q. Fang, A. Curatolo, and B. F. Kennedy, *Optical Coherence Elastography Imaging Probes.* AIP Publishing LLCAIP PublishingMelville, New York.

[270] S. Latus, C. Otte, M. Schlüter, J. Rehra, K. Bizon, H. Schulz-Hildebrandt, T. Saathoff, G. Hüttmann, and A. Schlaefer, “An approach for needle based optical coherence elastography measurements,” in *Medical Image Computing and Computer-Assisted Intervention- MICCAI 2017: 20th International Conference, Quebec City, QC, Canada, September 11-13, 2017, Proceedings, Part II 20*, Springer, 2017, pp. 655–663.

[271] H. Lee, C. B. Capron, H.-C. Liu, T. Roy, M. N. Guddati, J. F. Greenleaf, and M. W. Urban, “Measurement of wave propagation through a tube using dual transducers for elastography in arteries,” *Physics in medicine and biology*, 2022.

[272] H. Schulz-Hildebrandt, T. Pfeiffer, T. Eixmann, S. Lohmann, M. Ahrens, J. Rehra, W. Draxinger, P. König, R. Huber, and G. Hüttmann, “High-speed fiber scanning endoscope for volumetric multi-megahertz optical coherence tomography,” *Optics letters*, vol. 43, no. 18, pp. 4386–4389, 2018.

[273] M. Neidhardt, S. Latus, T. Eixmann, G. Hüttmann, and A. Schlaefer, “Deep learning for high speed optical coherence elastography with a fiber scanning endoscope,” *IEEE Transactions on Medical Imaging*, 2024.

[274] V. Y. Zaitsev, A. L. Matveyev, L. A. Matveev, G. V. Gelikonov, E. V. Gubarkova, N. D. Gladkova, and A. Vitkin, “Hybrid method of strain estimation in optical coherence elastography using combined sub-wavelength phase measurements and supra-pixel displacement tracking,” *Journal of Biophotonics*, vol. 9, no. 5, pp. 499–509, 2016.

[275] J. M. Schmitt, “Oct elastography: Imaging microscopic deformation and strain of tissue,” *Optics express*, vol. 3, no. 6, pp. 199–211, 1998.

[276] C. Sun, B. A. Standish, B. Vuong, X.-Y. Wen, and V. X. D. Yang, “Digital image correlation–based optical coherence elastography,” *Journal of Biomedical Optics*, vol. 18, no. 12, p. 121 515, 2013.

[277] A. Beisenova, A. Issatayeva, D. Tosi, and C. Molardi, “Fiber-optic distributed strain sensing needle for real-time guidance in epidural anesthesia,” *IEEE Sensors Journal*, vol. 18, no. 19, pp. 8034–8044, 2018.

[278] M. Sticker, C. K. Hitzenberger, R. Leitgeb, and A. F. Fercher, "Quantitative differential phase measurement and imaging in transparent and turbid media by optical coherence tomography," *Opt. Lett.*, vol. 26, no. 8, pp. 518–520, Apr. 2001.

[279] M. A. Herráez, D. R. Burton, M. J. Lalor, and M. A. Gdeisat, "Fast two-dimensional phase-unwrapping algorithm based on sorting by reliability following a noncontinuous path," *Applied Optics*, vol. 41, no. 35, pp. 7437–7444, 2002.

[280] E. Barnhill, P. Kennedy, C. L. Johnson, M. Mada, and N. Roberts, "Real-time 4d phase unwrapping applied to magnetic resonance elastography," *Magnetic Resonance in Medicine*, vol. 73, no. 6, pp. 2321–2331, 2015.

[281] V. Y. Zaitsev, A. L. Matveyev, L. A. Matveev, G. V. Gelikonov, A. A. Sovetsky, and A. Vitkin, "Optimized phase gradient measurements and phase-amplitude interplay in optical coherence elastography," *Journal of Biomedical Optics*, vol. 21, no. 11, p. 116 005, 2016.

[282] M. A. Kirby, I. Pelivanov, S. Song, Ł. Ambrozinski, S. J. Yoon, L. Gao, D. Li, T. T. Shen, R. K. Wang, and M. O'Donnell, "Optical coherence elastography in ophthalmology," *Journal of biomedical optics*, vol. 22, no. 12, pp. 121 720–121 720, 2017.

[283] A. Ramier, B. Tavakol, and S.-H. Yun, "Measuring mechanical wave speed, dispersion, and viscoelastic modulus of the cornea using optical coherence elastography," *Optics express*, vol. 27, no. 12, pp. 16 635–16 649, 2019.

[284] X. Feng, G.-Y. Li, and S.-H. Yun, "Ultra-wideband optical coherence elastography from acoustic to ultrasonic frequencies," *Nature Communications*, vol. 14, no. 1, p. 4949, 2023.

[285] I. Pelivanov, L. Gao, J. Pitre, M. Kirby, S. Song, D. Li, T. Shen, R. Wang, and M. O'Donnell, "Does group velocity always reflect elastic modulus in shear wave elastography?" *Journal of Biomedical Optics*, vol. 24, no. 7, pp. 1–11, 2019.

[286] P. Kijanka and M. W. Urban, "Local phase velocity based imaging: A new technique used for ultrasound shear wave elastography," *IEEE Transactions on Medical Imaging*, vol. 38, no. 4, pp. 894–908, 2019.

[287] K. J. Parker, J. Ormachea, and Z. Hah, "Group versus phase velocity of shear waves in soft tissues," *Ultrasonic imaging*, vol. 40, no. 6, pp. 343–356, 2018.

[288] S. Ahmed, U. Kamal, and M. K. Hasan, "Dswe-net: A deep learning approach for shear wave elastography and lesion segmentation using single push acoustic radiation force," *Ultrasonics*, vol. 110, p. 106 283, 2021.

[289] M. Neidhardt, M. Bengs, S. Latus, M. Schluter, T. Saathoff, and A. Schlaefer, "Deep learning for high speed optical coherence elastography," in *2020 IEEE 17th International Symposium on Biomedical Imaging (ISBI)*, IEEE, uuuu-uuuu, pp. 1583–1586.

[290] M. Feigin, D. Freedman, and B. W. Anthony, "A deep learning framework for single-sided sound speed inversion in medical ultrasound," *IEEE Transactions on Biomedical Engineering*, vol. 67, no. 4, pp. 1142–1151, 2020.

[291] F. Q. Jin, L. C. Carlson, T. J. Hall, H. Feltovich, and M. L. Palmeri, "Deep learning based quantitative uncertainty estimation for ultrasound shear wave elasticity imaging," in *2021 IEEE International Ultrasonics Symposium (IUS)*, IEEE, uuuu-uuuu, pp. 1–4.

[292] S. Grube, M. Bengs, M. Neidhardt, S. Latus, and A. Schlaefer, "Ultrasound shear wave velocity estimation in a small field of view via spatio-temporal deep learning," in *Medical Imaging 2023: Image Processing*, O. Colliot, Ed., SPIE / International Society for Optical Engineering, 2023, p. 83.

[293] P. Meemon, J. Yao, Y.-J. Chu, F. Zvietcovich, K. J. Parker, and J. P. Rolland, "Crawling wave optical coherence elastography," *Optics letters*, vol. 41, no. 5, pp. 847–850, 2016.

[294] S. Sen, M. Ge, A. Prabhakar, V. Moll, R. J. Kaye, E. M. Cornett, O. M. Hall, I. W. Padnos, R. D. Urman, and A. D. Kaye, "Recent technological advancements in regional anesthesia," *Best practice & research Clinical anaesthesiology*, vol. 33, no. 4, pp. 499–505, 2019.

[295] I. P. Pappas, P. Ryan, P. Cossmann, J. Kowal, B. Borgeson, and M. Caversaccio, "Improved targeting device and computer navigation for accurate placement of brachytherapy needles," *Medical physics*, vol. 32, no. 6Part1, pp. 1796–1801, 2005.

[296] B. Saugel, T. W. Scheeren, and J.-L. Teboul, "Ultrasound-guided central venous catheter placement: A structured review and recommendations for clinical practice," *Critical Care*, vol. 21, no. 1, p. 225, 2017.

[297] G. Reusz, P. Sarkany, J. Gal, and A. Csomos, "Needle-related ultrasound artifacts and their importance in anaesthetic practice," *British journal of anaesthesia*, vol. 112, no. 5, pp. 794–802, 2014.

[298] J. Dolan, P. Lucie, T. Geary, M. Smith, and G. N. Kenny, "The rectus sheath block: Accuracy of local anesthetic placement by trainee anesthesiologists using loss of resistance or ultrasound guidance," *Regional Anesthesia & Pain Medicine*, vol. 34, no. 3, pp. 247–250, 2009.

[299] D. Tran, K.-W. Hor, A. A. Kamani, V. A. Lessoway, and R. N. Rohling, "Instrumentation of the loss-of-resistance technique for epidural needle insertion," *IEEE Transactions on Biomedical Engineering*, vol. 56, no. 3, pp. 820–827, 2009.

[300] S. P. DiMaio and S. E. Salcudean, "Needle insertion modeling and simulation," *IEEE Transactions on Robotics and Automation*, vol. 19, no. 5, pp. 864–875, 2003.

[301] J. Singh, A. R. Srinivasan, G. Neumann, and A. Kucukyilmaz, "Haptic-guided teleoperation of a 7-dof collaborative robot arm with an identical twin master," *IEEE transactions on haptics*, vol. 13, no. 1, pp. 246–252, 2020.

[302] W. Othman, Z.-H. A. Lai, C. Abril, J. S. Barajas-Gamboa, R. Corcelles, M. Kroh, and M. A. Qasaimeh, "Tactile sensing for minimally invasive surgery: Conventional methods and potential emerging tactile technologies," *Frontiers in Robotics and AI*, vol. 8, p. 705 662, 2021.

[303] E. Abdi, D. Kulic, and E. Croft, "Haptics in teleoperated medical interventions: Force measurement, haptic interfaces and their influence on user's performance," *IEEE transactions on bio-medical engineering*, vol. 67, no. 12, pp. 3438–3451, 2020.

[304] A. Talasaz, A. Luisa Trejos, S. Perreault, H. Bassan, and R. V. Patel, "A dual-arm 7-degrees-of-freedom haptics-enabled teleoperation test bed for minimally invasive surgery," *Journal of Medical Devices*, vol. 8, no. 4, 2014.

[305] S. Misra, K. T. Ramesh, and A. M. Okamura, "Modeling of tool-tissue interactions for computer-based surgical simulation: A literature review," *Presence (Cambridge, Mass.)*, vol. 17, no. 5, p. 463, 2008.

[306] A. M. Okamura, C. Simone, and M. D. O'Leary, "Force modeling for needle insertion into soft tissue," *IEEE transactions on bio-medical engineering*, vol. 51, no. 10, pp. 1707–1716, 2004.

[307] J. T. Hing, A. D. Brooks, and J. P. Desai, "Reality-based needle insertion simulation for haptic feedback in prostate brachytherapy," in *Proceedings 2006 IEEE International Conference on Robotics and Automation, 2006. ICRA 2006*, IEEE, 2006, pp. 619–624.

[308] D. J. van Gerwen, J. Dankelman, and J. J. van den Dobbelsteen, "Needle–tissue interaction forces – a survey of experimental data," *Medical Engineering & Physics*, vol. 34, no. 6, pp. 665–680, 2012.

[309] G. Ravali and M. Manivannan, "Haptic feedback in needle insertion modeling and simulation," *IEEE reviews in biomedical engineering*, vol. 10, pp. 63–77, 2017.

[310] A. Wittek, G. Bourantas, B. F. Zwick, G. Joldes, L. Esteban, and K. Miller, "Mathematical modeling and computer simulation of needle insertion into soft tissue," *PLOS ONE*, vol. 15, no. 12, e0242704, 2020.

[311] Z. Lv, Q. Song, F. Gao, Z. Liu, Y. Wan, and Y. Jiang, "Three-dimensional modeling and simulation of muscle tissue puncture process," *Chinese Journal of Mechanical Engineering*, vol. 35, no. 1, pp. 1–13, 2022.

[312] J. Chen, Z. Lin, S. Zhou, T. Wen, and Q. Zeng, "A meshfree method for deformation field reconstruction of soft tissue in needle insertion," in *2021 10th International*

Conference on Bioinformatics and Biomedical Science, New York, NY, USA: ACM, 2021, pp. 45–53.

[313] A. A. Yakovenko, Y.-X. Lai, I. G. Goryacheva, M.-S. Ju, M. Z. Dosaev, and Y. D. Selyutskiy, "Modeling and experimental study of the needle indentation into a brain phantom," *International Journal of Non-Linear Mechanics*, vol. 137, p. 103 832, 2021.

[314] M. A. Alamilla, C. Barnouin, R. Moreau, F. Zara, F. Jaillet, H. T. Redarce, and F. Coury, "A virtual reality and haptic simulator for ultrasound-guided needle insertion," *IEEE Transactions on Medical Robotics and Bionics*, vol. 4, no. 3, pp. 634–645, 2022.

[315] L. SABERSKI, S. KONDAMURI, and O. OSINUBI, "Identification of the epidural space: Is loss of resistance to air a safe technique?†a review of the complications related to the use of air," *Regional Anesthesia and Pain Medicine*, vol. 22, no. 1, pp. 3–15, 1997.

[316] John Dolan, Anne Williams, Eileen Murney, Malcolm Smith, and Gavin N.C. Kenny, "Ultrasound guided fascia iliaca block: A comparison with the loss of resistance technique," *Regional Anesthesia & Pain Medicine*, vol. 33, no. 6, pp. 526–531, 2008.

[317] R. Barua, S. Das, S. Datta, P. Datta, and A. Roy Chowdhury, "Study and experimental investigation of insertion force modeling and tissue deformation phenomenon during surgical needle-soft tissue interaction," *Proceedings of the Institution of Mechanical Engineers, Part C: Journal of Mechanical Engineering Science*, vol. 237, no. 5, pp. 1007–1014, 2023.

[318] S. Jiang, P. Li, Y. Yu, J. Liu, and Z. Yang, "Experimental study of needle–tissue interaction forces: Effect of needle geometries, insertion methods and tissue characteristics," *Journal of biomechanics*, vol. 47, no. 13, pp. 3344–3353, 2014.

[319] C. Otte, G. Hüttmann, and A. Schlaefer, "Feasibiliy of optical detection of soft tissue deformation during needle insertion," in *Medical Imaging 2012: Image-Guided Procedures, Robotic Interventions, and Modeling*, SPIE, vol. 8316, 2012, pp. 282–292.

[320] D. GAO, Y. LEI, and B. YAO, "Analysis of dynamic tissue deformation during needle insertion into soft tissue," *IFAC Proceedings Volumes*, vol. 46, no. 5, pp. 684–691, 2013.

[321] N. N. Stone, J. Roy, S. Hong, Y.-C. Lo, and R. G. Stock, "Prostate gland motion and deformation caused by needle placement during brachytherapy," *Brachytherapy*, vol. 1, no. 3, pp. 154–160, 2002.

[322] G. Wan, Z. Wei, L. Gardi, D. B. Downey, and A. Fenster, "Brachytherapy needle deflection evaluation and correction," *Medical physics*, vol. 32, no. 4, pp. 902–909, 2005.

[323] E. Scilingo, D. De Rossi, A. Bicchi, and P. Iacconi, "Sensors and devices to enhance the performances of a minimally invasive surgery tool for replicating surgeon's hap-

tic perception of the manipulated tissues," in *Proceedings of the 19th Annual International Conference of the IEEE Engineering in Medicine and Biology Society. 'Magnificent Milestones and Emerging Opportunities in Medical Engineering' (Cat. No.97CH36136)*, vol. 3, 1997, 961–964 vol.3.

[324] Y. Li and H. Li, "Penetration event identification based on neural network for needle tip location in robot assisted lumbar puncture surgery," *IEEE Robotics and Automation Letters*, vol. 9, no. 1, pp. 343–350, 2024.

[325] L. Yu, W. Wang, and F. Zhang, "External force sensing based on cable tension changes in minimally invasive surgical micromanipulators," *IEEE Access*, vol. 6, pp. 5362–5373, 2018.

[326] M. Sabieleish, K. Heryan, A. Boese, C. Hansen, M. Friebe, and A. Illanes, "Study of needle punctures into soft tissue through audio and force sensing: Can audio be a simple alternative for needle guidance?" *International Journal of Computer Assisted Radiology and Surgery*, vol. 16, no. 10, pp. 1683–1697, 2021.

[327] L. Wang, Z. Wang, and S. Hirai, "Modeling and simulation of friction forces during needle insertion using local constraint method," in *2012 IEEE/RSJ International Conference on Intelligent Robots and Systems*, 2012, pp. 4926–4932.

[328] D. de Lorenzo, Y. Koseki, E. de Momi, K. Chinzei, and A. M. Okamura, "Coaxial needle insertion assistant with enhanced force feedback," *IEEE transactions on biomedical engineering*, vol. 60, no. 2, pp. 379–389, 2013.

[329] N. Gessert, T. Priegnitz, T. Saathoff, S.-T. Antoni, D. Meyer, M. F. Hamann, K.-P. Jünemann, C. Otte, and A. Schlaefer, "Spatio-temporal deep learning models for tip force estimation during needle insertion," *International Journal of Computer Assisted Radiology and Surgery*, vol. 14, no. 9, pp. 1485–1493, 2019.

[330] J. B. Gafford, S. B. Kesner, A. Degirmenci, R. J. Wood, R. D. Howe, and C. J. Walsh, "A monolithic approach to fabricating low-cost, millimeter-scale multi-axis force sensors for minimally-invasive surgery," in *2014 IEEE International Conference on Robotics and Automation (ICRA)*, 2014, pp. 1419–1425.

[331] J. Radó, C. Dücső, P. Földesy, G. Szebényi, Z. Nawrat, K. Rohr, and P. Fürjes, "3d force sensors for laparoscopic surgery tool," *Microsystem Technologies*, vol. 24, no. 1, pp. 519–525, 2018.

[332] U. Kim, D.-H. Lee, H. Moon, J. C. Koo, and H. R. Choi, "Design and realization of grasper-integrated force sensor for minimally invasive robotic surgery," in *2014 IEEE/RSJ International Conference on Intelligent Robots and Systems*, 2014, pp. 4321–4326.

[333] U. Kim, Y. B. Kim, J. So, D.-Y. Seok, and H. R. Choi, "Sensorized surgical forceps for robotic-assisted minimally invasive surgery," *IEEE Transactions on Industrial Electronics*, vol. 65, no. 12, pp. 9604–9613, 2018.

[334] V. Mishra, H. Bouayad, A. Schned, A. Hartov, J. Heaney, and R. J. Halter, "A real-time electrical impedance sensing biopsy needle," *IEEE Transactions on Biomedical Engineering*, vol. 59, no. 12, pp. 3327–3336, 2012.

[335] G. Tholey and J. P. Desai, "A compact and modular laparoscopic grasper with tridirectional force measurement capability," *Journal of Medical Devices*, vol. 2, no. 3, 2008.

[336] S. Perreault, A. Talasaz, A. L. Trejos, C. D. Ward, R. V. Patel, and B. Kiaii, "A 7-dof haptics-enabled teleoperated robotic system: Kinematic modeling and experimental verification," in *Biomedical Robotics and Biomechatronics (BioRob), 2010 3rd IEEE RAS and EMBS International Conference on*, IEEE, 2010, pp. 906–911.

[337] R. Chadda, S. Wismath, M. Hessinger, N. Schäfer, A. Schlaefer, and M. Kupnik, "Needle tip force sensor for medical applications," in *2019 IEEE SENSORS*, 2019, pp. 1–4.

[338] S. Elayaperumal, J. H. Bae, D. Christensen, M. R. Cutkosky, B. L. Daniel, R. J. Black, J. M. Costa, F. Faridian, and B. Moslehi, "Mr-compatible biopsy needle with enhanced tip force sensing," in *2013 World Haptics Conference (WHC)*, 2013, pp. 109–114.

[339] S. Jäckle, T. Eixmann, H. Schulz-Hildebrandt, G. Hüttmann, and T. Pätz, "Fiber optical shape sensing of flexible instruments for endovascular navigation," *International Journal of Computer Assisted Radiology and Surgery*, vol. 14, no. 12, pp. 2137–2145, 2019.

[340] F. Khan, A. Denasi, D. Barrera, J. Madrigal, S. Sales, and S. Misra, "Multi-core optical fibers with bragg gratings as shape sensor for flexible medical instruments," *IEEE Sensors Journal*, vol. 19, no. 14, pp. 5878–5884, 2019.

[341] H. Su, M. Zervas, G. A. Cole, C. Furlong, and G. S. Fischer, "Real-time mri-guided needle placement robot with integrated fiber optic force sensing," in *2011 IEEE International Conference on Robotics and Automation*, IEEE, 2011, pp. 1583–1588.

[342] Z. Mo and W. Xu, "Temperature-compensated optical fiber force sensing at the tip of a surgical needle," *IEEE Sensors Journal*, vol. 16, no. 24, pp. 8936–8943, 2016.

[343] S. Beekmans, T. Lembrechts, J. van den Dobbelsteen, and D. van Gerwen, "Fiber-optic fabry-pérot interferometers for axial force sensing on the tip of a needle," *Sensors (Basel, Switzerland)*, vol. 17, no. 1, 2016.

[344] G. Wei and Q. Jiang, "A temperature-compensated force sensor based on a cascaded fpi for needle force sensing," *Measurement*, vol. 202, p. 111 748, 2022.

[345] M. Gromniak, N. Gessert, T. Saathoff, and A. Schlaefer, "Needle tip force estimation by deep learning from raw spectral oct data," *International Journal of Computer Assisted Radiology and Surgery*, vol. 15, no. 10, pp. 1699–1702, 2020.

[346] J. B. Gafford, R. J. Wood, and C. J. Walsh, "Self-assembling, low-cost, and modular mm-scale force sensor," *IEEE Sensors Journal*, vol. 16, no. 1, pp. 69–76, 2016.

[347] B. Carotenuto, A. Micco, A. Ricciardi, E. Amorizzo, M. Mercieri, A. Cutolo, and A. Cusano, "Optical guidance systems for epidural space identification," *IEEE Journal of Selected Topics in Quantum Electronics*, vol. 23, no. 2, pp. 371–379, 2017.

[348] G. Lan, M. Singh, K. V. Larin, and M. D. Twa, "Common-path phase-sensitive optical coherence tomography provides enhanced phase stability and detection sensitivity for dynamic elastography," *Biomedical optics express*, vol. 8, no. 11, pp. 5253–5266, 2017.

[349] U. Sharma, N. M. Fried, and J. U. Kang, "All-fiber common-path optical coherence tomography: Sensitivity optimization and system analysis," *IEEE Journal of selected topics in quantum electronics*, vol. 11, no. 4, pp. 799–805, 2005.

[350] M. Marrese, H. Offerhaus, E. Paardekam, and D. Iannuzzi, "70 mm diameter optical probe for common-path optical coherence tomography in air and liquids," *Optics Letters*, vol. 43, no. 24, pp. 5929–5932, 2018.

[351] S. Guo, N. R. Sarfaraz, W. G. Gensheimer, A. Krieger, and J. U. Kang, "Demonstration of optical coherence tomography guided big bubble technique for deep anterior lamellar keratoplasty (dalk)," *Sensors*, vol. 20, no. 2, p. 428, 2020.

[352] S. Guo and J. U. Kang, "Convolutional neural network-based common-path optical coherence tomography a-scan boundary-tracking training and validation using a parallel monte carlo synthetic dataset," *Optics Express*, vol. 30, no. 14, p. 25 876, 2022.

[353] M. Nijas, P. Kumar, A. Vijay, and R. John, "Oct-assisted needle for epidural injection," in *Unconventional Optical Imaging III*, M. P. Georges, G. Popescu, and N. Verrier, Eds., SPIE, 3.04.2022 - 23.05.2022, p. 56.

[354] C.-P. Liang, J. Wierwille, T. Moreira, G. Schwartzbauer, M. S. Jafri, C.-M. Tang, and Y. Chen, "A forward-imaging needle-type oct probe for image guided stereotactic procedures," *Optics Express*, vol. 19, no. 27, pp. 26 283–26 294, 2011.

[355] Q. Tang, C.-P. Liang, K. Wu, A. Sandler, and Y. Chen, "Real-time epidural anesthesia guidance using optical coherence tomography needle probe," in *CLEO: Applications and Technology*, Optica Publishing Group, 2014, AM2O–3.

[356] X. Sun and J. Li, "Design of a long working distance graded index fiber lens with a low na for fiber-optic probe in oct application," in *Optical Fibers and Sensors for Medical Diagnostics and Treatment Applications XIV*, SPIE, vol. 8938, 2014, pp. 64–70.

[357] S. Liang, J. Zhou, Z. Guo, D. He, W. Yang, Z. Ye, W. Shao, L. Jing, and S.-L. Chen, "Miniature probe for optomechanical focus-adjustable optical-resolution photoacoustic endoscopy," *IEEE Transactions on Medical Imaging*, vol. 42, no. 8, pp. 2400–2413, 2023.

[358] D. Lorenser, X. Yang, R. W. Kirk, B. C. Quirk, R. A. McLaughlin, and D. D. Sampson, "Ultrathin side-viewing needle probe for optical coherence tomography," *Optics Letters*, vol. 36, no. 19, pp. 3894–3896, 2011.

[359] L. Scolaro, D. Lorenser, R. A. McLaughlin, B. C. Quirk, R. W. Kirk, and D. D. Sampson, "High-sensitivity anastigmatic imaging needle for optical coherence tomography," *Optics Letters*, vol. 37, no. 24, pp. 5247–5249, 2012.

[360] Y. Wu, J. Xi, L. Huo, J. Padvorac, E. J. Shin, S. A. Giday, A. A. Lennon, M. I. F. Canto, J. H. Hwang, and X. Li, "Robust high-resolution fine oct needle for side-viewing interstitial tissue imaging," *IEEE Journal of Selected Topics in Quantum Electronics*, vol. 16, no. 4, pp. 863–869, 2010.

[361] R. A. McLaughlin, B. C. Quirk, A. Curatolo, R. W. Kirk, L. Scolaro, D. Lorenser, P. D. Robbins, B. A. Wood, C. M. Saunders, and D. D. Sampson, "Imaging of breast cancer with optical coherence tomography needle probes: Feasibility and initial results," *IEEE Journal of Selected Topics in Quantum Electronics*, vol. 18, no. 3, pp. 1184–1191, 2012.

[362] X. Yang, D. Lorenser, R. A. McLaughlin, R. W. Kirk, M. Edmond, M. C. Simpson, M. D. Grounds, and D. D. Sampson, "Imaging deep skeletal muscle structure using a high-sensitivity ultrathin side-viewing optical coherence tomography needle probe," *Biomedical optics express*, vol. 5, no. 1, pp. 136–148, 2013.

[363] W.-C. Kuo, M.-C. Kao, K.-Y. Chang, W.-N. Teng, M.-Y. Tsou, Y. Chang, and C.-K. Ting, "Fiber-needle swept-source optical coherence tomography system for the identification of the epidural space in piglets," *Anesthesiology*, vol. 122, no. 3, pp. 585–594, 2015.

[364] W.-C. Kuo, M.-C. Kao, M.-Y. Tsou, and C.-K. Ting, "In vivo images of the epidural space with two- and three-dimensional optical coherence tomography in a porcine model," *PLOS ONE*, vol. 12, no. 2, e0172149, 2017.

[365] M.-C. Kao, Y.-T. Wu, M.-Y. Tsou, W.-C. Kuo, and C.-K. Ting, "Intelligent epidural needle placement using fiber-probe optical coherence tomography in a piglet model," *Biomedical optics express*, vol. 9, no. 8, pp. 3711–3724, 2018.

[366] W.-N. Teng, M.-C. Kao, C.-K. Ting, and W.-C. Kuo, “Fiber-needle swept-source optical coherence tomography for the real-time visualization of the transversus abdominis plane block procedure in a swine model,” *Anesthesia and analgesia*, vol. 133, no. 2, pp. 526–534, 2021.

[367] E. Y.-H. Huang, M.-C. Kao, C.-K. Ting, W. J. S. Huang, Y.-T. Yeh, H.-H. Ke, and W.-C. Kuo, “Needle-probe optical coherence tomography for real-time visualization of veress peritoneal needle placement in a porcine model: A new safety concept for pneumoperitoneum establishment in laparoscopic surgery,” *Biomedicines*, vol. 10, no. 2, 2022.

[368] P. Herz, Y. Chen, A. Aguirre, K. Schneider, P. Hsiung, J. Fujimoto, K. Madden, J. Schmitt, J. Goodnow, and C. Petersen, “Micromotor endoscope catheter for in vivo, ultrahigh-resolution optical coherence tomography,” *Optics letters*, vol. 29, no. 19, pp. 2261–2263, 2004.

[369] C. Wang, P. Calle, N. B. Tran Ton, Z. Zhang, F. Yan, A. M. Donaldson, N. A. Bradley, Z. Yu, K.-M. Fung, C. Pan, and Q. Tang, “Deep-learning-aided forward optical coherence tomography endoscope for percutaneous nephrostomy guidance,” *Biomedical optics express*, vol. 12, no. 4, pp. 2404–2418, 2021.

[370] C. Wang, P. Calle, J. C. Reynolds, S. Ton, F. Yan, A. M. Donaldson, A. D. Ladymon, P. R. Roberts, A. J. de Armendi, K.-m. Fung, et al., “Epidural anesthesia needle guidance by forward-view endoscopic optical coherence tomography and deep learning,” *Scientific Reports*, vol. 12, no. 1, p. 9057, 2022.

[371] E. J. Seibel, Q. Y. Smithwick, C. M. Brown, and P. G. Reinhall, “Single-fiber flexible endoscope: General design for small size, high resolution, and wide field of view,” in *Biomonitoring and Endoscopy Technologies*, SPIE, vol. 4158, 2001, pp. 29–39.

[372] L. Huo, J. Xi, Y. Wu, and X. Li, “Forward-viewing resonant fiber-optic scanning endoscope of appropriate scanning speed for 3d oct imaging,” *Optics Express*, vol. 18, no. 14, pp. 14 375–14 384, 2010.

[373] N. Zhang, T.-H. Tsai, O. O. Ahsen, K. Liang, H.-C. Lee, P. Xue, X. Li, and J. G. Fujimoto, “Compact piezoelectric transducer fiber scanning probe for optical coherence tomography,” *Optics Letters*, vol. 39, no. 2, pp. 186–188, 2014.

[374] K. Liang, O. O. Ahsen, Z. Wang, H.-C. Lee, W. Liang, B. M. Potsaid, T.-H. Tsai, M. G. Giacomelli, V. Jayaraman, H. Mashimo, X. Li, and J. G. Fujimoto, “Endoscopic forward-viewing optical coherence tomography and angiography with mhz swept source,” *Optics Letters*, vol. 42, no. 16, pp. 3193–3196, 2017.

[375] S. Vilches, S. Kretschmer, Ç. Ataman, and H. Zappe, “Miniaturized fourier-plane fiber scanner for oct endoscopy,” *Journal of Micromechanics and Microengineering*, vol. 27, no. 10, p. 105 015, 2017.

[376] H. Schulz-Hildebrandt, T. Pfeiffer, T. Eixmann, S. Lohmann, M. Ahrens, J. Rehra, W. Draxinger, P. König, R. Huber, and G. Hüttmann, “High-speed fiber scanning endoscope for volumetric multi-megahertz optical coherence tomography,” *Optics letters*, vol. 43, no. 18, pp. 4386–4389, 2018.

[377] T. Wu, L. Zhang, J. Wang, W. Huo, Y. Lu, C. He, and Y. Liu, “Miniaturized precalibration-based lissajous scanning fiber probe for high speed endoscopic optical coherence tomography,” *Optics Letters*, vol. 45, no. 8, pp. 2470–2473, 2020.

[378] Y. Huang, “Full-range fourier domain optical coherence tomography imaging probe with a magnetic-driven resonant fiber cantilever,” *Optical Engineering*, vol. 50, no. 11, p. 119 002, 2011.

[379] E. J. Min, J. G. Shin, Y. Kim, and B. H. Lee, “Two-dimensional scanning probe driven by a solenoid-based single actuator for optical coherence tomography,” *Optics Letters*, vol. 36, no. 11, pp. 1963–1965, 2011.

[380] A. Boi, A. D. Jamthikar, L. Saba, D. Gupta, A. Sharma, B. Loi, J. R. Laird, N. N. Khanna, and J. S. Suri, “A survey on coronary atherosclerotic plaque tissue characterization in intravascular optical coherence tomography,” *Current Atherosclerosis Reports*, vol. 20, no. 7, p. 33, 2018.

[381] J. J. Rico-Jimenez, D. U. Campos-Delgado, M. Villiger, K. Otsuka, B. E. Bouma, and J. A. Jo, “Automatic classification of atherosclerotic plaques imaged with intravascular oct,” *Biomedical optics express*, vol. 7, no. 10, pp. 4069–4085, 2016.

[382] J. M. Schmitt, A. Knüttel, M. Yadlowsky, and M. A. Eckhaus, “Optical-coherence tomography of a dense tissue: Statistics of attenuation and backscattering,” *Physics in Medicine & Biology*, vol. 39, no. 10, pp. 1705–1720, 1994.

[383] G. van Soest, T. Goderie, E. Regar, S. Koljenović, G. L. J. H. van Leenders, N. Gonzalo, S. van Noorden, T. Okamura, B. E. Bouma, G. J. Tearney, J. W. Oosterhuis, P. W. Serruys, and A. F. W. van der Steen, “Atherosclerotic tissue characterization in vivo by optical coherence tomography attenuation imaging,” *Journal of Biomedical Optics*, vol. 15, no. 1, p. 011 105, 2010.

[384] K. A. Vermeer, J. Mo, J. J. A. Weda, H. G. Lemij, and J. F. de Boer, “Depth-resolved model-based reconstruction of attenuation coefficients in optical coherence tomography,” *Biomedical optics express*, vol. 5, no. 1, pp. 322–337, 2013.

[385] S. Chang and A. K. Bowden, “Review of methods and applications of attenuation coefficient measurements with optical coherence tomography,” *Journal of Biomedical Optics*, vol. 24, no. 9, pp. 1–17, 2019.

[386] R. A. McLaughlin, L. Scolaro, P. Robbins, C. Saunders, S. L. Jacques, and D. D. Sampson, “Parametric imaging of cancer with optical coherence tomography,” *Journal of Biomedical Optics*, vol. 15, no. 4, p. 046 029, 2010.

[387] P. Gong, M. Almasian, G. van Soest, D. de Bruin, T. van Leeuwen, D. Sampson, and D. Faber, “Parametric imaging of attenuation by optical coherence tomography: Review of models, methods, and clinical translation,” *Journal of Biomedical Optics*, vol. 25, no. 4, pp. 1–34, 2020.

[388] R. Rasti, H. Rabbani, A. Mehridehnavi, and F. Hajizadeh, “Macular oct classification using a multi-scale convolutional neural network ensemble,” *IEEE transactions on medical imaging*, vol. 37, no. 4, pp. 1024–1034, 2017.

[389] P. Strenge, B. Lange, W. Draxinger, C. Grill, V. Danicke, D. Theisen-Kunde, C. Hagel, S. Spahr-Hess, M. M. Bonsanto, H. Handels, R. Huber, and R. Brinkmann, “Differentiation of different stages of brain tumor infiltration using optical coherence tomography: Comparison of two systems and histology,” *Frontiers in Oncology*, vol. 12, p. 896 060, 2022.

[390] J. Möller, E. Popanda, N. H. Aydın, H. Welp, I. Tischoff, C. Brenner, K. Schmieder, M. R. Hofmann, and D. Miller, “Accurate oct-based diffuse adult-type glioma who grade 4 tissue classification using comprehensible texture feature analysis,” *Biomedical Signal Processing and Control*, vol. 88, p. 105 047, 2024.

[391] S. S. Tucker, J. T. Giblin, K. Kiliç, A. Chen, J. Tang, and D. A. Boas, “Optical coherence tomography-based design for a real-time motion corrected scanning microscope,” *Optics Letters*, vol. 48, no. 14, pp. 3805–3808, 2023.

[392] N. Gessert, J. Beringhoff, C. Otte, and A. Schlaefer, “Force estimation from oct volumes using 3d cnns,” *International Journal of Computer Assisted Radiology and Surgery*, vol. 13, no. 7, pp. 1073–1082, 2018.

[393] N. Gessert, M. Bengs, M. Schlüter, and A. Schlaefer, “Deep learning with 4d spatiotemporal data representations for oct-based force estimation,” *Medical image analysis*, vol. 64, p. 101 730, 2020.

[394] A. A. Nazari, F. Janabi-Sharifi, and K. Zareinia, “Image-based force estimation in medical applications: A review,” *IEEE Sensors Journal*, vol. 21, no. 7, pp. 8805–8830, 2021.

[395] M. Schlüter, L. Glandorf, M. Gromniak, T. Saathoff, and A. Schlaefer, “Concept for markerless 6d tracking employing volumetric optical coherence tomography,” *Sensors*, vol. 20, no. 9, p. 2678, 2020.

[396] M. Bengs, N. Gessert, M. Schlüter, and A. Schlaefer, “Spatio-temporal deep learning methods for motion estimation using 4d oct image data,” *International journal of computer assisted radiology and surgery*, vol. 15, pp. 943–952, 2020.

[397] J. Sprenger, M. Neidhardt, M. Schlüter, S. Latus, T. Gosau, J. Kemmling, S. Feldhaus, U. Schumacher, and A. Schlaefer, “In-vivo markerless motion detection from volumetric optical coherence tomography data using cnns,” in *Medical Imaging 2021:*

Image-Guided Procedures, Robotic Interventions, and Modeling, SPIE, vol. 11598, 2021, pp. 400–405.

[398] M. Draelos, G. Tang, B. Keller, A. Kuo, K. Hauser, and J. A. Izatt, "Optical coherence tomography guided robotic needle insertion for deep anterior lamellar keratoplasty," *IEEE Transactions on Biomedical Engineering*, vol. 67, no. 7, pp. 2073–2083, 2019.

[399] B. Keller, M. Draelos, G. Tang, S. Farsiu, A. N. Kuo, K. Hauser, and J. A. Izatt, "Real-time corneal segmentation and 3d needle tracking in intrasurgical oct," *Biomedical optics express*, vol. 9, no. 6, pp. 2716–2732, 2018.

[400] R. Mieling, C. Stapper, S. Gerlach, M. Neidhardt, S. Latus, M. Gromniak, P. Breitfeld, and A. Schlaefer, "Proximity-based haptic feedback for collaborative robotic needle insertion," in *International Conference on Human Haptic Sensing and Touch Enabled Computer Applications*, Springer, 2022, pp. 301–309.

[401] S. Latus, M. Neidhardt, M. Lutz, N. Gessert, N. Frey, and A. Schlaefer, "Quantitative analysis of 3d artery volume reconstructions using biplane angiography and intravascular oct imaging," *IEEE Engineering in Medicine and Biology Society. Annual International Conference*, vol. 2019, pp. 6004–6007, 2019.

[402] R. Mieling, S. Latus, N. Gessert, M. Lutz, and A. Schlaefer, "Deep learning-based rotation frequency estimation and nurd correction for ivoct image data.," *(Suppl1) International Journal of CARS'2020*, vol. 15, no. (1), pp. 162–163, Jun. (2020).

[403] S. Latus, F. Griese, M. Gräser, M. Möddel, M. Schlüter, C. Otte, N. Gessert, T. Saathoff, T. Knopp, and A. Schlaefer, "Towards bimodal intravascular oct mpi volumetric imaging," in *Medical Imaging 2018: Physics of Medical Imaging*, SPIE, vol. 10573, 2018, pp. 611–616.

[404] S. Latus, F. Griese, M. Schlüter, C. Otte, M. Möddel, M. Graeser, T. Saathoff, T. Knopp, and A. Schlaefer, "Bimodal intravascular volumetric imaging combining oct and mpi," *Medical Physics*, vol. 46, no. 3, pp. 1371–1383, 2019.

[405] F. Griese, S. Latus, M. Schlüter, M. Graeser, M. Lutz, A. Schlaefer, and T. Knopp, "In-vitro mpi-guided ivoct catheter tracking in real time for motion artifact compensation," *PLOS ONE*, vol. 15, no. 3, e0230821, 2020.

[406] D. F. Dementhon and L. S. Davis, "Model-based object pose in 25 lines of code," *International Journal of Computer Vision*, vol. 15, no. 1-2, pp. 123–141, 1995.

[407] A. A. Taha and A. Hanbury, "Metrics for evaluating 3d medical image segmentation: Analysis, selection, and tool," *BMC medical imaging*, vol. 15, pp. 1–28, 2015.

[408] S. Latus, S. Grube, T. Eixmann, M. Neidhardt, S. Gerlach, R. Mieling, G. Huttmann, M. Lutz, and A. Schlaefer, "A miniature dual-fiber probe for quantitative optical coherence elastography," *IEEE Transactions on Biomedical Engineering*, vol. PP, 2023.

[409] X. Sun and J. Li, "Design of a long working distance graded index fiber lens with a low na for fiber-optic probe in oct application," in *Optical Fibers and Sensors for Medical Diagnostics and Treatment Applications XIV*, SPIE, vol. 8938, 2014, pp. 64–70.

[410] S. Latus, J. Sprenger, M. Neidhardt, J. Schadler, A. Ron, A. Fitzek, M. Schluter, P. Breitfeld, A. Heinemann, K. Puschel, and A. Schlaefer, "Rupture detection during needle insertion using complex oct data and cnns," *IEEE transactions on bio-medical engineering*, vol. 68, no. 10, pp. 3059–3067, 2021.

[411] S. Latus, P. Breitfeld, M. Neidhardt, and A. Schlaefer, "Boundary prediction during epidural punctures based on oct relative motion analysis," *European journal of anaesthesiology*, vol. 2020, 2020.

[412] D. Bhattacharya, S. Latus, F. Behrendt, F. Thimm, D. Eggert, C. Betz, and A. Schlaefer, "Tissue classification during needle insertion using self-supervised contrastive learning and optical coherence tomography," in *2023 45th Annual International Conference of the IEEE Engineering in Medicine Biology Society (EMBC)*, 2023, pp. 1–4.

[413] K. Singh, D. Yamada, and G. Tearney, "Astigmatism corrected common path probe for optical coherence tomography," *Lasers in Surgery and Medicine*, vol. 49, no. 3, pp. 312–318, 2017.

[414] J. L. Barron, D. J. Fleet, and S. S. Beauchemin, "Performance of optical flow techniques," *International journal of computer vision*, vol. 12, pp. 43–77, 1994.

[415] K. He, X. Zhang, S. Ren, and J. Sun, "Deep residual learning for image recognition," in *Proceedings of the IEEE conference on computer vision and pattern recognition*, 2016, pp. 770–778.

[416] J. Deng, W. Dong, R. Socher, L.-J. Li, K. Li, and L. Fei-Fei, "Imagenet: A large-scale hierarchical image database," in *2009 IEEE conference on computer vision and pattern recognition*, Ieee, 2009, pp. 248–255.

[417] A. Tharwat, "Classification assessment methods," *Applied computing and informatics*, vol. 17, no. 1, pp. 168–192, 2020.

[418] A. Weber, F. Werner, J. Weizenecker, T. M. Buzug, and T. Knopp, "Artifact free reconstruction with the system matrix approach by overscanning the field-free-point trajectory in magnetic particle imaging," *Physics in Medicine & Biology*, vol. 61, no. 2, p. 475, 2015.

[419] A. Forte, F. D'amico, M. Charalambides, D. Dini, and J. Williams, "Modelling and experimental characterisation of the rate dependent fracture properties of gelatine gels," *Food Hydrocolloids*, vol. 46, pp. 180–190, 2015.

[420] T. Buranakarl, K. Jaisanuk, R. Varatorn, C. Suchato, and S. Srisuphap, "Stentoplasty (cemented kyphoplasty with stent) under biplane digital subtraction angiography (biplane dsa)," *The Bangkok Medical Journal*, vol. 2, pp. 48–48, 2011.

[421] B. Friedrich, C. Maegerlein, D. Lobsien, S. Mönch, M. Berndt, D. Hedderich, S. Wunderlich, D. Michalski, M. Lehm, T. Boeckh-Behrens, et al., "Endovascular stroke treatment on single-plane vs. bi-plane angiography suites: Technical considerations and evaluation of treatment success," *Clinical Neuroradiology*, vol. 29, pp. 303–309, 2019.

[422] S. Liu, J. Eggermont, R. Wolterbeek, A. Broersen, C. A. Busk, H. Precht, B. P. Lelieveldt, and J. Dijkstra, "Analysis and compensation for the effect of the catheter position on image intensities in intravascular optical coherence tomography," *Journal of biomedical optics*, vol. 21, no. 12, pp. 126 005–126 005, 2016.

[423] A. C. Bakenecker, M. Ahlborg, C. Debbeler, C. Kaethner, T. M. Buzug, and K. Lüdtke-Buzug, "Magnetic particle imaging in vascular medicine," *Innovative surgical sciences*, vol. 3, no. 3, pp. 179–192, 2018.

[424] M. O. Pacheco, I. K. Gerzenshtein, W. L. Stoppel, and C. M. Rinaldi-Ramos, "Advances in vascular diagnostics using magnetic particle imaging (mpi) for blood circulation assessment," *Advanced Healthcare Materials*, vol. 13, no. 23, p. 2 400 612, 2024.

[425] J. E. Phipps, T. Hoyt, D. Halaney, J. J. Mancuso, S. Elahi, A. Cabe, M. Cilingiroglu, T. E. Milner, and M. D. Feldman, "Intravascular oct imaging artifacts," *Cardiovascular OCT Imaging*, pp. 53–66, 2020.

[426] D. Liu, Y. Liu, Y. Xin, and Q. Li, "Correcting motion artifacts of heart for intravascular optical coherence tomography images," in *Optics in Health Care and Biomedical Optics X*, SPIE, vol. 11553, 2020, pp. 31–38.

[427] M. Möddel, F. Griese, T. Kluth, and T. Knopp, "Estimating the spatial orientation of immobilized magnetic nanoparticles with parallel-aligned easy axes," *Physical review applied*, vol. 16, no. 4, p. L041003, 2021.

[428] M. Möddel, F. Griese, T. Kluth, and T. Knopp, "Estimating orientation using multi-contrast mpi," *International Journal on Magnetic Particle Imaging IJMPI*, vol. 6, no. 2 Suppl 1, 2020.

[429] S. Zheng, D. Jiejie, Y. Yue, M. Qi, and S. Huifeng, "A deep learning method for motion artifact correction in intravascular photoacoustic image sequence," *IEEE Transactions on Medical Imaging*, vol. 42, no. 1, pp. 66–78, 2022.

[430] G. Liao, O. Caravaca-Mora, B. Rosa, P. Zanne, D. Dall'Alba, P. Fiorini, M. de Mathelin, F. Nageotte, and M. J. Gora, "Distortion and instability compensation with deep

learning for rotational scanning endoscopic optical coherence tomography," *Medical image analysis*, vol. 77, p. 102 355, 2022.

[431] H. Zhang, J. Yang, J. Zhang, S. Zhao, and A. Zhang, "Cross-attention learning enables real-time nonuniform rotational distortion correction in oct," *Biomedical Optics Express*, vol. 15, no. 1, pp. 319–335, 2023.

[432] Y. Fang and M. Yu, "Oct-guided pci in elderly patients," *Aging Medicine*, 2024.

[433] J. Frizzell and D. J. Kereiakes, "Calcified plaque modification during percutaneous coronary revascularization," *Progress in Cardiovascular Diseases*, 2024.

[434] Y. Gharaibeh, D. Prabhu, C. Kolluru, J. Lee, V. Zimin, H. Bezerra, and D. Wilson, "Coronary calcification segmentation in intravascular oct images using deep learning: Application to calcification scoring," *Journal of Medical Imaging*, vol. 6, no. 4, pp. 045 002–045 002, 2019.

[435] G.-A. Cheimariotis, M. Riga, K. Haris, K. Toutouzas, A. K. Katsaggelos, and N. Maglaveras, "Automatic classification of a-lines in intravascular oct images using deep learning and estimation of attenuation coefficients," *Applied Sciences*, vol. 11, no. 16, p. 7412, 2021.

[436] Y. S. Lau, L. K. Tan, C. K. Chan, K. H. Chee, and Y. M. Liew, "Automated segmentation of metal stent and bioresorbable vascular scaffold in intravascular optical coherence tomography images using deep learning architectures," *Physics in Medicine & Biology*, vol. 66, no. 24, p. 245 026, 2021.

[437] Y. Gharaibeh, J. Lee, V. N. Zimin, C. Kolluru, L. A. Dallan, G. T. Pereira, A. Vergara-Martel, J. N. Kim, A. Hoori, P. Dong, et al., "Prediction of stent under-expansion in calcified coronary arteries using machine learning on intravascular optical coherence tomography images," *Scientific Reports*, vol. 13, no. 1, p. 18 110, 2023.

[438] T. M. Hommels, R. S. Hermanides, E. Fabris, and E. Kedhi, "Exploring new insights in coronary lesion assessment and treatment in patients with diabetes mellitus: The impact of optical coherence tomography," *Cardiovascular Diabetology*, vol. 22, no. 1, p. 123, 2023.

[439] D. Cronin and C. Falzon, "Characterization of 10% ballistic gelatin to evaluate temperature, aging and strain rate effects," *Experimental mechanics*, vol. 51, pp. 1197–1206, 2011.

[440] H. Xu, Q. Xia, C. Shu, J. Lan, X. Wang, W. Gao, S. Lv, R. Lin, Z. Xie, X. Xiong, et al., "In vivo endoscopic optical coherence elastography based on a miniature probe," *Biomedical Optics Express*, vol. 15, no. 7, pp. 4237–4252, 2024.

[441] A. J. Engel and G. R. Bashford, “A new method for shear wave speed estimation in shear wave elastography,” *IEEE Transactions on Ultrasonics, Ferroelectrics, and Frequency Control*, vol. 62, no. 12, pp. 2106–2114, 2015.

[442] P. Santos, A. M. Petrescu, J. P. Pedrosa, M. Orlowska, V. Komini, J.-U. Voigt, and J. D’hooge, “Natural shear wave imaging in the human heart: Normal values, feasibility, and reproducibility,” *IEEE transactions on ultrasonics, ferroelectrics, and frequency control*, vol. 66, no. 3, pp. 442–452, 2019.

[443] F. P. Johnson, “The isolation, shape, size, and number of the lobules of the pig’s liver,” *American Journal of Anatomy*, vol. 23, no. 2, pp. 273–283, 1918.

[444] T. M. Bauman, T. M. Nicholson, L. L. Abler, K. W. Eliceiri, W. Huang, C. M. Vezina, and W. A. Ricke, “Characterization of fibrillar collagens and extracellular matrix of glandular benign prostatic hyperplasia nodules,” *PLoS one*, vol. 9, no. 10, e109102, 2014.

[445] H. J. Scholten, A. Pourtaherian, N. Mihajlovic, H. H. Korsten, and R. A. Bouwman, “Improving needle tip identification during ultrasound-guided procedures in anaesthetic practice,” *Anaesthesia*, vol. 72, no. 7, pp. 889–904, 2017.

[446] C. Sun, F. Nolte, K. H. Y. Cheng, B. Vuong, K. K. C. Lee, B. A. Standish, B. Courtney, T. R. Marotta, A. Mariampillai, and V. X. D. Yang, “In vivo feasibility of endovascular doppler optical coherence tomography,” *Biomedical optics express*, vol. 3, no. 10, pp. 2600–2610, 2012.

[447] M. Gromniak, N. Gessert, T. Saathoff, and A. Schlaefer, “Needle tip force estimation by deep learning from raw spectral oct data,” *International Journal of Computer Assisted Radiology and Surgery*, vol. 15, no. 10, pp. 1699–1702, 2020.

[448] M. Sahlabadi and P. Hutapea, “Tissue deformation and insertion force of bee-stinger inspired surgical needles,” *Journal of Medical Devices*, vol. 12, no. 3, 2018.

[449] R. Mieling, M. Neidhardt, S. Latus, C. Stapper, S. Gerlach, I. Kniep, A. Heinemann, B. Ondruschka, and A. Schlaefer, “Collaborative robotic biopsy with trajectory guidance and needle tip force feedback,” in *2023 IEEE International Conference on Robotics and Automation (ICRA)*, 2023, pp. 6893–6900.

[450] G. Lan, M. Singh, K. V. Larin, and M. D. Twa, “Common-path phase-sensitive optical coherence tomography provides enhanced phase stability and detection sensitivity for dynamic elastography,” *Biomedical optics express*, vol. 8, no. 11, pp. 5253–5266, 2017.

[451] R. Kafieh, H. Rabbani, and S. Kermani, “A review of algorithms for segmentation of optical coherence tomography from retina,” *Journal of Medical Signals & Sensors*, vol. 3, no. 1, pp. 45–60, 2013.

[452] I. A. Viedma, D. Alonso-Caneiro, S. A. Read, and M. J. Collins, "Deep learning in retinal optical coherence tomography (oct): A comprehensive survey," *Neurocomputing*, vol. 507, pp. 247–264, 2022.

[453] Y. Wang, S. Wei, R. Zuo, M. Kam, J. D. Opfermann, I. Sunmola, M. H. Hsieh, A. Krieger, and J. U. Kang, "Automatic and real-time tissue sensing for autonomous intestinal anastomosis using hybrid mlp-dc-cnn classifier-based optical coherence tomography," *Biomedical Optics Express*, vol. 15, no. 4, pp. 2543–2560, 2024.

[454] R. Mieling, S. Latus, F. Behrendt, D. Bhattacharya, M. Neidhardt, and A. Schlaefer, "Can complex-valued neural networks improve force sensing with optical coherence tomography?" In *2024 IEEE International Symposium on Biomedical Imaging (ISBI)*, 2024, pp. 1–4.

[455] L. Wang, S. Chen, L. Liu, X. Yin, G. Shi, and J. Mo, "Axial super-resolution optical coherence tomography via complex-valued network," *Physics in Medicine & Biology*, vol. 68, no. 23, p. 235 016, 2023.

[456] E. Cole, J. Cheng, J. Pauly, and S. Vasanawala, "Analysis of deep complex-valued convolutional neural networks for mri reconstruction and phase-focused applications," *Magnetic resonance in medicine*, vol. 86, no. 2, pp. 1093–1109, 2021.

[457] M. Yang, M. Q. Ma, D. Li, Y.-H. H. Tsai, and R. Salakhutdinov, "Complex transformer: A framework for modeling complex-valued sequence," in *ICASSP 2020-2020 IEEE International Conference on Acoustics, Speech and Signal Processing (ICASSP)*, IEEE, 2020, pp. 4232–4236.

[458] S. Moon and Z. Chen, "Phase-stability optimization of swept-source optical coherence tomography," *Biomedical optics express*, vol. 9, no. 11, pp. 5280–5295, 2018.

[459] H. Fu, X. Wang, K. Diao, S. Huang, H. Liu, Y. Gao, Q. Zhao, Z.-g. Yang, and Y.-k. Guo, "Ct compared to mri for functional evaluation of the right ventricle: A systematic review and meta-analysis," *European Radiology*, vol. 29, pp. 6816–6828, 2019.

[460] S. Zhang, A. A. Joseph, D. Voit, S. Schaetz, K.-D. Merboldt, C. Unterberg-Buchwald, A. Hennemuth, J. Lotz, and J. Frahm, "Real-time magnetic resonance imaging of cardiac function and flow—recent progress," *Quantitative imaging in medicine and surgery*, vol. 4, no. 5, p. 313, 2014.

[461] P. Bhattacharji and W. Moore, "Application of real-time 3d navigation system in ct-guided percutaneous interventional procedures: A feasibility study," *Radiology Research and Practice*, vol. 2017, no. 1, p. 3 151 694, 2017.

[462] A. E. Campbell-Washburn, M. A. Tavallaei, M. Pop, E. K. Grant, H. Chubb, K. Rhode, and G. A. Wright, "Real-time mri guidance of cardiac interventions," *Journal of Magnetic Resonance Imaging*, vol. 46, no. 4, pp. 935–950, 2017.

[463] M. Ahlborg, T. Friedrich, T. Göttsche, V. Scheitenberger, R. Linemann, M. Wattenberg, A. T. Buessen, T. Knopp, P. Szwargulski, M. G. Kaul, et al., "First dedicated balloon catheter for magnetic particle imaging," *IEEE transactions on medical imaging*, vol. 41, no. 11, pp. 3301–3308, 2022.

[464] J. Salamon, M. Hofmann, C. Jung, M. G. Kaul, F. Werner, K. Them, R. Reimer, P. Nielsen, A. Vom Scheidt, G. Adam, et al., "Magnetic particle/magnetic resonance imaging: In-vitro mpi-guided real time catheter tracking and 4d angioplasty using a road map and blood pool tracer approach," *PloS one*, vol. 11, no. 6, e0156899, 2016.

[465] S. Herz, P. Vogel, P. Dietrich, T. Kampf, M. A. Rückert, R. Kickuth, V. C. Behr, and T. A. Bley, "Magnetic particle imaging guided real-time percutaneous transluminal angioplasty in a phantom model," *Cardiovascular and interventional radiology*, vol. 41, pp. 1100–1105, 2018.

[466] M. Möddel, F. Griese, T. Kluth, and T. Knopp, "Estimating the spatial orientation of immobilized magnetic nanoparticles with parallel-aligned easy axes," *Physical review applied*, vol. 16, no. 4, p. L041003, 2021.

[467] M. P. Bui, T.-A. Le, and J. Yoon, "A magnetic particle imaging-based navigation platform for magnetic nanoparticles using interactive manipulation of a virtual field free point to ensure targeted drug delivery," *IEEE Transactions on Industrial Electronics*, vol. 68, no. 12, pp. 12 493–12 503, 2020.

[468] A. C. Bakenecker, A. von Gladiss, H. Schwenke, A. Behrends, T. Friedrich, K. Lüdtke-Buzug, A. Neumann, J. Barkhausen, F. Wegner, and T. M. Buzug, "Navigation of a magnetic micro-robot through a cerebral aneurysm phantom with magnetic particle imaging," *Scientific reports*, vol. 11, no. 1, p. 14 082, 2021.

[469] A. C. Bakenecker, A. von Gladiss, T. Friedrich, U. Heinen, H. Lehr, K. Lüdtke-Buzug, and T. M. Buzug, "Actuation and visualization of a magnetically coated swimmer with magnetic particle imaging," *Journal of Magnetism and Magnetic Materials*, vol. 473, pp. 495–500, 2019.

[470] R. Mieling, M. Neidhardt, F. Behrendt, S. Latus, A. Heinemann, B. Ondruschka, and A. Schlaefer, "A-scan sequence transformers for palpation with optical coherence elastography," *Biomedical Optics Express*, vol. 16, no. 5, pp. 1925–1943, 2025.

List of Tables

List of Figures

List of Symbols

$\mathbf{E}(z, t)$	Electromagnetic field of an infrared light wave
$\mathbf{E}_0$	Electromagnetic field amplitude
λ_o	Wavelength
k_o	Wavenumber
$k_{\mathrm{o},0}$	Central wavenumber
f_o	Frequency
w_o	Angular frequency
ϕ	Phase shift angle
Δz_o	Optical path length difference
$\Delta\lambda_\mathrm{o}$	Optical bandwidth
Δk_o	Spectral bandwidth
$\lambda_{\mathrm{o},0}$	Central wavelength
l_c	Coherence length
δz_o	OCT axial resolution
$\mathbf{E}_\mathrm{i}$	Electromagnetic field amplitude of light emitted by the laser light source
$\mathbf{E}_\mathrm{R}(z, t)$	Electromagnetic field refracted from the OCT reference arm
$\mathbf{E}_\mathrm{S}(z, t)$	Electromagnetic field refracted from the OCT sample arm

$r_\mathrm{S}(z_\mathrm{S})$	Sample arm reflectivity function
z_S	Sample arm length
$z_{\mathrm{S},m}$	Tissue boundary depth m in sample arm
M	Number of tissue boundaries
$r_\mathrm{R}(z_\mathrm{R})$	Reference arm reflectivity function
z_R	Reference arm length
$\mathbf{E}_\mathrm{D}$	Electromagnetic wave field amplitude measured at the OCT detector
ρ_o	Responsivity of the OCT detector
δk_o	Spectral sampling interval
$I_\mathrm{D}(k_\mathrm{o})$	Spectral interference pattern
R_R	Amplitude of light reflections at the reference arm
$R_{\mathrm{S},m}$	Amplitude of light reflections at the different tissue depths in the sample arm
$\Delta\Phi$	Phase difference between sequentially acquired depth scans
$v_{\mathrm{rel},z}$	Particle velocity component measured along the OCT imaging axis
T_OCT	OCT A-scan sampling period
f_OCT	OCT A-scan frequency

n_o	Average refractive index along the optical beam
δx_o	Lateral resolution of OCT sample beam
NA	Numerical Aperture of optical lens setup
$FOV_{\mathrm{OCT},z}$	OCT axial FOV size
P	Number of pixels per OCT A-scan
H	Number of A-scans per cross-sectional IVOCT image
v_pull	Translation velocity of IVOCT probe
$\mathbf{p}$	Vascular boundary points
c_a	Acoustic wave velocity
ρ_a	Acoustic density of a material
κ_a	Acoustic compressibility of a material
Z	Acoustic impedance
f_a	Applied frequency at piezoelectric actuator
I_a	Acoustic intensity signal
$\alpha(f_\mathrm{a})$	Acoustic damping coefficient
C	Number of excitation cycles for US imaging
Δf_a	Frequency shift due to moving object
θ	Angle between US beam and the particle motion direction
v_rel	Relative particle motion velocity

z_{F}	Acoustic focus depth
w_{e}	Elevational resolution of acoustic beam
w_{e}	Lateral resolution of acoustic beam
SPL	Spatial pulse length
C	Number of cycles to create on US pulse
T_{RX}	Duration of one US transmit and receive sequence
N_{US}	Number of US scan lines
f_{US}	US B-Mode imaging frequency
β_{US}	US wave steering angle
f_{PRF}	US plane wave imaging frequency
I_{X}	Intensity measured at an X-ray detector
μ	X-ray attenuation coefficient
γ_{C}	Orientation angle of C-arm
f_{C}	X-ray imaging frequency
f_{MPI}	MPI actuation frequency
U_l	MPI measurements acquired over time
L	Number of MPI measurements per 3D position
G_{lq}	MPI system matrix
$c_{\mathrm{MPI},q}$	Particle concentration per 3D position

Q	Number of MPI positions evaluated
σ	Stress measured during tissue compression
ε	Strain measured during tissue compression
Δd	Local tissue deformations
d	Tissue width
F	Force
A	Area
E	Young's modulus
v_{s}	Shear wave velocity
ρ_{s}	Tissue density
ν	Poisson ratio of a material
Δs	Spatial distance between shear wave excitation and imaging
Δt_{s}	Runtime of a shear wave between excitation and imaging
λ_{s}	Shear wave length
f_{s}	Shear wave frequency
k_{s}	Shear wave number
$v_{\mathrm{s,ph}}$	Shear wave phase velocity
t_{I}	Time point of shear wave imaging

t_E	Time point of shear wave excitation
c_th	Threshold value for shear wave peak detection
$v_\mathrm{s,ST}$	Shear wave velocity extracted from OCE space-time maps
$v_\mathrm{s,DF}$	Shear wave velocity extracted from dual-fiber OCE
α_x	Spatial orientation of OCE probe to excitation source in x
α_y	Spatial orientation of OCE probe to excitation source in y
$v_\mathrm{s,US}$	Shear wave velocity extracted from USE
F_ind	Indentor force applied during compression testings
r_ph	Phantom radius
$h_\mathrm{ph,0}$	Initial phantom height
Δh_ph	Compressed phantom height
$\mathbf{e}$	Shear wave excitation positions
z_p	z-Axis of probe coordinate system
y_p	y-Axis of probe coordinate system
x_p	x-Axis of probe coordinate system
$S(z,t)$	Complex OCT signal expressed over depth and time
φ	Rotation angle for radial image acquisition

$S(z, \varphi)$	Complex OCT signal expressed over depth and rotation angle
f_{rot}	Angular rotation rate of imaging probe
$v_{\mathrm{p},x}$	Probe motion velocity in x-direction
$S(z, x)$	Complex OCT signal expressed over depth and probe motion in x
α_{p}	Rotation angle around probe x-Axis
β_{p}	Rotation angle around probe y-Axis
γ_{p}	Rotation angle around probe z-Axis
$\Delta p_{1,2}$	Distance between imaging optics
$\Delta t_{1,2}$	Run time of shear wave between dual-fiber OCE imaging optics
I	Number of Probe positions
a	Slope of boundaries in OCT M-scan
g	Number of connected pixels in a boundary
x_{FT}	Spatial x-axis of force measurements
y_{FT}	Spatial y-axis of force measurements
z_{FT}	Spatial z-axis of force measurements
F_z	Force values measured along the probe shaft

F_{avg}	Average force measured along the probe axis during insertion
ΔF_z	Force difference per insertion
$F_{z,\mathrm{max}}$	Maximal force during insertion
$F_{z,\mathrm{min}}$	Minimal force during insertion
∇F_z	Force gradient during insertion
ΔI_{US}	US image intensity brightness derivatives
$\mathbf{u}$	Particle motion vector pointing horizontal US image direction
$\mathbf{m}$	Particle motion vector pointing vertical US image direction
$d_{\mathrm{US,p}}$	Relative motion assessed from vectors in the positive needle motion direction
$d_{\mathrm{US,n}}$	Relative motion assessed from vectors in the negative needle motion direction
t_{R}	Time point of rupture event
$t_{\mathrm{R,US}}$	Time point of rupture event extracted from US
$t_{\mathrm{R,FT}}$	Time point of rupture event extracted from FT
b_{F}	Scaling factor to evaluate force values
b_{US}	Scaling factor to evaluate US deformation values

List of Acronyms

ARF	Acoustic Radiation Force
ARFI	Acoustic Radiation Force Imaging
CAD	Computer Aided Design
CCD	Charge-Coupled Device
CNN	Convolutional Neural Network
CT	Computed Tomography
DF-OCE	Dual-Fiber OCE
DICE	Dice Coefficient
DSA	Digital Subtraction Angiography
ECG	Electrocardiography
FBG	Fiber-Bragg Grating
FD-OCT	Fourier-Domain OCT
FEM	Finite Element Modeling
FFP	Field Free Point
FFT	Fast Fourier Transformation
FOV	Field of View
FT	Force-Torque
GRIN	Gradient-Index
IVOCT	Intravascular Optical Coherence Tomography
IVUS	Intravascular Ultrasound
LAO	Left Anterior Oblique
LOR	Loss-Of-Resistance
MIS	Minimal Invasive Surgery

MPI	Magnetic Particle Imaging
MRI	Magnetic Resonance Imaging
NURD	Non-Uniform Rotational Distorsion
OCE	Optical Coherence Elastography
OCT	Optical Coherence Tomography
PCI	Percutaneous Coronary Intervention
PRF	Pulse Repetition Frequency
PZT	Piezoelectric Transducer
RAO	Right Anterior Oblique
ROC	Receiver Operating Characteristic
SD-OCT	Spectral-Domain OCT
SF-OCE	Single-Fiber OCE
SMF	Single Mode Fiber
SNR	Signal-to-Noise Ratio
SPIONs	Superparamagnetic Iron Oxide Nanoparticles
SS-OCT	Swept-Source OCT
SVM	Support Vector Machine
SWEI	Shear Wave Elastography Imaging
TD-OCT	Time-Domain OCT
TGC	Time Gain Compensation
US	Ultrasound
USE	Ultrasound Elastography